



Wilkinson, Andrew James (2016) *Biomimetic topography in orthopaedic ceramic*. MD thesis.

<http://theses.gla.ac.uk/7791/>

Available under License Creative Commons Attribution Non-commercial Share Alike:
<https://creativecommons.org/licenses/by-nc-sa/4.0/>

Glasgow Theses Service
<http://theses.gla.ac.uk/>
theses@gla.ac.uk

Biomimetic topography in Orthopaedic Ceramic

Andrew James Wilkinson

MB, BCh, BAO, MRCS,

FRCS Trauma Orthopaedics (Edinburgh)



University
of Glasgow

Submitted in fulfilment of the requirements for the degree of MD

Centre for Cell Engineering
Institute of Molecular, Cell and Systems Biology
College of Medical, Veterinary and Life Sciences
University of Glasgow,
G12 8QQ

January 2016

Abstract

The primary objective of this research was to perform an in vitro assessment of the ability of microscale topography to alter cell behaviour, with specific regard to producing favourable topography in an orthopaedic ceramic material suitable for implantation in the treatment of arthritis.

Topography at microscale and nanoscale alters the bioactivity of the material. This has been used in orthopaedics for some time as seen with optimal pore size in uncemented hip and knee implants. This level of topography involves scale in hundreds of micrometres and allows for the ingrowth of tissue. Topography at smaller scale is possible thanks to progressive miniaturisation of technology.

A topographic feature was created in a readily available clinically licensed polymer, Polycaprolactone (PCL). The effect of this topography was assessed in vitro.

The same topography was transferred to the latest generation composite orthopaedic ceramic, zirconia toughened alumina (ZTA). The fidelity of reproduction of the topography was examined using scanning electron microscopy (SEM) and atomic force microscopy (AFM). These investigations showed more accurate reproduction of the topography in PCL than ZTA with some material artefacts in the ZTA.

Cell culture in vitro was performed on the patterned substrates. The response of osteoprogenitor cells was assessed using immunohistochemistry, real-time polymerase chain reaction and alizarin staining. These results showed a small effect on cell behaviour.

Finally metabolic comparison was made of the effects created by the two different materials and the topography in each.

The results have shown a reproducible topography in orthopaedic ceramics. This topography has demonstrated a positive osteogenic effect in both polycaprolactone and zirconia toughened alumina across multiple assessment modalities.

Table of Contents

Abstract

List of figures

Publications and presentations relating to the research

Acknowledgements

Authors Declaration

List of definitions and abbreviations

Biomimetic topography in Orthopaedic Ceramic 1

Abstract 2

Publications and presentations relating to this thesis 18

Acknowledgement 19

Author's Declaration 20

Abbreviations and definitions 21

1 Introduction 23

1.1 Biomaterials 23

1.1.1 First generation biomaterials 23

1.1.2 Second generation biomaterials 24

1.1.3 Third generation biomaterials 26

1.1.4 Bone biology 27

1.2	The historical perspective on orthopaedic first generation biomaterials	33
1.2.1	The early development of joint arthroplasty	33
1.2.2	Metal on Polyethylene	35
1.2.3	Ceramic development	36
1.3	Fixation techniques	39
1.3.1	Cemented fixation	39
1.3.2	Nanotechnology in the enhancement of cemented fixation	40
1.3.3	Uncemented fixation	40
1.3.4	Nanotechnology in the enhancement of uncemented fixation	42
1.4	Rationale for work, aims and objectives	43
1.4.1	Rationale for work	43
1.4.2	Aims and objectives	44
2	Materials and methods	46
2.1	Manufacture of nickel shims for embossing	46
2.2	Micropatterned polycaprolactone	47
2.2.1	Polycaprolactone (PCL)	47
2.2.2	Manufacture of embossed Polycaprolactone	47
2.3	Micropatterned Ceramic	48
2.3.1	Manufacture of Alumina and Zirconia toughened Alumina	48
2.3.2	Characterisation of embossed ceramics	49
2.3.3	Scanning Electron microscopy	51
2.4	Cell Harvest	51
2.5	Cell extraction	52
2.6	Cell Culture	54

2.6.1	Cell maintenance and passage	54
2.6.2	Collecting cells for expansion or experimentation on substrates.	54
2.6.3	Counting cells	54
2.6.4	Seeding cells	55
2.7	Immunofluorescent protein imaging	56
2.7.1	Immunofluorescent microscopy	56
2.7.2	Immunofluorescent staining	57
2.8	Alizarin red staining	60
2.9	Brilliant blue staining	61
2.10	Polymerase chain reaction	61
2.10.1	RNA purification	61
2.10.2	Reverse transcription	63
2.10.3	Polymerase chain reaction	64
2.10.4	Real time qualitative Polymerase Chain Reaction	64
2.11	Polarised light microscopy	65
2.12	Metabolomics	65
2.13	Discussion	66
3	Testing the osteogenic potential of circular topographical features	68
3.1	Introduction	68
3.2	Materials and methods	69
3.2.1	Creating embossed polymer	69
3.2.2	Microscopy	69
3.3	Results	70

3.3.1	Culture for three days, staining for cytoskeleton, tubulin network and focal adhesions	70
3.4	Discussion	75
3.4.1	Focal adhesions and cytoskeleton	75
3.4.2	Osteopontin expression	76
3.4.3	Alizarin staining	76
3.5	Conclusion	77
4	Materials characterisation.	78
4.1	Introduction	78
4.2	Materials and topographies	78
4.2.1	Polycaprolactone	78
4.2.2	Masks used for embossing ceramics	79
4.2.3	Alumina and Zirconia toughened alumina	80
4.3	Discussion	90
4.3.1	PCL	90
4.3.2	Optical Microscopy for assessment of Masks	91
4.3.3	Topography in ceramic	91
4.4	Conclusion	95
5	Testing the osteogenic capacity of the circular topography in ceramic with primary human cells.	97
5.1	Introduction	97
5.2	Materials and methods	97
5.2.1	Focal adhesions	97
5.2.2	Phenotype immunostaining for osteopontin and osteocalcin	100

5.2.3	PCR	101
5.2.4	Alizarin Red staining	101
5.2.5	Statistical analysis	103
5.3	Results	104
5.3.1	Immunofluorescent staining	104
5.3.2	PCR	124
5.3.3	Alizarin	128
5.4	Discussion	134
5.4.1	Immunofluorescent microscopy	134
5.4.2	PCR	138
5.5	Conclusion	140
6	Metabolomics, the response of cells cultured on different materials and different topographies.	142
6.1	Introduction	142
6.2	Materials and Methods	142
6.2.1	Cell culture and sample processing	142
6.2.2	IDEOM	143
6.2.3	Metaboanalyst	143
6.2.4	Ingenuity pathway analysis	143
6.3	Results	143
6.3.1	From Metaboanalyst	143
6.3.2	Results from Ingenuity Pathway Analysis	149
6.4	Discussion	154
6.4.1	Materials differences	154

6.4.2 Topographical differences	156
6.5 Conclusion	156
7 Summary	157
7.1 Why is there a need for this research	157
7.2 Is it reasonable to make judgements on the bone implant interface based on an in vitro model and cell behaviour?	158
7.3 Rationale for research choices	159
7.4 Positive results	159
7.5 Other results	162
7.6 Weaknesses	163
7.7 Future work	165
7.8 Conclusion.	165
List of References	167
8 Appendices	192
8.1 Osteogenic array plate format	192

List of figures

Figure 1-1 Orthopaedic implants in contact with bone. Clockwise from top left, a sliding hip screw with the barrel and threads in the medullary bone, an uncemented femoral implant against the medullary bone and screws through a plate, contacting both the cortical and medullary bone.	28
Figure 2-1 Schematic representation of Atomic Force microscopy. Reproduced from Wikimedia under a share alike creative commons licence. Original author Grzegorz Wielgoszewski.	50

- Figure 2-2 Harvesting bone marrow at total hip replacement. Left Box, chisel in position to remove cancellous bone from the proximal femur. Right, aspirating quill placed in the medullary cavity of the femur aspirating marrow contents. 52
- Figure 2-3 - FICOLL gradient separation of constituent parts 53
- Figure 2-4 Schematic of an immunofluorescent microscope. 57
- Figure 2-5 - Schematic of antibody staining technique 59
- Figure 3-1 A scanning electron microscopy image of a rat osteoclast leaving behind a resorption pit. Reproduced with permission from Professor T Arnett University College London 68
- Figure 3-2 Immunofluorescent microscopy images for tubulin and vinculin staining after three days of culture. Red = actin, green = tubulin/vinculin, blue = nucleus. Reprinted with permission from Elsevier {Wilkinson:2011bo} 71
- Figure 3-3 Phenotype staining for osteopontin (in green in the left hand column) at 21 days of culture and calcium staining by alizarin red (red in the right hand column light microscopy images) at 28 days of culture. . Reprinted with permission from Elsevier {Wilkinson:2011bo} 73
- Figure 3-4 Graphical representation of the ANOVA for particles of calcium on substrates cultured for 28 days. Far fewer alizarin red-positive areas were noted on the control compared to on the pitted surfaces. Most alizarin red-positive areas were noted on the 30 μ m diameter pits, tying in well with main script qualitative data. Results are mean \pm SD. *p < 0.05 compared to control; \$p < 0.05 compared to other test substrates by ANOVA. 74
- Figure 3-5 SEM images of PCL with a cell monolayer covering the substrate. The substrates are seen from 20 μ m circular pit most superior and the 40 μ m pit most inferior. The high magnification views in the right had column show cells distributed evenly across the surface with no particular change in appearance around the circular pits. The left hand column shows some nodular structures across the surface of the substrates. The nature of the nodules is uncertain. There does not appear to be any correlation between these features and the embossed topography. 74
- Figure 4-1 SEM pictures of the embossed substrates of polycaprolactone easily visible through the monolayer of human osteoblastic cells. The morphology of the shapes is clear and the features have sharp well-defined edges. Each image within the montage contains a scale bar. Using this bar the dimensions for the features have been measured. The measurements may be seen in the right hand column of the image. Interestingly the dimensions of the features are reduced compared to the intended size. Reduction of between 10 % (for the 20 μ m substrate) and 7.5% (for the 40 μ m substrate). 79

Figure 4-2 Light microscopy images of the masks created for embossing zirconia toughened alumina. The right hand column shows measurement lines created in ImageJ from the included scale bar. These confirm the pitch of the features to be accurate at 100 μm for each mask; likewise the intended features are accurate for each mask. 80

Table 4-1 detection of elemental composition for Zirconia alumina ceramic. There is wide variation in the detection of the composite parts. The outlier for the samples is clearly the 40 μm sample with almost 70% oxygen detected. 81

Table 4-2 ratio of alumina to zirconia content. Calculation of the ratios for the two elements highlights the significant variation in detected elements. Although this may not be reflective of the materials in bulk it shows that the surface presented to the cells is variable by chemistry 81

Figure 4-3 Two dimensional surface trace and dimension assessment of 20 μm embossed ZTA. The right hand image shows the width of the feature as 15 μm and the maximum depth of the feature is 500 nm (or half the intended value). The red line shows the background trace has some variation in height with many small features on the scale of a few micrometres. 82

Figure 4-4 Two dimensional surface trace of 30 micron embossed ZTA. Two variations on surface profiling. The left image shows a surface trace along three lines; blue and red lines trace the embossed feature and the green line traces the background surface. The red and blue lines confirm the presence of the feature, they also confirm the dimensional reduction and the slope to the sides of the pit. These two aspects are further emphasised by the right hand trace. The left hand green trace clearly demonstrates the background surface irregularities at a scale of 1 or 2 μm , additionally a significant rise is noted, this approaches 1 μm in height - the same magnitude as the depth of embossed feature. 83

Figure 4-5 Two dimensional surface trace of 40 micron embossed ZTA. While clearly visible as a feature the sides of the feature are not straight, the base of the feature contains many islands of nanometre size and the dimensions of the feature are smaller in both axes that intended or achieved by the manufacturing for the masks. Also note the oblong shape to the feature 83

Figure 4-6 These three dimensional renders of all the sizes of substrates provide good visual data on the multiple peak surface presented to the cells. Where the embossed features are clearly reproduced and present the background surface to the materials is significant. Some depressions are seen as are some islands which are a magnitude of size smaller (nanometre size) 84

Figure 4-7 distortion of 30 μm embossed ceramic. This valley feature is smooth sided and very large but of a similar depth to the intended features. The typical peak structure seen across the rest of the substrate (and indeed all the other examples) is missing at the left hand side of the surface image - this absence of peaks suggests that there may be an error in tip contact

however the continued presence of the defect through the entire length of the substrate can not be explained by a technical error. 85

Figure 4-8 Distortion of a 40 μm embossed ceramic. There appears to be a folding of the substrate affecting the feature and the background surface, presumably this has occurred with removal of the embossing mask prior to sintering. The artefact is of similar magnitude to the intended feature. Referring to the blue and red markers on the left hand image shows little difference between the cross sectional profile of the red markers (background surface trace) and the blue markers (cross sectional profile of the substrate including the embossed feature) 85

Figure 4-9 - high-resolution image of the surface of the zirconia (small white grains) with Alumina (large grey grains). Note the presence of zirconia mostly along the grain boundary (best position to act as a toughening agent), also note the greatly increased size of the alumina grains. This phenomenon is well recognised during sintering is related to dissipation of energy after heating, it is still a consideration in the presentation of surface features to the cells. 86

Figure 4-10, Low and medium magnification views of the embossed ZTA ceramic. The 20 μm feature (row 1) is difficult to see, the magnification has been increased, and two features have been marked for more straightforward identification. The 30 μm features are more easily seen, clearly reproducible however there is a significant manufacturing artefact through the entire sample, this ridge like artefact will have a topographical influence on cell behaviour and is a similar magnitude to the intended size of feature. The 40 μm embossed feature is the most obvious, both on the 500 x view (left column) and the 4000 x view (right column), although there is little artefact in this substrate there is definitely variation in the depth of the features (the pits in the top three rows particularly for the first four columns are much more shallow than those at the opposite corner of the sample. 88

Figure 4-11 Direct measurement from the Scanning electron microscope. These direct measurements confirm that there is significant dimensional reduction during the processing of the ceramics. The percentage shrinkage varies from 15% (40 μm) to 30% (20 μm) although the measurement bars for the 20 μm are inaccurately placed in this example. 89

Figure 4-12 - Artefact in the ceramic surface. This slide shows a concerning crevice type structure, likely a side effect of the drying and sintering process clearly this presents a feature to the cells that is much greater than the depth of intended feature. The effect of such a deep feature on the cells is uncertain, however this feature will cause mechanical difficulty for the implant, it would not survive proof testing and is unlikely therefore to be a real concern in vivo. 89

Figure 4-15 3 dimensional reconstruction of a 40 micron pit, colour variation shows the difference in height. The edge of the feature is definitely sloping

rather than sharp and defined, likely related to the granular structure of the ceramic this may have an effect on cell behaviour 90

Figure 4-16 A Schematic showing the difficulty in using a pyramidal cantilever tip to attempt detection of a sheer edge feature. The interpretation of the side of the feature will inevitably be influenced by the geometry of the probe 94

Figure 5-1 side by side images of the same cell, showing the difficulties in focus on an entire cell. 98

Figure 5-2 illustration for separately labelling in focus areas of a cell. In the top row the two images are focussed on different portions of the cell. The focal adhesions in these areas are then highlighted as shown in the bottom row (40x magnification) 98

Figure 5-3 Combining labelled images. Once the in focus areas are labelled, the relevant images are converted to an image stack, this image stack may then be combined focussing on the areas of high light intensity in a Z-plane projection (x40 magnification) 99

Figure 5-4 Thresholded combined image of focal adhesions. The combined images are then subjected to a threshold for light intensity (allowing for a dark background) the filter level for light intensity is set to capture only the focal adhesions 99

Figure 5-5 focal adhesions highlighted for planar and patterned ceramics. Three rows for each set of substrates. Labelled on the far right of the image. At first inspection there is no great difference between any of the sets of images. A closer inspection shows differences in cell shape and spread with greater spread (and therefore tension) in the topographical substrates when compared to the controls. Any qualitative comparison of focal adhesions is unreliable and statistical analysis of size and number of particles has been used. (40x magnification) 106

Table 5-1 - 3 way ANOVA of the distribution of focal adhesions across the planar and patterned ZTA ceramic. The results here show that the focal adhesions on the 40 μm substrate are greater than all the other surfaces with significant p values in all the comparisons. Surprisingly the focal adhesions for the 20 μm and 30 μm samples are down regulated in comparison to the control again with significance. The differences between the 20 μm ad 30 μm substrates did not reach statistical significance. 107

Figure 5-6 Graphical representation of the distribution by size (y axis) for particles detected for each substrate. The red indicators represent the triplicate samples for the 20 μm substrate, the blue represent the 30 μm substrates, the 40 μm substrates are shown in green and the variable shades of purple show the particles found on the planar controls. \blacklozenge statistical significance for larger focal adhesions compared to the control, 20 μm and

30 μm samples. ★ statistical significance for greater focal adhesion size compared to 20 μm and 30 μm samples. 108

Figure 5-7 graphical representation of the distribution of focal adhesions separated by topography. The majority of the focal adhesions are concentrated around the same size. Significant increase in the presence of larger focal adhesions in the 40 μm substrate. 109

Figure 5-8 Graphical representations of the ratios of variance for a two way ANOVA on the left image. This two way assessment evaluated variation arising from within the sample (that is between triplicates) or due to the pattern (between samples). It shows that while intra-samples variation is present, it is much less than variation between samples. 109

Figure 5-9 the graph and table from a three way ANOVA assessing the variance arising from the pattern and the substrate, related to each technical replicate. Much greater variance is seen from the pattern than the different substrates 110

Figure 5-10 images for planar ZTA stained for OPN. Very little extracellular protein is seen in these images. Protein levels are generally low within and outwith the cells, the presence of intracellular protein makes the position and clustering of the cells a slightly greater artefact in assessing the protein level. 112

Figure 5-11 Images for the 20 μm ZTA stained for OPN. While there is still relatively little extracellular expression of OPN there does appear to be more for the 20 μm substrate than for the planar control. The effect of cell clustering is more obvious here given the stronger intracellular expression of protein compared to the control. (x20 magnification) 113

Figure 5-12 Images for the 30 μm ZTA stained for OPN. As with the images seen for the 20 μm substrate there appears to be greater intracellular and extracellular protein in these images as compared to those for the control. 114

Figure 5-13 Images for the 40 μm ZTA stained for OPN. These images appear very similar to those captured for the other two embossed substrates. There may be slightly greater extracellular protein expression but this is by no means a clear difference. 115

Figure 5-14. Box plots for the data showing the thresholded particle count for OPN, with expression of total area of protein. The left hand image shows the data as processed. The patterned substrates show more particles of OPN than the control, although there is significant variance. On the right the data is shown post square root transformation. The differences in the data become more easily seen with the 20 μm substrate generating more particles than the other embossed substrates and the control producing the least OPN. The data is shown as IQR and median, ★ significance over

control $P < 0.05$, significance over the other patterned substrates $p < 0.05$
(GLM gamma transformation) 116

Figure 5-15. Box plots showing the mean particle size for OPN. The left hand graph again shows the positive results for the 20 μm patterned substrate. The variance is skewed inferiorly (positive or to the left). In order to overcome the skew and variance the data was transformed by square root. This is represented on the right hand graph, showing a clear increase in size for the protein expressed on the 20 μm patterned substrate. All three patterned substrates perform more strongly than the control substrate. Data is shown as median and IQR ★ Significance over control $p < 0.05$ (GLM gamma transformation). 116

Figure 5-16. Box plot for OPN particle count. As with the other assessments here the 20 μm substrate produces more particles than any of the other surfaces. ◆ significance over control $p < 0.05$, ★ significance over 40 μm substrate $p < 0.05$, ■ significance over 30 μm substrate (GLM poisson transformation) 117

Figure 5-17 Images for the control ZTA stained for OCN. The wide variation in background light levels creates a difficulty in accurately assessing the expression of protein. There is clearly a much greater level of protein expression here than for the OPN. The extracellular protein expression is highly varied across the captured images. 119

Figure 5-18 Images for 20 μm ZTA stained for OCN. A similar level of background variation affects these images as is seen in those for the control. Extracellular protein expression appears more consistent across all the images and so may be greater in total. 120

Figure 5-19 Images for the 30 μm ZTA stained for OCN. Visual inspection of these images suggests a lesser expression of protein than in the other surfaces. 121

Figure 5-20 images for the 40 μm ZTA stained for OCN, these images are by far the most consistent for production of OCN, although the summative protein deposition may not be greater than the control, the spread of protein from sample to sample is much more uniform. 122

Figure 5-21. Box plots for the area covered by the OCN protein for all substrates. Left shows the positive skew to the data and suggests a greater total coverage by the flat control. With the best performance in the patterned substrates seen in the 40 μm substrate. The right hand graph shows the data transformed to improve the distribution. This shows the same pattern of result, the greatest area covered by the OCN protein was seen on the control, with the optimal topography for OCN production being the 40 μm substrate. ★ significance over 30 μm substrate $p < 0.05$, ◆ significance over 20 μm substrate $p < 0.05$, ■ significance over 40 μm substrate $p < 0.05$ (GLM gamma transformation). 123

Figure 5-22. Box plot showing the mean OCN particle size per image for the substrates. The size of particles across the samples is greatest on the 40 μm substrate. It is interesting to note the similar pattern of result as seen with the focal adhesions, with the 20 μm substrate producing a less favourable result than the control. ◆significance over 20 μm substrate $p < 0.05$, ★ significance over planar control $p < 0.05$ and ■ significance over 30 μm substrate $p < 0.05$ (GLM gamma transformation) 123

Figure 5-23. Box plot for OCN particle count. Mean for the control substrate is the highest but also with the greatest variation and the most skew. The mean for the 40 μm pattern is the next highest followed by the 20 μm and then the 30 μm . The high levels of particle expression explain the great surface coverage seen in the control even though the particles are small. ★ significance over 30 μm substrate, ◆ significance over 20 μm substrate, ■significance over 40 μm substrate $p < 0.05$ (GLM poisson transformation) 124

Figure 5-24 Changes in expression of RUNX2 normalised to the planar control surface after 6 days of culture. Upregulation was seen for all topographies compared to control. Greatest upregulation was seen for the 40 μm surface, error bars are standard deviation. Control values are 0. No statistically significant change for any topography over control (p values of 0.46, 0.47 and 0.19 for the 20 μm 30 μm and 40 μm substrates)(Excel ® Microsoft). 125

Figure 5-25 Upregulation of osteopontin expression normalised to the planar control after 9 days of culture. Upregulation was noted for all surfaces compared to control, notably for the 20 μm and 40 μm surfaces than the 30 μm surface. Error bars represent standard deviation. Control values are 0. No statistically significant difference for any substrate over control (p values of 0.17, 0.47 and 0.19 for 20 μm , 30 μm and 40 μm substrates) (Excel ® Microsoft). 125

Figure 5-26 Expression of Osteonectin (Blue) and BMPR2 (red) in PCR for culture at 7 days and 14 days on alumina ceramic. The patterned substrates generate an upregulation in gene expression at both time points. The standard deviation (represented with the error bars are much smaller at 14 days. The 7 day results while showing a greater increase in expression over control samples do not reach statistical significance ($p = 0.07$ for osteonectin, $p = 0.1$ for BMPR2) however for both results after 14 days of culture the results are statistically significant ($p = 0.04$ for osteonectin, $p = 0.001$ for BMPR2). 126

Figure 5-27 Graphical representation of gene expression with standard deviation error bars for the osteogenic array. For all the above results where upregulation is seen the standard deviation is high enough to prevent a statistically significant result with the only statistically significant result with $p < 0.05$ being for GDF10. 127

Figure 5-29 Montage of all the scanned images of ZTA in triplicate across each pattern. There is no discernable difference on these scanned image,

assessment for overall colour reveals a great similarity, neither are there any appreciable differences in the presence of any large nodules. 129

Figure 5-30 Montage of alizarin stained cells on ZTA ceramic. Inspection of these images does not reveal any great difference in the presence of calcium across the different substrates (x5 magnification). 130

Figure 5-31 montage of images from polarising microscope with 20x objective lens. The features in the substrate have been highlighted. These images were captured to assess the position of calcium deposits in relation to the topographical features in the samples. Accounting for the greater surface area covered by the larger features (bigger feature with maintained centre - centre spacing) no appreciable difference is seen across the difference sizes of feature. It is noteworthy that almost all the calcium deposits in the photographs are intracellular, with very few free nodules (x20 magnification). 131

Figure 5-32 Montage of the alizarin stained patterned substrates after counterstaining with brilliant blue stain. Surface features have been highlighted where they were visible, in this representative sample of images the cell sheet appears to cover most of the material surface. This suggests that the cells will certainly be exposed to the features in some part. There is no relationship between the location of the features and the position of the cells (x20 magnification). 132

Figure 5-33 box plot of the size of particles stained by Alizarin red detected across the planar control ceramic and the three patterned substrates. The lower section of the graph may appear empty; the whisker representing the lowest is too small to be appreciated. The upper whisker shows the upper quartile. There is no statistically significant difference between any of the topographies 133

Figure 5-34 Frequency histograms of the distribution of particle size. No significant difference for particle size is found, the data is all significantly skewed to the left. 133

Figure 6-1 The overall heatmap for the metabolome of the samples. The colour legend in the top left corner shows red dark blue for the PCL samples and pale blue and green for the ZTA samples. The grouping in the figure has the patterned materials superiorly and the planar samples inferiorly. The colour graduation scale shows blue spectrum indicates downregulation and into the red spectrum indicating upregulation. This graph is included for general trend as there are too many metabolites included than could be sensibly interpreted. The result from the graph indicates metabolic activity more related to material than topography. 144

Figure 6-2 PCA for the overall metabolome of the samples. Three markers in each colour indicate the location of each of the triplicates, colour coding in the top right corner shows green for the patterned ceramics, pale blue for the flat ceramic, red for patterned PCL and dark blue for planar PCL. Each

triplicate sample is outlined according to distribution. Progression of the X-axis indicates the primary differentiating variable. This accounts for over 98 % of the distribution, the PCL samples are grouped with significant overlap, where the ceramic materials are independent of each other. The Y-axis shows the distribution in the second component, (in this instance 1.2% contribution), the ceramics and plastics are clearly separated with no significant effect of the topography visible. 145

Figure 6-3 Heat map for lipid metabolism only. The colour legends show red and green for patterned PCL and ZTA with dark blue and pale blue for flat PCL and ZTA. The PCL samples are generally down regulated compared with the ZTA samples, the 40 μm ZTA (green) samples show the most activity. 146

Figure 6-4 PCA for lipid metabolism. The green results for patterned ZTA are the stand out group, with the tightest grouping and most separation to the pale blue of the control ZTA, which overlaps the red of the patterned PCL in both axes. The dark blue of the control PCL overlaps both the patterned PCL and control ZTA in the first component but only the patterned PCL in the second component. 147

Figure 6-5 Heatmap for energy metabolism. Note the distinct differences in activity between topographies rather than between material type. The patterned surfaces create a greater upregulation than the controls. 147

Figure 6-6 PCA for energy metabolism. Allowing for the outlier (highlighted in purple), these results show a tight grouping by topography rather than by material type. The difference is most obvious for the the ZTA pattern against ZTA control. 148

Figure 6-7 Bar Chart of planar ZTA normalised to planar PCL. This bar chart reflects the organisation of results into diseases and functions. The results show increased activity of the cells cultured on ZTA compared to those on PCL, this demonstrates the material effect on planar substrates 149

Figure 6-8 Network map for the increased activity of cells of planar ZTA normalised to those on planar PCL. Demonstrating the material effect on planar substrates. The up-regulation of note is ERK, involved in cell signalling that relates to differentiation. 150

Figure 6-9 Stacked bar chart on the canonical pathways. Comparison made of patterned ZTA to patterned PCL. The material effect in patterned substances shows increase activity in the cells cultures on the ceramic material. 151

Figure 6-10 Stacked bar chart of the involvement of canonical pathways for the topographical effect on PCL. There is up-regulation of all the activities shown in red on the patterned PCL over the planar material. 151

Figure 6-11 Stacked bar chart, canonical pathway involvement of the topographical effect on ZTA. The overall trend is upregulation on the pitted material over the planar. 152

Figure 6-12 Bar chart of the metabolic cell activity as it relates to cell function, note the strongly positive results for energy production, cell signalling and molecular transport. Also note the increase lipid metabolism in the cells from the patterned substrate. This upregulation across cell activity is reflected at all levels - general activity such as signalling, specific activity such as cell morphology but also in cell survival and indicators of cellular compromise. 153

Figure 6-13 Network for metabolic activity, 40µm topography ZTA over planar ZTA. This network map shows upregulation of ERK on patterned ZTA over planar ZTA. A few small pathways are inhibited. ERK is notable due to it's role in cell differentiation. 154

Publications and presentations relating to this thesis

Wilkinson, A., Hewitt, R.N., McNamara, L.E., McCloy, D., Dominic Meek, R.M., Dalby, M.J., Biomimetic microtopography to enhance osteogenesis in vitro, *Acta Biomaterialia* (2011), doi: 10.1016/ j.actbio.2011.03.026

Biomimetic microtopography to enhance osteogenesis in vitro - podium presentation at Glasgow Meeting for Orthopaedic Research 2011

Acknowledgement

I must express my gratitude to those who have helped and encouraged me through this research.

I offer my thanks to Professor Matt Dalby and Mr Dominic Meek for their patient supervision and guidance from creation of an idea to the completion of this thesis.

To all those in CCE, thank-you for all of your help and understanding. Most especially to Monica Tsimbouri and Carol-Anne Smith. Monica, thank you for all your time explaining everything that I had questions about and working through the results I had difficulty processing, a special thanks for all your help with processing the results for the metabolomics. Carol-Anne, thank-you for steering me to every: ingredient, lab book, procedural text and recipe; a special thanks to you for all your help with PCR processing.

Thank-you Gabriela Kelna for her advice and assistance processing some of the statistics. Thank-you Karl Burgess with his help undertaking the processing of the metabolomics data.

Thank-you Mr David Large, for your support in this project and your broader support in general through my surgical training.

To my wife and children, thank-you for being patient with me as I worked through this project.

This work was funded by an award from Joint Action. Thank-you for supporting me in this research project.

Author's Declaration

I declare that, except where explicit reference is made to the contribution of others, that this dissertation is the results of my own work and has not been submitted for any other degree at the University of Glasgow or at any other institution

Andrew J Wilkinson

January 2016

Abbreviations and definitions

AFM	Atomic Force Microscopy
BSA	Bovine Serum Albumin
BMP	Bone Morphogenic protein
BMPR2	Receptor for BMP
CCE	Centre for Cell engineering
CBFA1	Core Binding factor Alpha 1
CFU	Colony Forming Unit
DMEM	Dulbecco's modified Eagles Medium
DNA	Deoxyribonucleic acid
GAPDH	Glyceraldehyde 3-phosphate dehydrogenase (a house keeping gene responsible for proteins used in glycolysis)
GDF10	Growth differentiation factor 10
HA	Hydroxyapatite
HCA	Hydroxycarbonate
MSC	Mesechymal Stem Cell
mT	milliTesla (magnetic flux density)
OPN	Osteopontin
OCN	Osteocalcin
PBS	Phosphate Buffered Saline

PCL	Polycaprolactone
PCR	Polymerase Chain reaction
PMMA	Polymethylmethacrylate
RUNX2	Runt related Transcription Factor 2
RNA	Riboxynucleic acid
ROH ₂ O	Reverse Osmosis water
SEM	Scanning Electron Microscopy
SCCM	Standard Cubit centimetres per minute (measurement of flow)
ZTA	Zirconia toughened Alumina

1 Introduction

1.1 Biomaterials

Pathological conditions of the musculoskeletal system cause significant morbidity mediated by pain and loss of function. They can be caused primarily following excessive normal use of a healthy system, secondarily following a traumatic, inflammatory or infective insult to a previously healthy system, or they may present after normal limited use of an abnormal system as seen with dysplastic conditions (Creek et al. 2011; Agricola et al. 2013; Jungmann et al. 2013).

For some of these degenerative conditions the damaged portions of the system may be replaced. Total joint replacement with artificial bearing surfaces is one of the most common examples of the successful substitution of artificial materials. Any material that acts to augment or replace part of the body may be referred to as biomaterials. The range of biomaterials is vast and they serve many different functions. The development of biomaterials has progressed through three generations (Boccaccini et al. 2005).

1.1.1 First generation biomaterials

The first generation have been adopted from other disciplines, this generation of materials are constructed to replace or augment tissues, they function well if they elicit no or at least very little tissue reaction. The most common materials used in the manufacture of trauma surgery implants are first generation biomaterials, these are mostly stainless steel and titanium, they are not designed to generate a specific response from the body but support the body while it heals with the potential to be removed at a later time (Hui et al. 2007; Pate et al. 2009); in a similar vein the successful first generation arthroplasty (joint replacement) materials work well when no significant tissue reaction is generated.

Away from orthopaedics the artificial intraocular lens is a superb example of a successful first generation biomaterial. Whilst cataract had been recognised and treated in various fashions for many years no suitable material had been found

to replace the human lens (RIDLEY 1952). Harold Ridley working as an ophthalmic surgeon noted the well-tolerated retention of particle of polymethylmethacrylate (PMMA) in the eyes of World War II aircraft pilots (the windshield was manufactured from PMMA and splintered on crashing). Following this observation the PMMA lens was developed and implanted for the first time in the late 1940s (Apple & Sims 1996), this adaptation of an existing material to a biomaterial is present in many of the first generation biomaterials. The PMMA both as shards in the eyes of pilots or as polished lenses replacing cataracts generated very little tissue reaction.

Materials such as PMMA in lens implants and the titanium and stainless steel used for trauma reconstruction are thought of as bioinert. Within first generation biomaterials this inert quality was integral to the success of the implant. With increasing research into the interaction between tissue, fluid and artificial materials we now understand that no material is truly inert. All materials when implanted in the body are exposed to contact with proteins (Santin et al. 1997). The surface of the material induces a conformational change in the protein (Norde 1986) and the entire surface of the material is coated. In the right settings the protein layer is sessile and the materials are very well tolerated, this represents the inert end of the biocompatibility spectrum (Kasemo & Lausmaa 1988) and allows first generation biomaterials to function well. What is the potential to use the process of tissue contact to deliberately move away from inert materials to those that actively promote tissue response?

1.1.2 Second generation biomaterials

Where first generation biomaterials sought as little host reaction as possible second-generation biomaterials represent a desire to move towards a positive action and reaction, in order to enhance the interface of the material and the host tissues (Hench & Wilson 1984). These second generation materials are still biocompatible but demonstrate properties that may be biomimetic, bioactive and bioresponsive. The engineered action and reaction seen with second-generation biomaterials varies by material and design but may be regarded broadly as improving fixation of a permanent implant or providing function for a limited period of time after which the biomaterial will degrade to be replaced by normal tissues.

The two most widely acknowledged materials to increase fixation and bone formation in the host are hydroxyapatite (Epinette & Manley 2008; Voigt & Mosier 2011) and the bioglasses (Stavropoulos et al. 2012; Heikkilä et al. 2011; J.-Y. Sun et al. 2009). These are both forms of bioceramic (1.2.3 Ceramic development). Hydroxyapatite is biomimetic for the mineral phase of bone and as such it seems intuitive that it should be a successful material (de Groot et al. 1998; Goyenvalle et al. 2003) this is reflected in the widespread clinical success of hydroxyapatite coated implants (Kirsh et al. 2000; Furlong & Osborn 1991; Batta et al. 2014). It is however interesting to note that clinical research has now highlighted the equivalent effectiveness of non coated porous metal implants (Li et al. 2013; Valancius et al. 2013). This does not denigrate the value of hydroxyapatite coatings but serves to highlight the potential for topography and other material properties to influence osteoinduction as powerfully as chemical mediators. Bioglasses and Bioglass® 45S5 behave differently than HA coatings, there are two principle mechanisms underpinning the bioactivity of the traditional melt quenched bioglasses. The first path is the formation of the hydroxycarbonate (HCA) apatite layer on the surface of the bioglass, this is a very active layer and promotes very rapid bonding with bone it has five proposed stages (Hench 1991; A. E. Clark et al. 1976) with the transformation depending on the silica ions. The development of the HCA layer is well understood, less so are the reactions that follow, the second path is determined by the dissolution of the bioglass, which then stimulate an osteogenic response. These materials can be used as coatings, as blocks and as particulates. In situ particulate bioactive glass filling of bone defects demonstrates good targeted local tissue regeneration (Xynos et al. 2001).

A range of materials is used in the manufacture of degradable implants for medical use. These include Polylactic acid, polyglycolic acid and polyglycaprone. Polylactic acid is a thermoplastic manufactured from renewable sources (Garlotta 2001), although labelled as acids these materials are technically polyesters (REF), their greatest clinical application to date has been in the manufacture of degradable suture material: Dexon™ (polylactic acid) a braided absorbable suture is manufactured by Covidien Ltd (Medtronic 15 Hampshire Street, Mansfield, MA 02048), Monocryl® manufactured from polyglycaprone by Ethicon LLC (4545 Creek Road, Cincinnati, OH 45242) is a monofilament suture.

These materials have become so commonplace in the world of surgery the comprehensive list of available materials is beyond the requirements of this passage, this serves as an indicator of the success found for this type of second-generation biomaterial.

These polyesters have also been manufactured into more solid form for use in the fixation of fractures (Athanasίου et al. 1996). The results for clinical application have been mixed, with some success demonstrated for use in children (Böstman et al. 1993; Hope et al. 1991) . A number of studies have highlighted the risk of reaction to the breakdown products of these fixation materials (Böstman 1992; Böstman et al. 1992; Bergsma et al. 1993; Böstman 1991). Histological examination has shown abundant giant cells with a non specific foreign body reaction including the formation of granulomata (Böstman et al. 1990; Böstman 1992). These changes may be detected on magnetic resonance scans of knees following anterior cruciate reconstruction up to ten years after the index procedure (Warden et al. 2008). Importantly the presence of a non specific foreign body reaction does not routinely correlate to manifestation of symptoms (Warden et al. 2008; Böstman et al. 1990).

Further applications have been found in the world of sports medicine; suture anchors and interference screws are manufactured from various biodegradable polymers (Weiler et al. 2000). Further advances have also been made combining the polyester with hydroxyapatite (P. L. Lin et al. 2007; J. Chen et al. 2006) with clinical studies showing acceptable results regarding fixation, longevity and tissue reaction. (Cox et al. 2014).

1.1.3 Third generation biomaterials

Third generation biomaterials are being developed to target specific and on-going stimulus to the host tissues at the cellular and genetic level. The roles and challenges for the third generation of biomaterials in the 21st century are extensively explored in a lead article by Professor Hench, who discovered bioglass (Hench 2006) where five separate challenges are identified. (Hench & Thompson 2010) These five challenges are; the regeneration of tissues, tissue engineering, stem cell engineering, infection control, in vitro testing of toxicity and compatibility of biomaterials and nanoparticles. In the setting of

arthroplasty these five challenges may be applied to regeneration of damaged and worn systems (Jenis & Banco 2010; Pimenta et al. 2008; Best et al. 2008; Bartlett 2005; Behrens et al. 2006) or they may be applied to the materials selected to augment or replace the worn system.

Really, the materials facets that can be controlled to achieve third-generation materials are chemistry, mechanical properties (within physiological levels to influence cells - up to 40 kPa) and topography and combinations of these. For example, as has been described, hydroxyapatite and the bioglass show that chemistry is important, then Annaz et al. demonstrate that even a chemically suitable and attractive material such as hydroxyapatite can be improved with optimal topographical features (Annaz et al. 2004). In order to understand the physical and chemical features that contribute to a favourable host reaction and therefore a successful biomaterial the details and behaviour microenvironment for the implant should also be investigated.

The majority of implants in orthopaedics are applied to the surface of or the inside of bones, this is true for trauma implants with plates on the surface and rods and screws exposed to the central portions of bone, as it is true for joint replacement components, placed against the exposed surface of medullary bone Figure 1-1. The primary cells of this microenvironment will be bone cells within the extracellular matrix.

1.1.4 Bone biology

Bone is a multiple composite structure; the elements involved are: organic and inorganic, cellular and extracellular; the forms of bone are mature and immature, cortical and trabecular bone in varied composition according to functional requirement.

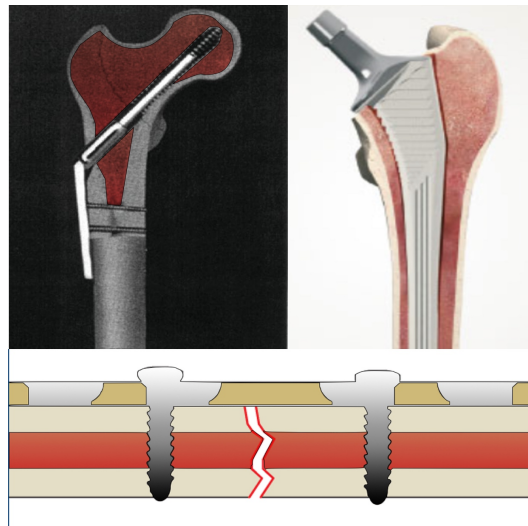


Figure 1-1 Orthopaedic implants in contact with bone. Clockwise from top left, a sliding hip screw with the barrel and threads in the medullary bone, an uncemented femoral implant against the medullary bone and screws through a plate, contacting both the cortical and medullary bone.

Bones exist in a variety of shapes and sizes. Tubular bones have repeated recognisable features, diaphysis, metaphysis and epiphysis. Examples of the tubular bones are the femur, tibia, metatarsals and metacarpals. Flat bones share fewer features, they often have projections for attachment of soft tissue or articulations with other bones; examples include the scapula and the skull. Sesamoid bones are bones within tendons, the best example of which is the patella. The specialised bones of the wrist and foot are irregularly shaped to accommodate the advanced functions of these compound articulations. The structural arrangement of tissue within each bone is varied but shares a common template.

Each bone is constructed of two forms, outer cortical bone and inner spongy or trabecular bone. Cortical bone is constructed of a circumferential section of compact bone and a series of inner osteons, all formed from lamellar bone. Each osteon consists of many layers of tightly packed bone surrounding a central canal; each canal contains a blood vessel, nerve endings and lymphatics. The structure of lamellar bone in this way allows adequate blood supply to a structure that would otherwise be too dense. Trabecular bone on the other hand is constructed of multiple thin bridges or strands; each trabecula is constructed of several lamellae, collectively thin enough to be sustained by the blood in the spaces between the strands, without requiring the structure of an osteon. The brief outline of structure above pertains to mature bone. All mature bone is lamellar, whether trabecular or cortical; woven bone is immature with a

disorganised collagen structure and a high number of cells. This immature bone is normal in a number of circumstances such as embryonic skeletal development and fracture callus; in other situations the presence of woven bone is concerning - examples being woven bone produced by osteogenic sarcoma, or in Paget's disease of bone.

1.1.4.1 The extracellular constituents of bone.

The extracellular matrix of bone comprises inorganic and organic components. The inorganic portion of bone is mostly crystalline calcium phosphate salt, in the form of hydroxyapatite, it constitutes around 60% of the dry weight of bone (Junqueira & Carneiro 2003). Other inorganic components are smaller amounts of carbonate, fluoride acid phosphate, magnesium and citrate. The organic component of the extracellular matrix is composed of: Type I collagen, multiple non-collagenous proteins and growth factors.

Type I collagen is a fibrillar protein is a super twisted helix (Hulmes 2002). It is produced primarily by osteoblasts as procollagen. Once procollagen is excreted from the cell (packaged in vesicles) the polypeptide chains aggregate in units of three to produce tropocollagen. Tropocollagen in turn gathers in order to produce a microfibril. Fibres of collagen are formed by several microfibrils. (Hulmes 2002; Hulmes 1992) Collagen fibres are arranged with pores between the adjacent fibres and holes between the ends of fibrils have spaces between adjacent fibres. Calcification occurs in the pores and holes and formation of the crystalline hydroxyapatite occurs parallel to the fibres of collagen (Sela et al. 1987).

There are a number of non-collagenous matrix proteins. One of the families of non-collagenous proteins is the Small Integrin-Binding Ligand N-Linked Glycoproteins (SIBLING). The SIBLING family contains bone sialoprotein (BSP (IBSP)), dentin matrix protein 1 (DMP1), dentin sialophosphoprotein (DSPP) and matrix extracellular phosphoglycoprotein (MEPE). These proteins may be found in multiple sites, they are mostly expressed in dentin and bone and are excreted into the extracellular matrix during osteoid formation and mineralization (Staines et al. 2012).

As one of the SIBLING proteins, osteopontin is involved with regulation of mineralization. It appears to have a modulating or inhibitory effect on hydroxyapatite formation (Hunter 2013; Boskey et al. 2012). OPN is produced both by osteoclasts and osteoblasts (Dodds et al. 1995; Sodek et al. 1995; Zohar et al. 1997) It is found in abundance at sites of ectopic bone formation (Hunter 2013) and likely has an inhibitory role at these sites. The role it performs in osteogenesis and bone remodeling is less certain but it is telling that it was first identified as a bridging protein between cells and the hydroxyapatite component of the extracellular matrix in bone (Sodek et al. 2000).

Osteocalcin is another non-collagenous protein found abundantly in bone (Wolf 1996). OCN is produced by osteoblasts in the late stages of differentiation after the proliferation phase is complete under the control of the RUNX2/Cbfa1 transcription factor (Carvallo et al. 2008). The presence of osteocalcin may therefore be used as an indicator of the presence of mature differentiated osteoblasts. The precise role of osteocalcin is still a little unclear, with some data to show that addition of osteocalcin to an in vitro study improves the adhesion of osteoblast like cells to a biocement (Knepper-Nicolai et al. 2002). One animal model has shown that OCN added to a composite implant improves bone healing and the appearance of active osteoblasts. This positive evidence is balanced by a knockout animal model demonstrating higher bone mass in animals without OCN (Ducy et al. 1996). Rather than suggesting that OCN inhibits bone formation the combination of these additive and subtractive effects of OCN on bone formation suggest an integral role in bone homeostasis.

1.1.4.2 Cellular components of Bone

Osteoblasts, osteocytes and osteoclasts are the cells common to bone throughout (Revell 1983; Freemont 1993). Osteoblasts are mononuclear specialised cells with a large Golgi apparatus and abundant endoplasmic reticulum (Marks & Popoff 1988), once mature they secrete non-mineralised bone matrix (Gori et al. 2000). Osteoblasts originate from mesenchymal cells, during embryonic development they are involved in the two types of bone formation (Marks & Popoff 1988). During intramembranous ossification the flat bones (for example the skull) are formed as condensations of mesenchymal cells differentiate into osteoblasts and form non-calcified bone matrix (osteoid). The

bone matrix is then mineralised, flat bones grow by apposition (that is bone growing on existing bone), allowing a lamellar structure. During enchondral ossification a cartilage model of the bone is slowly remodelled to bone through the combined action of osteoclasts and osteoblasts; the processes of enchondral ossification are more complex than those for intramembranous ossification. First stem cells differentiate to cartilage cells and create a cartilage model, once the chondrocytes stop dividing they become hypertrophic and produce fibronectin and type X collagen, this allows the matrix to be mineralised. Finally vascular invasion begins the process of ossification; the hypertrophic cartilage cells die, stem cells differentiate to osteoblasts and lay down matrix on the degrading cartilage matrix. The matrix is then ossified completing the replacement of the cartilage model.

Osteoclasts are multinucleate cells related to the monocyte/macrophage line. They require a number of conditions to successfully develop: the presence of osteoblasts, Tumour Necrosis Factor, Colony stimulating factor and a variety of interleukins. Osteoclasts are bone resorbing cells, found in areas of active bone turn over they are seen sitting in Howship's lacunae (or resorption pits). Resorption of bone occurs in a confined area. Osteoclasts have several specialised features that facilitate bone resorption; the ruffled border and the clear zone are critical to this function. The ruffled border is formed by extensive folding of the plasma membrane (Chambers 1985), Carbonic anhydrase in the cell cytoplasm provides H^+ ions that are secreted via the ATP pump into the sealed space under the ruffled border. The clear zone is abundant in actin filaments; it allows the cell to bind closely to the bone matrix and provide a contained space for the H^+ ions. The acidic environment combined with the release of hydrolases creates an environment for resorption of bone and degradation of collagen (Freemont 1993). When the osteoclast moves on the resorbed area is a circular defect named as a Howship's lacuna. This is the feature I have selected to copy for embossing on implant materials.

The bone-remodelling unit is made of osteoclasts and osteoblasts working together. Old bone is removed by the osteoclasts with new osteoid being laid down by osteoblasts as the osteoclasts move on. The osteoid is then mineralised. During the remodelling of cartilage and the continued remodelling of the

skeleton through life some of the osteoblasts will be enveloped within the osteoid matrix and become osteocytes (Marks & Popoff 1988). The osteoid forming function of osteoblasts then is not their final function with some becoming embedded, others remaining on the surface and others still proceeding to apoptosis (Hock et al. 2001).

The control of multiplication and terminal differentiation is influenced by transcription factors, growth factors and hormones (Aubin & Triffitt 2002). Expression of the osteoblast phenotype through expression of bone specific proteins such as osteocalcin and osteopontin (expressed by immature osteoblasts) is controlled by the *cbfa1* genetic pathway (Ducy et al. 1999) (Komori 2009). Such transcriptional control is down-stream of growth factor and adhesion driven signalling pathways.

Parathyroid hormone and parathyroid related peptide stimulate differentiation of osteoprogenitors (Hock et al. 2002) and has been proven to be anabolic in the setting of osteoporosis (Stewart et al. 2000). Clearly the relationship is highly complex as parathormone is also related to apoptosis of osteoblasts and bone turnover (Hock et al. 2001).

The bone morphogenic proteins are a subgroup of the transforming growth factor Beta family. These potent factors, held in the extracellular matrix, are released by osteoclasts during the remodelling process and are active on osteoblast precursors to stimulate new bone formation. The balanced action of the catabolic and anabolic remodelling of bone persists throughout life; given the entrapment of some osteoblasts and apoptosis of others, a continuing source of osteoblasts from osteoprogenitor cells must be present in reservoirs in adults. Within the cambium layer of periosteum and medullary bone are multipotent cells of mesenchymal lineage (Freemont 1993) these cells are known as Mesenchymal Stem Cells (MSCs). The current accepted criteria that determine a stem cell are; a cell that can continue to divide and produce a clonogenic colony forming unit (CFU) and that the cells in that colony forming unit can specialise into multiple different cell type. The idea of a stem cell for the haematopoietic system is attributed to Alexander Maximow (Lashkouskaya et al. 2010) and may have been postulated as early as 1908. The ability of bone marrow cells to

produce colony forming units was demonstrated in the early 1960s (BECKER et al. 1963; SIMINOVITCH et al. 1963). The first in vitro demonstration of cells that were capable of multiplication and differentiation into different mesenchymal groups was produced by A J Friedenstein in the 1960s, he is generally regarded as the first to produce evidence that adult bone marrow contains MSCs and demonstrated the multipotent CFU with differentiation into adipocytes, chondrocytes, osteoblasts and highlighted their role as haematopoietic supporting stroma (Friedenstein et al. 1966; Friedenstein 1976). (Friedenstein 1995) (Triffitt et al. 1998; Mirmalek-Sani et al. 2006). The adult bone marrow contains all four types of mature specialised bone cells as well as MSCs; this is the microenvironment for intramedullary implants. The presence of a first generation biomaterial in this environment must interfere with the normal control over the multiplication and differentiation of osteoprogenitor cells. This disruption of normal differentiation may help to explain the fibrous encapsulation of implants. Second generation biomaterials attempt to mimic bone properties to improve bone apposition and third generation aim to further exploit known regulators of bone growth to further enhance fixation of materials.

1.2 The historical perspective on orthopaedic first generation biomaterials

1.2.1 The early development of joint arthroplasty

The history of orthopaedics may be traced back through time. There is documented evidence of musculoskeletal disease present in remains several thousand years old with references to limb setting by the ancient Egyptians in treating trauma (MacLennan 1999). For the vast majority of human history joint disease has not had any form of reliable treatment. The earliest records of attempts to manage arthritis begin with the work of Henry Park in the Royal Infirmary Liverpool, in a letter to Percival Pott, Park describes how he excised the affected joint (Anon 2005). Park was performing this operation to relieve arthritis primarily in the elbow and knee joint. The first evidence of an excision arthroplasty of the hip joint is credited to Anthony White working in the Westminster Hospital. Although he left no formal record of the operation it is highlighted in his obituary in the lancet (Anon. Anthony White (obituary)).

Lancet. 1849;1:324) This operation was rediscovered and popularised by Gathorne Robert Girdlestone in the 1940s (Girdlestone 2008)

Themistocles Gluck performed the first formal replacement of a joint in 1890. Dr Gluck experimented widely on animals prior to use of his inventions in his patients. He designed many different joint replacements and is credited with the first hip and first knee replacement (Gluck 2011). Indeed Dr Gluck experimented with many of the implant technologies in use today. His writings and drawings provide evidence of his use of the best press fit technologies of the day favouring ivory in addition to his experimentation with various types of cement (Gluck 2011). Tuberculosis was the clinical driver for joint replacement at that stage and his attempts at joint replacement in young patients with no antituberculous medical therapy came to an inevitable failure. In addition, as with Sammelweis and Codman, he was rejected for his opinions and writings, only later being acknowledged for his vision (Brand et al. 2011). Following the inevitable failure of the early design of these replacements, interposition arthroplasty, which is placing another material between two affected surfaces of a joint, became popular with a range of materials used. The most successful of these was Vitallium® an alloy of Cobalt, Chromium and Molybdenum - suggested to Marius Smith Peterson by his dentist (Hernigou 2014). The material had been used with success in dental prostheses already. Prior to Vitallium®, Smith Peterson had used glass with the aim of creating a reactive tissue layer, glass was mechanically unsuitable and failed through fracture, Vitallium® proved much more successful than all the previous materials he had tried following the initial failure of the glass mould, the Vitallium® prosthesis being used in 500 cases over ten years (Smith-Petersen 1948; Mahalingam & Reidy 1996; Hernigou 2014).

Ivory was used as a material for a hip prosthesis again in 1927 by Ernest Heygroves, the results, however, were poor (Ratliff 1983). A great deal of interest was found for the acrylic prosthesis of the Judet Brothers (Guilleminet & Judet 2014). However, the prosthesis demonstrated high wear rates and enthusiasm quickly waned (Guilleminet & Judet 2014). Vitallium®, which had shown promise as an interposition arthroplasty, was used by three surgeons; Thompson in 1950 developed his collared prosthesis with intramedullary

extension (THOMPSON 1954), Bohlman and Moore had first placed their prosthesis in 1940, they later refined the design to allow for bone ingrowth (Sarmiento & Grimes 1963). Both the Austin Moore and the Thompson prosthesis became extremely popular and were still commonly used at the turn of the 21st century for treatment of fractures of the neck of femur. Kenneth McKee (G. K. McKee 1970) and Peter Ring (Ring 1974) both developed metal on metal hip prostheses. Dental acrylic had first been described for fixing hip implants in 1953 (HABOUSH 1953) and McKee used dental acrylic to cement his prosthesis in place where Ring pursued an uncemented fixation. Both of these prosthetic designs provided some very encouraging results. However they were both surpassed and abandoned with the success of the low friction arthroplasty developed by Sir John Charnley (CHARNLEY 1972).

1.2.2 Metal on Polyethylene

The materials used for the articulation of prosthetic joints saw its greatest advance with the choice of metal on polyethylene by John Charnley following the initial failure of PTFE as a bearing. Metal on polyethylene remains the most common choice of bearing couple in arthroplasty surgery with little alternative in knee replacement and some use of ceramic on ceramic couple in total hip replacement (National Joint Registry for England et al. 2013). Early polyethylene was sterilised and packaged in air, this polyethylene failed by delamination. Investigation into delaminated polyethylene shed valuable light on the oxidative profile of the material (Landy & Walker 1988). The massive popularity of metal on polyethylene as a bearing follows polyethylene as the successor to polytetrafluoroethylene, this had been used initially by Charnley due to it's extremely low coefficient of friction, unfortunately it did not have robust wear characteristics and the wear particles generated caused tissue reaction and osteolysis (Gheorghiu et al. 2010). Osteolysis was also seen in metal on polyethylene hip replacements. This phenomenon, initially seen in cemented hip replacements, was thought to be a reaction to cement, it was poorly understood and was labelled 'cement disease' and has formed the foundation for the split in cemented and uncemented prostheses across the Atlantic (L. C. Jones & Hungerford 1987; Dunbar 2009). The process of macrophage induced osteolysis when exposed to small particles of polyethylene is now understood more clearly (Harris 1994; Atkins 2011; Orishimo et al. 2003; Goodman et al.

2013; Jacobs et al. 2001). This process causes aseptic loosening of prostheses and is the leading cause of revision arthroplasty. (National Joint Registry for England et al. 2013).

1.2.3 Ceramic development

In parallel with the development of metal on polyethylene bearings the advances in ceramic materials have been similarly impressive. Three forms of bioceramic are recognised; fully resorbable bioceramics such as plaster of paris and calcium phosphate, surface active bioceramics including bioglasses and hydroxyapatite and the third class, inert bioceramics, oxide ceramics that are of relevance to the experimental work that follows this introduction. Resorbable ceramics have been used for a variety of clinical purposes. Plaster of Paris has been used to fill defects in bone, with reported uses beginning in 1892; it has continued to be used successfully in orthopaedics as injectable putty to support voids encountered during fracture fixation, as pellets or graft extenders and a variety of other roles in dentistry (Thomas & Puleo 2009). Calcium phosphate is also a commonly used synthetic bone substitute, it has uses in bone tumour defects (Saikia et al. 2008) and fracture fixation augmentation (Cassidy et al. 2003). The surface active ceramics have been discussed already (Section 1.1.2 second generation biomaterials), Hydroxyapatite shows significant increases in interfacial bonding in the early stages when compared to porous metals without coating (Hench 1991). Other than a bioactive coating for joint arthroplasty implants Hydroxyapatite has also been used clinically in ophthalmic surgery as orbital implants (C.-W. Lin & Liao 2016). The bioglasses have not progressed to mainstream clinical application in orthopaedics although there are some bone substitutes with bioglass S53P4 gaining some interest in the treatment of bone infection (Munukka et al. 2008; Romanò et al. 2014).

1.2.3.1 Inert ceramic as an uncemented biomaterial

The first recorded manufacture of an oxide ceramic was by Smith in 1983 who mixed an epoxy resin with 48% porous aluminate ceramic (Hulbert et al. 1982). Patented and manufactured, Cerosium underwent a number of clinical tests. Animal trials revealed that this hybrid material was very well tolerated by the hosts, eliciting a mild early inflammatory response around the time of insertion,

the pores in the material were not surrounded by a membrane (Rhineland et al. 1970) but filled with host tissue ingrowth and notable progression of ordered bone formation within the pores (Bhaskar et al 1971). Further experimental work was carried out when Hulbert (Hulbert et al. 1972) investigated three different calcium oxide ceramics, $\text{CaO} \cdot \text{Al}_2\text{O}_3$, $\text{CaO} \cdot \text{TiO}$ and $\text{CaO} \cdot \text{ZrO}_2$. In a rabbit model the materials were introduced both as porous and non-porous ceramics for 9 months into connective tissue. The degree of fibrous capsule formation was inversely related to the size of the pore, with pore size of 100 to 150 μm much more favourable for bone growth than size 45 to 100 μm . The same author had contributed previously to the relationship of pore size to tissue ingrowth showing in 1970 (Hulbert et al. 1970) that a larger pore size (up to 200 μm) encouraged much more penetrative tissue ingrowth with some primary osteons visible in a few of the larger pores. Pore size, therefore, is a static determinant of tissue reaction in a dynamic system. Ducheyne in 1977 (Ducheyne et al. 1977) observed the effect of movement at the bone implant interface; dynamic systems required greater pore size for ingrowth than static systems. In addition to pore size and system dynamics, the composition of the material also influences tissue response. Calcium aluminate implants demonstrate a consistent interfacial seam of osteoid; this appears to be absent when aluminium oxide is assessed (Hulbert et al. 1982).

1.2.3.2 Development of inert ceramic as a bearing surface

Alumina has been a standardised mineral since 1984 (ISO 6474) however ceramic on ceramic bearing were introduced to hip arthroplasty in the 1970s by Boutin, Gris and Mittlemeier using bulk alumina cups that were cemented or pressfit (Mittlemeier & Heisel 1992; Griss & Heimke 1981; Boutin et al. 1988). The material was extensively researched by several groups, a summary of the early research and clinical use is provided by Boutin (Boutin 2014). The material characteristics, safety and tolerance profiles for first generation alumina from experiments in the 1960s and 1970s are described and underpin much of the current understanding of alumina ceramics (Boutin 1972). Two primary difficulties were encountered in the early use of the material: aseptic loosening of the implant and fracture of the ceramic. Crystalline aluminium oxide formed the first series of ceramic bearings, reduction in grain size and improvements in manufacture progressively decreased the rate of ceramic fracture, and the

combination of zirconia in small quantities with alumina has produced a material with excellent fracture toughness. Where improvements in ceramic material science have reduced the fracture rate aseptic loosening remained problematic (Mahoney & Dimon 1990; O'Leary et al. 1988; Petsatodis et al. 2010). Hulbert has illustrated the importance of pore size in achieving tissue penetration, alumina as a bearing is fully sintered and, for the purposes of tissue ingrowth, completely without pores - direct tissue anchorage at this level seems highly improbable. Never the less fully sintered implants have been used without cement, Boutin's work described over 1200 cases of joint replacement with alumina ceramic as the bearing material, concluding that the 'material exhibits low friction negligible wear and excellent compatibility, the prosthesis can be replaced with or without cement' (P & D 1981). Boehler reported results from Vienna for uncemented alumina acetabular implants (Boehler et al. 1994) demonstrating a fibrous membrane around all of the retrieved implants (4 out of 59 at a mean of 12 years) with a loose socket experiencing much higher rates of wear, the 10 year revision rate for these uncemented alumina sockets was 12.4% although the radiographic evidence of loosening was higher at 16%. Boutin further published outcomes with a minimum 18.5 year follow up (Hamadouche et al. 2002) showing survival of the uncemented sockets at 86%.

Metal on polyethylene articulations cause wear particles of polyethylene stimulate osteolysis leading to aseptic loosening; the aseptic loosening seen with bulk alumina cups is not driven by osteolysis (Garcia-Cimbrelo et al. 1996; Jazrawi et al. 1999). Unlike the reactive wear debris found generated from metal on polyethylene articulations ceramic wear debris is extremely inert, and very well tolerated in the body. (Hatton et al. 2003; Howie 1990; Hatton et al. 2002). The surface finish and sliding properties are far superior to those of metal on polyethylene, with a linear wear rate approximately 4000 times better (Dorlot 1992). The favourable tribological properties result in significantly lower generation of wear particles, this combined with the inert nature of the particles themselves results in a greatly reduce incidence of osteolysis when comparing ceramic on ceramic to metal on polyethylene articulations (Lerouge et al. 1997). Given the lasting wear properties, low generation of wear debris and favourable tissue response to any generated wear fully sintered ceramic bearings make an attractive option when compared to the osteolysis generated

caused by polyethylene particles or the irreparable tissue destruction seen with 'Adverse reaction to metal debris' found in some metal on metal bearing systems (Langton et al. 2009; Junnila et al. 2015; Langton, Joyce, et al. 2011). The remaining weakness in this non porous ceramic is aseptic loosening of the implant.

1.3 Fixation techniques

Implants have been fixed to bone by pressfit, mechanical interlocking using screw in mechanisms, transfixion by screws and pegs or held in place by the *in situ* polymerisation of cement from the first replacements by Gluck up to and including the cemented low friction arthroplasty by Charnley in the 1970s.

1.3.1 Cemented fixation

PMMA is a common material used to aid fixation. In the place of joint arthroplasty it behaves as a grout, which provides macroscopic fixation into the structure of the bone. It is well documented that a fibrous layer between the PMMA and host bone is commonly seen (Mao et al. 2009; Charnley 2010; CHARNLEY 1964). Despite this observation, cemented implants behave well with excellent clinical results (National Joint Registry for England et al. 2013; Wroblewski 2005; Lewthwaite et al. 2008). As PMMA obtains secure fixation by a macroscopic inter-digitation with the pattern of the bone there is no requirement for a period of protected movement to allow definitive fixation as it achieves maximal stability within hours of polymerisation. It is therefore immediately suitable for load bearing and has a particular use in the compromised patient (those with malignant deposits within the bone)(Vielgut et al. 2013). As previously mentioned the preliminary hypothesis behind osteolysis was 'cement disease', the understanding of polyethylene debris related osteolysis has allowed the continued successful use of PMMA. There have been a number of attempts to provide alternatives. These include calcium phosphate cements and bioactive coatings on polymer cements designed to increase and enhance the bone cement bond (Müller-Rath et al. 2008; Ni et al. 2006; Sakai et al. 2000; Oonishi et al. 2000). These alternatives to standard PMMA have not yet gained widespread clinical use.

1.3.2 Nanotechnology in the enhancement of cemented fixation

The advances in cemented joint replacement have focussed on the method of use of the PMMA. Vacuum mixing, retrograde filling of the implant cavity and pressurisation of the cement all improve the mechanical properties of PMMA. With the advent of nanotechnology the focus is likely to move to improving the bulk properties of the material and the interfacial bond between bone and cement. The potential advantages of nanotechnology in cement are; improved mechanical properties reduced delta temperatures during the exothermic polymerisation process and improved radiopaque features. (Liu-Snyder & Webster 2008) Carbon fibre nanotubes have been shown to dramatically improve the mechanical properties when assessed for fatigue failure and compression with greater affinity for bone at the facial boundary seen in PMMA containing nano-sized titania particles (Goto et al. 2005; Marrs et al. 2006). PMMA has been used in its current form for many years and this may appear to be an area ripe for developmental and translational research. Whilst the exothermic reaction generated during the curing of PMMA holds some theoretical concern it should be noted that so far the decrease achieved so far is very small and unlikely to prove significant unless it may be significantly bettered. Seeking improvements in the mechanical properties of PMMA is only of real benefit if PMMA failure is the weakness of the current systems, where this may not be the case; in addition the increase of mechanical strength in PMMA may increase the propensity for stress shielding of host bone, this is currently one of the advantages of PMMA with a Young's modulus very similar to cortical bone (Johnson & D. W. Jones 1994). Nanoinfused polymers may have a major role in improving the facial bonding between the polymer and bone, providing a potential benefit in preventing osteolysis. Some improvements have been made in this field already with hydroxyapatite, strontium and amphiphilic bonding agents demonstrating improvement (Müller-Rath et al. 2008; Ni et al. 2006; Oonishi et al. 2000).

1.3.3 Uncemented fixation

Uncemented implants are made possible through mechanical interlocking, press-fit or interference-fit. Fitted technologies rely on initial (or primary) stability followed by secondary stability. Primary stability is commonly achieved through

impaction of a slightly oversized implant into a prepared matched cavity. Hemispherical acetabular components achieve the highest levels of primary stability if impacted into a space 1 mm smaller than the final implant with or without the added security of screw fixation into the pelvis (Adler et al. 1992; Illgen & Rubash 2002; Stiehl et al. 1991). These modern pressfit cups build on the early experiences of Charnley (CHARNLEY 1971) and Ring (Ring 1968). The femoral components are also impacted into a matched cavity within the femur, the Corail® (Depuy Synthes) fully hydroxyapatite coated tapered stem relies on seating into impacted cancellous bone and has excellent results (vidalain 2011) where the comparably successful Zweymüller® stem is implanted against cortical bone (Huo et al. 1995; Kolb et al. 2012).

In terms of secondary, or cell-level, fixation, previous attempts at uncemented implants have been associated with the development of an interposing fibrous layer, although this has not universally caused a failure of the stability of the implant (Boehler et al. 1994; Ring 1974; G. K. McKee 1970), it reflects a biological failure to obtain secure secondary stability. As discussed in the development of ceramics, it was Hulbert's work on the association of porous surfaces and active on-growth without bioactive substances that demonstrated the potential successful use of bioinert materials by manipulating the surface of the material (Hulbert et al. 1970). It was titanium that became the first metal to show affinity for a genuine on-growth of bone without a fibrous layer. The first significant results for titanium were published by Branemark (Albrektsson et al. 1981). The interface relationship between the titanium and the host bone was at this point described as 'osseointegration', a term that is now commonplace. Secondary stability in the setting of arthroplasty implants can be obtained through ingrowth as seen in porous implants (Bobyne et al. 1999) or bone ongrowth as seen with grit blasted implants (K.-T. Hwang et al. 2012; Aldinger et al. 2009).

It is thus now understood that primary fixation must therefore be viewed as temporary. Some design feature should be incorporated into the implant to allow for secondary stability reliant upon tissue bonding at the interface created at the time of primary stability. It is noteworthy, however, that bioactive materials can only provide real benefit if primary stability is effective, as

excessive micromotion may contribute to the formation of a fibrous layer at the bone implant interface (Plenk 1998; Brunski 1999) rather than direct osseointegration. This has been studied under experimental conditions (Søballe et al. 1992; Pilliar et al. 1986). Given levels of micromotion below the threshold, the bone immediately surrounding the implant will remodel and effective interlocking can be seen, this is seen clinically in hip replacements without a good pressfit (Engh et al. 1987). The threshold for micromotion to allow secondary stability was previously thought to be fixed at a value less than 150 μm (Szmukler-Moncler et al. 1998). More recent work has suggested a more specific relationship to the interfacial strain at the implant bone boundary indicating that surface geometry modulates interfacial strain for a given amount of micromotion (Wazen et al. 2013). The hypothesis of an optimal interfacial strain marries well to the established theory of optimal strain for fracture healing and is related to gap distance. In the setting of fracture healing the advent of fixed angle locked plating has shown the importance of strain during secondary fracture healing (Bottlang 2010). The current gold standard primary and secondary fixation for ceramic bearing is provided by modular assembly of ceramic liner into a titanium shell, secured to bone either by press-fit alone or reinforced with screw fixation.

1.3.4 Nanotechnology in the enhancement of uncemented fixation

Features of an implant that engender secondary stability may be regarded as the bulk material, the surface landscape and the surface chemistry. In general for orthopaedics the bulk the forces acting on the implant predicate the material properties. These may be modified within engineering tolerances, as an example the manufacture of tantalum in a porous structure provides implants which are sound from an engineering standpoint yet have matched the young's modulus of bone and present a sufficiently porous structure to allow significant ingrowth of bone (Bobyin et al. 1999; Christie 2002; Niinomi et al. 2012). These modifications are limited where the materials must also act as bearing couples. Surface chemistry modification, with hydroxyapatite coating a well-established example, is effective although temporary and relies in the long term on the bulk qualities and surface of the material that has been coated. Surface modification promoting tissue on growth to enhance secondary stability is attractive. The miniaturisation of the microelectronics industry has allowed greater study of the

interactions between cells and surfaces at the micro topographic and Nano topographic scales. The ability to create ordered structure at this scale provides an exciting prospect for permanently bioactive topography in future implants. The first step when an implant is placed within tissue is the adsorption of protein. While the contact of initial proteins is random the presence of plasma fibronectin and chemotaxis of fibroblasts producing insoluble cellular fibronectin ensures that fibronectin will be present in the immediate and short term ensuing microenvironment, topographical features have been shown to influence fibronectin (González-García et al. 2010; Pérez-Garnes et al. 2011) furthermore the type of protein the overall amount and the conformational changes seen in the protein is dependent on the material surface (Kogler et al. 2012). The influence of topography and cell behaviour is well recognised. Alterations in cell adhesion, migration, cytoskeletal organisation, genome regulation and cell differentiation have been documented in cells cultured on different topographies controlled at the micron scale (P. Clark et al. 1987; P. Clark et al. 1990; Wójciak-Stothard et al. 1995; Wójciak-Stothard 1995; Britland et al. 1996; Dalby et al. 2003). As miniaturization of technology has continued Nano scale control of topography has become more readily possible and reliably reproducible, with Nano scale topographies affecting cell response, driving changes in cell adhesion, genomic regulation and differentiation (Andersson, Bäckhed, et al. 2003; Andersson, Olsson, et al. 2003; Andersson, Brink, et al. 2003; Dalby, Riehle, Johnstone, Affrossman & Curtis 2002b; Dalby, Riehle, Johnstone, Affrossman & Curtis 2002a; Dalby, Gadegaard, Tare, et al. 2007; Dalby 2002; Zouani et al. 2012; Lai et al. 2013; de Peppo et al. 2014; Cipriano et al. 2014; Teo et al. 2013). The topographical control of skeletal response will have a major role in the design and function of the future generations of implants.

1.4 Rationale for work, aims and objectives

1.4.1 Rationale for work

Zirconia toughened Alumina (ZTA) is the most recent ceramic bearing surface; it possesses some qualities that make it an ideal bearing surface; in testing it has been proven to be stable as a material with use (Al-Hajjar et al. 2013), it is resistant to third body wear (wear in a bearing system caused by loose particles

at the articulating interface) (A. Wang & Schmidig 2003), it may be polished to an extremely smooth finish around 2 nm (information provided by Ceramtec in relation to Biolox Delta®), in testing it generates a 40% lower steady state wear profile than cobalt chrome (Galvin et al. 2010). The fracture problems that have been associated with previous generations of ceramic are much reduced particularly with regards to head fracture (W. Wang et al. 2014) however some problems remain. Stripe wear and noise from the ceramic bearing remain and are interrelated and may be dependent on the position of the acetabular component (Korim et al. 2014; Chevillotte et al. 2012; Restrepo et al. 2010; Tai et al. 2015).

Fully sintered uncemented ceramic prostheses in the hand and foot have not enjoyed high levels of clinical success (Kaszap et al. 2012; Hansen & Vainorius 2008; Barwick & Talkhani 2008; Dawson-Bowling et al. 2012) and while comparative studies are lacking, ceramic replacement at the metatarsophalangeal joint in the foot appears much less successful than hemiarthroplasty (Sorbie & Saunders 2008) alternative total joint replacement (Erkocak et al. 2013) or arthrodesis (Erdil et al. 2013). The work published by Boutin showing revision rates of uncemented alumina sockets of 12% at ten years (Boutin 2014; Hamadouche et al. 2002) compares very poorly with the revision figures for total hip replacement in the 2014 National Joint registry report, showing ten year revision figures at less than five per cent for all fixation methods and bearing couples (with exceptions for revision surgery in metal on metal bearing couples and patients under 55 years of age) (Borroff et al. 2014). From this evidence it is clear that uncemented fixation of ceramic implants must be significantly improved if non-modular uncemented ceramic prostheses are to be successful.

1.4.2 Aims and objectives

Cell engineering aims to alter cell behaviour, alterations may be performed in vitro for later implantation of the engineered cells or cell behaviour may be altered in vitro. Ceramic bearing surfaces are superior in many ways to the other currently available technologies but have been let down by poor secondary fixation; where this issue has been circumvented in the hip by modular components it remains a problem for uncemented implantation of ceramic in other anatomical locations. The primary aim of this research is to evaluate the

ability of osteogenic topography in implant grade orthopaedic ceramic to increase the formation of bone on the surface of ceramic implants thereby creating greater secondary stability.

The process of bone remodelling involves resorption by osteoclasts, leaving behind a Howship's lacuna. The first stage of the work will be to evaluate this pattern (circular recess), over a number of sizes, regarding any osteogenic potential. This feature will be created and evaluated in a readily available polymer (Polycaprolactone). These experiments form chapter 3.

Creating microscale or nanoscale topography in a thermoplastic is very different to creating one in ceramic; the two materials have very different handling and manufacturing properties. Any topography identified as having suitable osteogenic potential in PCL will be translated to ceramic; the ability to reproduce the topography will be assessed using Scanning Electron Microscopy and Atomic Force Microscopy. The process of creating the pattern in the materials is outlined in chapter 2, the experimental evaluation of the pattern in ceramic is outlined in chapter 4.

Once the reproduction of the feature is complete in the ceramic, the osteogenic activity will be assessed using primary human cells. Assessment will be performed with a combination of Polymerase Chain Reaction, direct staining and light microscopy and immunofluorescent microscopy. The results for these experiments are detailed in chapter 5

To evaluate the confounding effect of material properties between PCL and ceramic non-image based assessment will be performed to analyse differences in cell behaviour. This assessment will take the form of a Metabolomics experiment. This involves extraction and assessment of the metabolic profile of cells. These experiments and the results are detailed in chapter 6.

2 Materials and methods

Patterns in the surface of a material may be accomplished using a variety of techniques. Materials may be melted and poured or injected into moulds - a form of casting, solid materials may have the pattern added after the overall form is created, this may be done by carving or milling the surface, or by forcing the pattern into the surface using a negative of the desired pattern. For creation of the topographical features in the polymer and in the composite Zirconia/Alumina ceramic embossing will be used. This involves creating the negative and repeatedly imprinting this into the test material. For creating the high resolution dies for embossing the PCL and ceramic I have used photolithography.

2.1 Manufacture of nickel shims for embossing

Photolithography is an optical process designed to create patterns in photosensitive materials. A light sensitive covering (photoresist) is applied to the surface of a substrate. The photoresist is applied with spin coating to a desired thickness and then cured or baked. The resist is then exposed to light in the desired pattern. For these experiments the pattern was created in a chrome mask, allowing light through to the surface to expose the resist. Two methods of developing the resist are possible, light exposure in the resist decomposes a development inhibitor leaving the unexposed resist as the basis for the pattern (a positive photoresist) or the exposed resist is polymerised by the exposure rendering it insoluble in the developing agent (a negative photoresist), to create the masks for the circular patterns a negative photoresist technique was used (Creek et al. 2012; Smith et al. 2006; Wood 2007; Scheltema et al. 2011; Betancourt & Brannon-Peppas 2006).

Silicon wafers (Compart Technologies, UK) were cleaned under acetone in an ultrasonic bath for 5 min. They were then rinsed thoroughly in reverse osmosis water (ROH₂O) (Bunnik 1986) and blow dried with an air gun. Next, they were spun with primer (Shipley AZ Coupler, Shipley, UK) for 30 s at 4000 rpm, then spun with S1818 photoresist (Shipley, UK) for 30 s at 4000 rpm and baked for 30 min at 90 °C. The resulting layer was measured to be 1.8 µm thick. The photoresist layer was exposed to ultraviolet light through a chrome mask on a

Karl Suss MA6 mask aligner for 3.8 s, then the resist layer was developed for 75 s in 50:50 Microposit developer (Shipley, UK): and rinsed in ROH₂O.

The developed circular patterns were then used as a mask for reactive ion etching. The silicon substrate was etched in the silicon tetrachloride gas plasma of a Plasmalab System 100 machine (gas flow = 18 sccm, pressure = 9 mT, rf power = 250 W, DC bias = 300 V). Each wafer was etched individually at 18 min at a nominal etch rate of 18 nm min⁻¹. All three wafers were stripped of resist in an acetone ultrasound bath for 5 min, followed by a 5 min soak in concentrated sulphuric acid/hydrogen peroxide mixture before being rinsed thoroughly in ROH₂O and dried in an air gun.

Nickel dies were made directly from the patterned resist samples. A thin (50 nm) layer of Ni-V was sputter coated on the samples. This layer acted as an electrode in the subsequent electro- plating process. The dies were plated to a thickness of ca. 300 µm. Once returned from the plater, the nickel shims were cleaned by first stripping the protective polyurethane coating using chloroform in an ultrasound bath for 10-15 min. Second, silicon residue was stripped by being wet etched in 25% potassium hydroxide at 80 °C for 1 h. Shims were rinsed thoroughly in ROH₂O and then air- gun dried. The shims were finally trimmed to approximately 30 x 30 mm sizes using a metal guillotine (Dalby et al. 2006).

2.2 Micropatterned polycaprolactone

2.2.1 Polycaprolactone (PCL)

Polycaprolactone is a frequently used low melting point (around 74°C) polymer. It has been used in hot embossing (Gadegaard et al. 2003; McMurray et al. 2011) and has been combined with HA and nanotopography to improve osteogenic potential in stem cells (Maclaine et al. 2012; Maclaine et al. 2013)

2.2.2 Manufacture of embossed Polycaprolactone

Individual pellets of polycaprolactone (65 kDa) were melted at 70 °C on glass slides on a hot plate. Patterns of circular pits diameter 20 µm, 30 µm or 40 µm were embossed onto the melted PCL by inverting the shim and loading the

construct with thumb pressure. The samples were heat shocked on ice to preserve the embossed pattern, removed from the shim and trimmed to a circle of approximately 1cm diameter to fit within a 24 well plate. Flat controls were manufactured in the same way, embossed with blank shims.

2.3 Micropatterned Ceramic

2.3.1 Manufacture of Alumina and Zirconia toughened Alumina

Zirconia toughened alumina is the fourth generation ceramic bearing surface produced by Ceramtec (Ceramtec AG, Plochingen, Germany) as BioloX delta®. An alternative zirconia alumina composite is manufactured by Mathys medical (Mathys Ltd Bettlach), marketed as Ceramys®. The combination of zirconia and alumina has produced a much tougher material than alumina in isolation. Both forms of the composite ceramic have superior wear properties in vitro in a microseparation model (Al-Hajjar et al. 2013). While some monoclinic phase transformation of zirconia in aged composite ceramic has been shown to occur in vitro (Uribe et al. 2013), the phase transformation was significantly less than for monolithic zirconia (Pezzotti et al. 2010) the wear characteristics were still more favourable than alumina (Uribe et al. 2013).

Micropatterned ceramic substrates were produced by embossing of visco-plastic green ceramic tapes at room temperature followed by sintering (Su et al. 2002). Green ceramic tapes were fabricated using a polymer viscous process (VPP) (Su & Button 2009). For Alumina ceramic, alumina powder (CT3000SG, Almatix, USA) with an average particle size of 0.5 µm was mixed with a polymer binder, polyvinyl butyral (PVB, Dow Chemicals, USA), and cyclohexanone (Sigma-Aldrich, UK) as a solvent. For Alumina Zirconia composite ceramic, 90 wt.% alumina powder (CT3000SG, Almatix, USA) with an average particle size of 0.5 µm and 10 wt.% zirconia powder (Tosoh TZ-3YS-E, Japan) with an average particle size of 0.6 µm was added to the same binding agent and same solvent as described above the alumina ceramic. The pre-mixed powder and polymer binder/solvent was milled under high shear stress on a twin-roll mill for 10-15 min to form a visco-plastic VPP dough. Green ceramic tapes were obtained by calendaring, a process that involves passing folded material through a series of rollers to obtain material of uniform thickness. Embossing was carried out on 50x50mm squares of

green ceramic tape using a mechanical testing machine (Z020, Zwick Roell, Germany) under controlled pressure and loading rate. Embossing was carried out at 5MPa, at a rate of 0.05MPas^{-1} up to the required pressure. After drying at $150\text{ }^{\circ}\text{C}$ overnight, the micropatterned ceramics were sintered using the following sintering regime: the temperature was first increased at a heating rate of $1\text{ }^{\circ}\text{C}/\text{min}$, to $600\text{ }^{\circ}\text{C}$ with a duration of 2 hrs, followed by a further increase in temperature at a heating rate of $10\text{ }^{\circ}\text{C}/\text{min}$, to $1600\text{ }^{\circ}\text{C}$ with a duration of 2 hrs.

2.3.2 Characterisation of embossed ceramics

Once prepared, the fully sintered patterned ceramics were assessed for the dimensions and integrity of the embossed pattern using atomic force microscopy and scanning electron microscopy. The composition of the ceramics was assessed using X-ray photoelectron spectroscopy.

2.3.2.1 X-ray photoelectron spectroscopy

This technique provides quantitative surface information of a material. The material is bombarded with X-rays and the escaping electrons are assessed for number and kinetic energy. This information provides detail of the elemental composition of the material surface in parts per thousand. (Watts 1990)

The samples were placed into a SAGE 100 system (Specs GmbH, Germany). The base pressure in the analysis chamber was approximately 2^{-7} mbar. X-rays were generated from a magnesium source, electron ejected from the K shell ($\text{MgK}\alpha$) operating with an anode voltage of 12.5kV and 250W power. Spectra were recorded at a take off angle of 90 degrees. The pass energy for survey scans was 50eV and 15eV for high energy scans. CasaXPS software was used to analyse the detected spectra. The atomic composition was determined by integration of peak areas using a standard Shirley background.

2.3.2.2 Atomic Force Microscopy

Atomic force microscopy (AFM) uses the deflection of a probe or cantilever to map the surface of a material. It may be used in three different modes; contact, tapping and non-contact. For the purposes of mapping the alumina and zirconia toughened alumina samples the AFM was used in tapping mode. In this

mode the tip of the cantilever oscillates above the substrate with amplitude in the region of 100 nanometers, forces interacting with the tip cause alterations of the expected amplitude (typically the forces at the surface of the material are repulsive to the cantilever tip and decrease the amplitude (Binnig et al. 1986; Neuman & Nagy 2008)).

Substrates were placed on a double-sided segment of adhesive tape and secured to a sample holding disc, the holding disc is held magnetically and the cantilever or probe is contacted with the material surface. Silicon nitride cantilevers were used to trace the surface topography over a $90 \mu\text{m}^2$ area for each of the patterned substrates and the controls. As the probe moves across the surface the repulsive force from the surface causes deflection of the cantilever. A laser is targeted to the end of the cantilever and displacement of the laser is detected on a photodiode Figure 2-1.

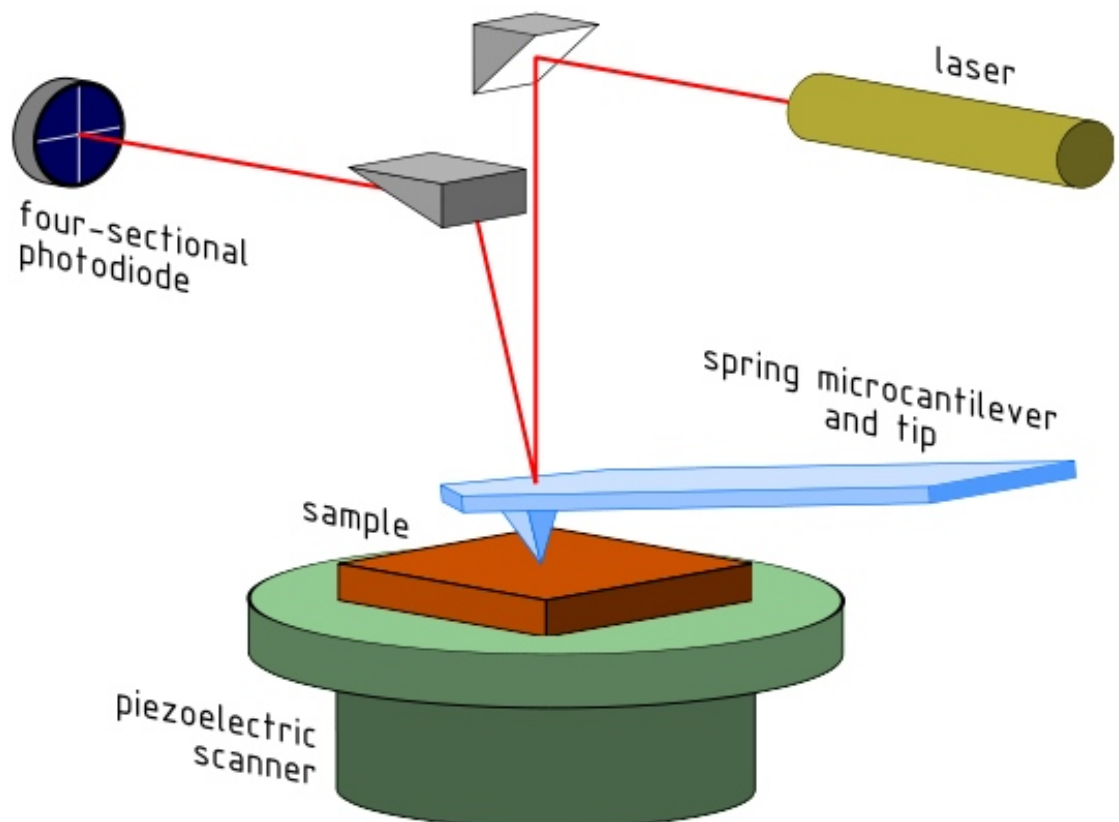


Figure 2-1 Schematic representation of Atomic Force microscopy. Reproduced from Wikimedia under a share alike creative commons licence. Original author Grzegorz Wielgoszewski.

2.3.3 Scanning Electron microscopy

Scanning electron microscopy produces images of a material by scanning the surface with electrons. Thermionic emission results in an electron beam from the cathode of the electron gun (the cathode is most commonly tungsten). One or two condenser lenses focus the electron beam with diameter ranging from 0.4 nm to 5 nm. The beam of electrons is manipulated in the x and y axes by scanning coils or deflector plates that allow the beam to scan over a selected area of the surface. When the electron beam strikes the surface a number of responses occur, these can be measured. The most common method of data capture is collection of secondary electrons; secondary electrons are emitted from very close to the surface of the material they provide very accurate detail about the material surface.

Scanning electron microscopy can produce greatly magnified images at a very high resolution. Magnification of the surface can be up to 500,000 times. This is possible, as the microscope does not rely on lenses for magnification. Magnification is achieved by scanning a smaller area for the same given display screen, resolution can be between 0.4 nm and 20 nm.

2.4 Cell Harvest

Harvesting of human cells was approved under ethics agreement 04/S0702/22. Each patient provided consent for his or her surplus tissue generated during routine primary hip arthroplasty (performed as treatment for osteoarthritis) to be used in this research. During surgery for total hip replacement the medullary cavity of the femur is exposed. For total hip replacement this occurs once the femoral neck is sectioned with a saw, a small section of medullary bone is also removed Figure 2-2. Once the section of bone is removed from the medullary cavity a plastic quill attached to a syringe is inserted into the cavity and the fluid is aspirated Figure 2-2. The section of bone removed from the canal is also included in the sample. The fluid and bone are placed in 20 ml of pre-prepared transport media.

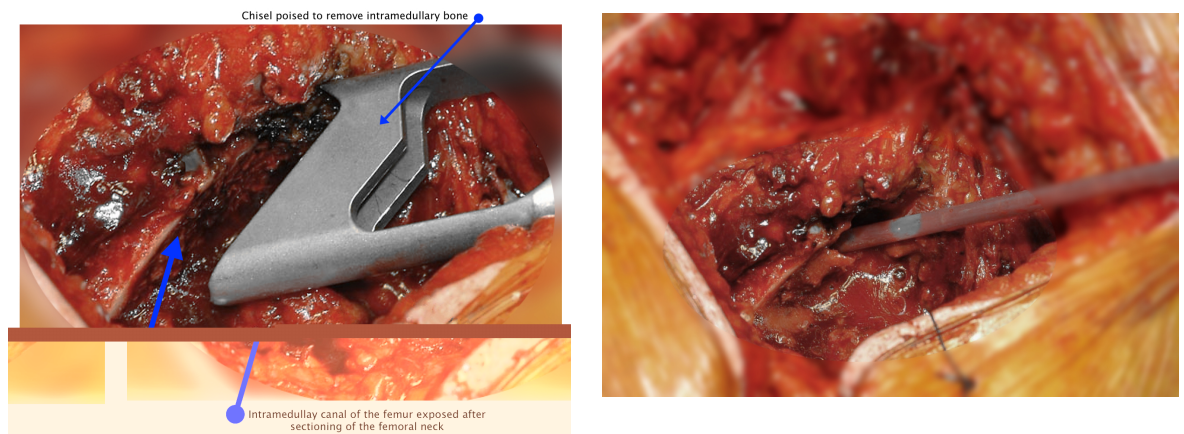


Figure 2-2 Harvesting bone marrow at total hip replacement. Left Box, chisel in position to remove cancellous bone from the proximal femur. Right, aspirating quill placed in the medullary cavity of the femur aspirating marrow contents.

2.5 Cell extraction

The human cells were transported from the harvest site to the class II laboratory at the Center for Cell Engineering in the Joseph Black Building at the University of Glasgow. Here, the liquid content of the sample of aspirated marrow was divided into two universal containers. Each sample was washed in culture media up to 30 mL and split again. The four containers with primary aspirate and culture media were centrifuged at 1400 rpm (376 G) for 10 minutes. Spent media was discarded and the pellet was re-suspended in 10 mls of culture media. This suspension was then carefully overlaid on 7.5 mls of FICOLL paque gradient (1.077 gram/decilitre (g/dl)) (GE healthcare bio-sciences AB, Uppsala, Sweden). FICOLL is a hydrophilic polysaccharide and once centrifuged with marrow separates into a solid pellet and clearly defined layers (Yeo et al. 2009; Sulc et al. 1977). The pellet contains, granulocytes and erythrocytes, then there is a layer of residual FICOLL paque, an interface layer (or buffy coat) containing mononuclear cells and a final layer of plasma/transport media. Figure 2-3

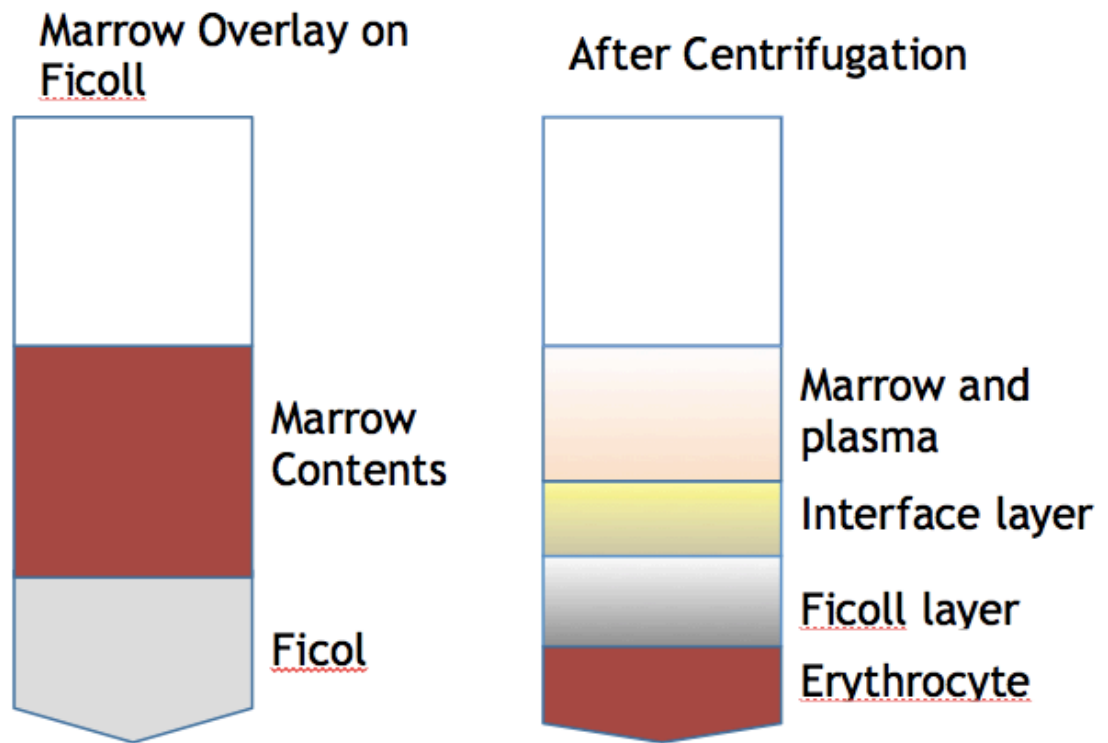


Figure 2-3 - FICOLL gradient separation of constituent parts

The FICOLL/marrow was centrifuged at 1513 rpm (440 G) for 45 minutes. The interface layer was aspirated with a pipette and suspended in up to 10 mls of culture media. After a further centrifuge at 376 G for 10 minutes, media was discarded and the cell pellet was re-suspended to 10 ml with culture media, this process was repeated again and the final cell suspension in cell culture media placed into a 25 cl culture flask.

Culture medium was made with 87% Dulbecco's Modified Eagle Medium (Invitrogen UK), 9% Foetal Bovine Serum, 2% antibiotic mixture (details), 1% sodium pyruvate (100mM, Sigma Aldrich, UK) and 1% non-essential amino acids (Sigma Aldrich, UK). The culture media was exchanged during passage and experimental culture twice each week with removal of the spent media and replacement with fresh media. The cells were maintained both for passage and culture in incubators at 37.5 °C with a 5% CO₂ rich environment.

2.6 Cell Culture

2.6.1 Cell maintenance and passage

All experimental work with human cells was performed in a class II safety cabinet. Cells were incubated and isolated from any other cell type in the department. Culture media was exchanged twice per week until 70% confluent and then expanded from the initial 25 cl to 75 cl culture flasks. Once cells had progressed to over 70% confluence they were split into two flasks.

2.6.2 Collecting cells for expansion or experimentation on substrates.

To remove cells from the culture flasks the culture media was removed and the cells washed in 4 ml of trypsin versene for 7 minutes at 37°C. Trypsin is a proteolytic enzyme solution used to detach cells in monolayer culture from the tissue culture flask. Versene is an EDTA (Ethylenediaminetetraacetic acid) solution used for non-enzyme based cell separation. The solution is composed of 700 µL of trypsin in 20 mL of versene. The cell medium is removed from the tissue culture flask, and the cell monolayer is washed with 5mls hepes saline. Once washed the cell monolayer is incubated for at least two minutes in trypsin versene, the volume required to immerse the cell layer in a 75cL culture flask is 15 mls. Cell behaviour in the flask is observed, once the cells begin to detach the trypsin versene solution is neutralised with the addition of cell culture media (5 mL). The contents of the cell culture flask were transferred via pipette to a centrifuge column and spun for 5 minutes. When centrifuged a cell pellet is generated in the base of the centrifuge column this cell pellet was re-suspended in culture media. If for further passage, the cell pellet was re-suspended in fresh media and distributed to two flasks. If for experimental work the cells were resuspended in 1 mL of media and counted (Counting cells) and aliquoted at a density of 1×10^4 cells per ml on to the test materials.

2.6.3 Counting cells

Cells were counted using a haemocytometer with the volume of each large counting square being 1×10^4 ml. A centrifuged cell pellet was suspended in 1 ml of culture media, Cells per square were counted over three squares for each

sample. The average of the three counts was taken as representative for that sample and equated the cells $\times 10^4/\text{ml}$ for that suspension.

2.6.4 Seeding cells

2.6.4.1 Polycaprolactone

While freshly isolated cells were used for ceramics, for the preliminary experimental work on embossed polycaprolactone human osteoblasts were purchased from Promocell (Heidelberg Germany). Polycaprolactone substrates were sterilised in ethanol for 5 minutes and placed individually into the chambers of twenty-four well plates. Each substrate was cultured in triplicate including the planar controls.

2.6.4.2 Alumina and Zirconia toughened alumina for immunofluorescence and alizarin staining

Primary human cells were cultured following the extraction process described in 2.5 Cell extraction.

Substrates were sterilised in alcohol for 5 minutes and washed with PBS and placed in single chambers of a twenty-four well plate. Three substrates were placed for each topography and three were placed for planar controls. Cells were seeded at $1 \times 10^4 \text{ml}^{-1}$ to each substrate. Culture media was exchanged after three days and thereafter twice per week.

At three days of culture the cells were fixed to allow for the examination of focal adhesions using immunofluorescent staining. Cells were fixed at day 21 to allow for examination of expression of osteopontin and osteocalcin using immunofluorescent staining. Cells were fixed at day 28 for direct staining of calcium nodules with alizarin red.

2.6.4.3 Alumina and Zirconia toughened alumina for metabolomics

For analysis of metabolites from the cells on polycaprolactone and ceramic surfaces, human cells were used following the extraction process described in 2.5 Cell extraction.

Substrates were placed three per well in the chambers of a six well plate, planar and patterned polycaprolactone, planar and patterned zirconia toughened alumina. This pattern was replicated in triplicate. The cells were seeded at $1 \times 10^4 \text{ml}^{-1}$ per well, with triple volumes of cell media suspension as compared to the experiments using isolated substrates in 24 well plates.

2.7 Immunofluorescent protein imaging

2.7.1 Immunofluorescent microscopy

Fluorescent microscopy makes use of one form of photoluminescence called fluorescence. Fluorescence is a term describing the emission of optical radiation as a molecule transitions from a high energy state to a low energy state, this is accompanied by a photon. In the case of immunofluorescent samples the purpose of the stain is to attach a fluorophore to a specific protein within the sample. The fluorescent microscope contains a light source responsible for raising molecules to a higher energy state and a receiver to detect the emission of light as those molecules return to the ground state (Sanderson et al. 2014). The light source used for these experiments was a mercury lamp; this emits light across all wavelengths including ultraviolet. In order to identify specific emissions a dichroic filter is placed between the substrate and the detector Axiovert 200m Carl Zeiss, CCD (charge couple device) camera, see Figure 2-4.

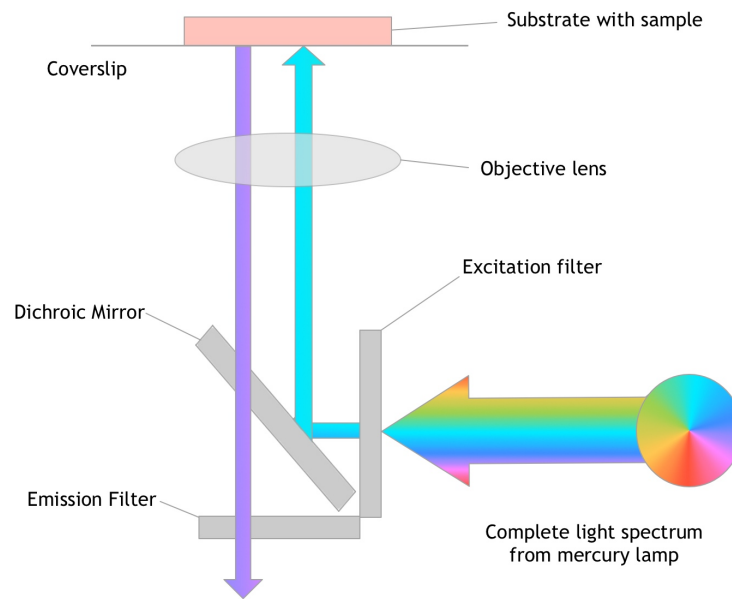


Figure 2-4 Schematic of an immunofluorescent microscope.

2.7.2 Immunofluorescent staining

2.7.2.1 Actin and tubulin - the cytoskeleton

The cytoskeleton is the protein scaffold that supports the cell and its organelles, but it is also involved in many cell processes such as cell motility and endocytosis (Kessels et al. 2001). Another important function of the fibres of actin that make up the cytoskeleton is the osteogenic differentiation of MSCs. As MSCs differentiate, those becoming osteogenic display changes in the cytoskeleton to more closely resemble osteoblasts (Rodríguez et al. 2004). Active inhibition or disruption of the cytoskeleton promotes adipogenic differentiation over osteogenic changes (Mathieu & Lobo 2012). These findings suggest that tension in the cytoskeleton is required for osteogenic differentiation. Analysis of changes in the cytoskeletal appearance may be used early in the differentiation process to predict whether or not MSCs are undergoing osteogenic change (Treiser et al. 2010).

The tubulins are a family of globular proteins, there are five types but the primary tubulins of interest for these experiments are the alpha and beta tubulins that polymerise to form microtubules. Microtubules are a constituent and essential part of the cytoskeleton (Wojcik-Stothard et al. 1995). They are

involved in: structural support, cell division and intracellular transport. When they group together they form cilia and flagella. Their role in differentiation has not been as well investigated as the role of actin.

2.7.2.2 Vinculin – Integrins and focal adhesions

Focal adhesions are anchor points for adherent cells to interact with their surroundings. They provide a dynamic link between the actin cytoskeleton and the extracellular matrix (in vivo) or culture material (in vitro). One of the membrane proteins that is involved in the formation and maturation of focal adhesions is vinculin (Bershadsky et al. 2006). Vinculin is a cytoskeletal protein involved in anchoring F actin at cell junctions. The integrins within the focal adhesion not only provide the anchor points they serve as a communication point between the external environment and the interior of the cell as part of this signaling process they may be involved in the expression of transcription factors that result in the expression of genes that result in differentiation of stem cells into osteoblasts, they have been shown to be important in cell survival and differentiation (Grigoriou et al. 2005) (Stupack et al. 2001) (Attwell et al. 2000)

2.7.2.3 Osteopontin

Osteopontin is discussed in 1.1.4.1, it is a non collagenous protein involved in bone homeostasis. Produced by osteoblasts and osteoclasts it can be used as a marker of bone activity.

2.7.2.4 Osteocalcin

Osteocalcin has also been discussed in 1.1.4.1, it is only produced by osteoclasts and so is a valuable marker for osteoblast differentiation and activity.

2.7.2.5 Staining protocol

In our laboratory it is standard practice to primarily stain for F-actin using Rhodamine phalloidin to stain the cytoskeleton and to secondarily stain using primary antibody and a biotin conjugated secondary antibody bound to fluorescent tertiary streptavidin-fluorescein isothiocyanate (FITC). Figure 2-5.

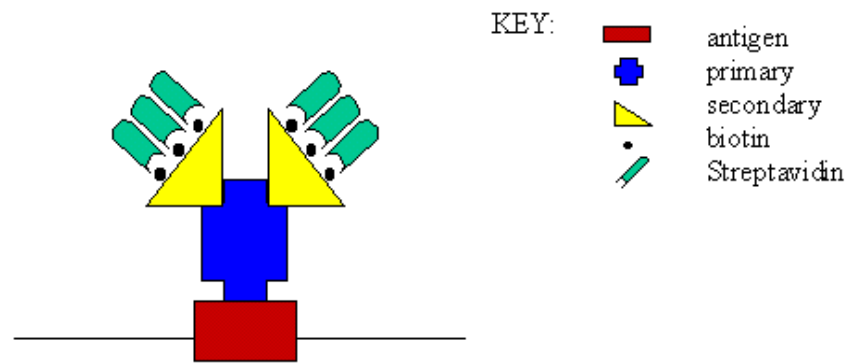


Figure 2-5 - Schematic of antibody staining technique

This is the protocol for staining polycaprolactone. The ceramics studied in these experiments demonstrate autofluorescence across much of the light spectrum, zirconia toughened alumina more so than alumina, most significantly in the same wavelength used for F actin immunofluorescent staining. For the analysis of these ceramic materials F-actin has not been analysed as it is not visible through the autofluorescence.

Once cultured for the appropriate time, the cells were fixed in situ in a solution of 4% formaldehyde/phosphate-buffered saline (PBS) with 1% sucrose at 37°C for 15 min and washed in PBS. The fixing solution arrests the cell cycle and preserves the cytoskeletal structure allowing later protein staining. At this time the cells were safely refrigerated in PBS at 4°C. The first stage in immunofluorescent staining is to create a condition in the cell membrane that allows the antibodies to penetrate the membrane, this was performed by immersion in a permeabilising buffer (10.3 g of sucrose, 0.292 g of sodium Chloride, 0.06 g of Magnesium Chloride, 0.476 g of HEPES buffer, 0.5 ml of Triton X, in 100 ml of water, pH 7.2) for five minutes at 4°C. After five minutes the permeabilising buffer was removed and the cells were washed for 5 minutes with a 1% solution of bovine serum albumin (BSA) in PBS (1gram of BSA dissolved in 100ml of PBS) at 37°C.

After five minutes the BSA/PBS was removed, the cells and substrate were actin stained with phalloidin and primary antibody (mouse antibody targeted against the primary antigen of interest) was added. Both phalloidin and primary antibody were added as 200 µl at a concentration of 1:50 PBS/BSA per substrate

and incubated at 37°C for 60 minutes the substrates were kept wrapped in foil to prevent the loss of fluorescence.

After one hour the stain was removed and the cells were gently triple washed (3 x 5 mins) in a solution of PBS and 0.5% Tween (detergent) (0.5ml of Tween 20 in 100ml of PBS). The secondary antibody was added, anti-mouse antibody 1:50 BSA/PBS 200 µl per substrate. The substrates were wrapped in foil and incubated again at 37°C for 60 minutes.

The substrates and cells were again triple washed with PBS/Tween. Following this fluorescein streptavidin was added to each substrate and incubated at 4°C for thirty minutes. Next the substrates were covered with a mounting agent containing a nuclear stain (4',6-diamidino-2-phenylindole) which binds strongly to DNA.

Rhodamine conjugated phalloidin (actin staining of the cytoskeleton) emits light in the wavelength range for red light, this is also the wavelength in which zirconia toughened alumina is most autofluorescent.

Streptavidin-FITC (Green staining of the target proteins) emits light in the wavelength range for green light. This is attached to the proteins of interest in all the immunofluorescent microscopy analysis performed for both polycaprolactone and ceramic analysis

DAPI (Blue nuclear stain) absorbs light in the ultraviolet wavelength and emits light at a blue wavelength. This stain is used to identify the nuclei - it may be used to easily count cells per field of view

2.8 Alizarin red staining

Alizarin red is an organic compound that binds to free calcium, staining it red.

2 grams of Alizarin Red S (Sigma Aldrich) was dissolved in 100 ml distilled water. Once dissolved the solution was pH balanced using 0.1% sodium hydroxide to achieve a pH between 4.1 and 4.3. Once pH balanced the stain was filtered.

After culture for 28 days cells were fixed. Once fixed and washed the cell monolayer on the substrate was submersed in the Alizarin staining solution and incubated in the dark for 45 minutes at room temperature. The substrates were then triple washed with PBS.

2.9 Brilliant blue staining

Brilliant blue R-250 (also known as coomassie blue) is one of two similar triphenylmethane dyes (the related dye in Brilliant blue G-250, nomenclature relates to subtle shades of red or green). Initially developed for textile staining it is commonly used in analytical chemistry. Brilliant blue stains proteins forming a protein-dye complex and the red form of the dye was first used to stain proteins in polyacrylamide gel after electrophoresis in 1965 (Meyer & Lamberts 1965).

Brilliant blue serves to stain the proteins of the cells, allowing them to be identified relating their position to the topographic features and their relationship to any nodules of calcium present in the samples.

100 ml of glacial acetic acid was mixed with 450 ml of purified water. Three grams of brilliant blue R-250 (Sigma Aldrich 27816-25G) was dissolved in 450 ml of reagent grade methanol. These two solutions were combined and filtered before use. For cell staining this solution was diluted by 1 equal part purified water. The cells on their substrates were submersed in the solution for 2 minutes, the solution was removed and the cells triple washed with PBS.

2.10 Polymerase chain reaction

2.10.1 RNA purification

At the appropriate time frame the cultured cells were washed in Hepes saline in situ. The substrates were then transferred to sterile petri dishes and submersed in trypsin versene for 8 minutes. The trypsin versene solution was neutralised using DMEM and the remaining cells were manually removed with a cell scraper. The solution was aspirated from the petri dish and transferred to a centrifuge column. The cell pellet was washed with PBS and centrifuged twice at which time the cell pellet was frozen and maintained at -80°C

RNA purification was performed using the RNeasy mini kit (Qiagen sample and assay technologies). 10 µl of betamercaptoethanol was added to each ml of Buffer RLT, from here on referred to as RLT. Each volume of buffer RPE was combined with 4 volumes of ethanol. 350 µl of RLT was added to each vial of harvested cells. Each vial was then placed in a vortex to homogenise the solution. 350 µl of 70 % ethanol was added to the lysate and this solution was further mixed with a pipette. Once mixed this was transferred to a 2 ml spin column and centrifuged for 15 seconds greater than 8000G. The flow through of ethanol and buffer RLT was discarded and 350 µl of Buffer RW1 was added to the spin column. The spin column was then centrifuged again for 15 seconds at greater than 8000G. The flow through of Buffer RW1 was discarded. DNASE 1 stock is combined with buffer RDD in a 1:7 ratio to allow for the addition of 80 µl of solution to each membrane (within the spin column) this was incubated between 20^oC and 30^oC. Once incubated 350 µl of buffer RW1 was added and the spin column was centrifuged at more than 8000G for 15 seconds. The spin column was placed in a fresh collection tube and 500 µl of Buffer RPE was added and centrifuged at more than 8000G for 15 seconds. The flow through buffer was discarded and 500 µL of 80% ethanol was added. The tube was centrifuged for 2 minutes and the spin column was then placed in a new tube. The spin column was then centrifuged with no lid at full speed for 5 minutes. Once placed in a new 1.5 mL spin tube 14 µl of RNase free water was added to the very centre of the membrane in the spin column and centrifuged for one minute at full speed.

The spin column was then discarded and the RNA water solution was tested for quantity and purity. 2 µl of the RNA and water solution was placed onto the sample testing platform for spectrophometric analysis. The nanodrop 2000 (Thermo scientific) is a spectrophotometer using ultraviolet light absorption to determine the quantity of nucleic acid present in a sample. Since proteins absorb at a different wavelength the purity of the sample may be expressed as a ratio of the wavelength absorbance.

The RNA samples were stored at -70^oC prior to reverse transcription PCR.

2.10.2 Reverse transcription

Reverse transcription is based on the reverse transcriptase enzyme that will detect RNA and reverse engineer the complementary DNA (cDNA), discovered in 1970 by two scientists independently (Baltimore 1970; Mizutani et al. 1970) reverse transcriptase proved that genetic information was not only passed from DNA to RNA (Crick 1970) but could also be passed in reverse. Once the cDNA has been reverse transcribed it is amplified using traditional PCR. Reverse transcription for all PCR was performed using the quantitect Reverse transcription kit (QIAGEN sample and assay technologies). This kit has two functions - eradication of genomic DNA followed by reverse transcription of target RNA to complementary DNA.

Sample RNA was thawed from -70°C on ice. Wipeout buffer (for eradication of genomic DNA) Reverse transcriptase, RT Buffer, RT Primer mix and RNase-free water were thawed at room temperature.

The solution for eradication of genomic DNA was mixed en masse allowing $14\ \mu\text{l}$ for each reaction and 10% wastage. For each reaction $2\ \mu\text{l}$ of gDNA wipeout buffer was mixed with a precalculated volume of sample RNA, this total reaction volume was increased to $14\ \mu\text{l}$ with RNase free water. Calculation of RNA volume was made using the spectrophotometric measurements of nucleic acid concentration. The target volume of RNA for each reaction was 20 ng. This reaction volume was incubated at 42°C for 2 minutes and then placed on ice.

The reverse transcription master mix consists of $1\ \mu\text{l}$ reverse transcriptase, $4\ \mu\text{l}$ RT buffer, $1\ \mu\text{l}$ RT primer. This $6\ \mu\text{l}$ was added to the $14\ \mu\text{l}$ reaction volume from the eradication of genomic DNA, providing a total reaction volume of $20\ \mu\text{l}$. Once combined the solution was mixed and incubated at 42°C for 15 minutes. Following this incubation the mix was heated to 95°C to inactivate the reverse transcriptase. This leaves complementary single stranded DNA from the RNA obtained from the cells.

2.10.3 Polymerase chain reaction

Polymerase chain reaction uses heat stable polymerase enzymes to amplify certain target areas of DNA. Complementary sections of DNA act as primers by pairing with the start of the target region, through a process of thermal cycling the target DNA may be multiplied many times. Where double stranded DNA is used the double helix is heated to separate the strands by breaking the hydrogen bonds (denaturing) this allows the oligonucleotide primers to pair with the substrate DNA (annealing). This small section of pairing on the otherwise single strand becomes the start point for the action of the polymerase enzyme as it builds more DNA from the hydroxyl group end (or 3') to the phosphate group end (5') on each strand (elongation). As this cycle of denaturing, annealing and elongating is repeated the double stranded DNA at each step acts as the substrate for the next thermal cycle, allowing an exponential reaction to occur. This exponential reaction may occur whilst the polymerase enzyme remains active, provided building blocks for further DNA are present. As the reagents are consumed and polymerase loses activity the exponential reaction tails off and eventually the reaction ceases.

The rate of progression in reaching and moving through the exponential phase of the reaction may be measured if a fluorescent marker is used as an indicator of the presence of double stranded DNA. For these experiments the fluorophore used was SYBR green (Navarro et al. 2015). This green dye fluoresces when it is attached to double-stranded DNA unbound SYBR green fluoresces much less. The intensity of fluorescence can be related to the exponential doubling of DNA.

2.10.4 Real time qualitative Polymerase Chain Reaction

In some instances qualitative PCR is satisfactory. However when attempting to assess up-regulation of genes across comparative samples clearly a quantitative approach is required. Real time qualitative polymerase chain reaction utilizes a DNA binding fluorescent reporter molecule. DNA binding dyes or fluorescently labelled sequence specific primers or probes may be used. Fluorescence only occurs with DNA binding; therefore the amount of detectable fluorescence may be used to measure the amount of double stranded DNA change per unit time

and also final amount. For the experiments described here the fluorophore used was SYBR® green dye (Navarro et al. 2015).

Detecting fluorescence from multiple samples in a multiple well plate results in multiple amplification curves represented on the same graph. Setting a threshold level to measure all the values at the same number of cycles allows a direct comparison of the amplicon presence between samples.

2.11 Polarised light microscopy

Following alizarin staining and counterstaining with Coomassie blue, ZTA substrates were examined using a polarising light microscope. (Leica DM2700 P with LED illumination). Using the polarizing filter detail was attained for the structure of the surface and then separately for the cellular detail. These images are then combined to provide relational information about cell placement, calcium nodule deposition and topography.

2.12 Metabolomics

Metabolomics is a relatively new discipline focussing on untargeted analysis of the small molecule components of biofluids and tissues. Metabolomic analysis can provide insights into regulation of biochemical pathways, metabolism of target compounds and the effects of an organism on its environment, in this case the analysis will attempt to derive the effect of the environment on cell behaviour. The process uses an accurate mass platform, backed up with a panel of unambiguous authentic standards to cover the majority of critical metabolism, as well as provide insight into the wider metabolic strata. Glasgow University has developed an in-house data analysis pipeline providing advanced filtering to remove ambiguous metabolites and provides quantitative information on hundreds of detected compounds. This pipeline will be used to help interpret the data (Creek et al. 2012).

Triplicate samples, with three substrates per sample for patterned and control polycaprolactone and patterned and control zirconia toughened alumina were, seeded with extracted human cells at a density of $1 \times 10^4 \text{ml}^{-1}$. Cells were cultured for three days. The spent media was removed and 5ml was kept aside and

added to 200 μ l of lysis buffer (1 part chloroform, 3 parts methanol, 1 part water). 200 μ l of lysis buffer was also added to 5 ml of fresh unused media. Both the used and unused media samples were frozen at -80°C . For cells on the materials, all samples were gently washed with PBS before transfer to universal containers. The substrates were placed side-by-side and immersed in the lysis buffer, and placed in a rotary shaker at 4°C for 60 minutes. The substrates were carefully removed from each sample. The remaining lysis buffer with lysed cells was vortexed and extracted to an Eppendorf tube. Each Eppendorf was then centrifuged at $13 \times 10^3 \text{G}$ for ten minutes. The supernatant from each tube was then extracted and transferred to a clean tube, these tubes were maintained at -80°C .

Samples were then used (note that total protein content was measured for normalisation purposes) for hydrophilic interaction liquid chromatography-mass spectrometry (UltiMate 3000 RSLC (Thermo Fisher) with a 150 x 4.6mm ZIC-HILIC column running at 300 μ l/min and Orbitrap Exactive (Thermo Fisher) respectively) analysis. The gradient ran from 20% H_2O 80% acetonitrile to 80% H_2O , 20% acetonitrile in 30 minutes, followed by a wash at 5% acetonitrile, 95% H_2O for 6 minutes, and equilibration at 20% H_2O , 80% acetonitrile for 8 minutes. Raw mass spectrometry data was processed using our standard pipeline, consisting of XCMS (Smith et al. 2006) (for peak picking), MzMatch (Scheltema et al. 2011) (for filtering and grouping) and IDEOM (Creek et al. 2012) (for further filtering, post-processing and identification). Core metabolite identifications were validated against a panel of unambiguous standards by mass and retention time. Additional putative identifications were assigned by mass and predicted retention time (Creek et al. 2011). Means and standard errors of the mean were generated for all groups of picked peaks and the resulting data was uploaded to Ingenuity pathway analysis software for pathway analysis.

2.13 Discussion

There are some fundamental differences between PCL and ceramic in the creation of topographical features. These differences can easily be seen in the different manufacturing processes. PCL can easily be warmed to a submelting point on a hot plate on the bench top, at this point it will easily take on the pattern, it is a repeatable process the pressures required are easily generated by

hand and PCL is readily available. The creation of a repeatable pattern in ceramic is similar only in principle, it is not a plastic and does not flow in the same manner, the heating required to process the material may not be achieved at the bench top and warming the material does not have the same effect as seen in the PCL.

3 Testing the osteogenic potential of circular topographical features

3.1 Introduction

There is a general trend to biomimicry in manipulation of stem cells towards osteogenic differentiation and bone production. This biomimetic approach may be chemical or physical. On the chemical side, adhesive proteins influence cell spreading (Kilian et al. 2010) and hydroxyapatite composes up to 50% by weight of human bone (Junqueira & Carneiro 2003) On the physical side, changing the stiffness of a material may influence the tendency to osteogenic differentiation (Engler et al. 2006) and a nanotopographical/microtopographical approaches may also influence MSC osteogenic induction (Dalby, Gadegaard, Tare, et al. 2007) (Zouani et al. 2012).

One topographical feature found in the bone remodelling cycle is the cavity or track of resorbed bone left by osteoclasts Figure 3-1. This feature may be a recognisable physical cue for osteoblastic cells and stem cells to differentiate to an osteogenic lineage and produce bone.

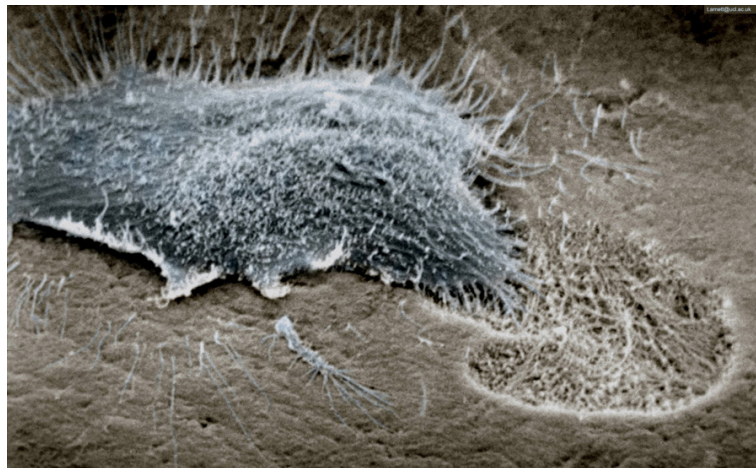


Figure 3-1 A scanning electron microscopy image of a rat osteoclast leaving behind a resorption pit. Reproduced with permission from Professor T Arnett University College London

The hypothesis to be tested is circular pits are topographic feature that promote osteoblastic differentiation of stem cells and encourage bone formation in vitro.

3.2 Materials and methods

3.2.1 Creating embossed polymer

Nickel shims were manufactured as described with three topographical features. Circular rises of 20 μm 30 μm and 40 μm diameters with a fixed height of 300 nm were fabricated. The shims were used to hot emboss PCL, creating pits with corresponding diameters and depths. Human osteoblastic cells (Promocell, Heidelberg, Germany) were seeded at $1 \times 10^4 \text{ml}^{-1}$ onto each of the patterned substrates and planar control in triplicate. The cells were cultured as described.

3.2.2 Microscopy

3.2.2.1 Focal adhesion

After three days in culture the cells were fixed and stained (2.7.2.5) for cytoskeleton (Rhodamine Phalloidin) tubulin and vinculin (2.7.2.1). Images were captured with the immunofluorescent microscope 2.7.1

3.2.2.2 Osteopontin production

After culture for 21 days the cells were fixed and stained (2.7.2.5) for actin in the cytoskeleton using rhodamine phalloidin, secondary antibody staining for osteopontin (2.7.2.3) and nuclear stained with DAPI (2.7.2.5).

3.2.2.3 Calcium production

Following 28 days in culture the cells were fixed (2.7.2.5) and stained directly with alizarin for calcium production (2.8). The cells were then counterstained with coomasie brilliant blue (2.9). Samples were viewed by bright-field optical microscopy (10x magnification, NA 0.3). Pictures were taken with a greyscale digital camera (Scion Corporation Model CFW-1310M). The stained areas of the alizarin red-stained samples were manually counted in 0.5 cm^2 areas. Statistics were calculated by analysis of variance (ANOVA) using Sigma Stat (Systat Software, UK).

3.3 Results

3.3.1 Culture for three days, staining for cytoskeleton, tubulin network and focal adhesions

Cytoskeletal and adhesion observation in osteoblasts cultured on the control and test topographies for 3 days are shown in the images in Figure 3-2

Immunofluorescent microscopy images for tubulin and vinculin staining after three days of culture. Red = actin, green = tubulin/vinculin, blue = nucleus. Figure 3-2 On all samples (20, 30 and 40 μm diameter pits and planar control) the osteoblasts spread well and had a well-developed actin cytoskeleton with abundant stress fibres. Tubulin microtubules, seen in the left hand column, are well organised, radiating from the organising centres next to the nuclei to the cell periphery. The pictures suggest that the microtubules were least well organised and the stress fibres least bundled in cells cultured on the planar control compared to those cultured on the topographies.

The stress fibers of the actin cytoskeleton, stained red, were generally thicker in cells cultured on the topographically patterned substrates and least well supported on the planar control substrate, this is evident on both columns. The focal adhesions magnified in the call out windows for the vinculin staining in the right hand column were clearly both larger and more intense in cells cultured on the embossed substrate surfaces compared to planar control, those on the planar substrate required higher contrast setting for visualisation.

Phenotypical and long-term culture staining for osteoblasts cultured on the control and test topographies are shown in Figure 3-3. Cells grew well on all substrates over the 28 day period, as shown by actin counterstaining in the osteopontin images, by Coomassie blue counterstaining in the alizarin red images and by SEM. Only background levels of osteopontin were noted in cells on the control after 21 days of culture. However, on the 20, 30 and 40 μm diameter pits, high-intensities of stain were noted; osteopontin was particularly highly expressed on the larger 30 and 40 μm diameter pits.

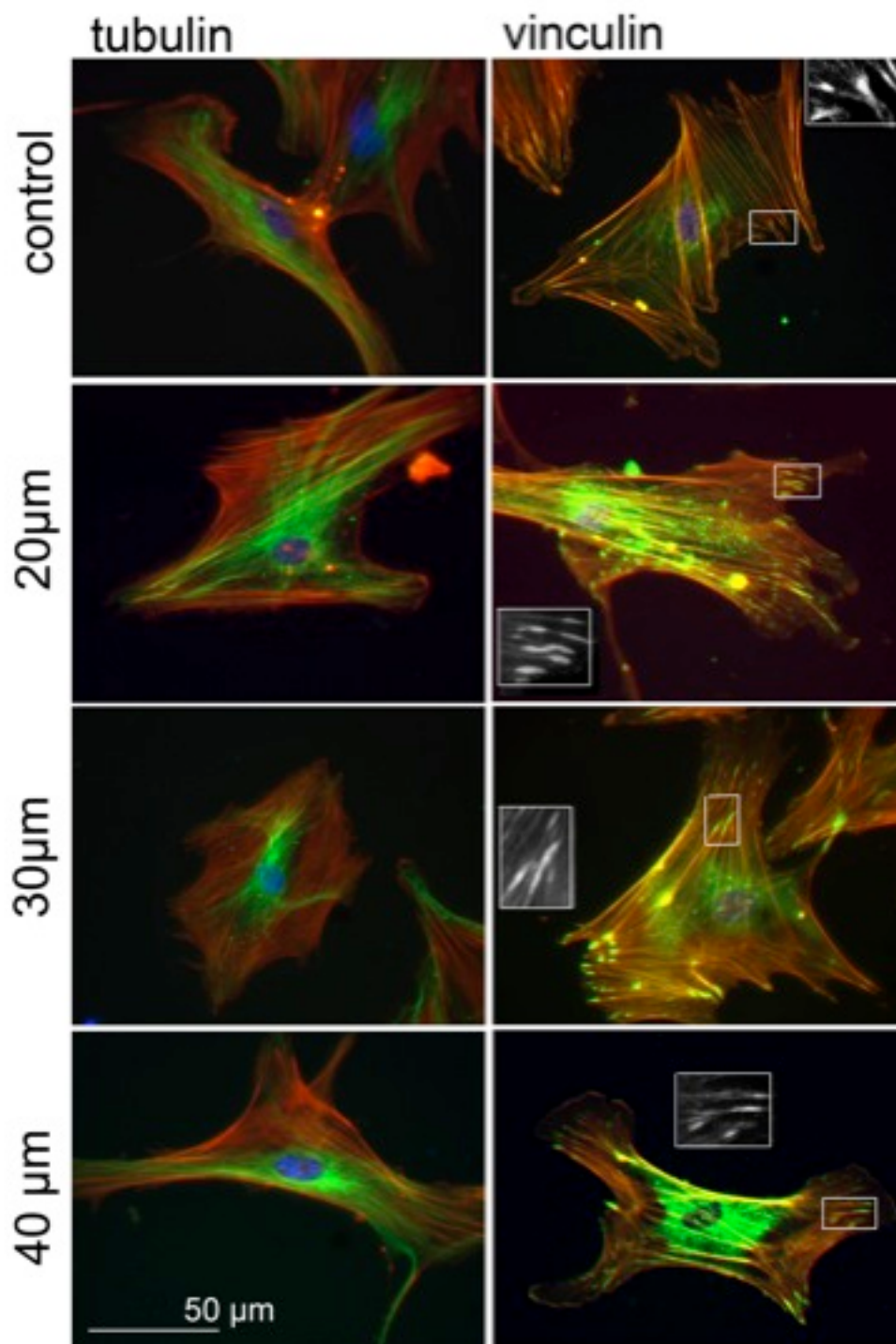


Figure 3-2 Immunofluorescent microscopy images for tubulin and vinculin staining after three days of culture. Red = actin, green = tubulin/vinculin, blue = nucleus. Reprinted with permission from Elsevier (A. Wilkinson et al. 2011)

Alizarin red staining for calcium at 28 days continued this trend, with only nascent nodules observed on the 20 μm pits (arrowheads), whereas large, mature nodules were noted on the 30 and 40 μm diameter substrates (arrows) Figure 3-3. SEM analysis showed that the pit features could still clearly be seen on the embossed polycaprolactone post culture, i.e. they had not biodegraded in this time Figure 3-5. For immunofluorescence, red = actin and green = osteopontin (OPN). For histology, red = calcium and blue = cell morphology.

Osteopontin staining after 21 days of culture on the materials showed large differences not only between the test topographies and the planar control, but also within the different pit diameters (Figure 3-3). On the planar control, whilst good cell growth was observed (as shown by dense cell coverage), very low levels of osteopontin expression were observed. However, on the samples, most notably the 30 and 40 μm diameter pits, not only good growth, but also strong expression of osteopontin were noted both intracellularly and extracellularly Figure 3-3. In cells on the 20 μm diameter pits only intracellular staining was noted, especially close to the nuclei.

By 28 days, alizarin staining revealed that this trend had continued and, whilst nascent nodules were observed produced by osteoblasts on the 20 μm diameter pits, large, mature nodules were noted on the 30 and 40 μm diameter pit materials Figure 3-3. Few nodules were noted on the planar control, just confluent cells with fibroblastic morphology (self-aligned bipolar) Figure 3-3. This is quantified in Figure 3-4 showing the graphical representation of the ANOVA count of calcium nodules in the Coomassie counterstained alizarin substrates. In Figure 3-4 ‘**’ represent significant increased in calcium nodule formation in the patterned substrates compared to the planar control and the separation sign (\$) shows significant difference in nodule formation for the 30 μm substrate as compared with the other embossed substrates and the planar control.

The scanning electron microscopy images in Figure 3-5 show confluent growth of the cell sheet. There is no clear difference in cell appearance within the pits as compared to those on the border or outside the feature. There are nodules seen across the surface of all the substrates. Optimistically these may be deposits of protein or calcium, they may also be debris from the cell monolayer. In any case the distribution of these nodules does not appear to relate to the position of the circular features.

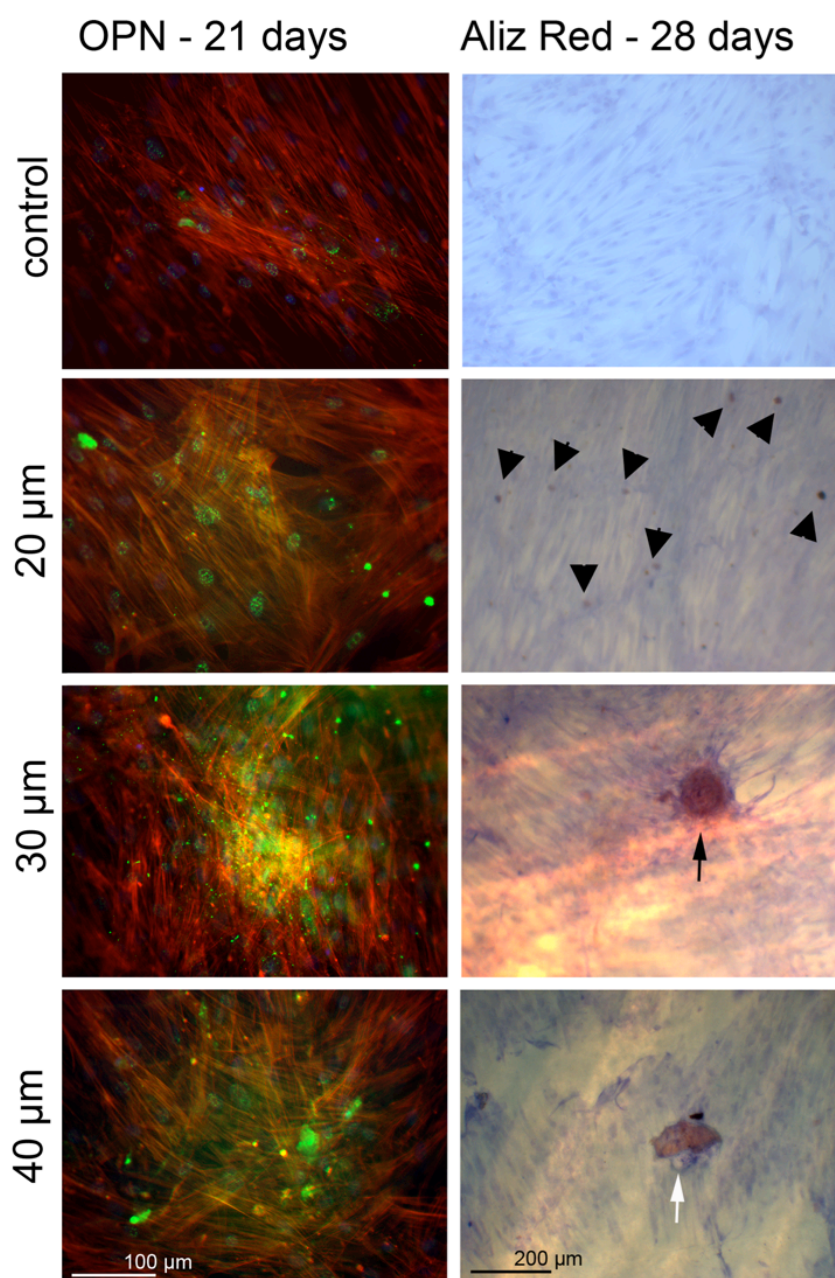


Figure 3-3 Phenotype staining for osteopontin (in green in the left hand column) at 21 days of culture and calcium staining by alizarin red (red in the right hand column light microscopy images) at 28 days of culture. . Reprinted with permission from Elsevier (**A. Wilkinson et al. 2011**)

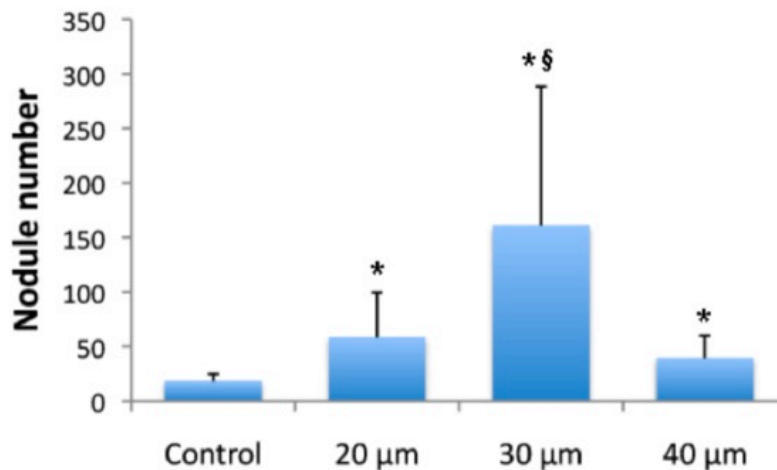


Figure 3-4 Graphical representation of the ANOVA for particles of calcium on substrates cultured for 28 days. Far fewer alizarin red-positive areas were noted on the control compared to on the pitted surfaces. Most alizarin red-positive areas were noted on the 30 μm diameter pits, tying in well with main script qualitative data. Results are mean ± SD. *p < 0.05 compared to control; §p < 0.05 compared to other test substrates by ANOVA.

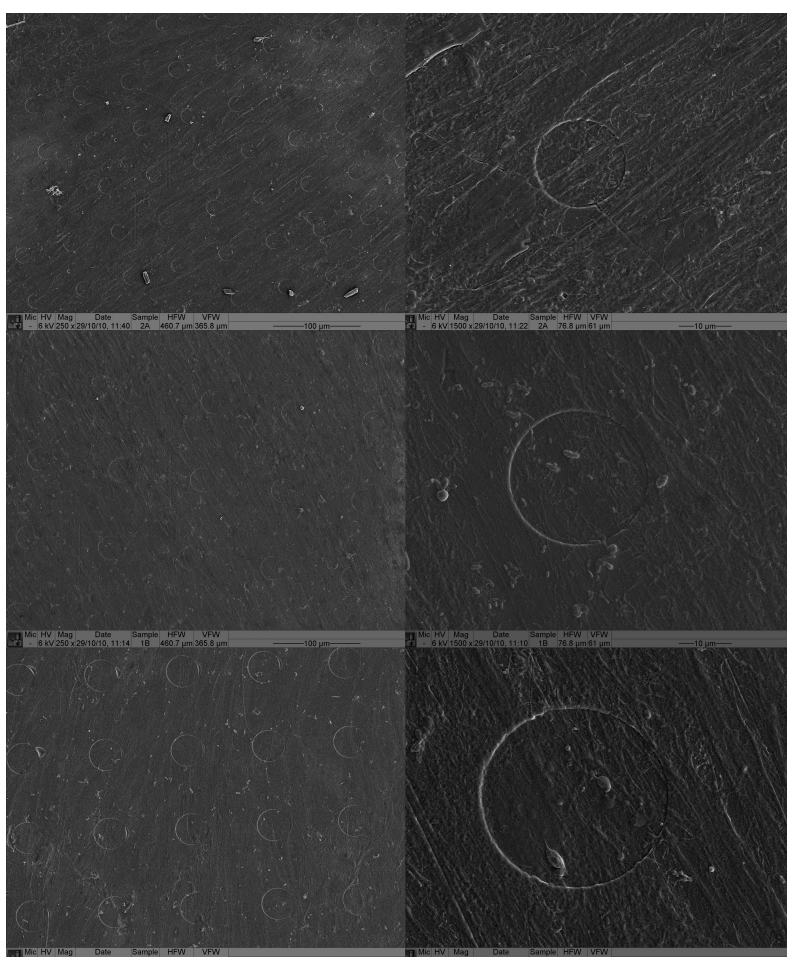


Figure 3-5 SEM images of PCL with a cell monolayer covering the substrate. The substrates are seen from 20 μm circular pit most superior and the 40 μm pit most inferior. The high magnification views in the right hand column show cells distributed evenly across the surface with no particular change in appearance around the circular pits. The left hand column shows some nodular structures across the surface of the substrates. The nature of the nodules is uncertain. There does not appear to be any correlation between these features and the embossed topography.

3.4 Discussion

3.4.1 Focal adhesions and cytoskeleton

Focal adhesions form the anchorage for cells into the extracellular matrix. This action is important as experiments performed comparing the changes in cytoskeletal structure when cultured on glass or fibronectin showed a delay in the cytoskeletal response in the cells cultured on glass of 72 hours culture time, where those cultured on fibronectin demonstrated change at 24 hours (Treiser et al. 2010), the cells require additional time when cultured on glass to produce extracellular matrix to provide anchor points. Osteoblasts contain a greater number of focal adhesion proteins (Ezrin, radixin and moesin family) than MSCs (Titushkin & Cho 2009) suggesting a greater number or size of focal adhesions. Previous work with knock out cells for these proteins has shown there is a decrease in the expression of alkaline phosphatase and messenger RNA levels for osteogenic markers (Titushkin & Cho 2011). The qualitative assessment of the focal adhesions in this experiment shows a greater number and size of focal adhesions in the patterned samples compared to the control. Between the samples with differing feature size the 30 μ m feature has shown the most favourable production of focal adhesions. The formation of large stable focal adhesions provides stable anchoring for the cell and is more likely to promote differentiation than proliferation.

The formation of large stable focal adhesions is linked to the increased level of cytoskeletal tension as demonstrated by actin staining. The organisation of the tension fibres with the cytoskeleton is an important marker of differentiation with clear differences seen between MSCs and osteoblasts (Titushkin & Cho 2009). Intracellular tension has also been shown to drive differentiation and osteogenesis (Li et al. 2013; de Groot et al. 1998; Valancius et al. 2013; McBeath et al. 2004; Goyenvalle et al. 2003; Kirsh et al. 2000; Kilian et al. 2010; Furlong & Osborn 1991; Batta et al. 2014). Disruption of the actin cytoskeleton in the presence of osteogenic differentiation medium creates a decrease in the levels of alkaline phosphatase when compared to the control (Rodríguez et al. 2004)

suggesting again that the cytoskeleton and tension across the cell are important for the development of bone forming cells.

3.4.2 Osteopontin expression

As described in 2.7.2.3 osteopontin as one of the sibling proteins has a role in bone production. Zohar in 1998 (Zohar et al. 1998) showed that osteopontin is expressed early in differentiation and may play a role in cell migration as it contains an RGD domain. Osteopontin production has been identified across two sites within cells in culture, perinuclear distribution and intracellular distribution (Zohar et al. 1998; Zohar et al. 1997). The results from this experiment show an increased level of both intracellular and perinuclear expression of osteopontin for the 30 μ m samples compared to the others. Expression of these matrix maturation proteins is indicative that the cells are preparing their environment for mineralisation.

3.4.3 Alizarin staining

The results shown in Figure 3-4 show a quantified and significant increase in the number of deposits of calcium stained with alizarin in the 30 μ m patterned substrate. The production of calcium may be intracellular (for example as an increase in intracellular messenger activity) or seen in extracellular matrix as discrete deposits of calcium. Overall detection of increased calcium by mass or volume does not equate with calcium nodules (used as a positive result given the mineral composition of bone). The detection of deposits of calcium in the ECM is more encouraging than if the increase in calcium levels were attributable to an increase in the intracellular levels only

This experiment has some weaknesses; PCL is a good material for embossing but does not possess the same handling properties or material characteristics as zirconia/alumina composite ceramic. The cells used for this portion of the study, are a cell line of osteoblasts, they may not behave in the same manner as primary human cells: osteoblast, osteoprogenitor or mesenchymal stem cell.

3.5 Conclusion

Circular pits are successful in increasing the production of bone related proteins and calcium nodules. Furthermore there is some evidence that the diameter of the feature is relevant to the behaviour of the cells. .

4 Materials characterisation.

4.1 Introduction

Hot embossing in thermoplastics is common and accepted. Influences on cell behaviour have been evaluated in polymers and the results have been encouraging. (A. Wilkinson et al. 2011; Maclaine et al. 2012; McMurray et al. 2011). Ceramics present altogether different manufacturing and embossing challenges. As part of the evaluation of topographical influence on cell behaviour it is vital the quality of surface features may be reproduced across various materials. In this chapter I set out to evaluate the quality of topography reproduction in PCL and to compare this to the quality of surface feature created in ceramics. The hypothesis to be tested is high fidelity reproduction of circular microscale circular feature will be possible in implant grade zirconia toughened alumina.

4.2 Materials and topographies

4.2.1 Polycaprolactone

Verification of the fidelity of topography from the nickel shims used to emboss PCL was performed with SEM (JEOL6400 running at 10 kV, tif images were captured using Olympus Scandium software). Figure 4-1 shows a collection of SEM images taken after 21 days of culture, the cell monolayer had already been fixed. Even through the cell monolayer the features are readily identified with a high fidelity of reproduction.

Using the scale bar incorporated with each image the true measured dimensions are recorded in the most right hand aspect of the image. The diameter for each feature in the polymer is less than the intended value. For the 20 μm feature the measured diameter is 18 μm , for the 30 μm feature the measured diameter is 28 μm and the measured diameter for the 40 μm feature is 37 μm . The centre-to-centre spacing for the features is also reduced from the intended. The intended pitch for the 30 μm and the 40 μm features is 100 μm , this measures 96 μm on both substrates pictured giving a decrease or shrinkage of 4%, the pitch for the

20 μm embossed substrate measures only 56 μm , where it was intended to measure 60 μm , showing shrinkage of around 7%.

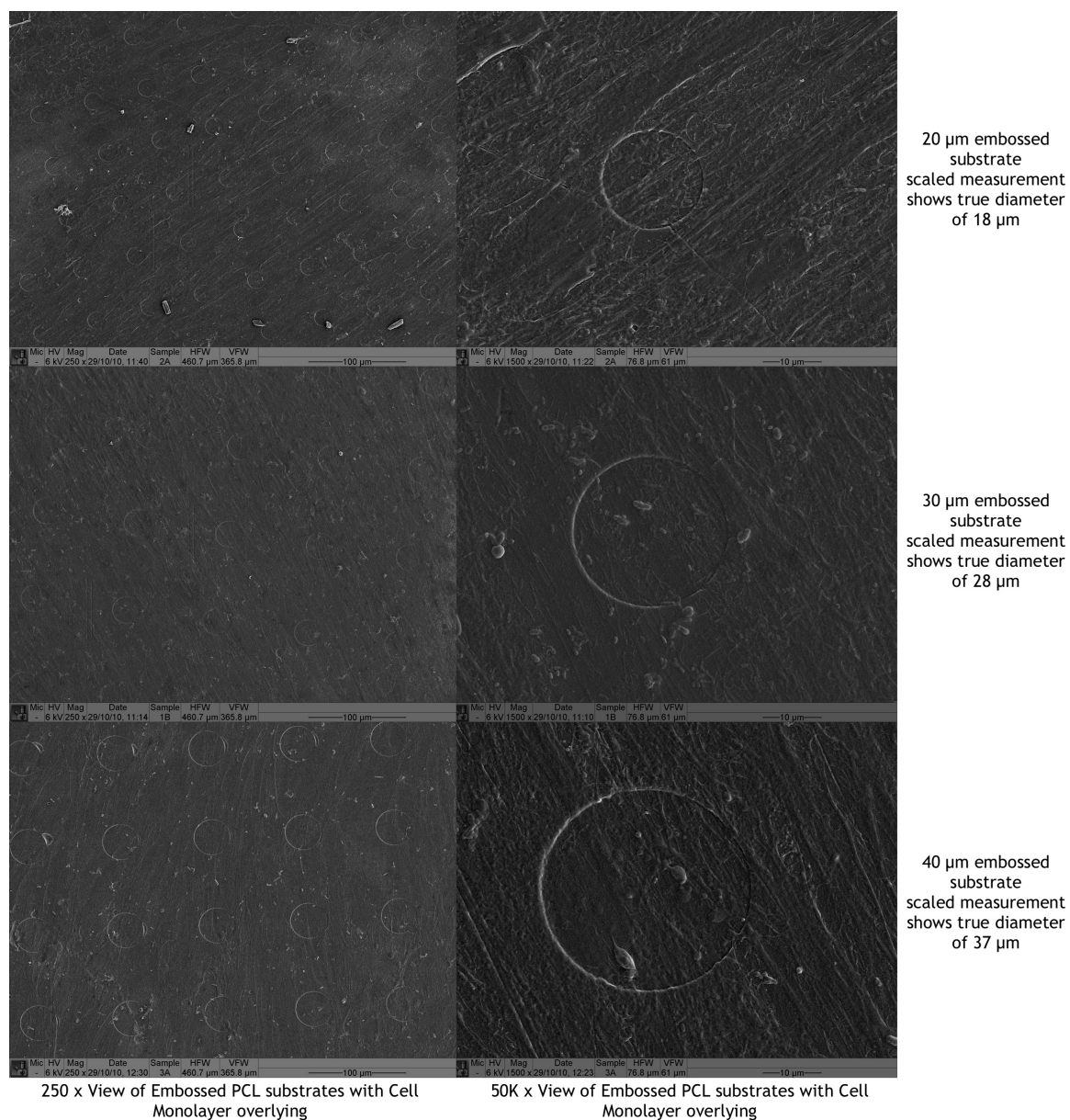


Figure 4-1 SEM pictures of the embossed substrates of polycaprolactone easily visible through the monolayer of human osteoblastic cells. The morphology of the shapes is clear and the features have sharp well-defined edges. Each image within the montage contains a scale bar. Using this bar the dimensions for the features have been measured. The measurements may be seen in the right hand column of the image. Interestingly the dimensions of the features are reduced compared to the intended size. Reduction of between 10 % (for the 20 μm substrate) and 7.5% (for the 40 μm substrate).

4.2.2 Masks used for embossing ceramics

Figure 4-2 shows light microscopy images of the masks manufactured for the embossing of the ZTA ceramic, pitch is 100 μm and the features are accurate for the intended size (measurements using the enclosed scale and ImageJ line measurement).

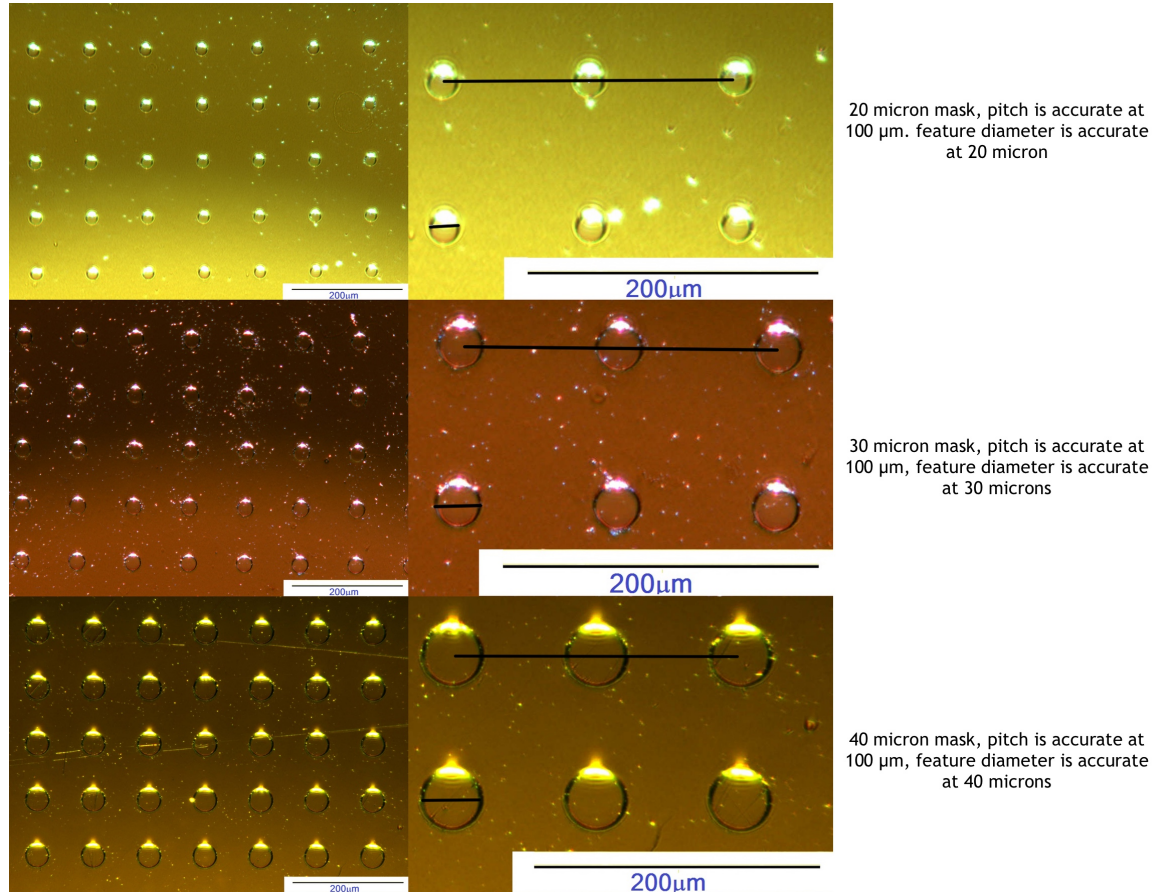


Figure 4-2 Light microscopy images of the masks created for embossing zirconia toughened alumina. The right hand column shows measurement lines created in ImageJ from the included scale bar. These confirm the pitch of the features to be accurate at 100 μm for each mask; likewise the intended features are accurate for each mask.

4.2.3 Alumina and Zirconia toughened alumina

4.2.3.1 X-ray photoelectron spectroscopy

Samples of planar and embossed alumina and zirconia toughened alumina were analysed as described in 2.3.2.1.

Comparison of the XPS data for alumina shows only Alumina present, ruling out any cross contamination from the other ceramics. In the samples assessed there

is an uneven balance of oxygen and Aluminium. The detection of elements shows 51.49% oxygen and 48.51%.

For the zirconia alumina composite ceramic there is also no detection of other elements. Just as with the alumina, there is not an even distribution of the component parts of the ceramic across the samples. There is also a difference in the percentage content of zirconia between the samples (Table 4-2). Allowing that both elements are fully oxidised in the material, expressing the alumina and zirconia content as a ratio it is seen that there is a wide variation. This may be a reflection of distribution of the molecules through the material.

	Oxygen	Aluminium	Zirconium
Planar Control	56.39	41.69	1.93
20 μm sample	50.00	48.12	1.88
30 μm sample	56.62	41.06	2.32
40 μm sample	69.94	29.21	0.85

Table 4-1 detection of elemental composition for Zirconia alumina ceramic. There is wide variation in the detection of the composite parts. The outlier for the samples is clearly the 40 μm sample with almost 70% oxygen detected.

	Percentage alumina	Percentage Zirconia	Ratio
Planar control	41.69	1.93	20:1
20 micron	28.12	1.88	25:1
30 micron	41.06	2.32	17:1
40 micron	29.21	0.85	34:1

Table 4-2 ratio of alumina to zirconia content. Calculation of the ratios for the two elements highlights the significant variation in detected elements. Although this may not be reflective of the materials in bulk it shows that the surface presented to the cells is variable by chemistry

4.2.3.2 Atomic force microscopy

The two-dimensional profile of the embossed zirconia toughened alumina demonstrates good fidelity of the embossed pattern Figure 4-3, Figure 4-4, Figure 4-5. Figure 4-3 shows two surface images accompanied by surface trace information for each image. The features of note are the red trace showing the level of trace from an area with no feature. The blue and green traces are perpendicular traces across one feature; these traces are very similar in appearance, suggesting a circular rather than elliptical feature. The right hand image and trace are taken on the same sample section but scaled differently to allow a more detailed inspection of the surface and feature.

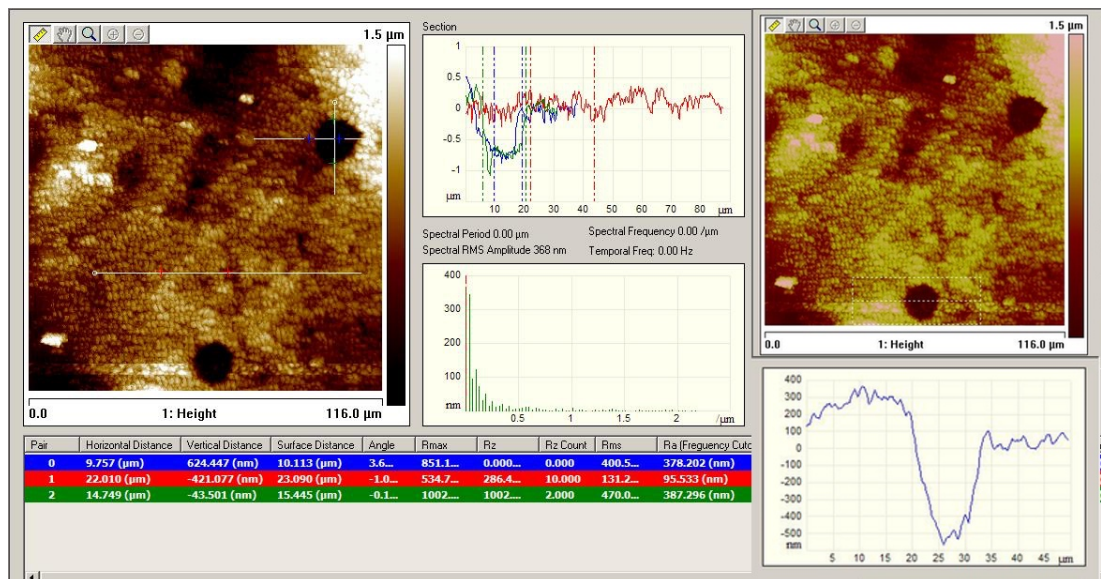


Figure 4-3 Two dimensional surface trace and dimension assessment of 20 μm embossed ZTA. The right hand image shows the width of the feature as 15 μm and the maximum depth of the feature is 500 nm (or half the intended value). The red line shows the background trace has some variation in height with many small features on the scale of a few micrometres.

Figure 4-4 displays the same information for the 30 μm patterned samples as shown in Figure 4-3 shows for the 20 μm patterned samples. The green trace in this figure shows the area of the sample without a feature, with the red and blue traces detailing the profile of the 30 μm feature. The image and trace on the right show the details of a feature profile in isolation.

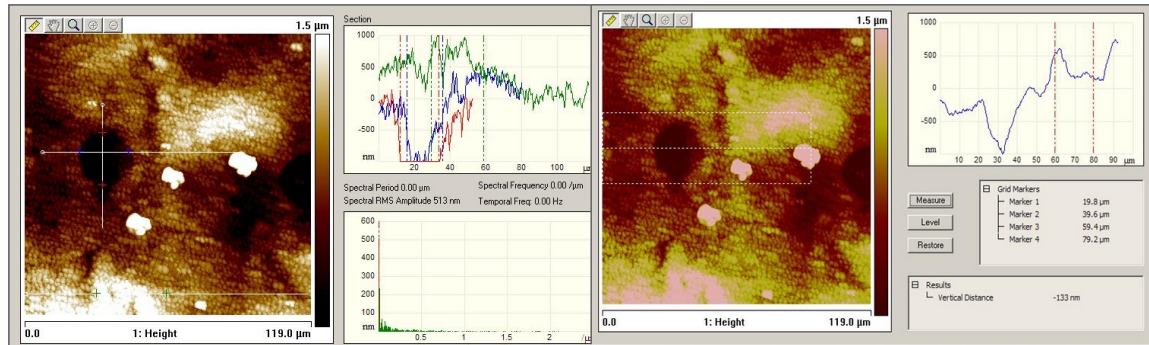


Figure 4-4 Two dimensional surface trace of 30 micron embossed ZTA. Two variations on surface profiling. The left image shows a surface trace along three lines; blue and red lines trace the embossed feature and the green line traces the background surface. The red and blue lines confirm the presence of the feature, they also confirm the dimensional reduction and the slope to the sides of the pit. These two aspects are further emphasised by the right hand trace. The left hand green trace clearly demonstrates the background surface irregularities at a scale of 1 or 2 μm , additionally a significant rise is noted, this approaches 1 μm in height – the same magnitude as the depth of embossed feature.

Figure Figure 4-5 shows a closer picture of the profile for a 40 μm feature. In this larger feature it is easier to appreciate the profile of the base of the circle. Interestingly in this profile the dimensions of the feature are not circular, the x axis (left to right axis) is definitely greater than the Y axis.

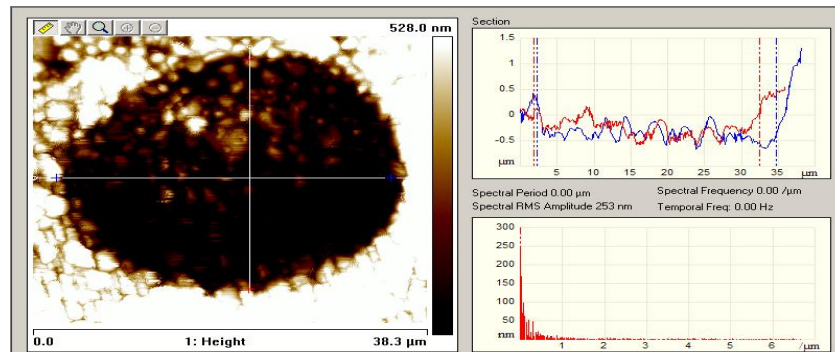


Figure 4-5 Two dimensional surface trace of 40 micron embossed ZTA. While clearly visible as a feature the sides of the feature are not straight, the base of the feature contains many islands of nanometre size and the dimensions of the feature are smaller in both axes that intended or achieved by the manufacturing for the masks. Also note the oblong shape to the feature

Although each feature is clearly identified, for each substrate the dimensions of the feature are less than those created in the manufacturing of the nickel shim. The diameter for the embossed pattern for the 20 μm pattern is 15 μm , for the 30 μm pattern the measured dimension is 25 μm and for the 40 μm pattern the measured dimension is 35 μm . This discrepancy is apparent in the cross sectional profile for each substrate in each of the figures.

The depth of the embossed features is not represented as uniform. For the 20 μm substrate in Figure 4-3, the deepest recording is 1 μm , the base of the feature is not a uniform depth with the rest sitting at 0.5 μm . A similar picture is seen for the 30 μm and 40 μm traces seen in Figure 4-4 and Figure 4-5. The tallest registered surface feature extends to around 0.5 μm in height in both the 30 μm and 40 μm substrates and while this may represent a slight asperity in the material around the edge of the feature, it is notably absent in the profile for the 20 μm substrate and does not suggest a true feature depth of 1 μm . The edge of the feature is not well defined as a sharp feature; the change in vertical dimension appears as more of a gradual slope than a sharp change in profile, this as with the other features is seen across all the embossed substrates.

Another readily apparent surface feature is the large aspect ratio (that is the general surface profile related to the profile of the embossed feature) present on these ceramic substrates. This is due to the granular structure of the ceramic, the variation, easily visualised in the three-dimensional renders of the embossed ceramics (Figure 4-6), is quantified in the cross sectional profile in the Figure 4-3, Figure 4-4 and Figure 4-5. Although this is simply the nature of the surface, the presence of such an aspect ratio may detract from any pure topographical effect provided by the embossed pattern.

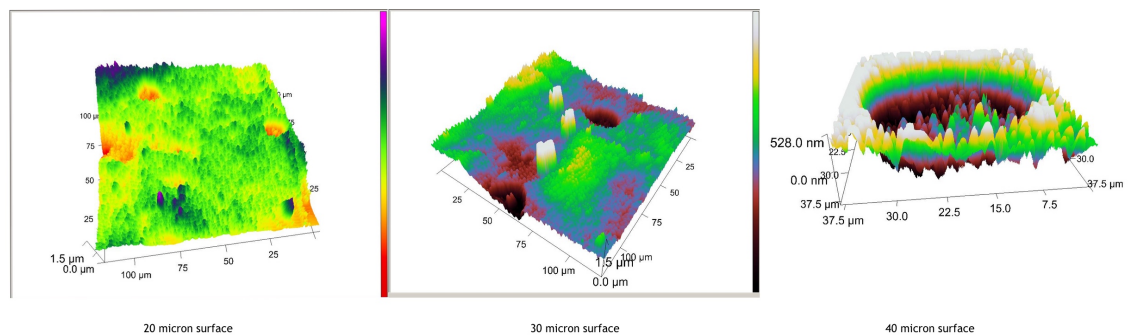
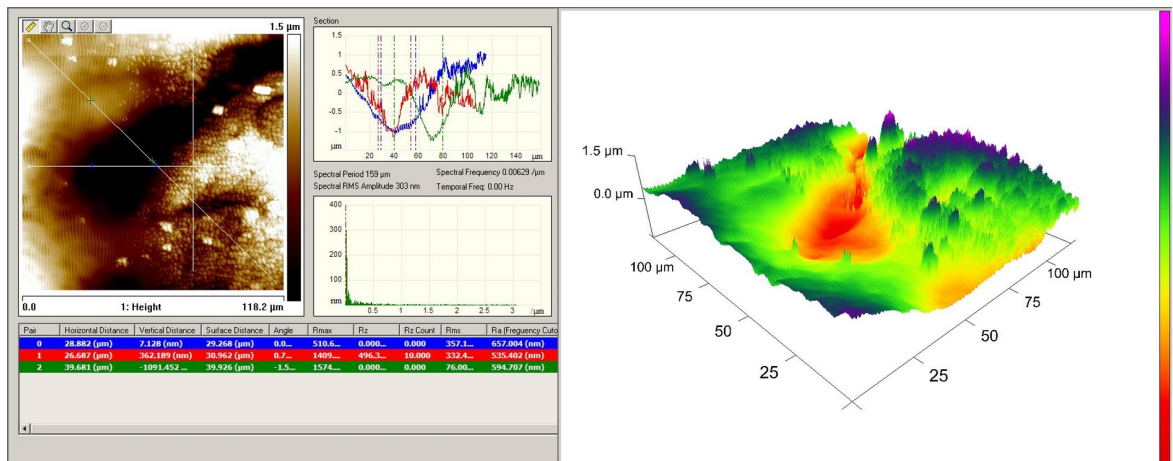


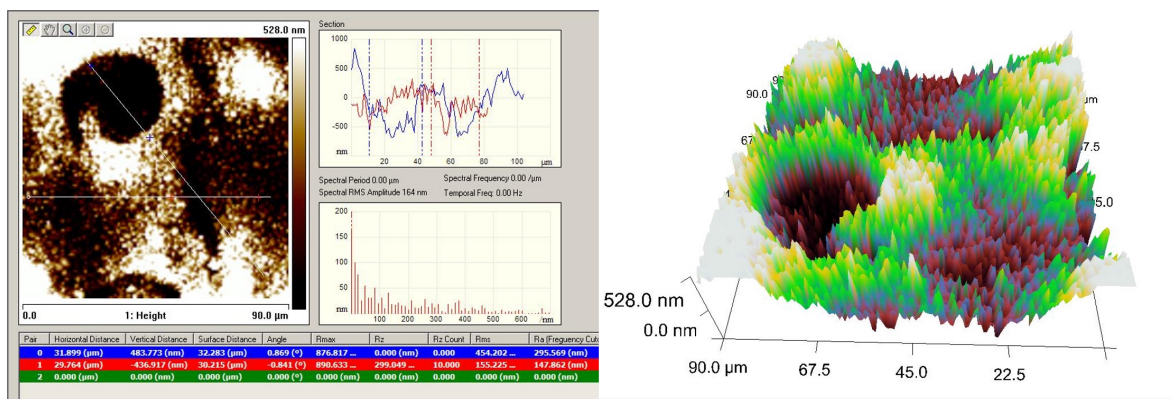
Figure 4-6 These three dimensional renders of all the sizes of substrates provide good visual data on the multiple peak surface presented to the cells. Where the embossed features are clearly reproduced and present the background surface to the materials is significant. Some depressions are seen as are some islands which are a magnitude of size smaller (nanometre size)

Figure 4-7 and Figure 4-8 are combined surface profile cross sections and three dimensional render of substrates found with significant surface artefacts remote from any aspect ratio provided by the granular structure. Figure 4-7 shows a valley artefact, extending to a depth of at least 1 μm and Figure 4-8 shows a smaller volume distortion in a 40 μm substrate, extending to only 0.5 μm in depth, it is however equal in depth to the intended surface feature.



Two dimensional surface profile and three dimensional render of a 30 micron embossed ZTA ceramic showing a significant surface variation

Figure 4-7 distortion of 30 μm embossed ceramic. This valley feature is smooth sided and very large but of a similar depth to the intended features. The typical peak structure seen across the rest of the substrate (and indeed all the other examples) is missing at the left hand side of the surface image – this absence of peaks suggests that there may be an error in tip contact however the continued presence of the defect through the entire length of the substrate can not be explained by a technical error.



Two dimensional surface profile and three dimensional render of a 40 micron embossed ZTA ceramic showing some background distortion of the surface

Figure 4-8 Distortion of a 40 μm embossed ceramic. There appears to be a folding of the substrate affecting the feature and the background surface, presumably this has occurred with removal of the embossing mask prior to sintering. The artefact is of similar magnitude to the intended feature. Referring to the blue and red markers on the left hand image shows little difference between the cross sectional profile of the red markers (background surface trace) and the blue markers (cross sectional profile of the substrate including the embossed feature)

4.2.3.3 Scanning electron microscopy

Beginning with a high magnification image, Figure 4-9 demonstrates the grain structure of the ceramic. The alumina grains are the large grey grains of material with the smaller white grains of zirconia often seen located at a grain boundary. During the sintering process the zirconia granules remain very close to their initial size (average $0.6\ \mu\text{m}$) where the grains of alumina, initially averaging $0.5\ \mu\text{m}$ in size, experience grain growth and are much larger after sintering. This is a well described phenomenon (Humphreys & Hatherly 2002) and relates to the recrystallization of materials and reduction in grain boundaries as an energy control mechanism at high temperature. The behaviour of these grains at high temperature also explains why the particles of zirconia are found mostly at the grain boundaries. The grain distribution in this sample appears even, although the XPS data suggests a possible variation in surface molecule distribution, the surface appearance shown in Figure 4-9 and comparison of the higher magnification views on the right hand side of Figure 4-10 show that grain distribution is even across all of samples assessed with the electron microscope

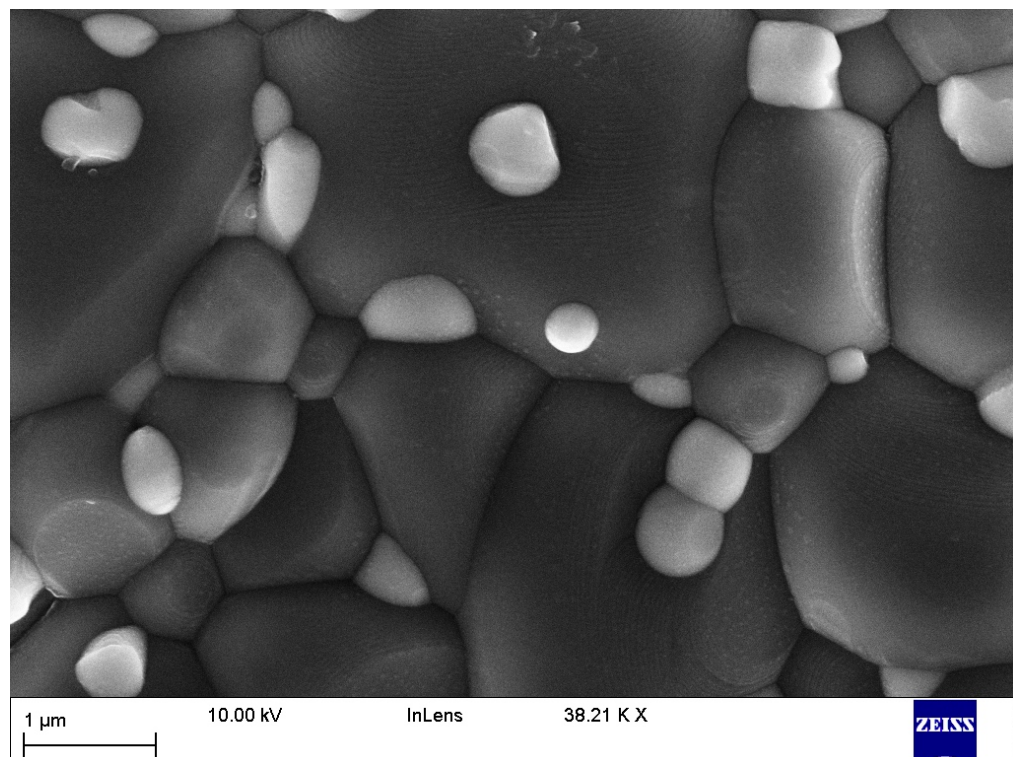


Figure 4-9 – high-resolution image of the surface of the zirconia (small white grains) with Alumina (large grey grains). Note the presence of zirconia mostly along the grain boundary (best position to act as a toughening agent), also note the greatly increased size of the alumina grains. This phenomenon is well recognised during sintering is related to dissipation of energy after heating, it is still a consideration in the presentation of surface features to the cells.

Figure 4-10 contains comparative images for the embossed ZTA ceramics. The left hand column contains images provide an overall view with the aim of showing the reproducibility of the embossing and any defects in the substrates. Several features are worthy of comment - a much greater level of magnification is required to perceive the features in the 20 μm substrate (1200 x magnification as compared with 500 x magnification for the 30 μm 40 μm substrates below), this results in fewer of the features being included in the field of view, even allowing for this the 20 μm features are much more difficult to appreciate and have been artificially highlighted with a black circle for the purposes of the figure. The column on the right shows much higher magnification views of the features. The 40 μm feature is the most readily seen. Using the included scale bar for each composite part of Figure 4-10 to calibrate the measurement tool in ImageJ allows accurate dimensional assessment. The pitch (centre to centre spacing) is 88 μm for the 20 μm substrate, 85 μm for the 30 μm substrate and 83 μm for the 40 μm substrate. Calculation with ImageJ shows the width of each feature to be 15 μm , 22 μm and 32 μm approximately. Although these values are approximated and prone to error with conversion to pixels and calibration they prove a reasonable approximation of true dimension when compared along side the values for the width of feature measured on the AFM Figure 4-3, Figure 4-4 and Figure 4-5 and the direct measurements from the SEM shown in Figure 4-11 with cursor widths 13.72 μm 22.05 μm and 33.83 μm .

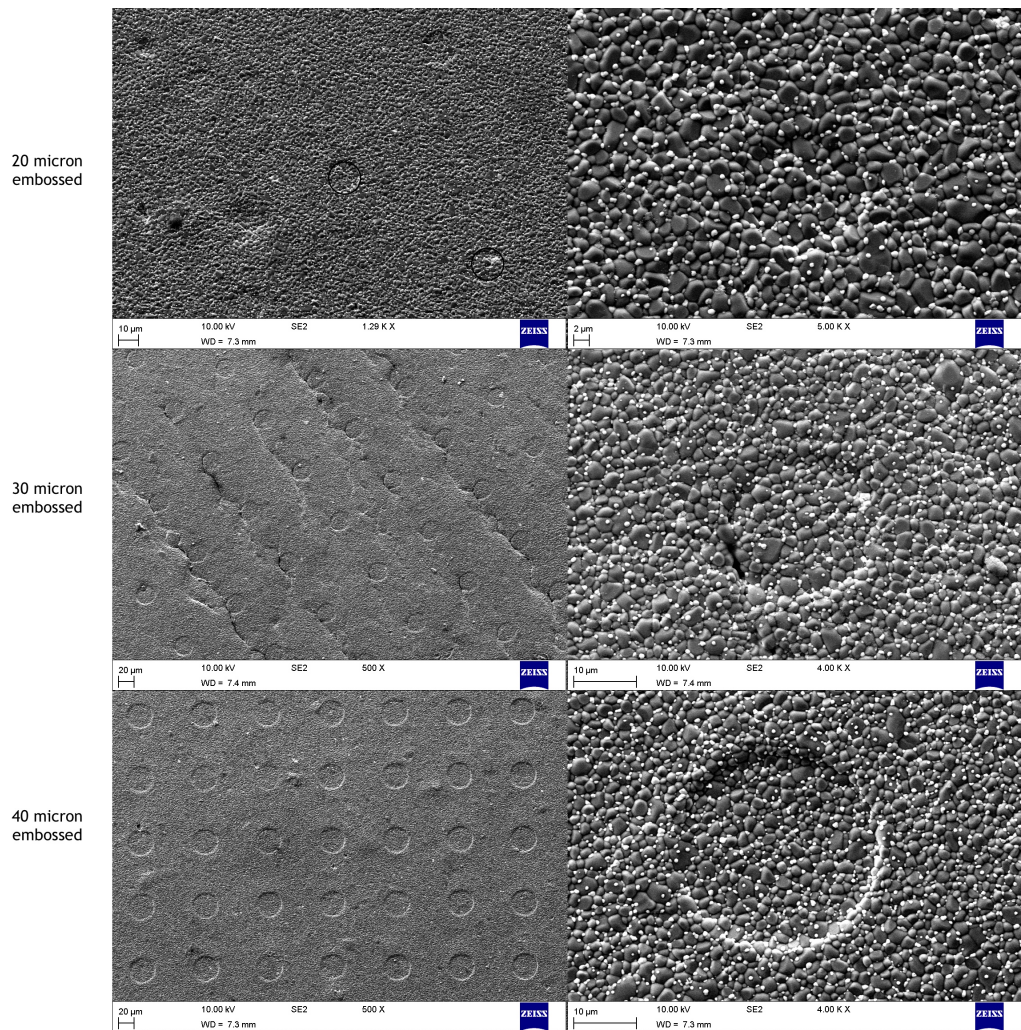


Figure 4-10, Low and medium magnification views of the embossed ZTA ceramic. The 20 µm feature (row 1) is difficult to see, the magnification has been increased, and two features have been marked for more straightforward identification. The 30 µm features are more easily seen, clearly reproducible however there is a significant manufacturing artefact through the entire sample, this ridge like artefact will have a topographical influence on cell behaviour and is a similar magnitude to the intended size of feature. The 40 µm embossed feature is the most obvious, both on the 500 x view (left column) and the 4000 x view (right column), although there is little artefact in this substrate there is definitely variation in the depth of the features (the pits in the top three rows particularly for the first four columns are much more shallow than those at the opposite corner of the sample).

Figure 4-12 shows a low magnification view of a 40 µm substrate, this shows a large defect across approximately 300 µm of the surface with a width of around 10 µm for the crevice this presents an area around 3000 µm², the middle row of images of Figure 4-10 shows the 30 micron substrate with a repeated artefact feature at each column (allowing for the rotated image taken in the microscope).

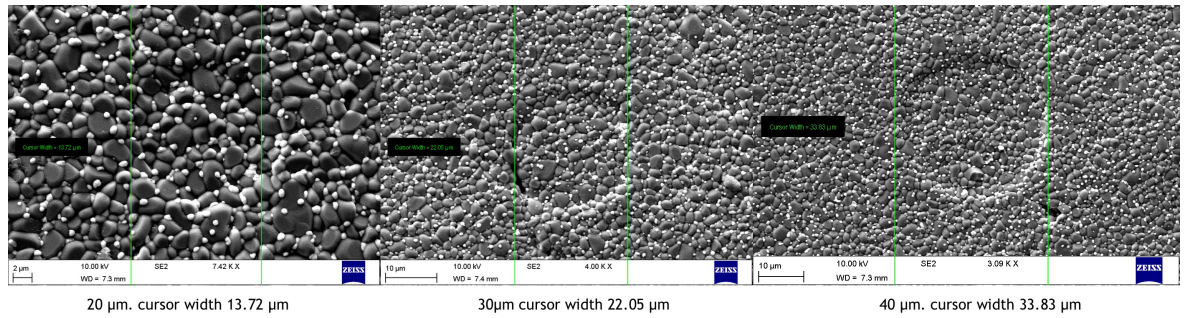
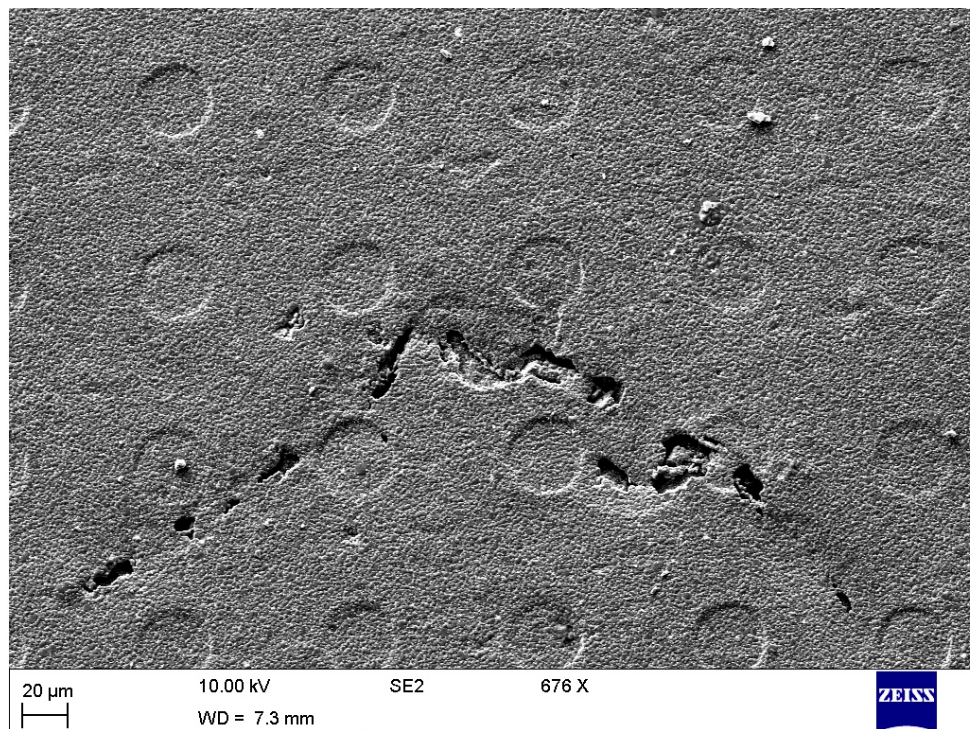


Figure 4-11 Direct measurement from the Scanning electron microscope. These direct measurements confirm that there is significant dimensional reduction during the processing of the ceramics. The percentage shrinkage varies from 15% (40 µm) to 30% (20 µm) although the measurement bars for the 20 µm are inaccurately placed in this example.



Low magnification view of a 40 micron embossed ZTA ceramic with crevice

Figure 4-12 - Artefact in the ceramic surface. This slide shows a concerning crevice type structure, likely a side effect of the drying and sintering process clearly this presents a feature to the cells that is much greater than the depth of intended feature. The effect of such a deep feature on the cells is uncertain, however this feature will cause mechanical difficulty for the implant, it would not survive proof testing and is unlikely therefore to be a real concern in vivo.

Figure 4-13 shows a three dimensional reconstruction of a 40 µm embossed circular pit, confirming the general reproduction of the circular pattern in the composite ceramic material and highlighting the presence of a slightly rounded sloping edge.

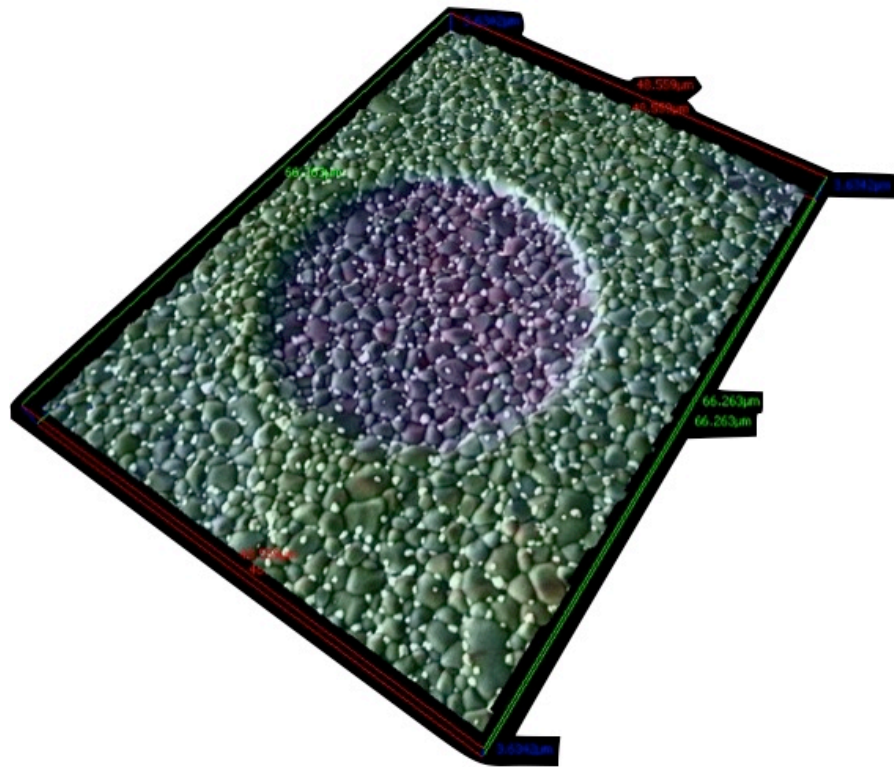


Figure 4-13 3 dimensional reconstruction of a 40 micron pit, colour variation shows the difference in height. The edge of the feature is definitely sloping rather than sharp and defined, likely related to the granular structure of the ceramic this may have an effect on cell behaviour

4.3 Discussion

4.3.1 PCL

High fidelity reproduction of topographies by hot embossing in PCL is straightforward. When heated, the thermoplastic material will conform to all the topographical features of the mask. It is interesting to note the slight shrink of the material. It is likely that these differences in dimension from the intended size are reflection of the shrinkage occurring in the polycaprolactone as it cools from the embossing temperature of 70°C. The embossing carried out for PCL was performed with a cold shim, which would therefore create an accurate topography in the warm polymer, which then cooled resulting in shrinkage of between 4% and 7% (4.2.1). It may be that matching the temperature of the nickel mask to the hot polymer would eradicate this dimensional alteration from the process. Alternatively oversize of the Nickel shim would allow for some reduction in size after hot embossing. SEM produces very high-resolution images; the measurements for the pitch on the images in Figure 4-1 was not performed directly instead the scale bar for each image was used to calibrate the measurement tool in Image J, this introduces the potential for error in

measurement, by using decrease in pitch I hope to have minimised that error although I have been unable to quantify it directly it seems unlikely to be responsible in isolation for the differences measured.

4.3.2 Optical Microscopy for assessment of Masks

Optical microscopy does not approach the same resolution as either SEM or AFM. The same method for measurement of feature size and pitch has been used for these images (Figure 4-2) as for the SEM images of the embossed PCL (Figure 4-1) therefore it is reasonable to assume the same level of potential error in scale and measurement. It is interesting to see completely accurate dimensions for pitch and feature geometry in the masks, it seems reasonable to conclude that the masks have been accurately manufactured - even with the comparatively poor resolution of optical microscopy compared to SEM

4.3.3 Topography in ceramic

X-ray photoelectron analysis of the surface components in the ceramics provided some interesting results. The results for alumina are very close to an even detection of oxygen and aluminium, the bias away is likely explained by measurement bias discuss below. I did not expect to see such variations in composition for the composite ceramic. Two possible sources for the results are variations in composition and measurement variation at the surface level of the samples. In order to more completely evaluate the possibility of material inconsistency it would have been valuable to process a larger number of samples selected at random. Unfortunately this was not performed at the time of the research. Variations in measurement could be possible given the nature of data capture from XPS; a beam of focussed X-rays is directed to the surface, the photo-emitted electrons emerge from the surface at an angle. The surface roughness and the angle of the sample in the analyser can influence the quantification of elements (Information supplied by CASA XPS). Assuming a consistent surface roughness (this was not formally measured as part of materials characterisation however the figures seen for the results of the AFM 4.2.3.2 show that the background profile is greater than 10 nm) and consistent placement of the samples in the analyser a measurement error for quantification should produce a consistent bias to one element or the other. This could explain

a consistent shift in quantification away from the 90% alumina 10% zirconia distribution by weight in the original green ceramic, but does not explain the variation between samples (Table 4-2). Electron escape is varied by the energy of the X-ray beam, the data capture relates only to around the top 10 nm of the surface, surface variations in composition may explain some of the variation seen in quantification. Altering the energy of the X-ray beam can change the quantification of elements, however given the consistent energy used for this experiment this could only help to explain the ratio of composition away from 90% alumina rather than the variation seen. It seems that measurement bias could explain the difference in ratio from the original ceramic to the quantified elemental composition; inter sample variation is better explained by a true difference in material composition in the samples measured.

Unlike topography in PCL, reproduction of the circular topographies in alumina and zirconia-toughened alumina, however, presents challenges. Ceramics were embossed at room temperature and then progressed through the required sintering process. It is unlikely that decrease in feature size and pitch is due to the same reason as that seen in PCL. The flow of PCL into the edges of the embossing shim is not mirrored by the ceramic

The dimensions of the topographies in processed ceramic are significantly different to those seen in the masks. This is due to the shrinkage of the ceramic that occurs during processing. Ceramics undergo two stages of shrinkage, the first is related to the drying and the second is related to the heating process. The figures provided for ceramics range from 4% to 20% (Maccauro et al. 2011; Volpato et al. 2011; Guglielmi et al. 2015); assessing the shrinkage of material and change in dimensions by light microscopy, AFM and SEM shows a greater change in dimension for the ceramics tested than 10%. When assessed as percentage change there is variation between the different ceramics. To allow for measurement error I chose to measure the change in centre-centre spacing. The pitch for the masks is 100 μm (Figure 4-2), the measurements of pitch from Figure 4-10 show that for these measured substrates the change in material dimension varies from 12% decrease to 17% decrease.

Change in material dimension caused by shrinkage is a three dimensional process. Given the accuracy of the measured components of the masks it seems safe to assume the accuracy of the features in the Z plane. This Z plane (or depth) has been measured by AFM and shown to be much less than the intended 1 μm this likely represents the overall decrease in material volume.

There is a very large aspect ratio (that is to say a rough granular surface) to the surface of the ceramic material. This may be thought of as background noise. This background noise is likely due to the granular structure of the ceramics and as mentioned previously will be contributed to by the phenomenon of grain growth resulting in alumina grains up to several microns in size (Figure 4-9). The aspect ratio is likely exaggerated by the AFM images but is certainly present on the surface of the material and also in the base of the features, it is certainly likely to decrease the ability of the cells to differentiate an embossed feature from the background.

AFM is imperfect in sharp edge detection. The nature of a triangular cantilever tip attempting to detect a sheer difference in surface height is represented in the schematic diagram Figure 4-14. The measurement of the feature edge will depend on the geometry of the cantilever tip. This limitation of AFM explains the consistent lack of straight edge detection across all the measured samples Figure 4-3, Figure 4-4, Figure 4-5. If the conclusion were to be made on the basis of AFM images alone, the absence of a sharp edge may be called into question. However, the appearance of a sloped edge with a slightly rounded edge is seen in the SEM three-dimensional close magnification image of the 40 μm substrate Figure 4-13. It is also worthy to consider the possibility that the depth of the cantilever tip could present a limiting factor in assessing the depth. The depth of cantilever tip used for surface mapping is greater than 10 μm and so not a confounder factor in the assessment of a feature at a size of 1 μm .

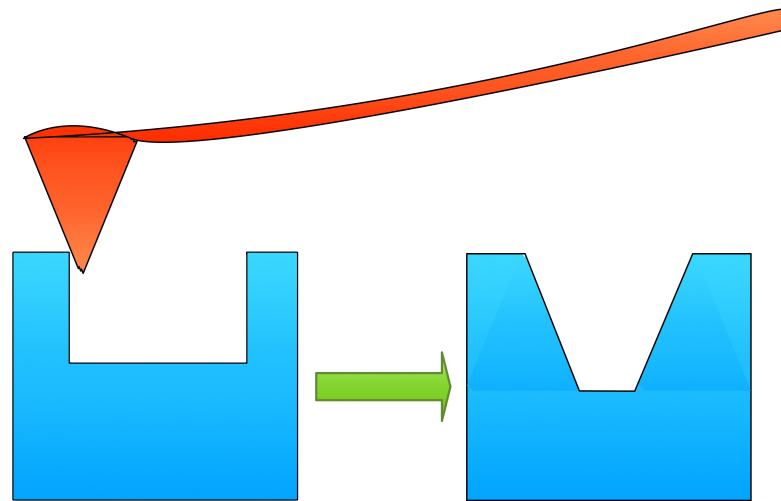


Figure 4-14 A Schematic showing the difficulty in using a pyramidal cantilever tip to attempt detection of a sheer edge feature. The interpretation of the side of the feature will inevitably be influenced by the geometry of the probe

The 40 μm feature as the most easily visualised and measured of the embossed features, however, it is still not uniformly seen. The most inferior left hand image in Figure 4-10 shows that although the feature is visible across all of the surface, the definition of the feature is variable across the image, this variability is more obvious when analysing the low magnification view of the 20 μm and 30 μm substrates (Figure 4-10).

There are several instances of manufacturing artefacts within the ceramic substrate. These are seen in Figure 4-7 and Figure 4-8 where there are significant non-intended surface features. Figure 4-7 clearly shows a large valley type defect in the material that is deeper than the achieved topography. This feature is large and smooth sided, as such the consequences of this feature are uncertain. The irregularities seen in Figure 4-8 are much smaller, they are close in size to the intended feature and the edges, whilst certainly not straight sided are more defined; this type of artefact is more likely to present as a recognisable feature to the cells than the smooth sided valley in Figure 4-7, it would be possible for this type of defect to be polished out, however the flaws seen are almost as deep as the intended feature, removing the flaws would be detrimental to the intended feature. Figure 4-12 clearly shows a bulk material flaw. Whilst this type of material artefact may at first appear concerning and would have the potential to affect cell behaviour, extracellular matrix and the bulk properties of the implant it seems unlikely that this sort of material defect would survive to implantation. Ceramic implants are closely scrutinised and

rigorously proof tested; it is unlikely that this defect would proceed past the scrutinising process. The potential for these types of manufacturing defects may still be concerning for the interpretation of results from experiments on these substrates.

4.4 Conclusion

Reproduction of micron scale topography is certainly possible in ZTA composite ceramic. The results discussed above show that while we have been successful in embossing the ceramic there are some interesting features appearing in the composite ceramic that have not been contending difficulties when working with embossed polymers.

There is shrinkage of the embossed ceramic during sintering; this shrinkage is greater than observed for the dimensional change in PCL. For future research this shrinkage of material and subsequently the desired features should be accounted for in the manufacture of the masks. My results suggest oversizing the masks by a minimum of 12% to provide accurate features and spacing, this percentage oversize will vary with ceramic composition and sintering technique. Further work is required in this ceramic to standardise the shrinkage, this would require a large number of batch tests followed by systematic and carefully assessed changes in embossing and sintering technique to guarantee a final product with reliable surface features

Grain structure and increase in grain size (grain growth) contribute to other aspects of the surface features. The first is a significant background aspect ratio to the surface; this is present on the surface and at the base of the embossed features. Removing the grain features from the surface of the ceramic would be possible by polishing; this may also provide some added benefit in the creation of a sharp edge. Polishing would not remove the grain features from the base of the topography and would reduce the relative depth of the features further. The background noise and grain growth combine to suggest that creating features in ceramic smaller than 1 μm will fail to present readily identifiable features by the target cells. In addition polishing will inevitably remove more of the surface

material, while this will not change the diameter of the surface features it will change the overall geometry of the implant and therefore requires careful consideration. The granular structure also creates detectable topography at the edges of the desired features; this is a particular difference to features created in polymer. In the PCL a well defined edge is readily created and therefore easily identified by the cells, these results shows a much more rounded edge with sloping sides in the ceramic. Embossing of ceramic at room temperature, the inherent properties of a granular material and time resting after embossing prior to sintering may all help to explain some of the difficulties in precisely replicating a sharp pattern in the ceramic.

To summarise, the hypothesis is proved but to a limited extent; microscale features similar to those in PCL can be embossed into ceramics pre-sintering. However, the precise geometry of the embossed features changes with ceramic processing. While not perfect and with much remaining to be improved into the future, substrates for initial cell screening are achieved.

5 Testing the osteogenic capacity of the circular topography in ceramic with primary human cells.

5.1 Introduction

The preliminary study in polycaprolactone has shown that circular pits are a successful topography for differentiation and production of bone related proteins and calcium in vitro; this conclusion is supported by other in vitro evidence in polymers (Dalby et al. 2006; Mata et al. 2009). Having also demonstrated that it is possible to reproduce this topography in ceramic the purpose of this experiment is to test the hypothesis that circular pits will produce the same reaction in ceramic as seen in PCL. The main experimental difference therefore is the use of ceramic rather than PCL. Other differences include the use of primary osteoprogenitor cells (rather than purchased osteoblastic cells) and the use of deeper topographical features for the ceramic (the rationale for this change is seen in the level of background topography found in the ceramics during characterisation of the materials).

5.2 Materials and methods

5.2.1 Focal adhesions

Extracted human marrow cells (2.4 2.5) were cultured on planar and topographical substrates of ZTA ceramic for three days (2.6), at this time the cells were fixed (2.7.2.5) and stained to show vinculin as a representation of forming the focal adhesion plaques (2.7.2.2).

Images were captured with the camera attached to the immunofluorescent microscope using a x40 objective lens (Zeiss axiovert 200M), 15 images were captured for each substrate. In order to allow for an analysis of number and length of focal adhesion the images were opened in an image processing software (Photoshop ®). A white line 2 pixels wide was manually drawn over the focal adhesions present in each cell. The substrates of composite ceramic were slightly convex on the topographic side; as a result occasionally it was not

possible to focus the microscope lens on a complete cell, this is seen in Figure 5-1.

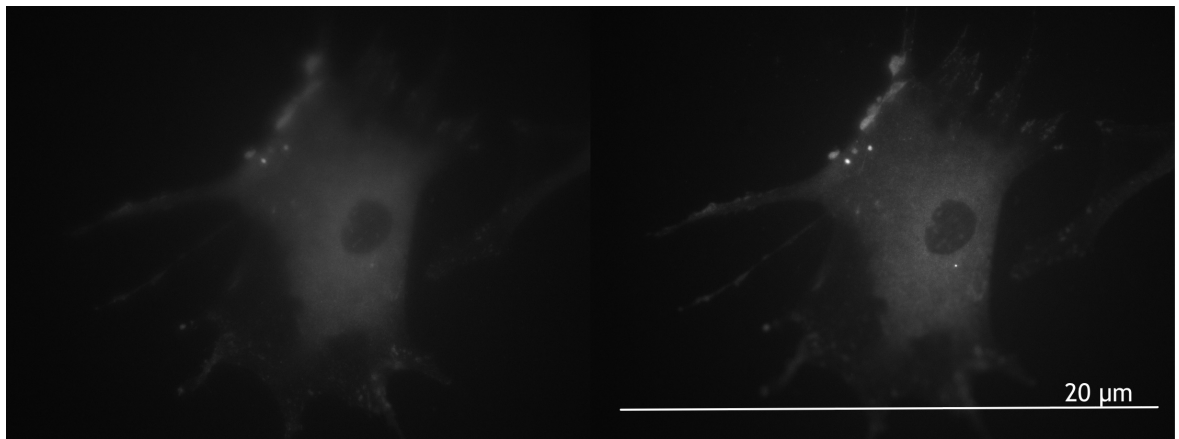


Figure 5-1 side by side images of the same cell, showing the difficulties in focus on an entire cell.

When this was the case two or more images of the cell were captured with different areas in focus, the relevant focussed areas were labelled jointly ensuring no duplication. Figure 5-2 and the images were then combined into a stack of two (or in some occasions 3 images), this stack was then combined using a Z-project combination plugin set for maximum light intensity (Image J), producing a composite image of highlighted focal adhesions Figure 5-3.

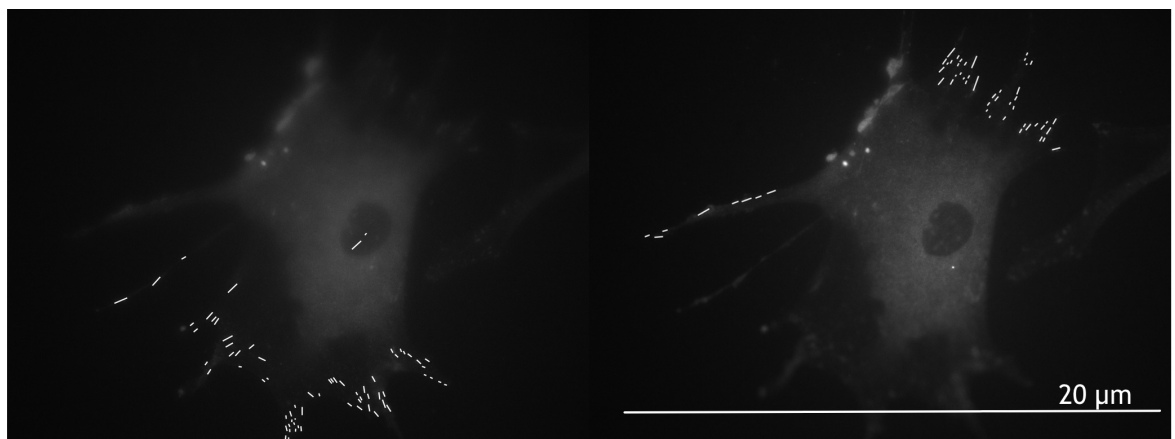


Figure 5-2 illustration for separately labelling in focus areas of a cell. In the top row the two images are focussed on different portions of the cell. The focal adhesions in these areas are then highlighted as shown in the bottom row (40x magnification)

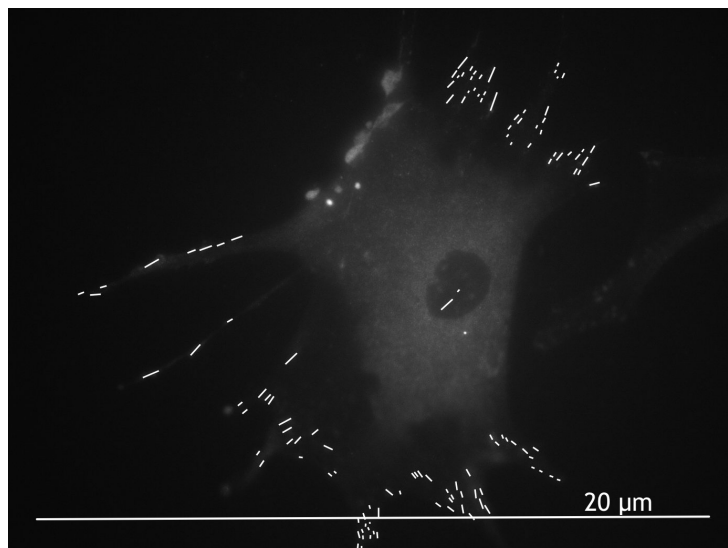


Figure 5-3 Combining labelled images. Once the in focus areas are labelled, the relevant images are converted to an image stack, this image stack may then be combined focussing on the areas of high light intensity in a Z-plane projection (x40 magnification)

Once the focal adhesions had been highlighted and any images combined the images were opened in image J. The scale calibration was set using the graticule captured with the relevant objective lens. The images were then thresholded to remove all data points other than the previously highlighted focal adhesions. Following thresholding a particle count was performed; the image created can be seen in Figure 5-4.

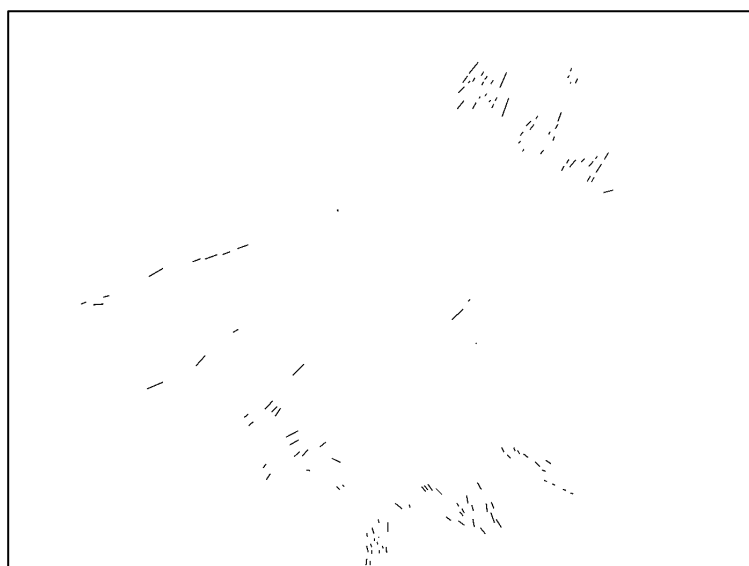


Figure 5-4 Thresholded combined image of focal adhesions. The combined images are then subjected to a threshold for light intensity (allowing for a dark background) the filter level for light intensity is set to capture only the focal adhesions

This provides data on the number and size of focal adhesions present in each image.

These results were then processed using analysis of variance with a significance value of less than 0.05. Given the distribution of the data, processing was performed both for the data raw and also the square root of the values (to convert the positively skewed data to parametric data and allow valid statistical analysis.)

5.2.2 Phenotype immunostaining for osteopontin and osteocalcin

Extracted human osteoprogenitor cells (2.4, 2.5) were maintained and cultured on planar and topographical ZTA substrates for 21 days (2.6.4.2); at this time the cells were fixed and stained (2.7.2.5) one batch were fixed and stained to show osteopontin (2.7.2.3). A further batch of cells was cultured for 21 days, fixed and stained to show osteocalcin (2.7.2.4).

Images were captured with the x10 objective lens on the relevant microscope. 45 random images were captured for each substrate; qualitative assessment of these images for all the substrates has been performed. Where fluorescent microscopy usually allows qualitative analysis of protein production and clustering in relation to cell position, the autofluorescent properties of the ZTA ceramic created difficulties with this method of data analysis. Allowing for the autofluorescent quality of the ceramic quantitative analysis of the protein production was also performed. All the images for each substrate were opened simultaneously in image J. Each image was optimised using a window level adjustment to minimise the background noise. Once optimised, the images were converted to a stack. The entire stack was adjusted to a threshold where only the proteins of interest remained (creating a standard for the set) the threshold level was maintained for the assessment of all images for any given protein expression. As for the analysis of focal adhesions the scale for image processing was set using the graticule captured using the x10 objective lens. A gated particle analysis was performed for each image in the processed stack with limits of greater than $0.005\mu\text{m}^2$ but less than $10\mu\text{m}^2$. These upper and lower limits were imposed to remove some background noise that remained in the images, the limits were set based on the measured size of large features that

represented cell folding or other artefact areas to determine the upper threshold and the measured area of the size of the smallest high intensity area that was clearly protein deposition rather than noise from the image. This data was analysed using analysis of variance with a significance level of less than 0.05.

5.2.3 PCR

Two groups of cells were cultured on the planar and all patterned surfaces for 6 and 9 nine days and then prepared for RNA extraction. At these time points the cells were prepared for RNA purification and PCR. The cells fixed at Day 6 were examined for the presence of GAPDH (housekeeping gene) and RUNX2; the cells fixed at day 9 were examined for the presence of GAPDH and osteopontin. In both instances the change in threshold for the target gene was normalised to GAPDH.

Given the general positive results for the 40 μm embossed substrates over the control and other topographies some further studies were carried out to assess the effect of the 40 μm topography against planar control both in ZTA ceramic but also in alumina ceramic. Cells were cultured for 7 days and 14 days PCR was performed to assess up regulation of BMP2 and osteonectin between 40 μm embossed alumina and planar alumina. Nine substrates (forming 3 groups of 3) were cultured for each topography.

A PCR array was performed with cells cultured for 11 days. The array was composed of 4 house keeping genes and 92 target genes involved in osteogenesis. Only the planar substrates and 40 μm substrates for ZTA were used. In order to generate a sufficient cell mass 12 planar controls for each of three control samples were seeded with osteoprogenitor cells at $1 \times 10^4 \text{ml}^{-1}$. Similarly 12 topographical substrates - 40 μm pits - were seeded at $1 \times 10^4 \text{ml}^{-1}$ for each of three patterned samples.

5.2.4 Alizarin Red staining

Extracted osteoprogenitor cells were cultured for 28 days (2.6). The cells were then fixed and stained directly with Alizarin Red (2.7.2.5, 2.8). Overall images

of the substrates were scanned in high resolution using a flatbed scanner. Once scanned the captured images were cropped to a standard size and subjected to a threshold light intensity within image J. Once the threshold level was set, the triplicate samples for each substrate were subjected to a particle analysis, the particle results were imported to excel and analysed. The substrates were then viewed under a polarising microscope (Leica DM2700 P with LED illumination). The polarising function of the microscope allows selection of the stain or the underlying substrate structure. For each patterned substrate a selection of images were captured highlighting both the structure and the stain. The separate images were then combined in Pixelmator ®. Both images were opened as layers within one picture, selecting the 'overlay' blending of layers allowed the layers to be aligned accurately providing an emphasised picture of the cell location and extracellular protein deposition in relation to the features in each substrate. Each substrate feature was then further highlighted by the application of an outline, using the shape palate within Pixelmator ®. The multiple layers were then combined and exported as a jpeg file.

Once all the relevant images were captured, each substrate was counterstained with brilliant blue stain. The acetic acid with the brilliant blue stain dissolved small deposits of calcium and much of the intracellular calcium to leave primarily extracellular deposits of calcium. The substrates were placed under the polarising microscope and the process of image analysis was repeated. In order to capture all the surface of each substrate, the triplicate samples were placed together; each substrate was then recorded as the samples were scanned in a column fashion using a low magnification lens. Manual recording of the number of deposits of calcium was made. Thereafter a 20x objective lens viewed the surface of the substrate, using the polarising filter as previously to focus on the structure and cell stain alternately. The images for each position capture were combined as layers of a picture as previously described and the underlying structure was emphasised.

5.2.5 Statistical analysis

5.2.5.1 Focal adhesions

Focal adhesion data was analysed with Analysis of variance (ANOVA) Partek ®. The aim behind this assessment was to examine the variability between the triplicate samples of each substrate (subgroup variability) and to examine the variability between the different pattern groups. Given the positive skew on all the data set a square root transformation was performed to normalise the data sets and to decrease the subgroup variability.

5.2.5.2 Osteopontin and Osteocalcin expression

Protein expression data for this immunofluorescent microscopy was analysed with the Generalised Linear Model (GLM) R; the GLM is a generalised linear regression model that allows for the analysis of non parametric data, this is achieved by linking the linear regression to the response variable and taking into account the variance of each measurement. Gamma transformation was used for the analysis of area with Poisson distribution used for the analysis of particle counts.

5.2.5.3 PCR

The results of the Real time PCR are expressed as threshold values. These values are processed according to a published and validated method - $2^{-\Delta\Delta Ct}$ (Livak & Schmittgen 2001; Arocho et al. 2006). This method was followed in Excel (microsoft corporation) according the standard process in our laboratory. The method allows for normalisation of the threshold data for the samples to be performed by a 'housekeeping gene' (a routinely present background gene, not altered by the experimental variables). This allows the data to be normalised allowing for small variations in starting volumes or sample response. With this normalisation in place experimental variables are causative for increased or decreased genetic expression in the samples. Once the data has been normalised to the house-keeping gene the groups of interest are then normalised against the control group and any fold change is assessed with the Students T-test (Excel ® Microsoft).

5.2.5.4 Alizarin staining of particle counts

Data for the alizarin staining of calcium produced heavily skewed data. Non-parametric assessment was performed with a Kruskal Wallis test (using the ranking of the data points).

5.3 Results

5.3.1 Immunofluorescent staining

5.3.1.1 Integrins and focal adhesions

Qualitative analysis of the cytoskeleton was much more limited for the auto fluorescent ceramic than with the analysis of the PCL. Assessment of the images in Figure 5-5 shows that the cells for the patterned ceramics were more spread with a greater number of projections from the main body of the cell than the cells on the planar substrates. It is difficult to say definitively from these images whether a genuine difference appears between the different sets of patterned ceramics.

The results of a three way ANOVA are seen in Table 5-1. These results show perhaps surprisingly, a negative fold change of focal adhesion number and size when comparing the 20 μm and 30 μm samples to those formed on the planar control. Both of these samples show smaller focal adhesions than the planar control and the differences reach statistical significance in both instances. In contrast the substrates with the 40 μm feature show a greater expression of focal adhesions compared to the control.

The middle third of the table also shows comparison of the different topographies to each other. These results show a decrease in the expression of focal adhesions in the 30 μm compared to both the 20 μm and 40 μm samples. The difference between the 30 μm and 20 μm substrates does not reach statistical significance. However the differences between the 40 μm and the other two embossed surfaces are significant with the greatest presence of focal adhesions being detected in the 40 μm patterned substrate. The increased presence in the 40 μm substrate over the others reached significance in all the analyses. The lower third of the table shows the effect of the intra-topographic

but inter-substrate variation on the results. These results show significant variation (reaching statistical significance) across the substrates. This highlights the importance of triplicate studies in biological experiments and does not devalue the results.

The patterns of distribution are represented in Figure 5-6 and Figure 5-7. Figure 5-6 shows the presence of focal adhesions in different size ranges across each of the substrates, larger sizes of focal adhesion are seen in the 40 μm substrate.

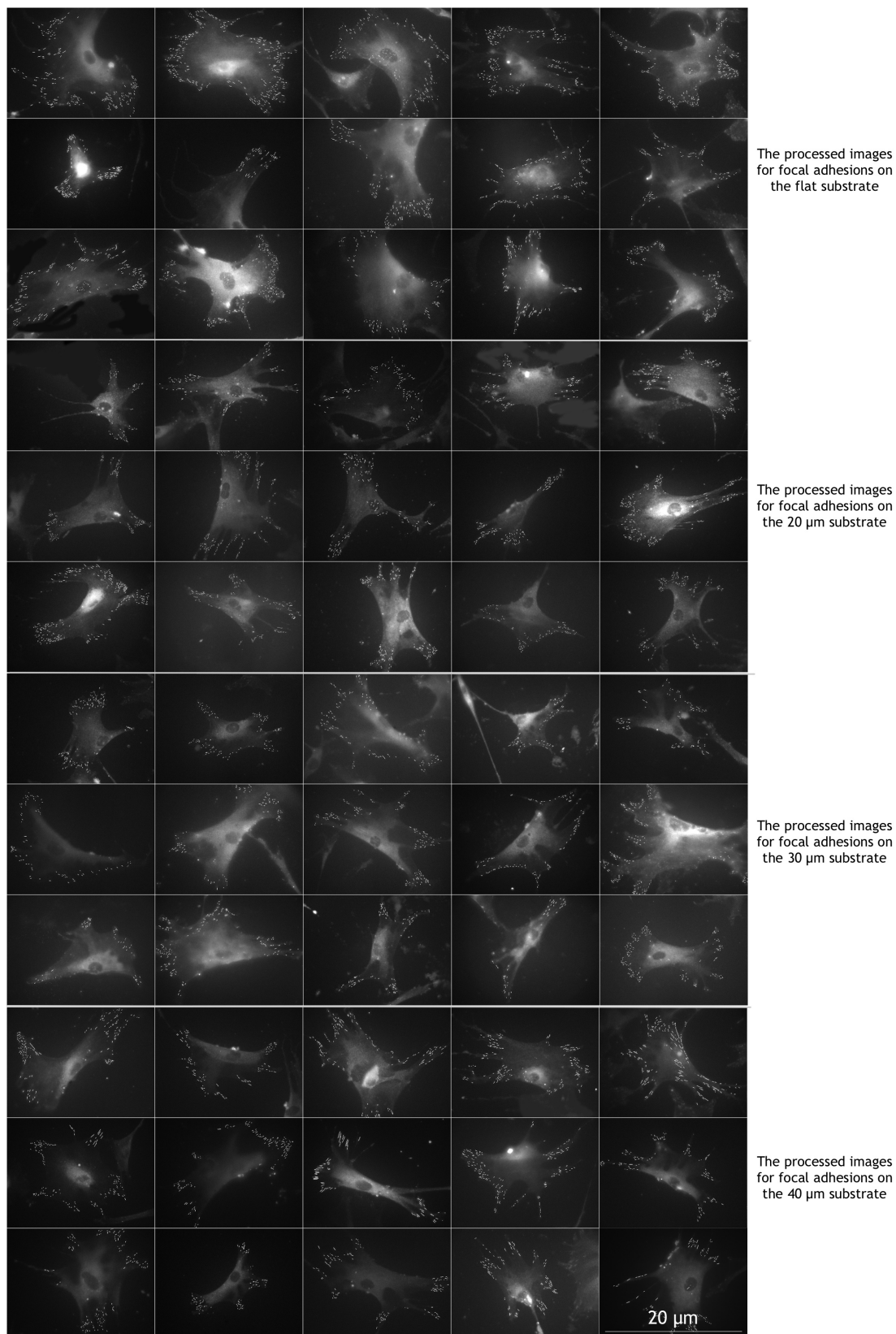


Figure 5-5 focal adhesions highlighted for planar and patterned ceramics. Three rows for each set of substrates. Labelled on the far right of the image. At first inspection there is no great difference between any of the sets of images. A closer inspection shows differences in cell shape and spread with greater spread (and therefore tension) in the topographical substrates when compared to the controls. Any qualitative comparison of focal adhesions is unreliable and statistical analysis of size and number of particles has been used. **(40x magnification)**

Column ID	Value	SqrtValue
p-value(Pattern)	0	0
p-value(Example)	8.53E-07	1.05E-06
p-value(Image(Pattern * Example))	0	0
p-value(20mics vs. flat)	3.49E-17	2.54E-14
MeanRatio(20mics vs. flat)	0.896119	0.954071
FoldChange(20mics vs. flat)	-1.11592	-1.04814
FoldChange(20mics vs. flat) (Description)	20mics down vs flat	20mics down vs flat
p-value(30mics vs. flat)	1.07E-15	3.87E-12
MeanRatio(30mics vs. flat)	0.891037	0.953868
FoldChange(30mics vs. flat)	-1.12229	-1.04836
FoldChange(30mics vs. flat) (Description)	30mics down vs flat	30mics down vs flat
p-value(40mics vs. flat)	1.84E-39	7.07E-34
MeanRatio(40mics vs. flat)	1.16597	1.0749
FoldChange(40mics vs. flat)	1.16597	1.0749
FoldChange(40mics vs. flat) (Description)	40mics up vs flat	40mics up vs flat
p-value(30mics vs. 20mics)	0.720668	0.97676
MeanRatio(30mics vs. 20mics)	0.994328	0.999788
FoldChange(30mics vs. 20mics)	-1.0057	-1.00021
FoldChange(30mics vs. 20mics) (Description)	30mics down vs 20mics	30mics down vs 20mics
p-value(40mics vs. 20mics)	0	0
MeanRatio(40mics vs. 20mics)	1.30113	1.12665
FoldChange(40mics vs. 20mics)	1.30113	1.12665
FoldChange(40mics vs. 20mics) (Description)	40mics up vs 20mics	40mics up vs 20mics
p-value(40mics vs. 30mics)	0	0
MeanRatio(40mics vs. 30mics)	1.30856	1.12689
FoldChange(40mics vs. 30mics)	1.30856	1.12689
FoldChange(40mics vs. 30mics) (Description)	40mics up vs 30mics	40mics up vs 30mics
p-value(Ex1 vs. Ex2)	0.0030212	1.39E-05
MeanRatio(Ex1 vs. Ex2)	0.965015	0.975215
FoldChange(Ex1 vs. Ex2)	-1.03625	-1.02541
FoldChange(Ex1 vs. Ex2) (Description)	Ex1 down vs Ex2	Ex1 down vs Ex2
p-value(Ex1 vs. Ex3)	1.36E-07	2.51E-06
MeanRatio(Ex1 vs. Ex3)	0.94034	0.973623
FoldChange(Ex1 vs. Ex3)	-1.06345	-1.02709
FoldChange(Ex1 vs. Ex3) (Description)	Ex1 down vs Ex3	Ex1 down vs Ex3
p-value(Ex2 vs. Ex3)	0.0257148	0.773615
MeanRatio(Ex2 vs. Ex3)	0.97443	0.998367
FoldChange(Ex2 vs. Ex3)	-1.02624	-1.00164
FoldChange(Ex2 vs. Ex3) (Description)	Ex2 down vs Ex3	Ex2 down vs Ex3

Table 5-1 - 3 way ANOVA of the distribution of focal adhesions across the planar and patterned ZTA ceramic. The results here show that the focal adhesions on the 40 μm substrate are greater than all the other surfaces with significant p values in all the comparisons. Surprisingly the focal adhesions for the 20 μm and 30 μm samples are down regulated in comparison to the control again with significance. The differences between the 20 μm and 30 μm substrates did not reach statistical significance.

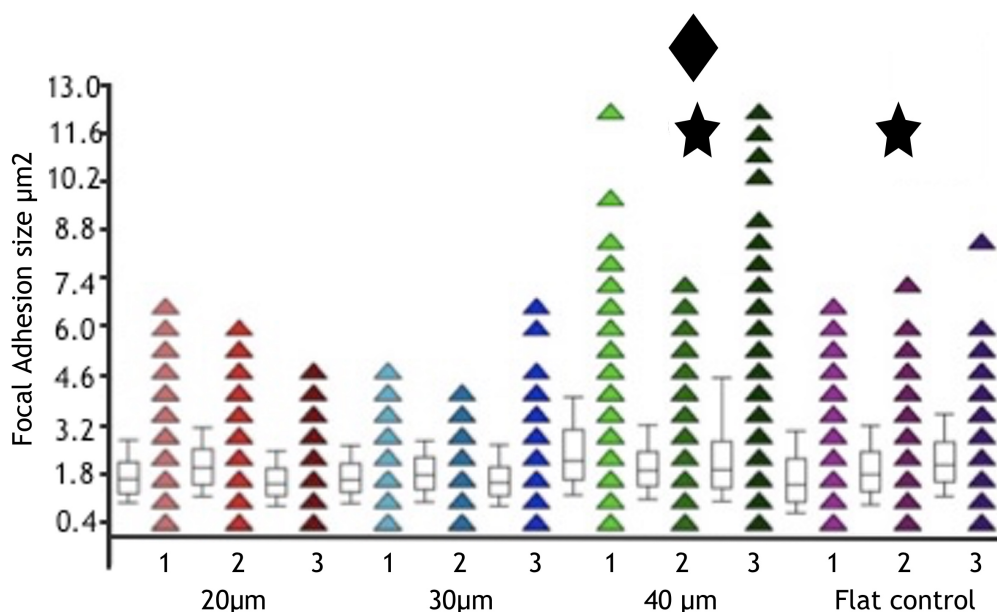


Figure 5-6 Graphical representation of the distribution by size (y axis) for particles detected for each substrate. The red indicators represent the triplicate samples for the 20 μm substrate, the blue represent the 30 μm substrates, the 40 μm substrates are shown in green and the variable shades of purple show the particles found on the planar controls. ◆ statistical significance for larger focal adhesions compared to the control, 20 μm and 30 μm samples. ★ statistical significance for greater focal adhesion size compared to 20 μm and 30 μm samples.

Figure 5-7 shows that most focal adhesions are distributed around the 1.8 μm^2 size with more obvious differences in the presence of larger focal adhesions. Whilst the graphical representation makes readily apparent the greater presence of larger focal adhesions in the 40 μm substrates there is also a subtle decrease in the number of small focal adhesions on this substrate. There are a greater number of these smaller focal adhesions on the control substrates than the topographical substrates.

One of the features worthy of note is the variation seen between different examples. This is seen in the lower third of Table 5-1. This variation between technical replicates could cause confounding interpretation for the assessment of the differences between biological samples. Graphs are presented in Figure 5-8 and Figure 5-9. Figure 5-8 shows two graphs, on the left of the image is a two way ANOVA with the F ratio displayed in the Y axis (the F ratio is a calculation of the variance within groups compared to the variation between groups, for an ANOVA the mean square between the groups is divided by the mean square within the groups). Figure 5-9 shows the graphical representation of this assessment; the F ratio for the pattern is clearly greater in both graphs.

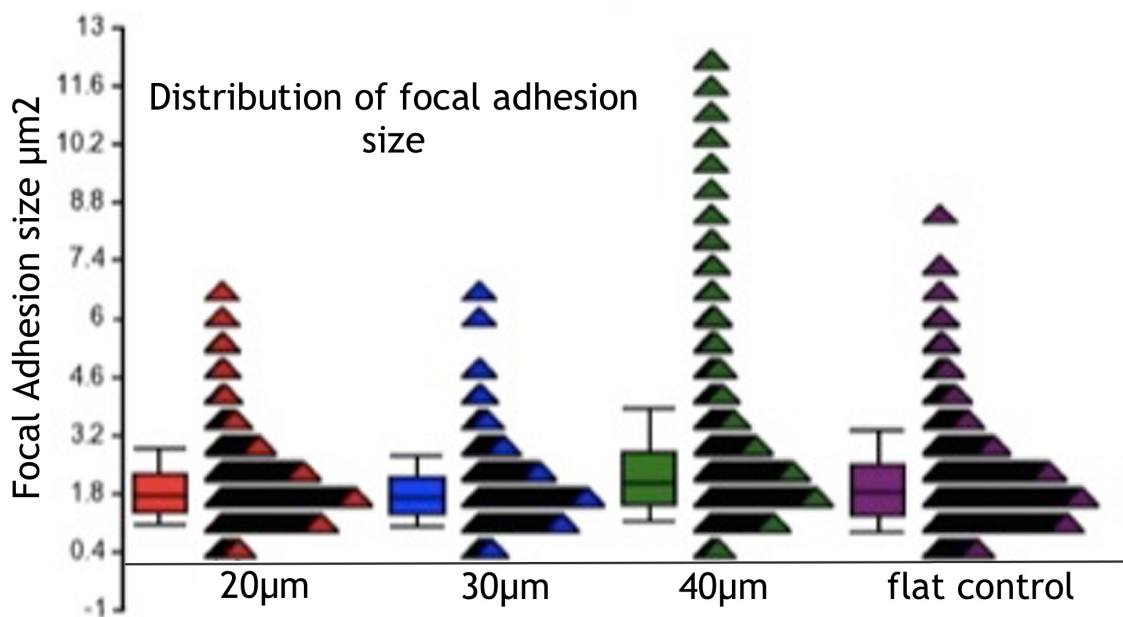


Figure 5-7 graphical representation of the distribution of focal adhesions separated by topography. The majority of the focal adhesions are concentrated around the same size. Significant increase in the presence of larger focal adhesions in the 40 µm substrate.

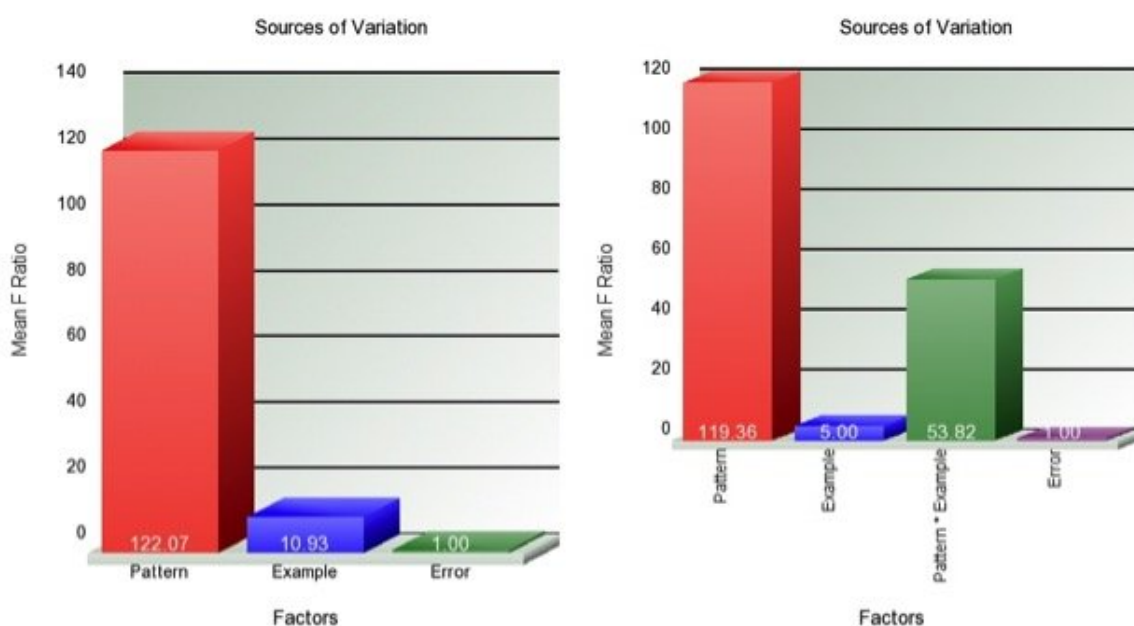


Figure 5-8 Graphical representations of the ratios of variance for a two way ANOVA on the left image. This two way assessment evaluated variation arising from within the sample (that is between triplicates) or due to the pattern (between samples). It shows that while intra-samples variation is present, it is much less than variation between samples.

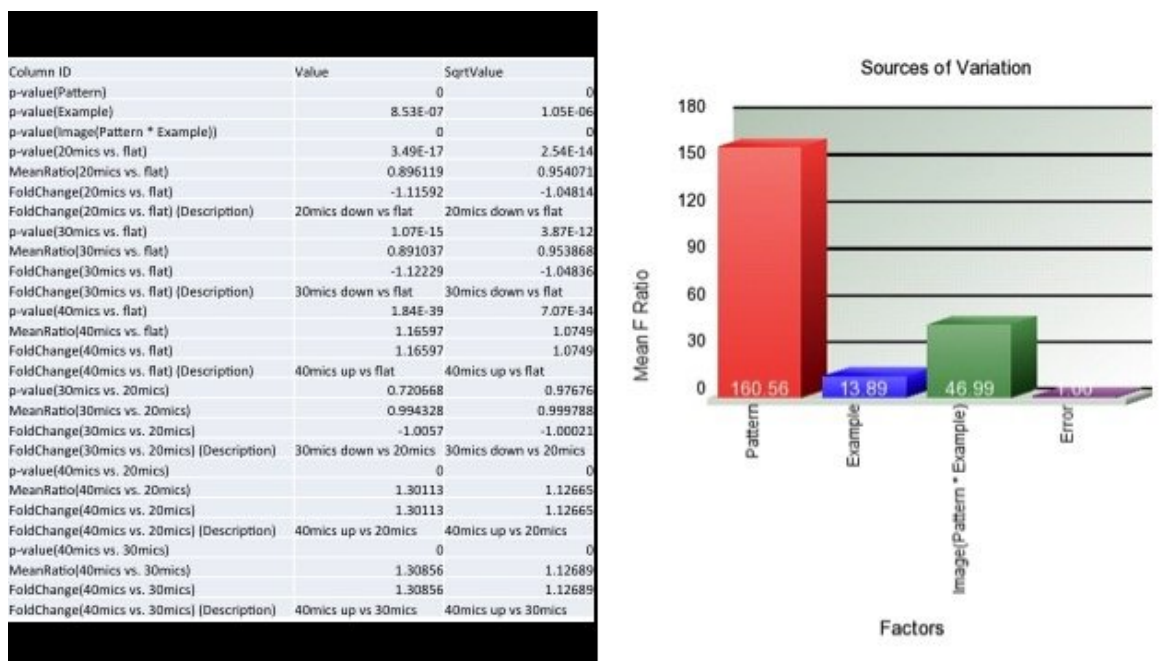


Figure 5-9 the graph and table from a three way ANOVA assessing the variance arising from the pattern and the substrate, related to each technical replicate. Much greater variance is seen from the pattern than the different substrates

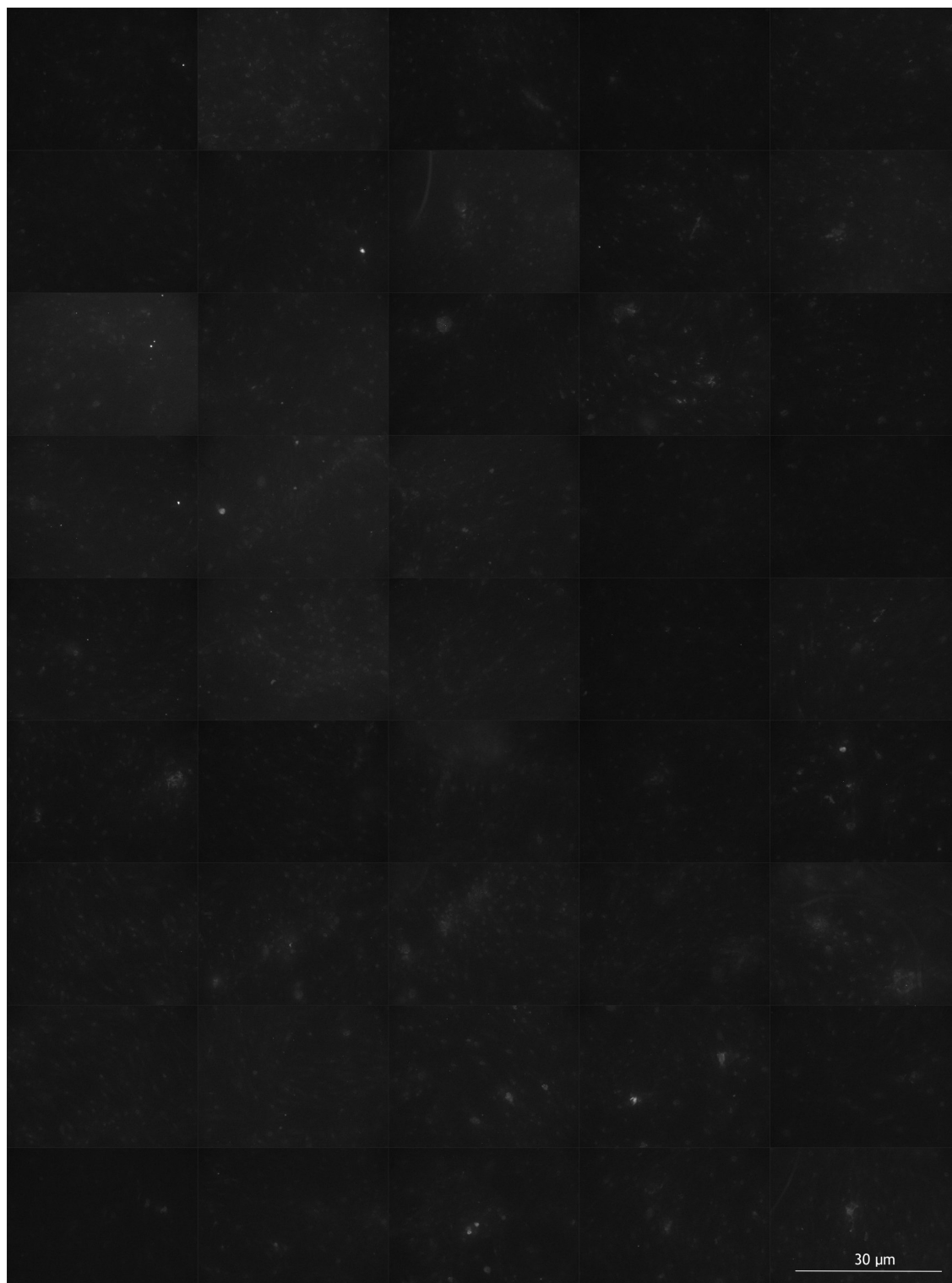
5.3.1.2 Osteopontin

Comparison of all the images used for the comparison of the presence of OPN may be seen in Figure 5-10 through Figure 5-13. The variation in the dark background for the images is a reflection on the auto fluorescent nature of the material. There is significant variation in the protein expression within each substrate and the cells are less clustered on the control substrate Figure 5-10 than for the patterned surfaces. The cell clustering is seen most strongly in the 20 μm and 30 μm substrates and may give the impression of higher levels of protein expression. Aside from the grouping of cells there does appear to be a greater level of protein expression in the patterned substrates when compared to the control. However there is no clear difference in the levels of protein seen across the patterned surfaces. Although there are not many large particles of OPN in any of the sets of images, the substrates that appear to have generated larger particles are the 40 μm samples and the planar control, with the protein expression on the 20 μm and 30 μm samples distributed more evenly in smaller particles throughout each image.

This type of qualitative assessment of particle expression provides a general overview but is unreliable and prone to bias. Figure 5-14 shows box plots for the

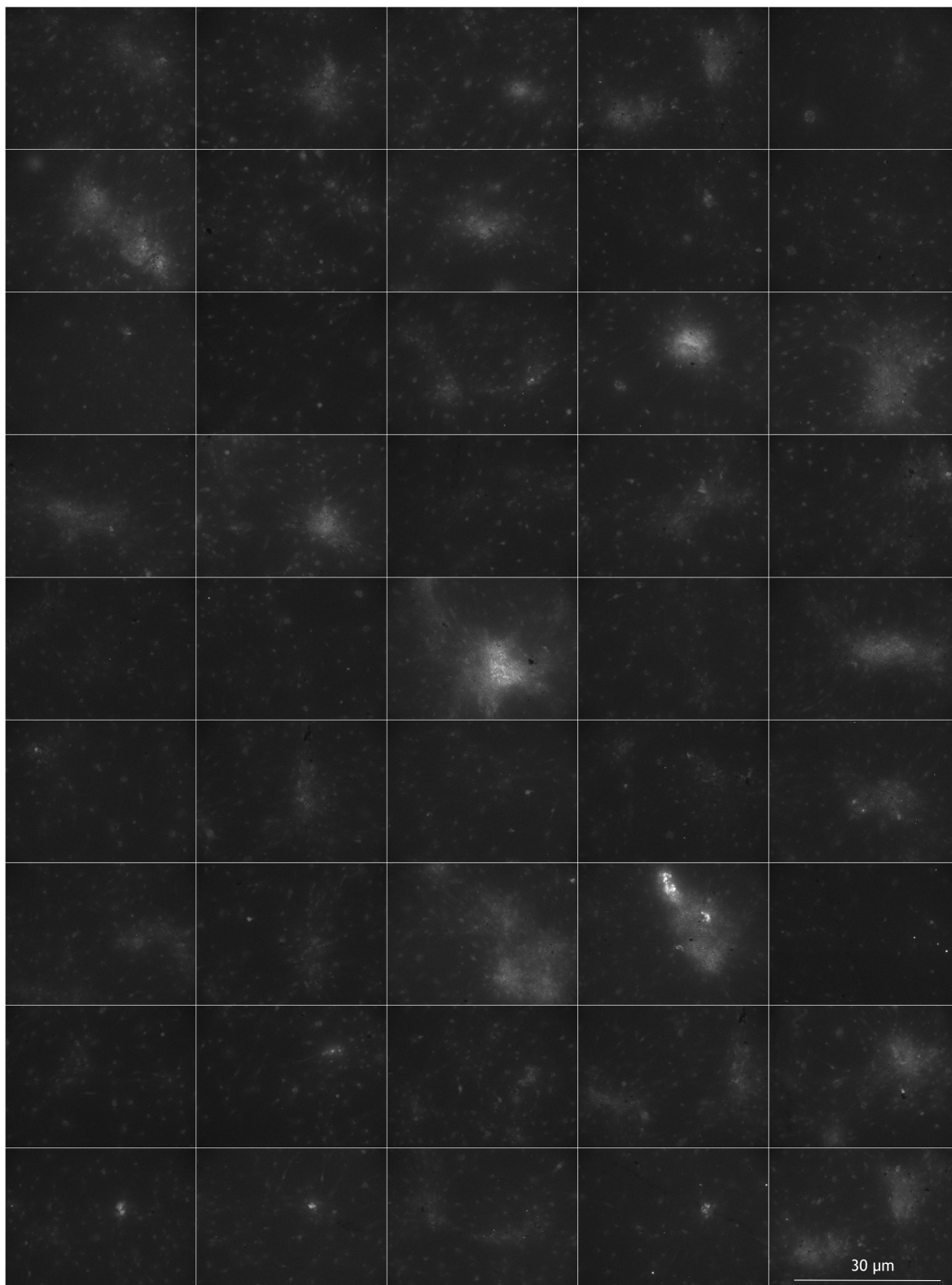
total area of protein detected for each substrate produced across the experiment. Data transformed by square root reduces the variance within the set and produces results that show the greatest overall area of OPN presenting from the 20 μm patterned substrate with a significance value of less than 0.05 (0.000133 after gamma transformation of the data). All of the patterned substrates produced a greater total area of OPN than the planar controls with significance levels less than 0.05. The increase in protein area was significantly different between the 20 μm substrate and both the 30 μm ($p=0.003$) and 40 μm ($p=4 \times 10^{-6}$) substrate. The difference between the 30 μm and 40 μm substrates did not reach significance ($p=0.3$).

Figure 5-15 shows box plot for the size of protein particle. Again the results for the 20 μm pattern are most positive reaching significant levels over the control ($p=0.03$) but not achieving significance over the other topographies. In this instance neither of the other two topographies reach significance in their difference over the control or each other. Figure 5-16 shows the box plot for particle count, as with the other results the most positive results are seen with the 20 μm substrate, followed by the 30 μm and 40 μm substrate over the control. All differences reach statistical significance. (GLM assessment with poisson correction).



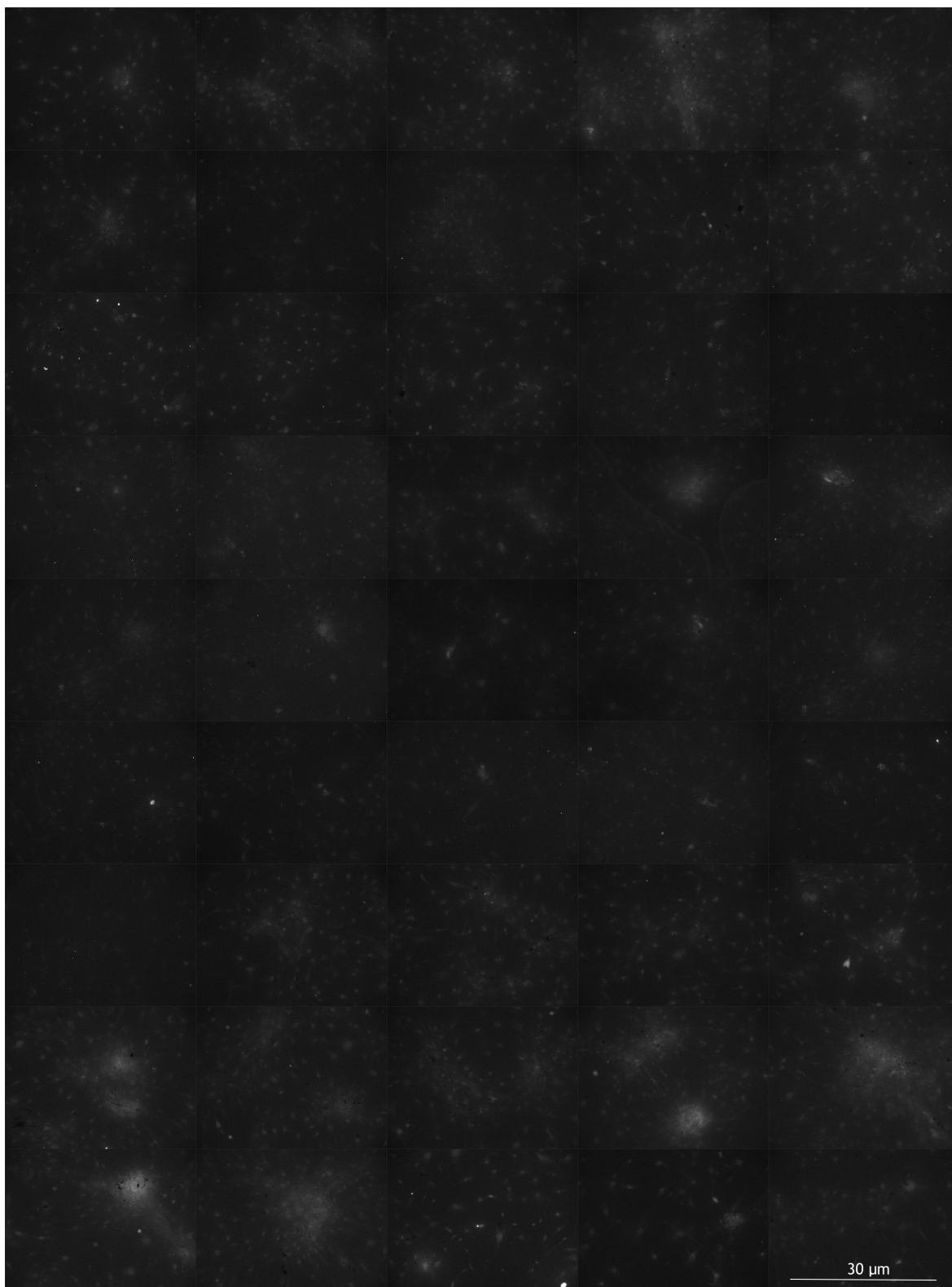
Combined images for the control substrate, ZTA stained for OPN

Figure 5-10 images for planar ZTA stained for OPN. Very little extracellular protein is seen in these images. Protein levels are generally low within and outwith the cells, the presence of intracellular protein makes the position and clustering of the cells a slightly greater artefact in assessing the protein level.



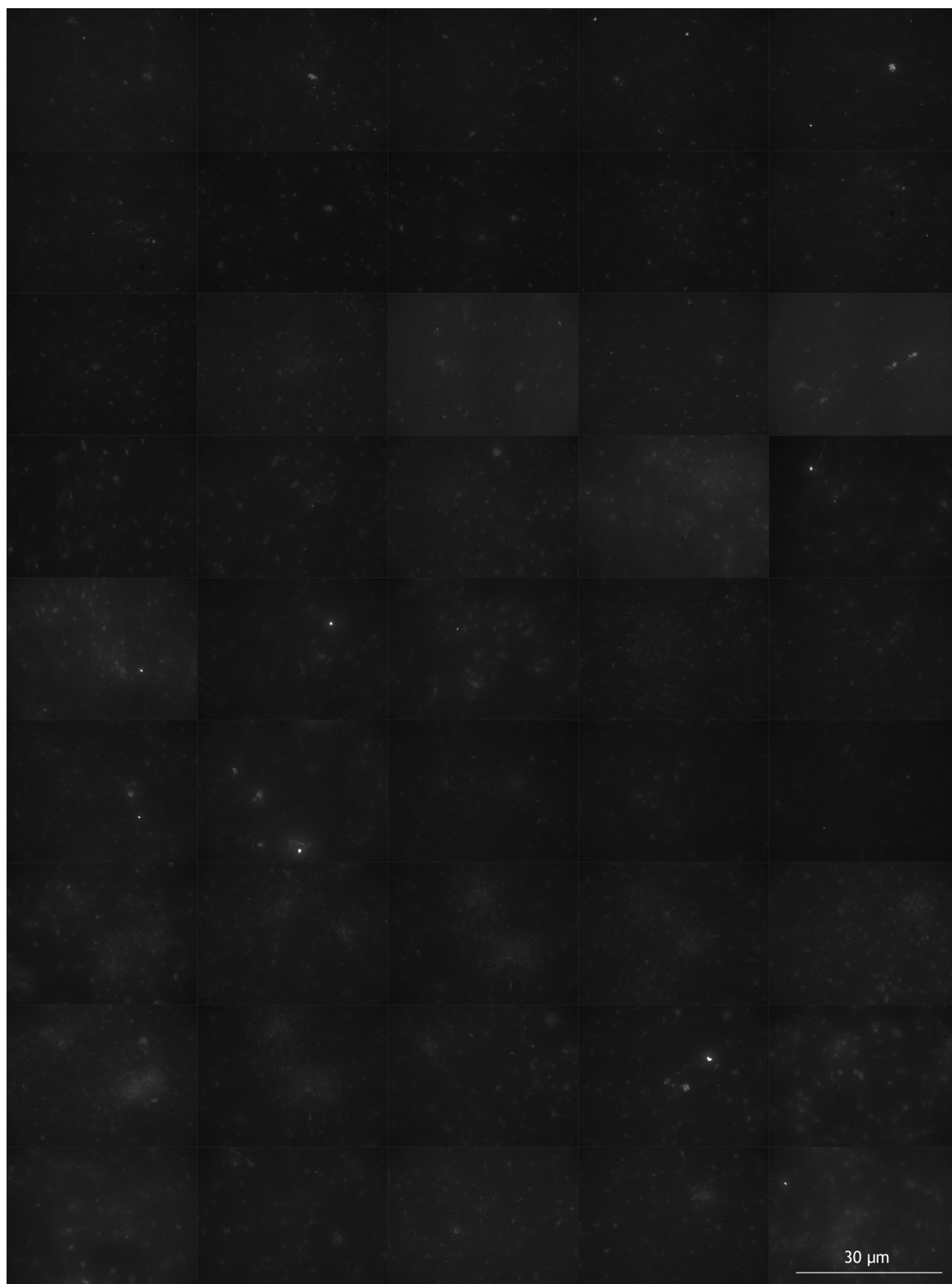
Combined images for the 20 μm substrate, ZTA stained for OPN

Figure 5-11 Images for the 20 μm ZTA stained for OPN. While there is still relatively little extracellular expression of OPN there does appear to be more for the 20 μm substrate than for the planar control. The effect of cell clustering is more obvious here given the stronger intracellular expression of protein compared to the control. (**x20 magnification**)



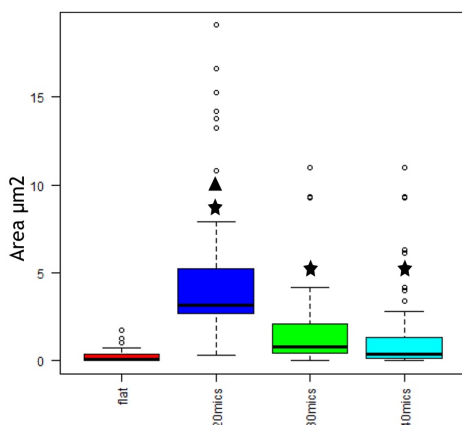
Combined images for the 30 μm substrate, ZTA stained for OPN

Figure 5-12 Images for the 30 μm ZTA stained for OPN. As with the images seen for the 20 μm substrate there appears to be greater intracellular and extracellular protein in these images as compared to those for the control.



Combined images for the 40 μm substrate, ZTA stained for OPN

Figure 5-13 Images for the 40 μm ZTA stained for OPN. These images appear very similar to those captured for the other two embossed substrates. There may be slightly greater extracellular protein expression but this is by no means a clear difference.



Box plots of the total area of OPN expression

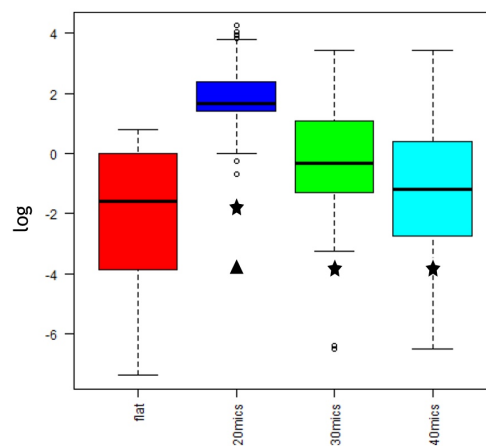
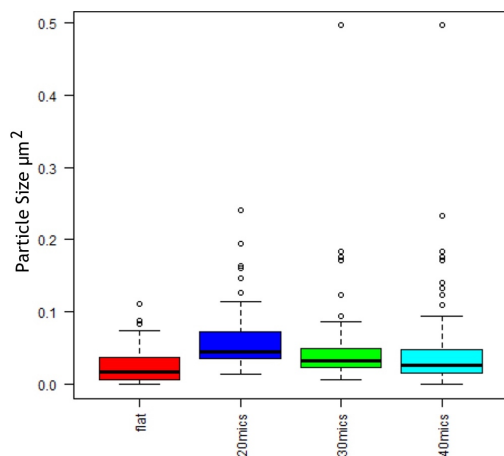
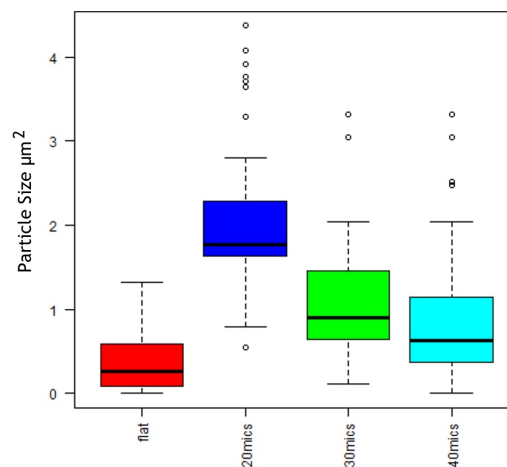
Box plots of the total area of OPN expression
The data here was log transformed to reduce the variance

Figure 5-14. Box plots for the data showing the thresholded particle count for OPN, with expression of total area of protein. The left hand image shows the data as processed. The patterned substrates show more particles of OPN than the control, although there is significant variance. On the right the data is shown post square root transformation. The differences in the data become more easily seen with the 20 μm substrate generating more particles than the other embossed substrates and the control producing the least OPN. The data is shown as IQR and median, ★ significance over control $P < 0.05$, ▲ significance over the other patterned substrates $p < 0.05$ (GLM gamma transformation)



mean particle size for OPN expression



mean particle size for OPN expression. With square root transformation to allow for variance

Figure 5-15. Box plots showing the mean particle size for OPN. The left hand graph again shows the positive results for the 20 μm patterned substrate. The variance is skewed inferiorly (positive or to the left). In order to overcome the skew and variance the data was transformed by square root. This is represented on the right hand graph, showing a clear increase in size for the protein expressed on the 20 μm patterned substrate. All three patterned substrates perform more strongly than the control substrate. Data is shown as median and IQR ★ Significance over control $p < 0.05$ (GLM gamma transformation).

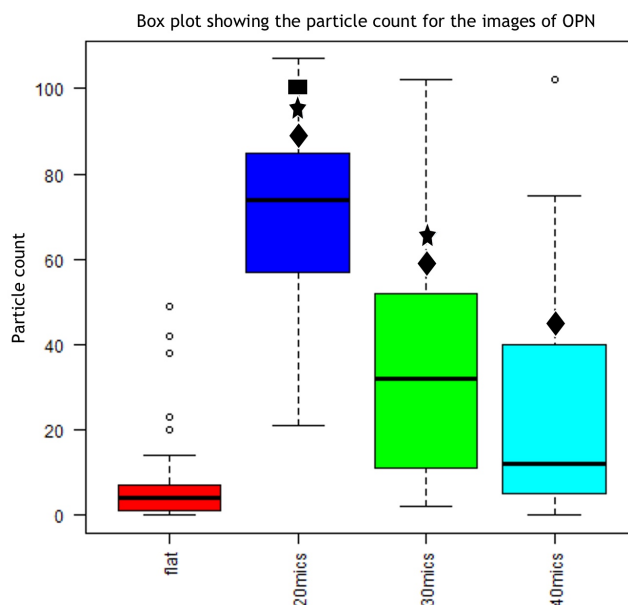


Figure 5-16. Box plot for OPN particle count. As with the other assessments here the 20 μm substrate produces more particles than any of the other surfaces. ◆ significance over control $p < 0.05$, ★ significance over 40 μm substrate $p < 0.05$, ■ significance over 30 μm substrate (GLM poisson transformation)

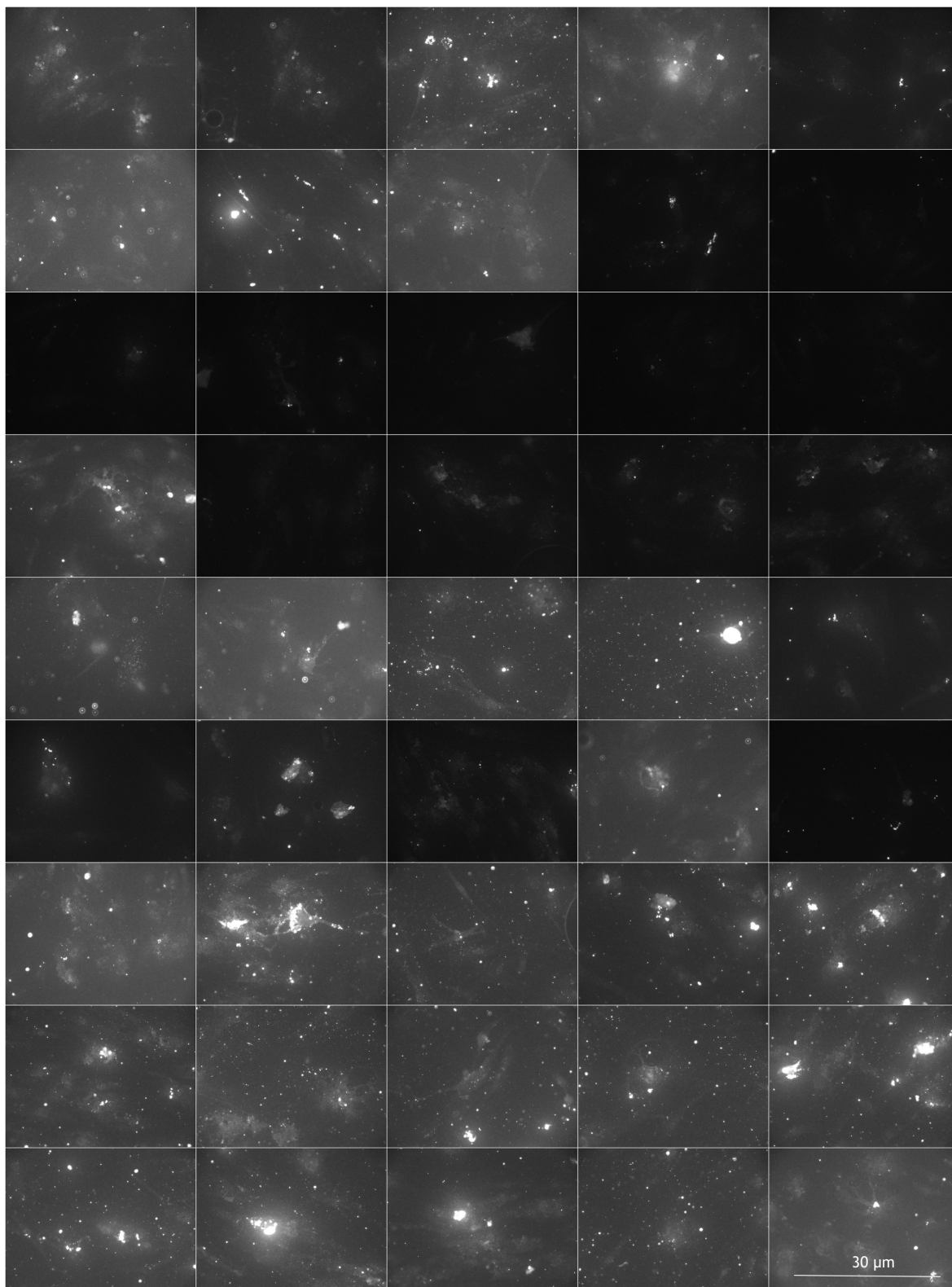
5.3.1.3 Osteocalcin

All the images used for analysis of OCN presence may be seen in the images Figure 5-17 through Figure 5-20. As for the images used for OPN expression there is obvious background variation in the light intensity both within the samples and between the substrates. In contrast to the images captured for OPN expression, there appears to be a much greater level of extracellular protein expression. Additionally the protein appears more distinct from the background noise of the image with the cell less visible; these features combine to reduce the influence of cell position and clustering on the analysis. Qualitative assessment of the images suggests that the greatest expression of OCN is seen in the images captured for the 40 μm substrate Figure 5-20. The images for the 20 μm Figure 5-18 and the 30 μm substrates Figure 5-19 appear equal in number and distribution, both these substrates generate less protein expression than the control substrate Figure 5-18. The size of OCN particle appears greater in the images for the 40 μm and planar substrates than for the 20 μm and 30 μm substrates.

Figure 5-21 shows the box plots for the area covered with OCN protein across the substrates. Interestingly the results for the control show the largest mean but also show the greatest variation. As with most biological data a positive skew is present. Even when the data is transformed with a log transformation (improving the distribution) the pattern is still clear with a greater area covered in protein for the control than the substrates. The results are statistically significant for all of the changes except the increased area in the control over the 40 μm (inverse Gaussian transformation of the data shows a p value of 0.06) although in this instance the p value is very close to becoming significant. The 40 μm substrate is certainly the most positive of the patterned materials, with statistical significance achieved in all comparisons.

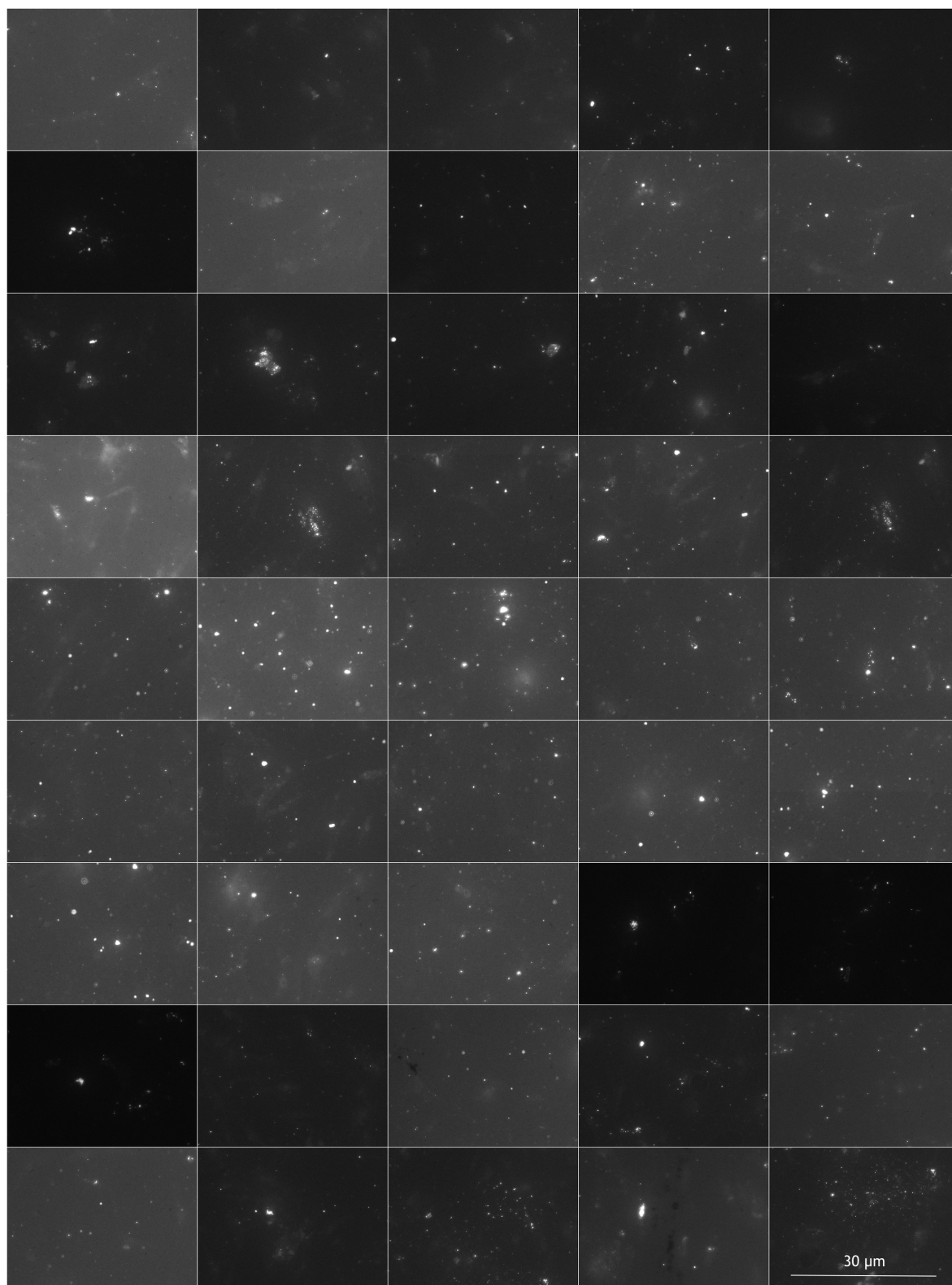
Figure 5-22 shows the box plot for comparison of mean OCN particle size across the captures images for the substrates. Both the natural data and the transformed data (log) show that the largest particles were seen with the 40 μm substrate. This difference reached significance for the comparison to the control ($p=0.001$) and the 20 μm substrate ($p<0.001$) but not for the 30 μm substrate ($p=0.1$). There was no statistically significant difference between the 30 μm substrate and planar control. The decrease in particle size on the 20 μm substrate compared to all other substrates was significant in each case with $p<0.05$.

Figure 5-23 shows the graphical representation of the data for particle count in OCN. Clearly the most particles are seen in the control substrate followed by the 40 μm substrate then the 20 μm and lastly the 30 μm substrate. In all these comparisons the difference is statistically significant.



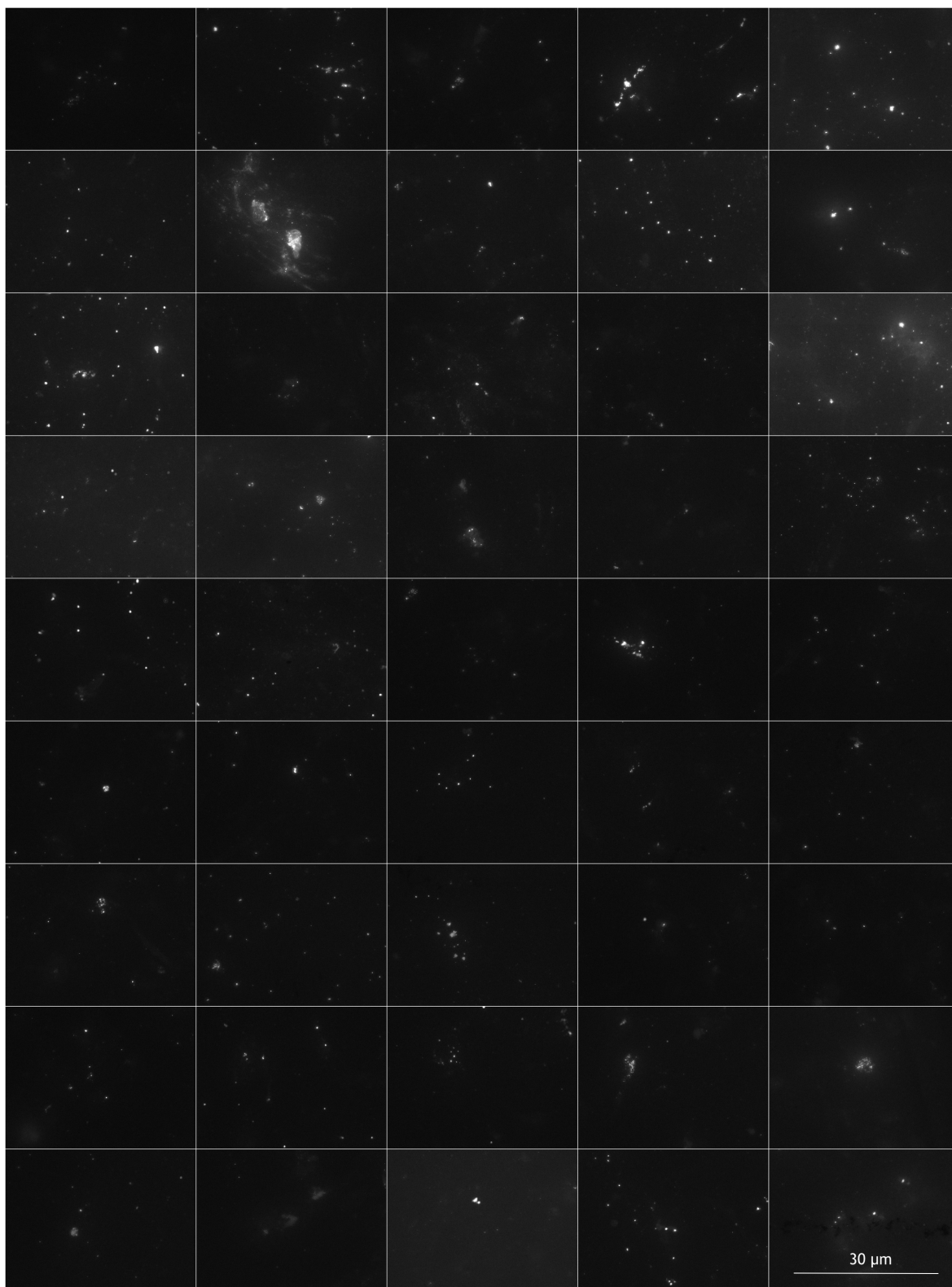
Combined images for the planar substrate - ZTA stained for OCN

Figure 5-17 Images for the control ZTA stained for OCN. The wide variation in background light levels creates a difficulty in accurately assessing the expression of protein. There is clearly a much greater level of protein expression here than for the OPN. The extracellular protein expression is highly varied across the captured images.



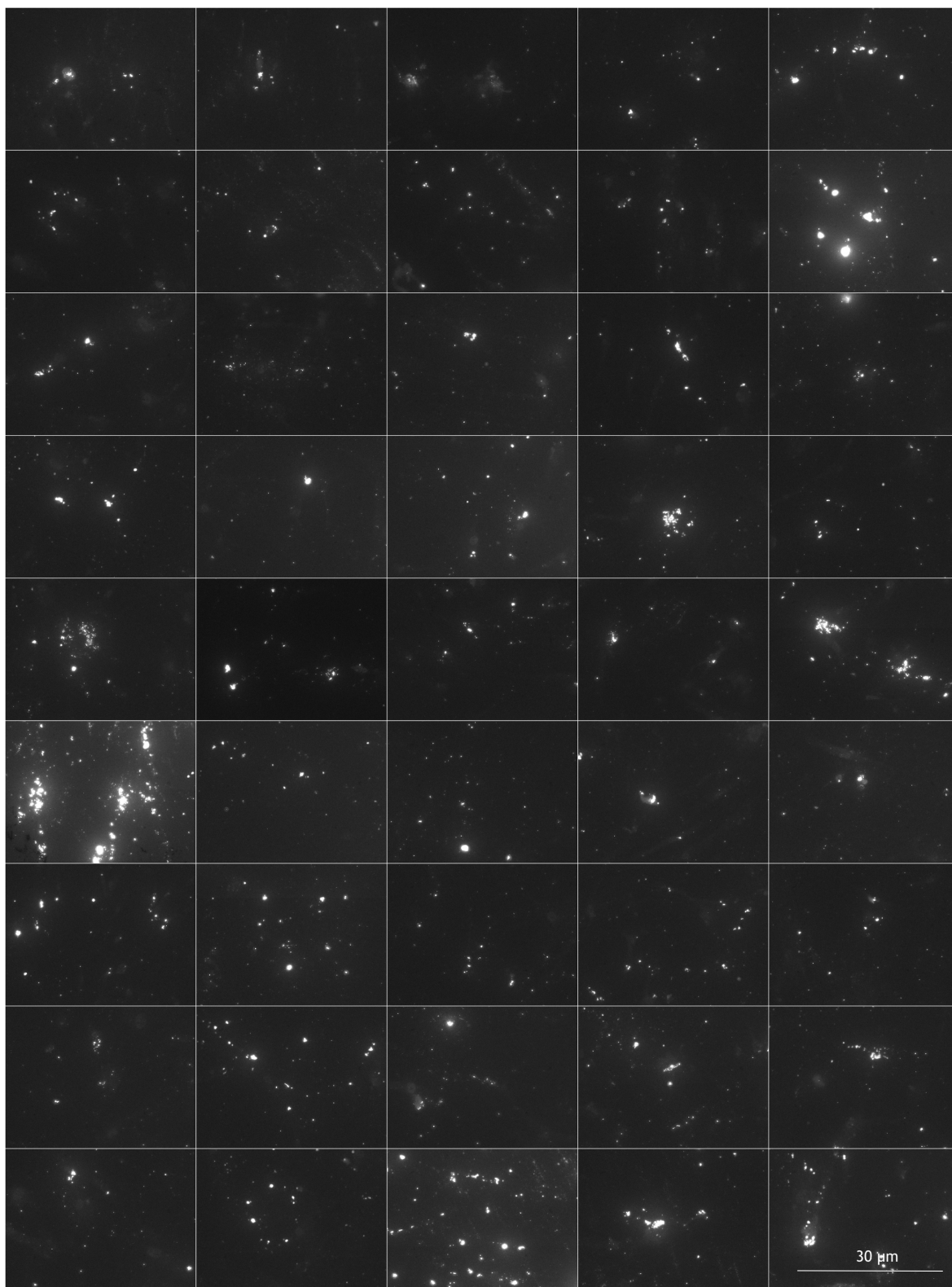
Combined images for the 20 μm substrate - ZTA stained for OCN

Figure 5-18 Images for 20 μm ZTA stained for OCN. A similar level of background variation affects these images as is seen in those for the control. Extracellular protein expression appears more consistent across all the images and so may be greater in total.



Combined images for the 30 μm substrate - ZTA stained for OCN

Figure 5-19 Images for the 30 μm ZTA stained for OCN. Visual inspection of these images suggests a lesser expression of protein than in the other surfaces.



Combined images for the 40 μm substrate - ZTA stained for OPN

Figure 5-20 images for the 40 μm ZTA stained for OCN, these images are by far the most consistent for production of OCN, although the summative protein deposition may not be greater than the control, the spread of protein from sample to sample is much more uniform.

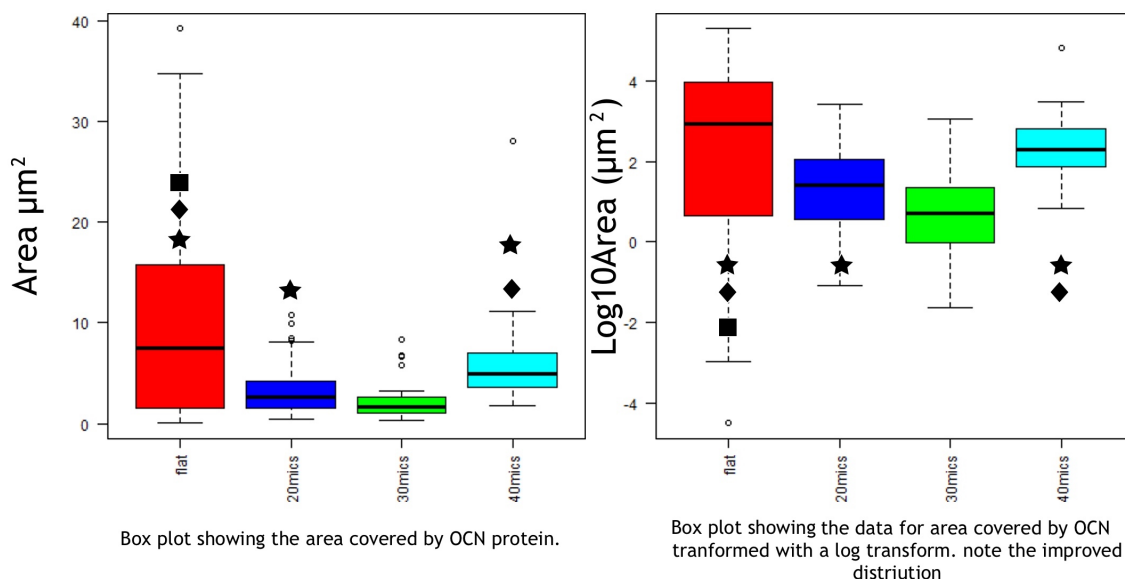


Figure 5-21. Box plots for the area covered by the OCN protein for all substrates. Left shows the positive skew to the data and suggests a greater total coverage by the flat control. With the best performance in the patterned substrates seen in the 40 μm substrate. The right hand graph shows the data transformed to improve the distribution. This shows the same pattern of result, the greatest area covered by the OCN protein was seen on the control, with the optimal topography for OCN production being the 40 μm substrate. ★ significance over 30 μm substrate $p < 0.05$, ◆ significance over 20 μm substrate $p < 0.05$, ■ significance over 40 μm substrate $p < 0.05$ (GLM gamma transformation).

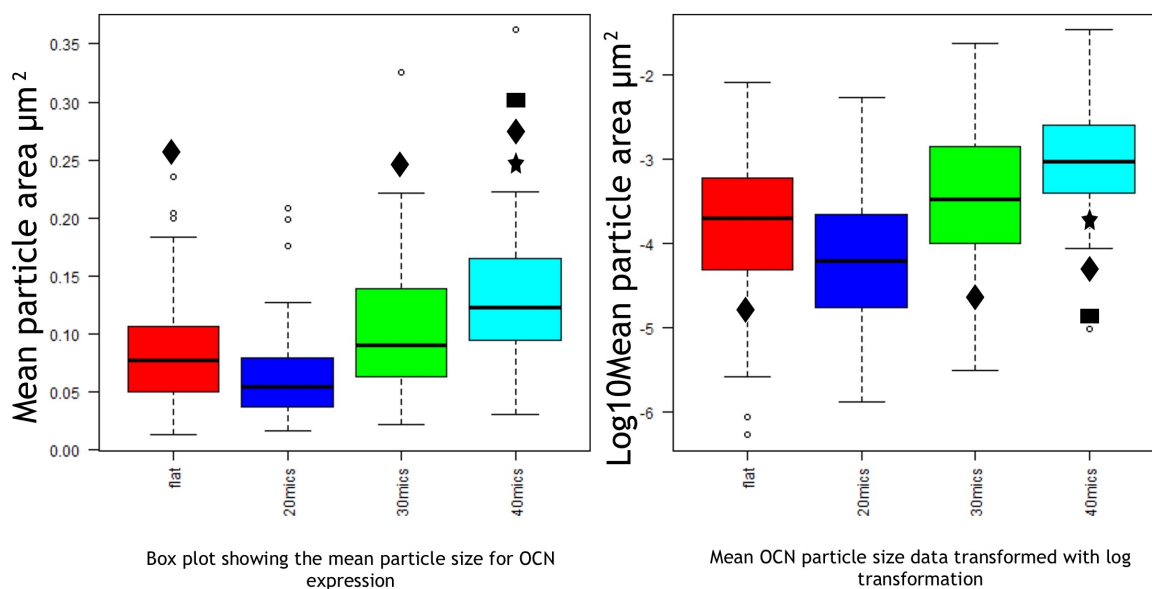
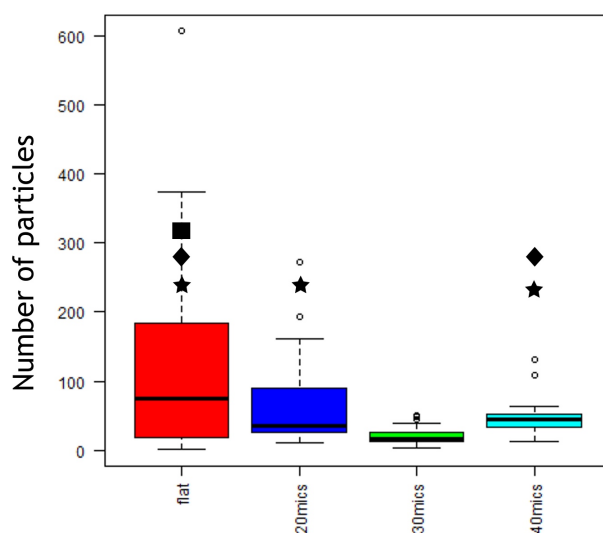


Figure 5-22. Box plot showing the mean OCN particle size per image for the substrates. The size of particles across the samples is greatest on the 40 μm substrate. It is interesting to note the similar pattern of result as seen with the focal adhesions, with the 20 μm substrate producing a less favourable result than the control. ◆ significance over 20 μm substrate $p < 0.05$, ★ significance over planar control $p < 0.05$ and ■ significance over 30 μm substrate $p < 0.05$ (GLM gamma transformation)



Box plot showing the particle count data for OCN protein expression

Figure 5-23. Box plot for OCN particle count. Mean for the control substrate is the highest but also with the greatest variation and the most skew. The mean for the 40 μm pattern is the next highest followed by the 20 μm and then the 30 μm . The high levels of particle expression explain the great surface coverage seen in the control even though the particles are small. ★significance over 30 μm substrate, ◆ significance over 20 μm substrate, ■significance over 40 μm substrate $p < 0.05$ (GLM poisson transformation)

5.3.2 PCR

5.3.2.1 Comparative PCR for all topographies.

After 6 days in culture RUNX 2 was up regulated on the patterned substrates when compared to the control substrates. This is shown in Figure 5-24. The error bars for the graph are the standard deviation. The standard deviation is very high; this prevents any statistically conclusive difference being stated with none of the fold changes reaching significance levels of less than 0.05.

After 9 days of culture Osteopontin expression was upregulated on the patterned substrates when compared to the planar control. As seen with the 6 day culture results with RUNX2 the standard deviation across the samples was sufficiently high to prevent any statistically significance being achieved, this is represented in Figure 5-25

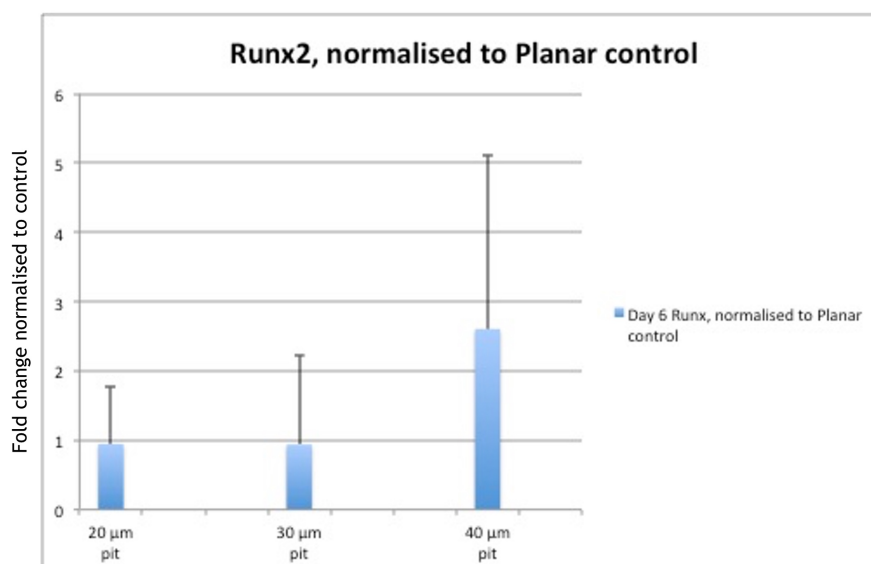


Figure 5-24 Changes in expression of RUNX2 normalised to the planar control surface after 6 days of culture. Upregulation was seen for all topographies compared to control. Greatest upregulation was seen for the 40 µm surface, error bars are standard deviation. Control values are 0. No statistically significant change for any topography over control (p values of 0.46, 0.47 and 0.19 for the 20 µm 30 µm and 40 µm substrates)(Excel © Microsoft).

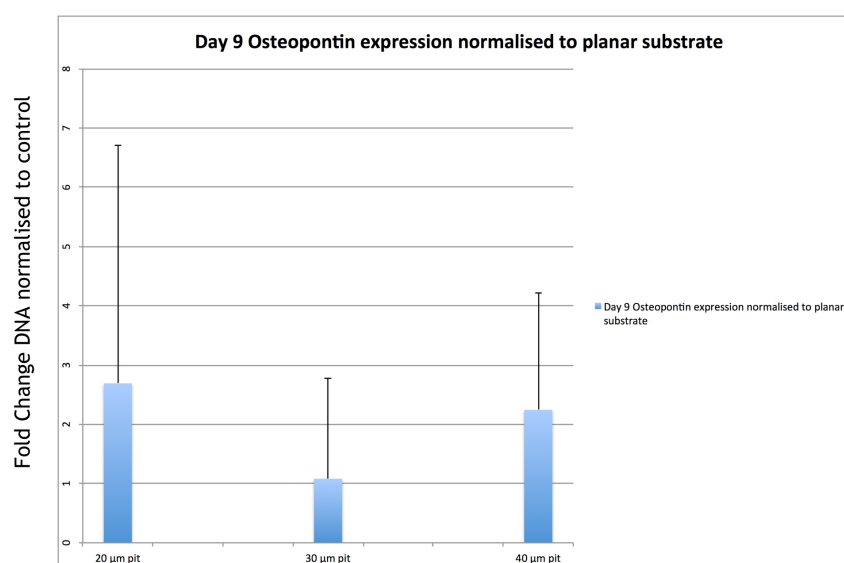


Figure 5-25 Upregulation of osteopontin expression normalised to the planar control after 9 days of culture. Upregulation was noted for all surfaces compared to control, notably for the 20 µm and 40 µm surfaces than the 30 µm surface. Error bars represent standard deviation. Control values are 0. No statistically significant difference for any substrate over control (p values of 0.17, 0.47 and 0.19 for 20 µm, 30 µm and 40 µm substrates) (Excel © Microsoft).

5.3.2.2 Comparative PCR for 40 µm substrates against control

After 7 days in culture both BMPR2 and Osteonectin were up-regulated when compared to the control. However the standard deviation for the samples was high preventing a statistically significant result with p values of 0.07 for osteonectin and 0.1 for BMPR2 (Figure 5-26). However the bars on the right hand side of the chart represent osteonectin and BMPR2 levels at fourteen days. We

see at this time point the levels of gene have begun to decrease but the standard deviation was reduced significantly. At this time point the lessening of variance allowed significant up-regulation to be seen for both genes on the 40 μm substrate over the planar control with p values less than 0.05. The results suggest a more homogeneously osteocommitting population at this later time in culture.

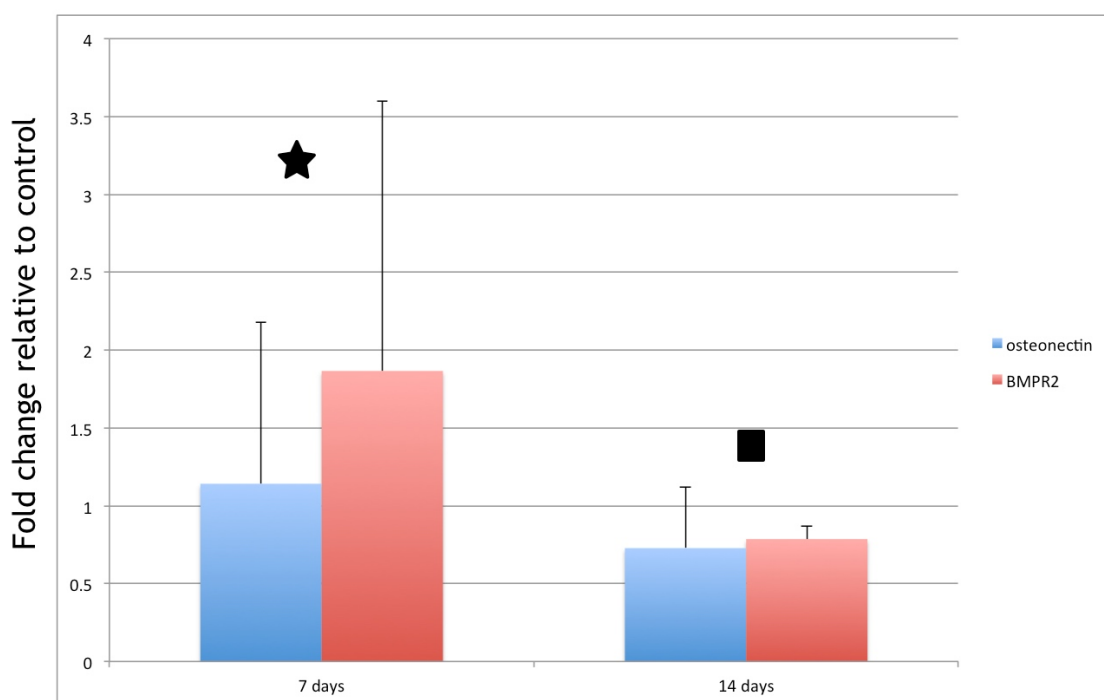


Figure 5-26 Expression of Osteonectin (Blue) and BMPR2 (red) in PCR for culture at 7 days and 14 days on alumina ceramic. The patterned substrates generate an upregulation in gene expression at both time points. The standard deviation (represented with the error bars) are much smaller at 14 days. The 7 day results while showing a greater increase in expression over control samples do not reach statistical significance ★ P > 0.05 (p = 0.07 for osteonectin, p = 0.1 for BMPR2) however for both results after 14 days of culture the results are statistically significant ■ P < 0.05 (p = 0.04 for osteonectin, p = 0.001 for BMPR2).

The results for the PCR array are seen over two figures. Figure 5-27 shows the graphical results for the PCR array, where a trend to increased gene expression across the results, some of the increases are very large, was noted. However the variation in the samples (represented as the standard deviation in the error bars) prevents statistically significant conclusions for the majority of the test. The only statistically significant result is for GDF10, which is significantly up regulated on the 40 μm patterned substrate and has very low standard deviation. This up-regulation is significant $p < 3.5 \times 10^{-5}$ (T-test Excel®Microsoft).

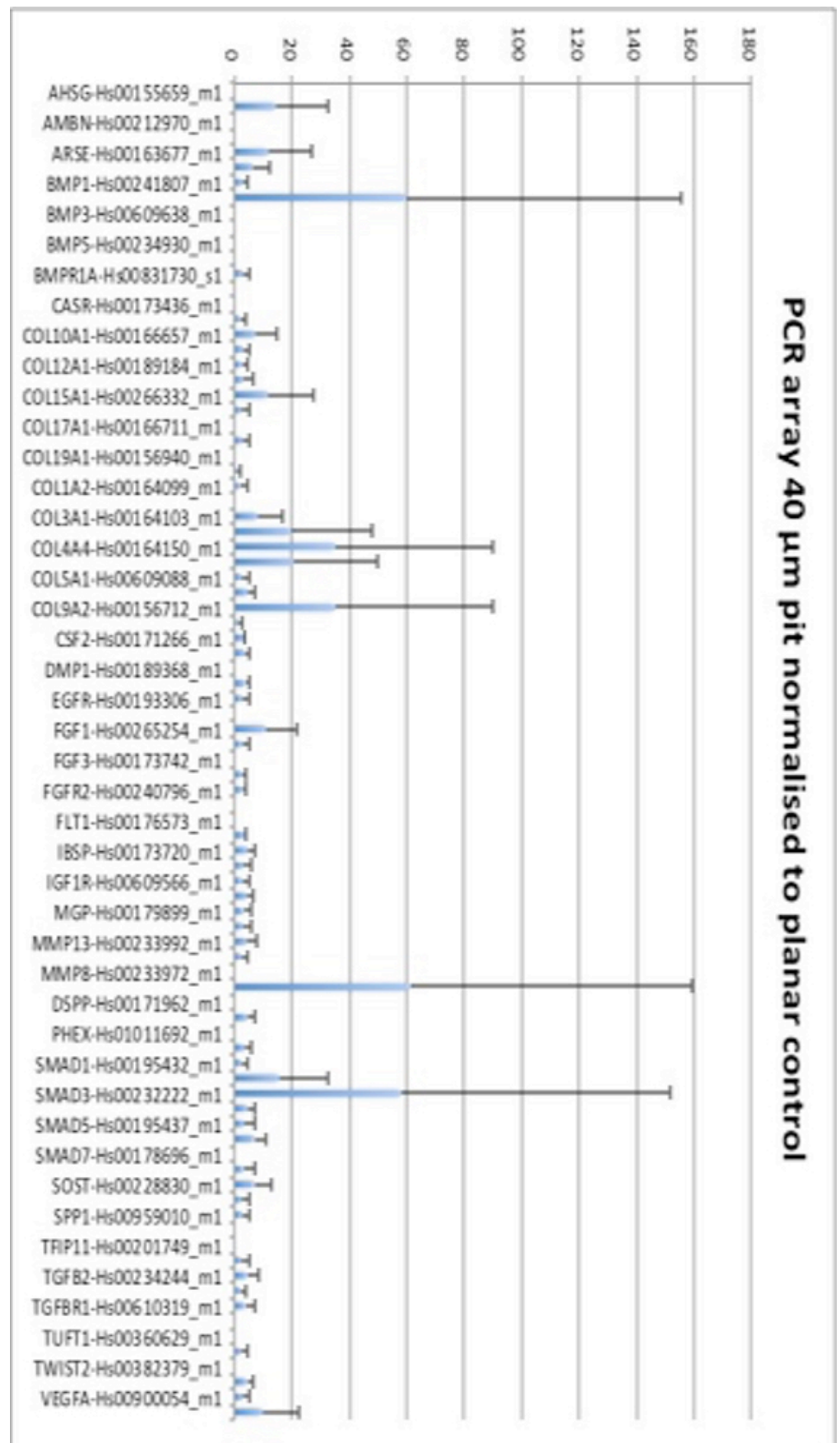


Figure 5-27 Graphical representation of gene expression with standard deviation error bars for the osteogenic array. For all the above results where upregulation is seen the standard deviation is high enough to prevent a statistically significant result with the only statistically significant result with $p < 0.05$ being for GDF10.

5.3.3 Alizarin

The combined images for the alizarin stained substrates are seen in Figure 5-28. The substrates for each group were scanned and combined. The macroscopic appearance of the samples is that of great similarity, for overall stain expression and distinct nodule formation. Figure 5-29 shows a collection of low power micrographs of the alizarin stain taken up by cells on the ZTA substrates. As with the macroscopic appearance of the substrates in Figure 5-28 there is little obvious difference between the substrates.

Figure 5-30 shows a collection of images from only the patterned substrates. Qualitative assessment was made of these images to compare the location of calcium nodules and cells to the features. The features have been highlighted in an image processing software (Pixelmator ©). Maintaining a steady pitch while increasing feature diameter results in less intervening space between the edges of consecutive features, this causes cells and any produced nodules to appear closer to the features when imaged on the sample with the largest feature embossed compared to the position of the cells relative to the features on the samples with the smallest diameter features. There is no discernable pattern regarding the position of cells and calcium deposits in relation to the circular pits in any of the images taken across the different pattern sizes.

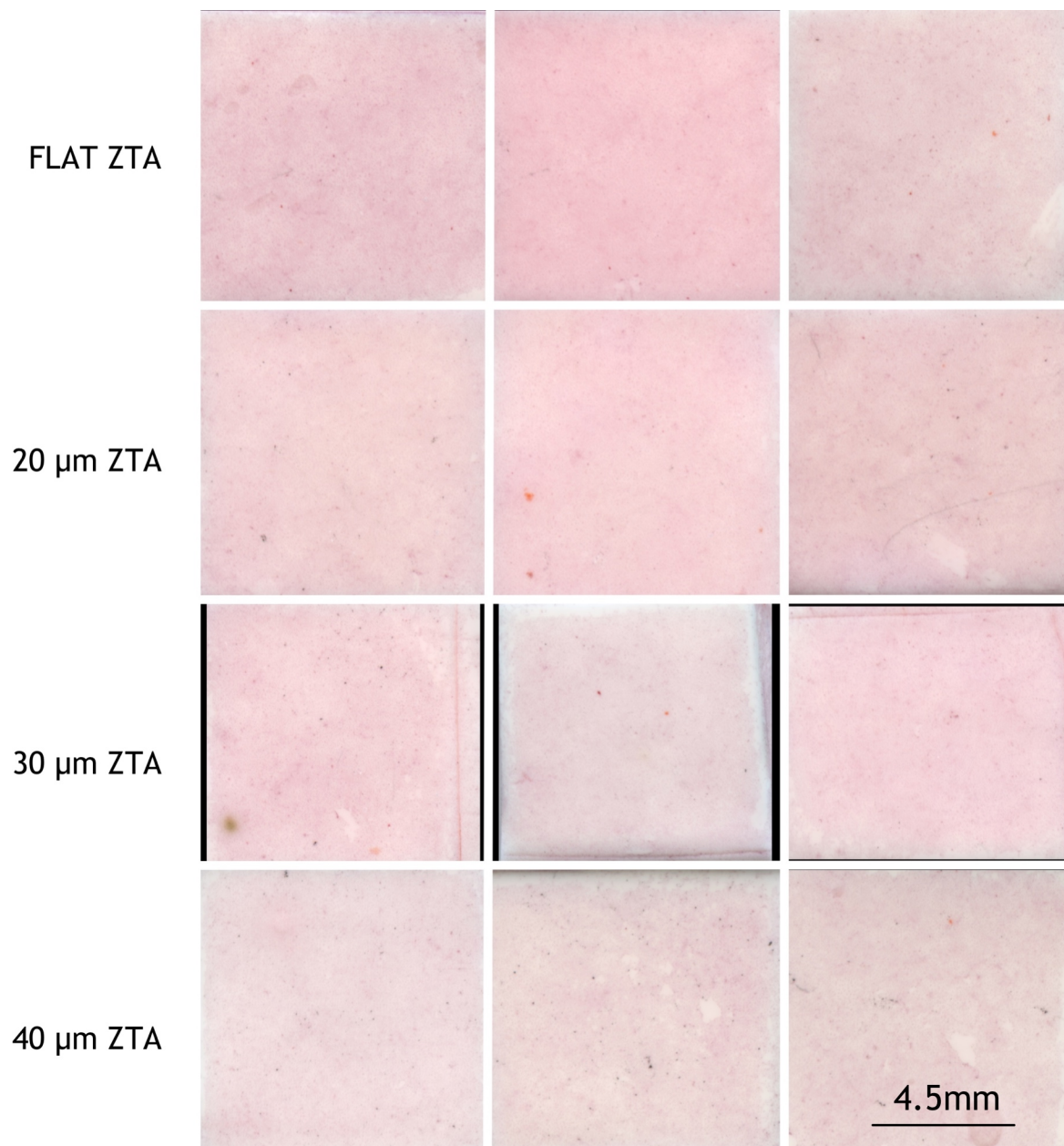


Figure 5-28 Montage of all the scanned images of ZTA in triplicate across each pattern. There is no discernable difference on these scanned image, assessment for overall colour reveals a great similarity, neither are there any appreciable differences in the presence of any large nodules.

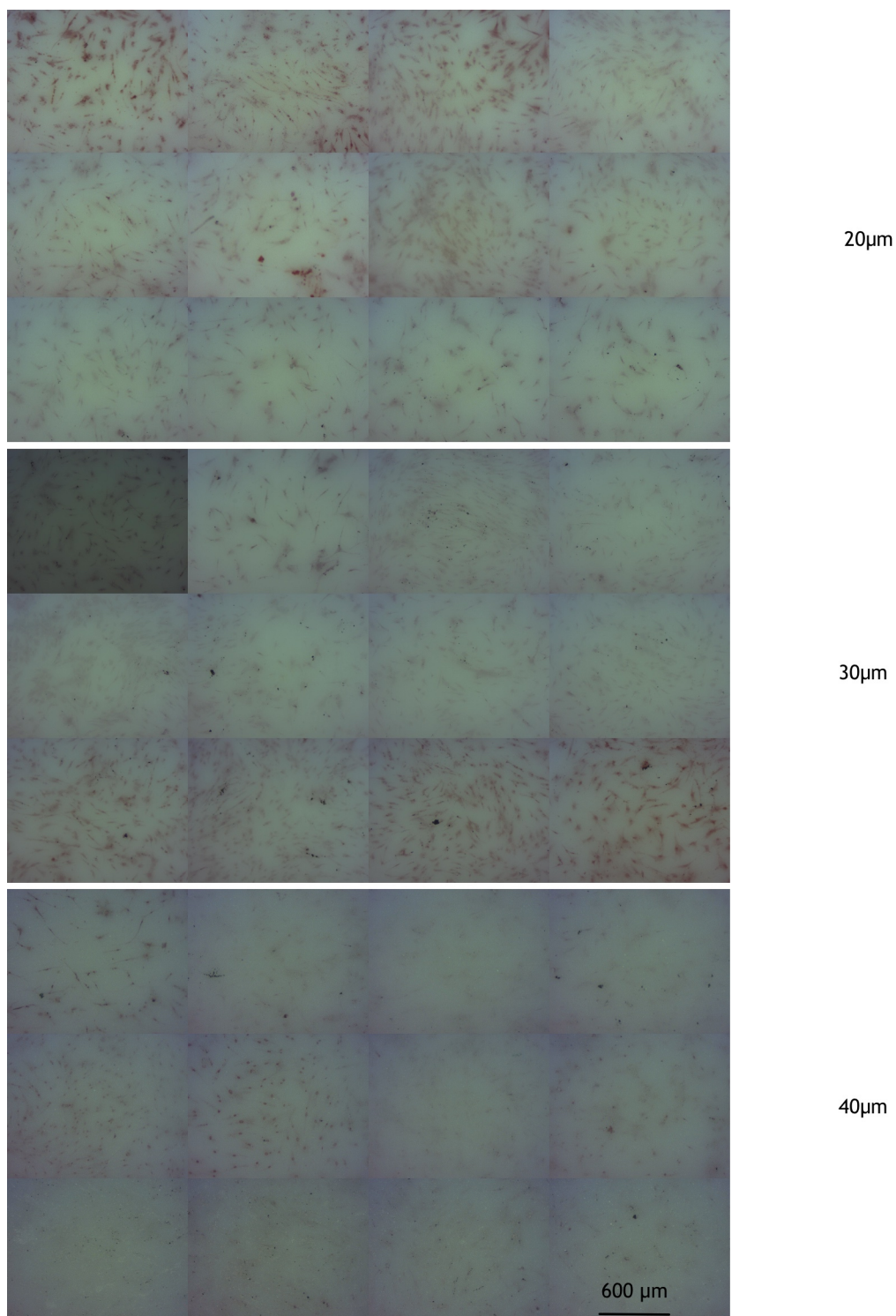


Figure 5-29 Montage of alizarin stained cells on ZTA ceramic. Inspection of these images does not reveal any great difference in the presence of calcium across the different substrates (x5 magnification).

Figure 5-31 shows a selection of images taken with a polarising microscope after staining with alizarin (2.8) and counterstaining with coomassie brilliant blue (2.9). The features have been highlighted where possible. No relationship is obvious from the deposition of calcium nodules related to feature position. The cells are seen covering the substrate completely.

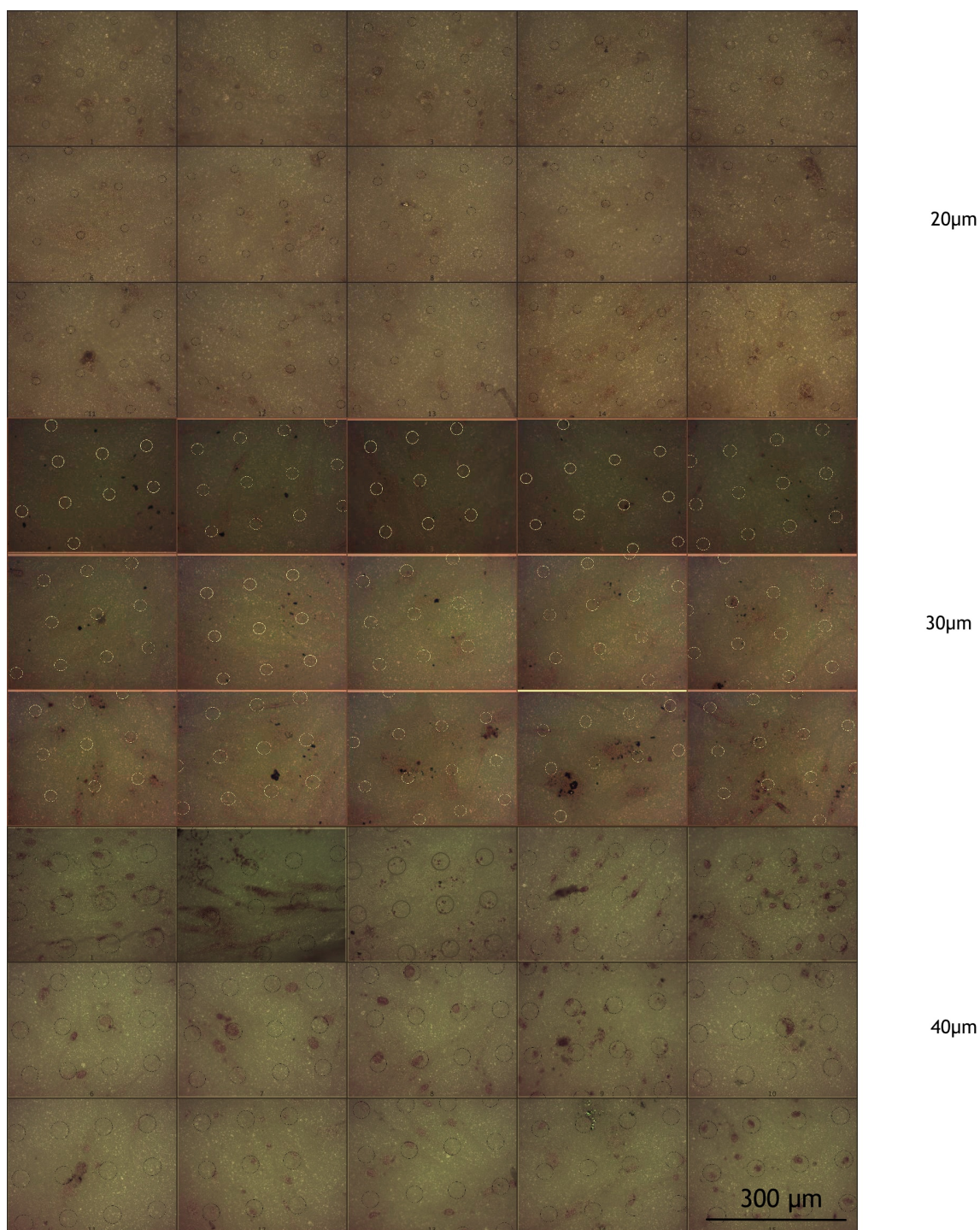


Figure 5-30 montage of images from polarising microscope with 20x objective lens. The features in the substrate have been highlighted. These images were captured to assess the position of calcium deposits in relation to the topographical features in the samples. Accounting for the greater surface area covered by the larger features (bigger feature with maintained centre - centre spacing) no appreciable difference is seen across the difference sizes of feature. It is noteworthy that almost all the calcium deposits in the photographs are intracellular, with very few free nodules (x20 magnification).

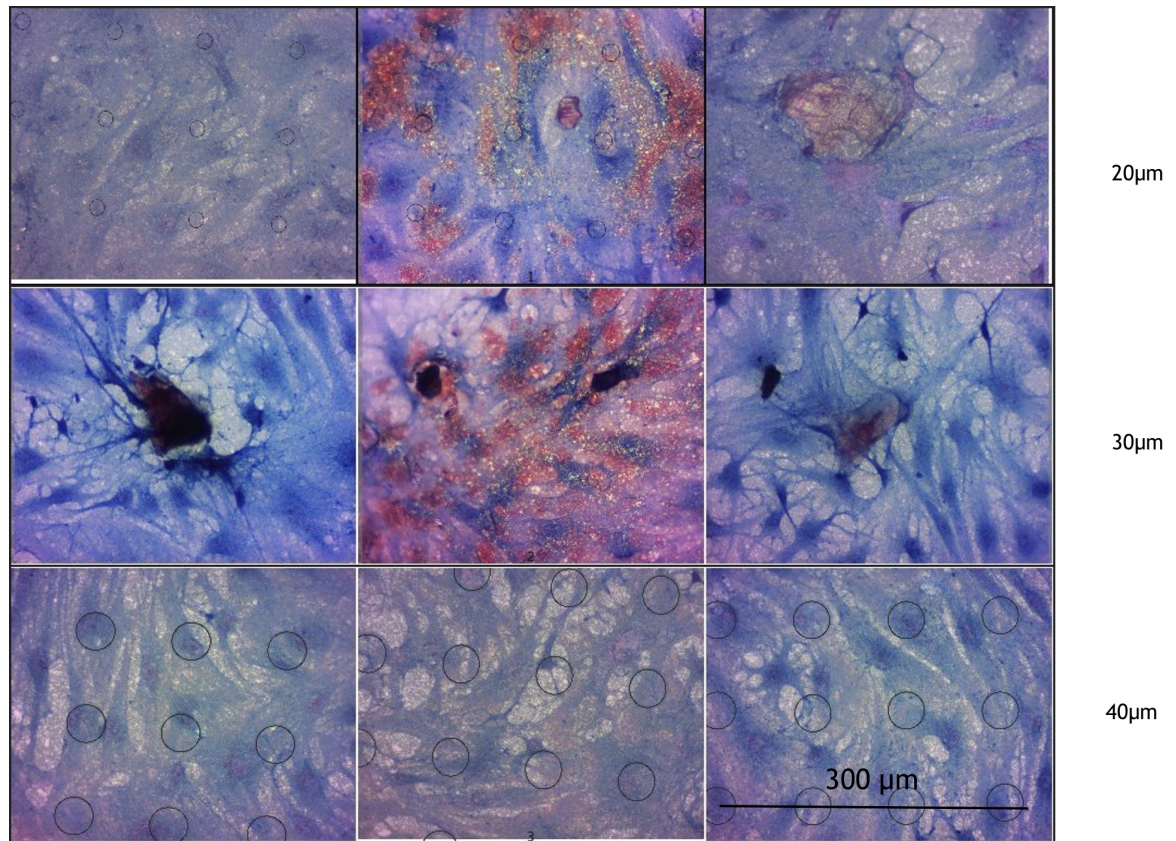
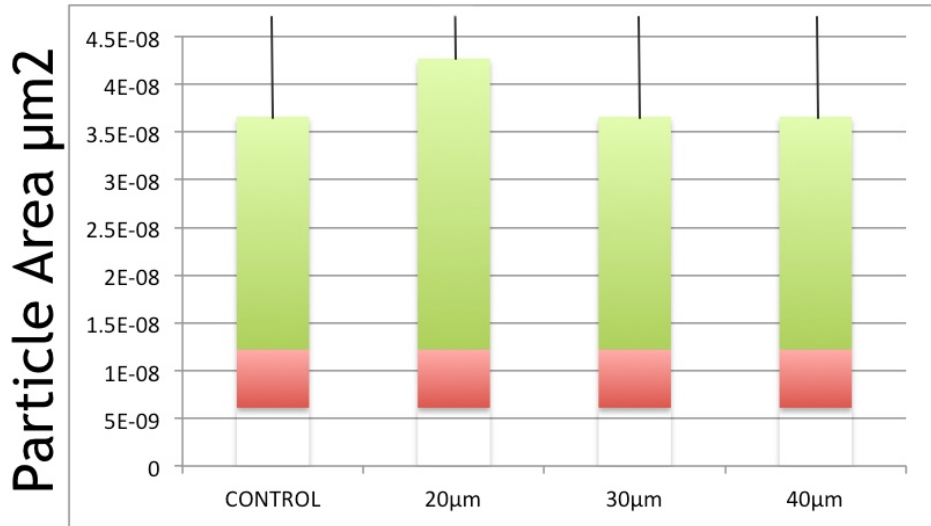


Figure 5-31 Montage of the alizarin stained patterned substrates after counterstaining with brilliant blue stain. Surface features have been highlighted where they were visible, in this representative sample of images the cell sheet appears to cover most of the material surface. This suggests that the cells will certainly be exposed to the features in some part. There is no relationship between the location of the features and the position of the cells (x20 magnification).

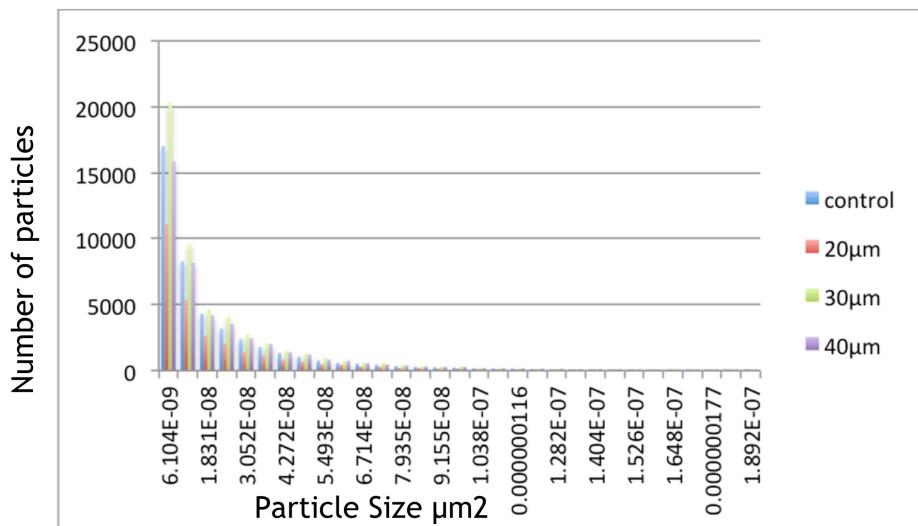
The results of the particle analysis are seen in the following figure, Figure 5-32 the box plots on the left show extreme positive skew with the lower whisker for the plot undetectable and the tail progressing from the chart area, the 2nd and 3rd quartiles for each substrate are remarkably similar. The right hand side of Figure 5-32 shows the appearance of the data when transformed by log (base 10) the particle size is remarkably similar across the substrates. Again the lower whisker for the first quartile is not visible given the proximity to the second quartile.

A frequency histogram of particle size may be seen in Figure 5-33 showing the distribution of particles of different size. The graphs show great similarity across all the groups with a massive tendency to small particle. Comparison of the groups via the Kruskal-Wallis (Excel © Microsoft) showed no statistically significant difference across the substrates with a p-value of 0.3



Box plot of particle area for alizarin staining on ZTA Red represents the second quartile, green the third quartile with the whiskers representing the upper and lower.

Figure 5-32 box plot of the size of particles stained by Alizarin red detected across the planar control ceramic and the three patterned substrates. The lower section of the graph may appear empty; the whisker representing the lowest is too small to be appreciated. The upper whisker shows the upper quartile. There is no statistically significant difference between any of the topographies



Frequency histogram of particle count by size for alizarin staining on ZTA

Figure 5-33 Frequency histograms of the distribution of particle size. No significant difference for particle size is found, the data is all significantly skewed to the left.

5.4 Discussion

5.4.1 Immunofluorescent microscopy

Much of the qualitative analysis shown in the chapter **Error! Reference source not found.** proved technically challenging in the ceramic material. The combination of stains in an image editing software package allows for interpretation of the distribution of proteins related to cell shape and tension. Most of the light spectrum was affected by the material fluorescence; this rendered it impractical to perform qualitative analysis of combined stains. Rather, I have quantified the expression of measurable proteins in an effort to compare the levels of proteins expressed across the substrates.

5.4.1.1 Focal adhesions

The role of focal adhesions in cell phenotype, migration and differentiation has been the subject of much study. There is a relationship between focal adhesion size and cell behaviour. Regions of the cell that are more static form larger focal adhesions (Ballestrem et al. 2001). Certain signalling events within the cell have been shown to produce larger focal adhesions (activation of e.g. Rho), increasing these signalling events restricts membrane protrusion (Arthur & Burridge 2001; Worthyake & Burridge 2003). A number of studies have demonstrated that focal adhesions at the leading edge of a migrating cell are smaller and transmit propulsive forces better than larger adhesions (Munevar et al. 2001; Ballestrem et al. 2001). These observations around cell mobility have been supported by work investigating the role of force in the development of focal adhesions. Internal and external forces act upon the cell. Rho is important for contraction within the cell creating an internal force. Activation of Rho associated Kinase (ROCK) increased cell contractility, it increases the direct phosphorylation of myosin light chain (Amano et al. 1996; Kureishi et al. 1997) and inhibits myosin light chain phosphatase (Kimura et al. 1996), these allow actin filaments to bundle together to create stress fibres, this clusters integrins and forms the focal adhesions (Chrzanowska-Wodnicka & Burridge 1996). External forces, from the extracellular matrix or substrate, are converted to biochemical responses via the integrins within the focal adhesions (N. Wang & Ingber 1995). The relationship to size of focal adhesion and force applied may

have a threshold. Tan et al (Tan et al. 2003) showed that there was no correlation between force and size once the focal adhesion was smaller than $1\mu\text{m}^2$, with a correlation being found above this value. The formation of focal adhesions and appearance of stress fibres within the cell are closely related.

Unfortunately it was not possible to assess the formation of stress fibres within the cells due to the fluorescence of the ceramic substrate. Table 5.1 shows the cells on both the 20 μm and 30 μm substrates expressed a decreased number of focal adhesion compared to the control and 40 μm patterned substrates Figure 5-6. The 40 μm patterned group produced more focal adhesions than the control group; the blunt comparison of numbers is only partially useful, in light of the points listed above relating to adhesion size. Figure 5-6 and Figure 5-7 illustrate a very similar profile of size distribution of focal adhesions across all the substrates. The peak size for each substrate is around 1.8 μm ; greater numbers are present at this size for the 40 μm and control substrates. The significant finding for these results is the presence of much larger focal adhesions in the 40 μm group than in the other groups. Assessment of the results as a whole shows the presence of these very large focal adhesions in the 40 μm cell group only. The culture conditions for all cell groups were identical. It is likely therefore that the cells within the 40 μm group are generating a greater internal force. Internal cellular process in response to the substrate may be assumed to be responsible for the result; the 40 μm pattern increases the number of large focal adhesions. This assessment method is open to bias as the focal adhesions are manually selected and highlighted; this bias is not a sound explanation for the decrease in focal adhesion size seen in the 20 μm and 30 μm samples since operator bias is likely to sway results in favour of the patterned substrates rather than the planar.

The results for focal adhesion differ for the ceramic compared to the PCL. There are potential reasons for the difference: there may be differences in assessment or they results may be genuinely different. Direct comparison is difficult because quantitative assessment of the focal adhesions for the PCL was not performed, the image quality was very high and qualitative assessment was used in isolation. If the differences are due to the assessment method it seems more likely the qualitative assessment is less reliable; the qualitative assessment may

be prone to bias, it is also less likely to detect small differences and so may not be as reliable as quantitative assessment. Quantitative assessment has shown poor results for the 20 μm and 30 μm samples, it is possible the material differences between ceramic and PCL can explain the difference in focal adhesion size. Another confounding issue is the difference in cell types; the primary human cells (experiments on ceramic) may not respond in the same way as the cell line (experiments on PCL), direct comparison of cell behaviour on the same material would have been ideal to provide a baseline assessment. Unfortunately this was not performed. Behaviour of the primary human cells more relevant than the cell line, the results for focal adhesions on ceramic are certainly not as encouraging as those for PCL.

5.4.1.2 Osteopontin

Osteopontin is expressed by osteoblasts as they prepare to mineralise the matrix as it interacts with calcium and contains the integrin binding RGD sequence (Zohar et al. 1998). Further, osteopontin is found around the nucleus in differentiating cells and in other cells displaying features of migration (CD44) it is found as an intracellular perimembranous protein (Zohar et al. 1998). A more recent study (Q. Chen et al. 2014) suggests an extracellular pathway for the effect of osteopontin but confirms with cell culture and a knock out mouse model that absence of osteopontin results in greater adipogenic differentiation. This was detectable at the cell level and in the animal model; a greater fat to body weight ratio was seen in the knock-out cohort.

Figure 5-10 through Figure 5-13 show the microscopic appearance of the osteopontin stain. The images for the 20 μm and 30 μm samples show more evidence of cell clustering and a greater level of perimembranous protein expression when compared to the control and 40 μm substrates. The levels of perinuclear expression of the protein appear similar across all the substrates.

In the quantitative analysis all the patterned substrates produced a greater amount of OPN compared to the planar control. This is seen in terms of number of particles and particle size, Figure 5-14 to Figure 5-16. .

The cell clustering seen for the 20 μm and 30 μm groups creates a bias for particle count and particle area as, the ability to distinguish clustered separate small particles from single larger deposits (as those seen for the 40 μm in Figure 5-13) is poor. Interpretation of the quantitative results must be tempered by this fact.

The detection of osteopontin is markedly different to the expression of vinculin. OPN has roles in mineralization and bone remodelling (M. D. McKee et al. 2005; Choi et al. 2008), it also has other intracellular roles including migration, fusion and cell mobility (Zohar et al. 2000; Suzuki et al. 2002; Zhu et al. 2004; Junaid et al. 2007). It is possible the up regulated expression of osteopontin seen on the composite ceramic is due to increased activity other than mineralization.

5.4.1.3 Osteocalcin

Osteocalcin production precedes mineralisation in vitro as with osteopontin it is calcium associated (Nakamura et al. 2009). It has been shown to correlate with bone formation during distraction osteogenesis in an animal model (Fink et al. 2002), it is produced by osteoblasts and is a useful marker for osteoblast activity. The results for size of OCN particle Figure 5-22 show a favourable response for the 30 μm and 40 μm samples over the control and 20 μm samples. I have been unable to discover any known relationship between size of OCN protein deposit and a favourable behaviour of osteoblasts or a subsequent increase in bone production. The presence of larger deposits of OCN is at least of uncertain significance, size of particle is less likely to be relevant than overall protein expression across the sample is much more relevant for osteogenic behaviour in vitro. Figure 5-21 shows the box plot distribution for osteocalcin across the samples. It is clear from all interpretation of Figure 5-21 and Figure 5-23 that the greatest detection of osteocalcin was in the control substrate. The expression of OCN most strongly by the control sample contrasts with previous immunofluorescent results for the composite ceramic. Unlike osteopontin osteocalcin is not involved in a great number of other functions other than mineralisation it is only secreted by osteoblasts and so is a valuable marker for bone production. In this experiment it has not been more heavily synthesised by cells cultured on patterned composite ceramic, this suggests a poor effect for topography influencing cell differentiation and osteogenesis in ceramic.

The results for immunofluorescent staining of the proteins selected are varied. The earliest time point measured for focal adhesion is encouraging but only for the 40 μm topography with negative results for the other two topographies. These results contrast with those obtained for the same protein expression on PCL. The results for the expression of OPN are the most encouraging with all patterned samples showing an increase in expression over control. With only the results for the 20 μm sample reaching statistical significance and not significantly different to the 30 μm and 40 μm samples

5.4.2 PCR

5.3.2 results for PCR shows a generally positive trend for upregulation of osteogenic genes. Figure 5-24 and Figure 5-25 show fold change for RUNX2 and osteopontin over control samples. This fold change occurs for all of the patterned substrates. Deriving significance from these results is difficult given the high standard deviations seen with each sample. Certainly no comment can be reliably offered regarding different responses across the pattern groups.

Figure 5-26 shows the results of further PCR analysis in a related ceramic material (alumina). These results demonstrate a particular response for the 40 μm group against control. One of the interesting features for this result is the significant decrease in standard deviation found in the samples measured at the 14-day time point. While it is incorrect to infer that a similar behaviour would follow in the day 6 and day 9 PCR assessment it would be interesting to know if a later assessment of gene activity would be generally accompanied by a decrease in variation.

Figure 5-27 shows that 62 out of the tested 96 osteogenic genes in the array demonstrate some degree of up-regulation. As with the tested samples on day 6 and day 9 Figure 5-24 and Figure 5-25 the standard deviation for the results are so high that no genuine inference may be made, the positive trend is encouraging. From the osteogenic array plate one gene showed statistically significant upregulation with a small enough standard deviation to allow the result to be unlikely from chance alone. The only positive and significant result was found for GDF10. GDF10 is a gene that codes a protein belonging to the bone morphogenic protein family, within the TGF β superfamily. It is also been

known as BMP3b. The role of GDF10 or BMP3b is not clearly defined but in-vivo work suggest that it is displayed across the growth plate (Nilsson et al. 2007).

One of the weaknesses of the use of PCR in this experiment is the time points at which the cells have been analysed. Another approach to assess the genetic activity of the cell culture would be to assess on regular consecutive time points. This approach would provide some insight to the timing of transcription activity; it would eliminate the possibility that peak activity for any given gene of interest would occur without notice. This approach was not taken due to high variation seen within the samples and the budgetary constraints for the research

5.4.3 Alizarin red

Calcium production into the extracellular matrix is a critical component of bone formation. It is the principle inorganic component of bone and is responsible for resistance to compression forces. Calcium also plays an important role as a signalling messenger (Tonelli et al. 2012) and has been shown to have a direct effect on the differentiation of stem cells (S. Sun et al. 2007) (Tonelli et al. 2012).

The comparison of calcium production across all the substrates has failed to show any difference between the groups; either for overall calcium production or the production of calcium nodules. Qualitative assessment of the location of cells related to the position of features within the substrate has failed to show any correlation. No correlation has been seen between the position of the Alizarin stained nodules of calcium and the features in the substrate. While some nodules have been identified within the features, so many nodules are seen outwith the features it seems highly likely the appearance of calcium within a feature is simply by chance.

The weaknesses of this experiment are the variation in cell type used and the subtle differences in topography for the ceramic compared to the PCL. All the experiments performed on ceramic were performed with primary human cells, these cells represent well the cell type exposed to the surface of implants, they may not behave in a similar fashion to the cell line used for the experiments in PCL. The grain structure of ceramic has been discussed (4.3.3) this prevents the

creation of a shallow feature in the ceramic; the deeper feature may have created a different response by the cells.

5.5 Conclusion

The results of the cell culture experiments on ceramic are mixed. The processes that lead to mineralisation in vitro have shown some results in favour of focal adhesion and cell tension, partial results for protein production (negative for OCN and partially positive for OPN), PCR has provided a slight positive trend but nothing concrete to provide a sure foundation for definite upregulation. Weaknesses in the methodology and difficulties with some material properties contribute to the inconsistencies in the results. Ceramic is fluorescent, assessment of gross protein production would be better carried out using techniques away from fluorescent microscopy. One example would be cell extraction from the ceramic and colorimetric assessment for the labelled proteins, this method is dependent of cell numbers per samples and would require standardisation.

No definite positive result is shown for mineralisation. This may be a genuine reflection of osteoblast activity and osteogenic differentiation on ceramic. It may be that 28 days of culture is too short a time period to assess calcium nodule formation on ceramic if that is the case a longer culture period may have provided a different result. Perhaps the positive osteogenic effect of topography is modulated by the surface roughness of the ceramic related to the feature size and is too small to be carried through to invitro mineralisation.

In summary, the balance of results, from this series of experiments show a common positive trend. The circular pit topography influences osteoprogenitor cells to more osteoblastic differentiation. The positive effect was not clearly evident in all of the results; in some of the results there is a positive trend only, without achieving statistical significance. This may be because the difference generated in ZTA is hard to distinguish. There may be material differences that modulate the effect of the topography. It is also possible that the material qualities of ceramic have been relative obstacles in detecting the markers of osteogenic differentiation.

I hypothesise the differences between ZTA and PCL have played a role in the different results across the two materials. I propose to further assess this hypothesis in the following chapter.

6 Metabolomics, the response of cells cultured on different materials and different topographies.

6.1 Introduction

Metabolomics the study of global metabolite profiles in a biological system, for this experiment the system consists of the cells cultured on each substrate, planar and patterned ceramic, planar and patterned polycaprolactone.

Metabolites make up the basic building blocks of biology comprising pathways involved in energy storage and use, amino acid and hence peptide biosynthesis etc. Metabolism can be anabolic (building up) or catabolic (breaking down).

In this chapter, an untargeted metabolomics approach was adopted to study global changes in cell metabolism. To achieve this, Fourier transform orbitrap mass spectrometry was used as a method suitable for detection of metabolites (Creek et al. 2011).

6.2 Materials and Methods

6.2.1 Cell culture and sample processing

Extracted human osteoprogenitor cells were cultured for three days (2.6). Cells were incubated until sufficient numbers were achieved to allow seeding of all substrate replicated with a cell density of $1 \times 10^4 \text{ml}^{-1}$ (2.6.4.3). Two groups of cells were cultured on ZTA ceramic with three ceramic substrates comprising a sample and three samples used for each pattern to be studied. The patterns used for this experiment were 40 μm ZTA against planar control. A further two groups were cultured on planar and 30 μm patterned polycaprolactone, again triplicate substrates per sample and three samples per topography. The micron sample of PCL had provided the best results therefore it was selected to compare with the 40 μm patterned ceramic. Once the cells had been cultured for three days the spent media was removed and the cells were processed as described (2.12).

6.2.2 IDEOM

Processing of data from mass spectrometry was performed according to the standard pipeline for our department (Creek et al. 2012). This takes the form of a macro enabled spreadsheet (excel © Microsoft).

6.2.3 Metaboanalyst

Metaboanalyst (Xia et al. 2009) is a web based analytical tool for processing metabolomics data. Within the software data is normalised and processed. It supports a number of assessments including: fold change, t-test, heat maps and principal component analysis (PCA). Principal component analysis groups variable in order of which contribute the most to variation within a sample, thereby identifying those input variable that are most responsible for change within the sample.

6.2.4 Ingenuity pathway analysis

Ingenuity pathway analysis (IPA®) by Qiagen® is a licenced analytical software that processes metabolic data in relation to established. It is based upon a well-curated database drawn from the primary literature to form inter-related gene/metabolite networks that allows signalling and functional pathway investigation. In this thesis, the network, canonical signalling and functional signalling modes were investigated.

6.3 Results

6.3.1 From Metaboanalyst

Figure 6-1 shows a complete heatmap generated as part of the report from Metaboanalyst. The heatmap shows colours in the red spectrum as up-regulated and colours in the blue spectrum as down-regulated. The rows are grouped by topography with 40 µm ZTA and 40 µm PCL in the top two rows and planar controls in the lower two rows.

Clearly the representation of such a volume of information may only provide an overview. In this instance it is clear that much greater differences in metabolic cell activity were seen based on variation in the material than any effect created by the topography. The heat map suggests a greater up-regulation of metabolic activity on the ceramic material than for the polycaprolactone.

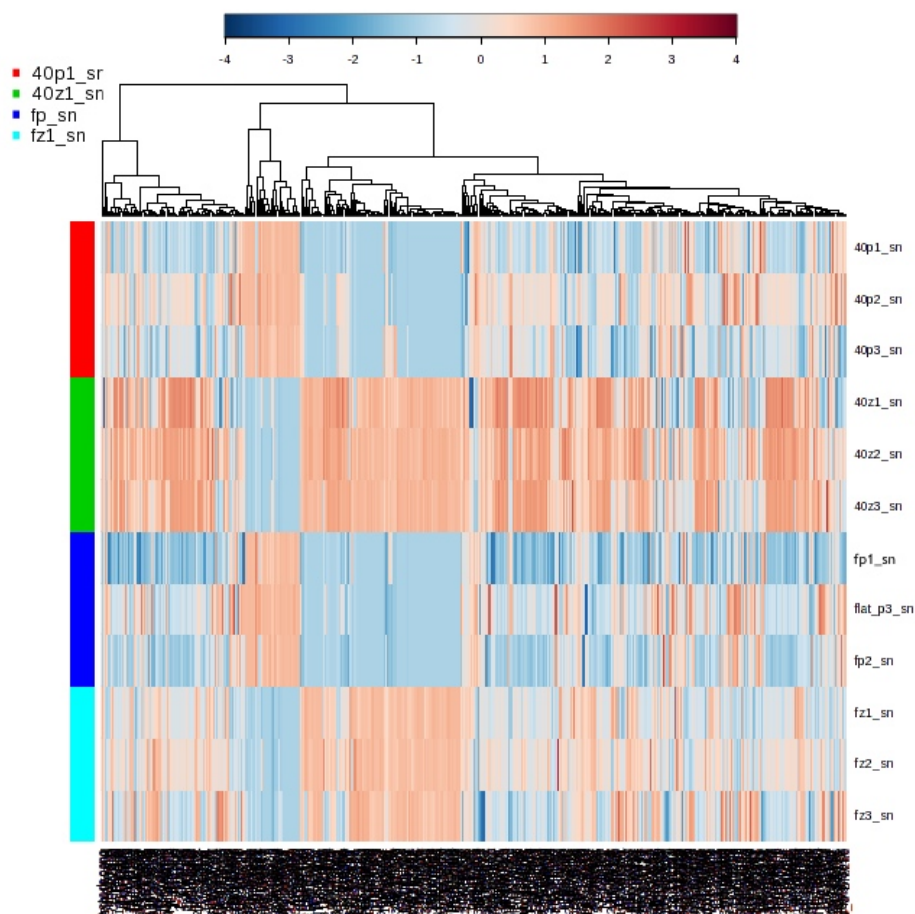


Figure 6-1 The overall heatmap for the metabolome of the samples. The colour legend in the top left corner shows red dark blue for the PCL samples and pale blue and green for the ZTA samples. The grouping in the figure has the patterned materials superiorly and the planar samples inferiorly. The colour graduation scale shows blue spectrum indicates downregulation and into the red spectrum indicating upregulation. This graph is included for general trend as there are too many metabolites included than could be sensibly interpreted. The result from the graph indicates metabolic activity more related to material than topography.

This primary effect exerted by the material is easily seen in the principal component analysis in Figure 6-2. This figure shows the X-axis representing the input variable most responsible for the sample distribution; the Y-axis shows the effect of the second largest variable. Along the X-axis the principal component is responsible for greater than 98% of the variation in the test samples. It is interesting to note that there is much better separation of metabolite data for the planar vs pitted ceramic than for planar vs pitted polymer. The distribution of results on the Y-axis accounts for 1.2% of the variation, thus separation along

this axis may be of exaggerated importance; however, it is notable that the ceramics and the polymers are clearly distance along PC2 suggesting that it is likely that this contribution is purely due to material chemistries.

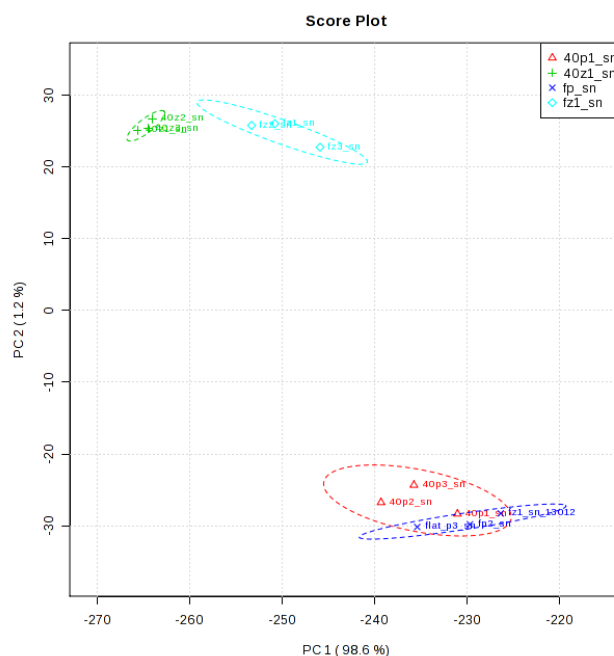


Figure 6-2 PCA for the overall metabolome of the samples. Three markers in each colour indicate the location of each of the triplicates, colour coding in the top right corner shows green for the patterned ceramics, pale blue for the flat ceramic, red for patterned PCL and dark blue for planar PCL. Each triplicate sample is outlined according to distribution. Progression of the X-axis indicates the primary differentiating variable. This accounts for over 98 % of the distribution, the PCL samples are grouped with significant overlap, where the ceramic materials are independent of each other. The Y-axis shows the distribution in the second component, (in this instance 1.2% contribution), the ceramics and plastics are clearly separated with no significant effect of the topography visible.

A similar pattern of metabolic activity is seen when a sub-selection of metabolic activity is isolated. Figure 6-3 shows a heat map for lipid metabolism.

This figure demonstrates some variability within the groups of samples. The overall picture matches that for the overall map, greater metabolic activity on the ceramic than on the PCL. The greatest activity levels are seen through the 40 μ m patterned ceramic with the greatest down-regulation seen on the planar control PCL.

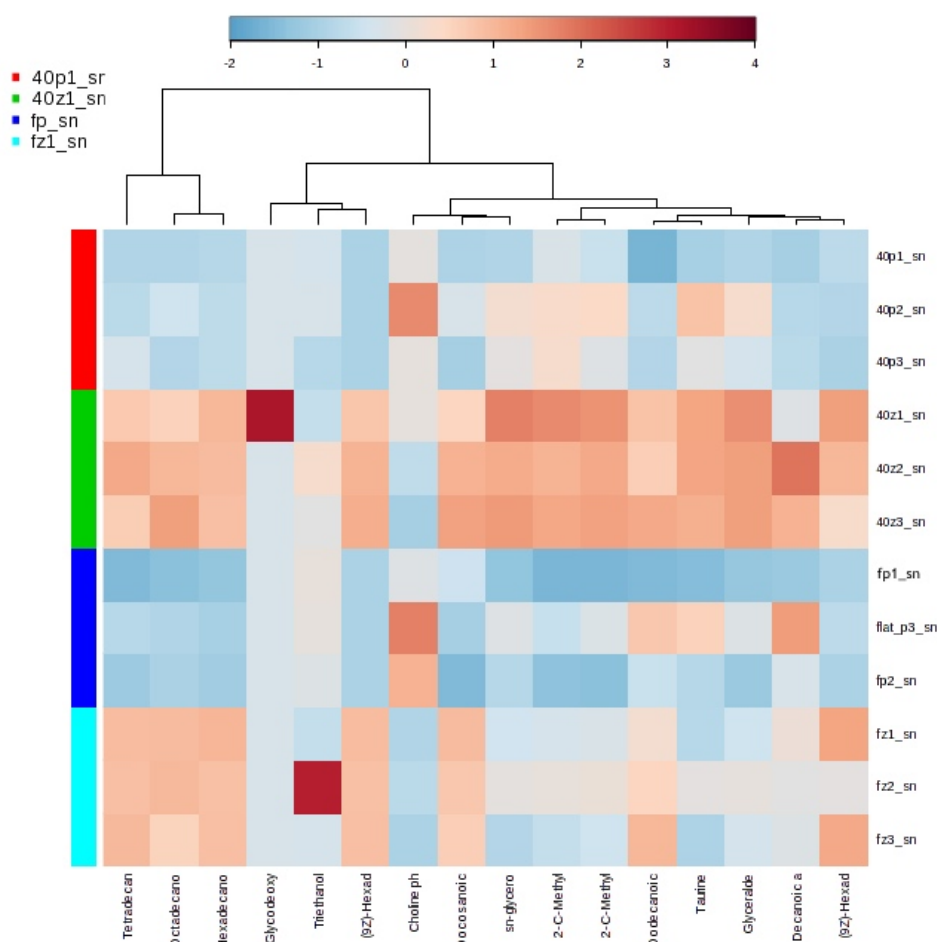


Figure 6-3 Heat map for lipid metabolism only. The colour legends show red and green for patterned PCL and ZTA with dark blue and pale blue for flat PCL and ZTA. The PCL samples are generally down regulated compared with the ZTA samples, the 40 μ m ZTA (green) samples show the most activity.

This result confirmed by the appearance of the PCA graph for lipid metabolism. Figure 6-4 shows the PCA for lipid metabolism, in this instance there is a clear difference in activity for the patterned ZTA over the other materials, the results for this material are also much closer in distribution than for the other samples. This suggests a highly activated, coherent cell population.

Interpretation of the graph relies on noting the contribution made by the components on the X and Y Axes. In this case the very obvious difference in the Y-axis only contributes 0.1% of overall distribution; it is encouraging that difference is also apparent on the principal component responsible for greater than 99% of the distribution. Both analyses also show an increase in lipid metabolism for cells on the pitted polymer compared to planar PCL that is smaller, but in line with, the increase from planar to patterned ZTA.

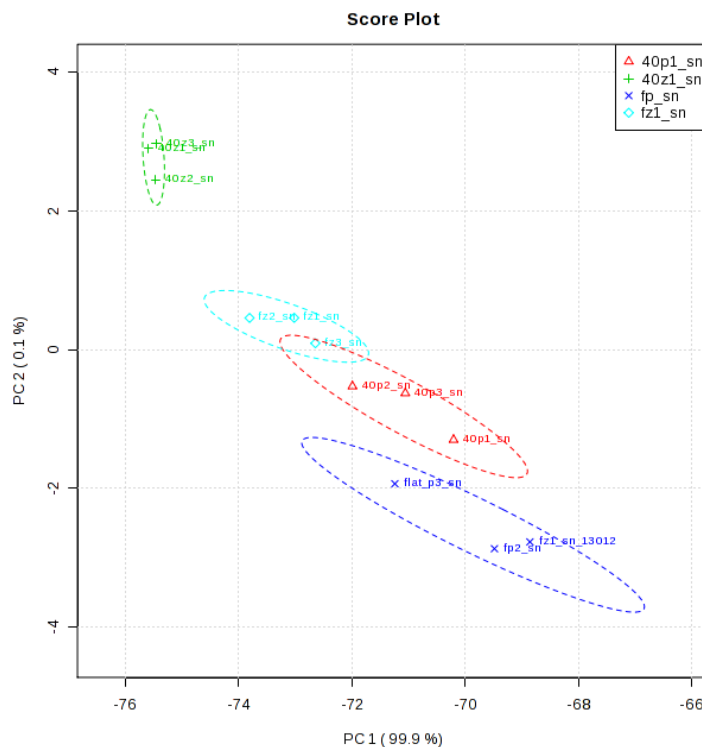


Figure 6-4 PCA for lipid metabolism. The green results for patterned ZTA are the stand out group, with the tightest grouping and most separation to the pale blue of the control ZTA, which overlaps the red of the patterned PCL in both axes. The dark blue of the control PCL overlaps both the patterned PCL and control ZTA in the first component but only the patterned PCL in the second component.

Another area of selected cell activity was energy metabolism. The heatmap can be seen in Figure 6-5.

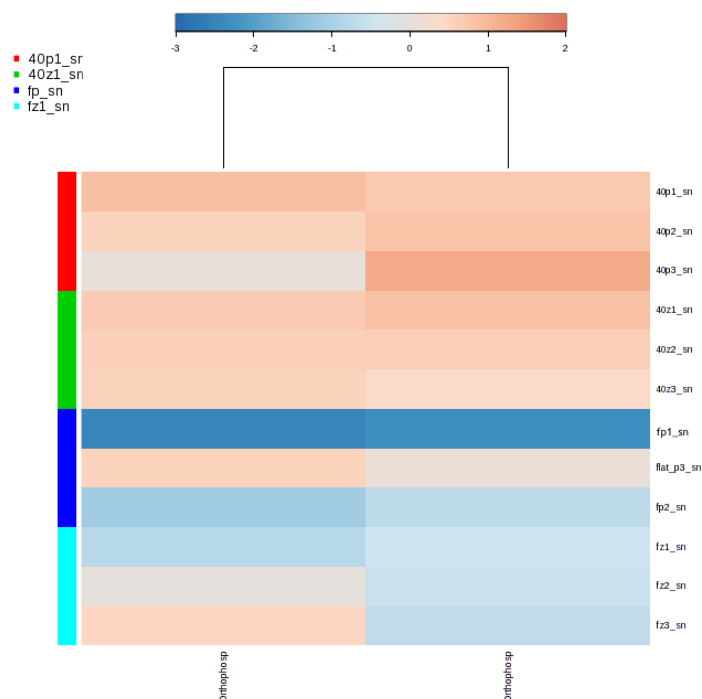


Figure 6-5 Heatmap for energy metabolism. Note the distinct differences in activity between topographies rather than between material type. The patterned surfaces create a greater upregulation than the controls.

There is clearly an outlying replicate for the planar control with little energy metabolism occurring in sample labelled 'fp1_sn'. Disregarding this outlier, distribution of results for this aspect of cell activity shows a distinct grouping associated with topography rather than material, this is in contrast to the other results. The PCA results for energy metabolism are seen in Figure 6-6. While differing from lipid metabolism in terms of chemistry being the main contributor there, this energy metabolism is in agreement with the increase in lipid metabolism and its predicted role in energy seen between the planar and patterned surfaces in Figure 6-3 and Figure 6-4.

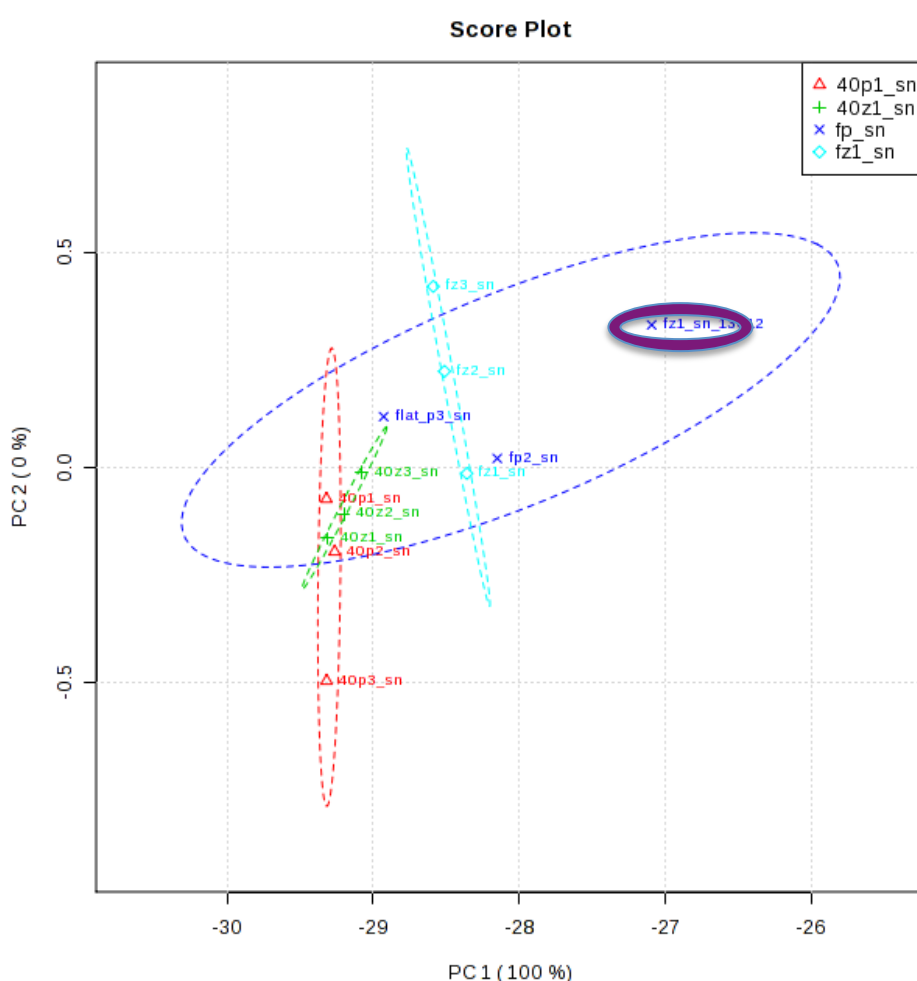


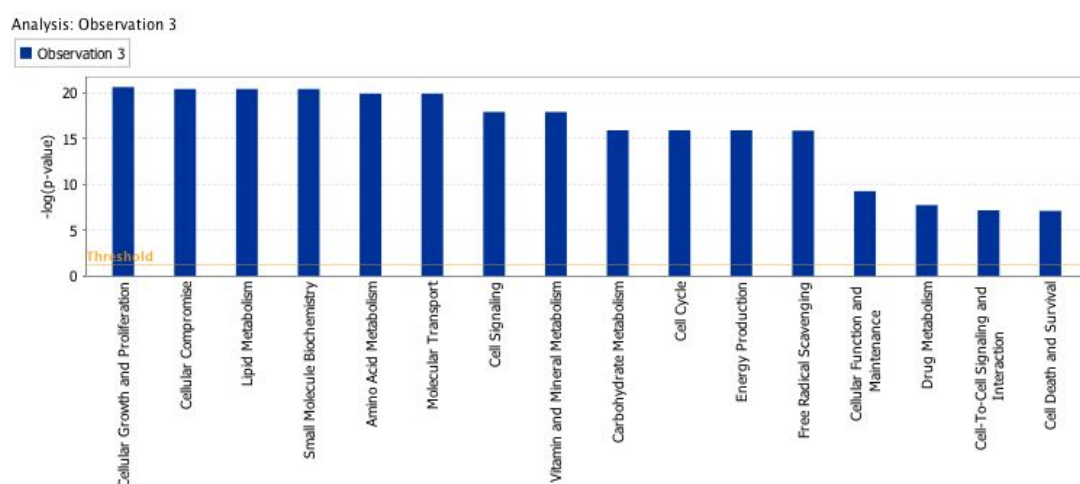
Figure 6-6 PCA for energy metabolism. Allowing for the outlier (highlighted in purple), these results show a tight grouping by topography rather than by material type. The difference is most obvious for the the ZTA pattern against ZTA control.

The outlier results likely creates a significant skew for the flat PCL data, however the patterned ceramic and plastic samples are clearly very tightly grouped along the X-axis, note also that there is no notable effect exerted by the second principal component (Y-axis 0%).

6.3.2 Results from Ingenuity Pathway Analysis

6.3.2.1 Material effect on planar samples

Figure 6-7 shows a bar chart of metabolism of cells cultured on planar ZTA compared to those cultured on planar PCL. The results show that many cellular actions are increased on ceramic when compared to polycaprolactone.



© 2000–2016 QIAGEN. All rights reserved.

Figure 6-7 Bar Chart of planar ZTA normalised to planar PCL. This bar chart reflects the organisation of results into diseases and functions. The results show increased activity of the cells cultured on ZTA compared to those on PCL, this demonstrates the material effect on planar substrates

This comparison of material effect on planar materials is further shown in the network map (Figure 6-8). Predicted activation of pathways are shown in orange and predicted deactivation shown in blue. Note that extracellular receptor kinase (ERK) signalling is up-regulated by most of the pathway. The relationship of ERK signalling to cell activities of interest is shown by the tagged canonical pathway labels within the figure. Those listed include signalling for: Bone Morphogenic Protein, Platelet Derived Growth Factors and Receptor Activator for Nuclear factor Kappa B (RANK) signalling for osteoclasts.

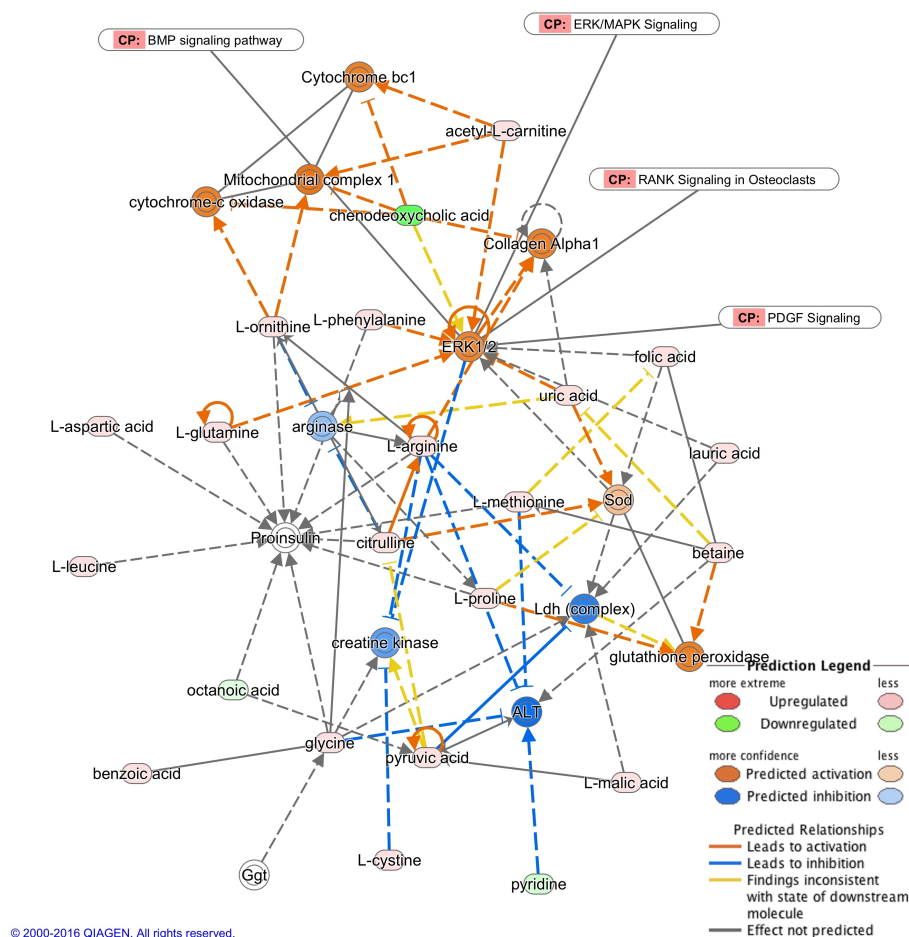
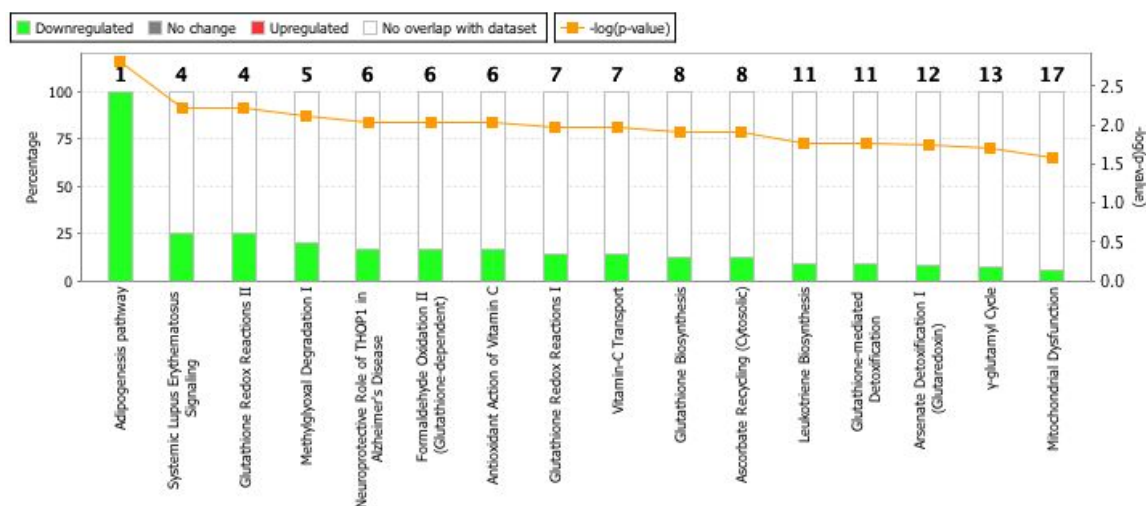


Figure 6-8 Network map for the increased activity of cells of planar ZTA normalised to those on planar PCL. Demonstrating the material effect on planar substrates. The up-regulation of note is ERK, involved in cell signalling that relates to differentiation.

6.3.2.2 Material effect on patterned samples

Comparison of the results for patterned PCL to patterned ZTA provide an insight into the effect exerted by the material of the substrate with similar topographical features in place. A stacked bar chart is seen in Figure 6-9, this graph relates metabolic activity into canonical pathways. Across the board for these results the cell activity for culture on patterned PCL are down-regulated when compared with the results seen for the cells cultured in the patterned ZTA. Strikingly, reduced expression of adipogenesis based pathways is noted suggesting that the more adhesive ZTA is surface is more amenable to osteogenesis.

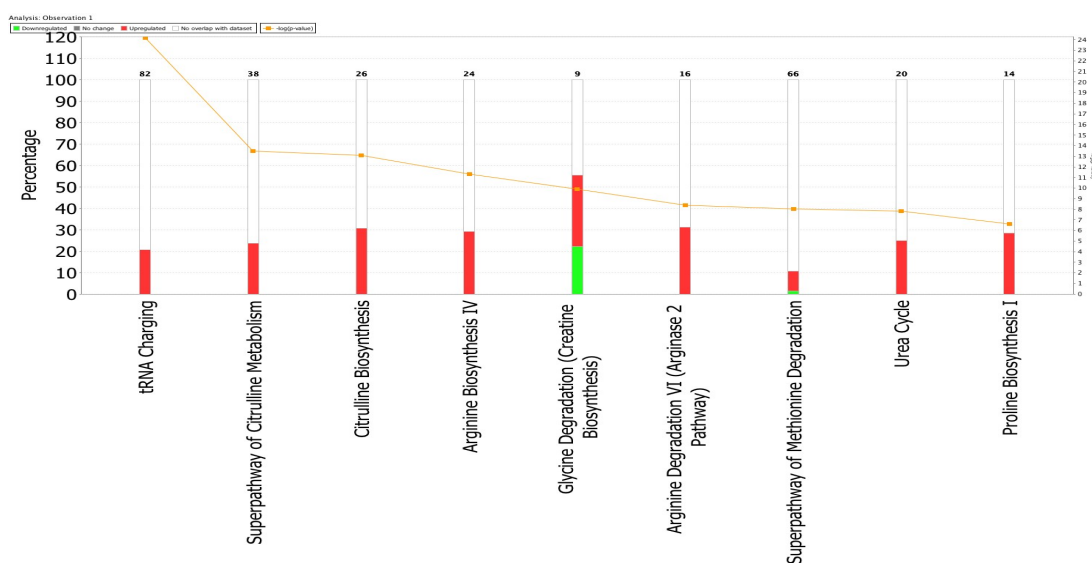


© 2000–2016 QIAGEN. All rights reserved.

Figure 6-9 Stacked bar chart on the canonical pathways. Comparison made of patterned ZTA to patterned PCL. The material effect in patterned substances shows increase activity in the cells cultures on the ceramic material.

6.3.2.3 Topographical effect on PCL

Comparison of the data sets for patterned and planar PCL allow an assessment of the effect of topography. The stacked bar chart for canonical pathway, Figure 6-10 shows general up-regulation in the cells cultured on the patterned PCL. This is made from e.g. a number of contributions from amino acid biosynthesis (e.g. arginine, glycine, methionine and proline) suggesting potential changes in protein expression.



© 2000–2016 QIAGEN. All rights reserved.

Figure 6-10 Stacked bar chart of the involvement of canonical pathways for the topographical effect on PCL. There is up-regulation of all the activities shown in red on the patterned PCL over the planar material.

6.3.2.4 Topographical effect on ZTA

The final comparison is for the effect of topography on ZTA. A stacked bar chart of the involvement of canonical pathways is seen in Figure 6-11. This graph shows that for the majority of pathways related to the measured metabolic activity, the activity is up-regulated on the ZTA with topography. It is notable that for less than half of the included pathways there is a shared down-regulation, of a much lesser value in all but one of the results (creatine-phosphate biosynthesis has roughly equal proportions of up-regulation and down-regulation)

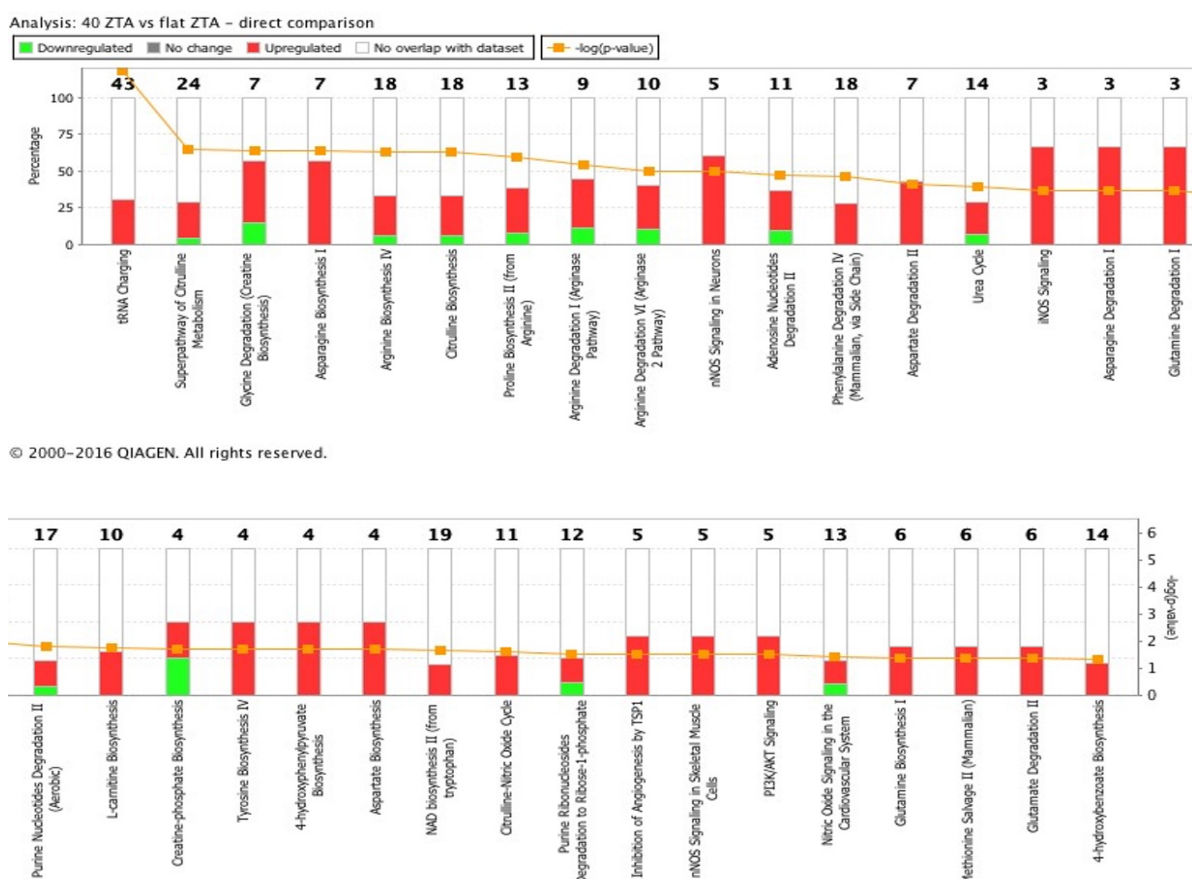


Figure 6-11 Stacked bar chart, canonical pathway involvement of the topographical effect on ZTA. The overall trend is upregulation on the pitted material over the planar.

Processing the metabolic activity in relation to disease and function is seen in Figure 6-12, in general this figure shows a large positive influence of topography over planar ceramic. Most notable, and most highly significant changes, are seen in energy-based pathways such as carbohydrate, lipid and energy metabolism

and also in amino-acid pathways related to protein expression. These are sensible as differentiation is an energetic process where extracellular matrix is expressed (McMurray et al. 2011).

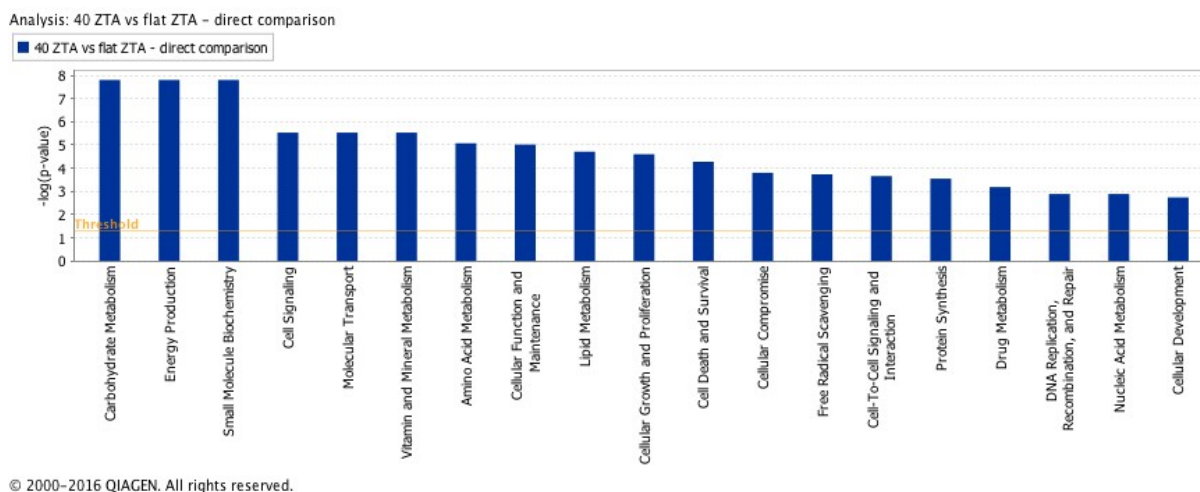


Figure 6-12 Bar chart of the metabolic cell activity as it relates to cell function, note the strongly positive results for energy production, cell signalling and molecular transport. Also note the increase lipid metabolism in the cells from the patterned substrate. This upregulation across cell activity is reflected at all levels – general activity such as signalling, specific activity such as cell morphology but also in cell survival and indicators of cellular compromise.

The final figure for this chapter is Figure 6-13. This figure is a network map demonstrating metabolite changes due to the topographical effect on cell behaviour when cultured on ZTA. The topographical effect is clear, patterned surfaces of ZTA upregulate metabolic activity over planar surfaces. ERK is highlighted in the figure, it is predicted to be activated by five factors within the network.

Network 1 : 40 ZTA vs flat ZTA - direct comparison : FznVS040znKEGGforIPA : 40 ZTA vs flat ZTA - direct comparison

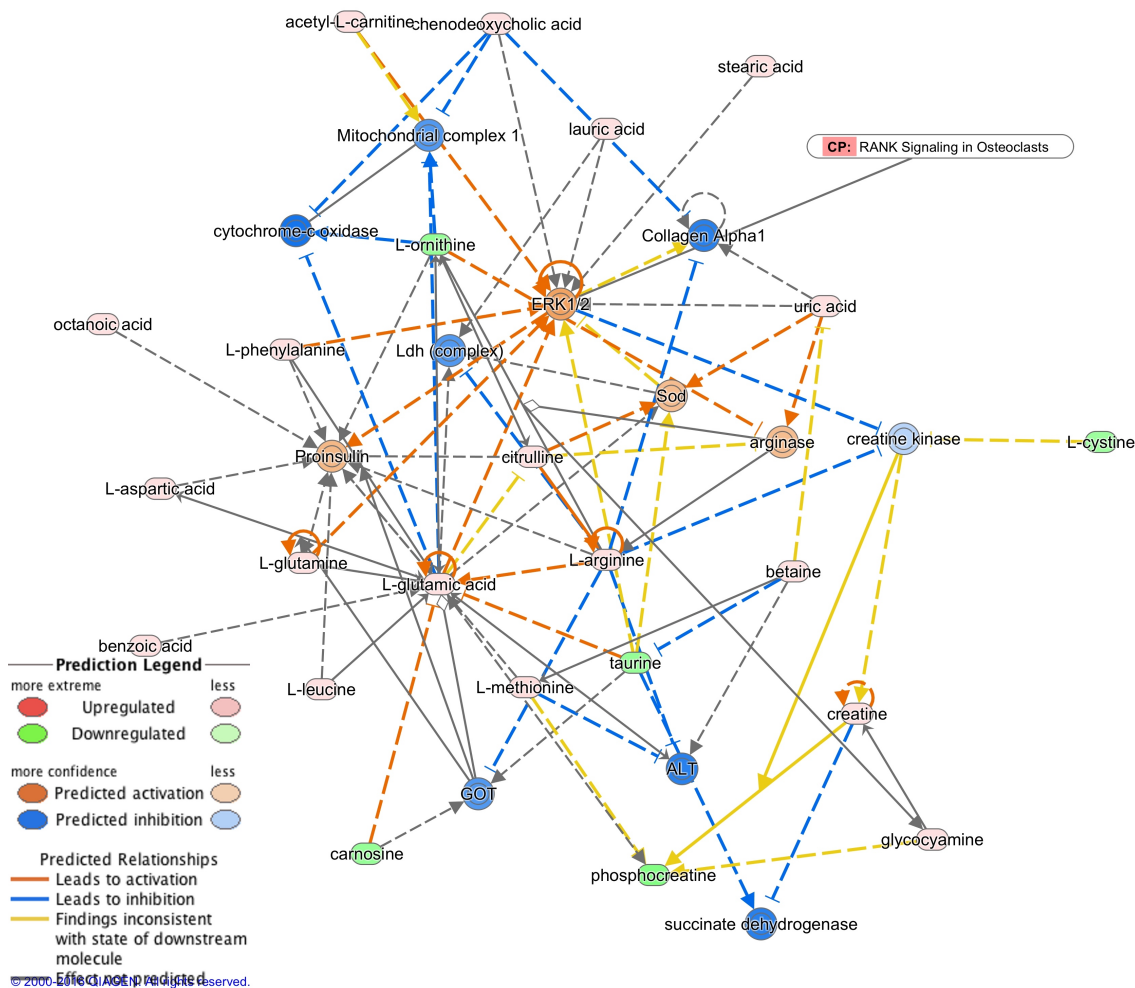


Figure 6-13 Network for metabolic activity, 40 μ m topography ZTA over planar ZTA. This network map shows upregulation of ERK on patterned ZTA over planar ZTA. A few small pathways are inhibited. ERK is notable due to its role in cell differentiation.

6.4 Discussion

6.4.1 Materials differences

It is not surprising to see the metabolic evidence of the difference that material have on cell behaviour in culture. Since it is protein adsorption that forms first contact with material surface (Santin et al. 1997) it follows that the material properties will determine some aspect of the further recruitment of proteins, cell attachment and activity (Kasemo & Lausmaa 1994).

ZTA is inert. The wear particles from bearing systems in the body generate very little host response (Hatton et al. 2002; Hatton et al. 2003; Howie 1990). The bulk implant of ceramics in general generate little short term reaction and are well tolerated (Maccauro et al. 2010). PCL is a biodegradable biomaterial widely used in, in vitro cell and tissue culture (Woodruff & Hutmacher 2009) and also in

animal models (Rohner et al. 2003). It is interesting to see then an increase in metabolic activity and energy expenditure on the 'inert' material of the bioactive material 6.3.1, whether the material is planar 6.3.2.1, or patterned 6.3.2.2. The interpretation of these results, suggests that this increased energy expenditure is required for the cells to attach, grow and function on the ceramic material. Best illustrated by the increase in lipid metabolism Figure 6-3, Figure 6-4, it is simple to infer cells in culture have to work harder on an inert material.

Further, pathway investigation suggests that these differences are also seen at the canonical level with e.g. adipogenesis being repressed on ZTA compared to PCL.

Assessment of the network maps shows predicted increased activity of ERK. ERK performs intracellular signalling, it is associated with many core signalling events. ERK can be activated by focal adhesion kinase (FAK) or G protein signalling (Dai et al. 2007; Ge et al. 2007; Meloche & Pouyssegur 2007; Ward et al. 2007; Tamama et al. 2008; Kim et al. 2008). Cell proliferation during surface attachment is part driven by ERK activation (Kriegsheim et al. 2006). ERK activation feeds back to proliferation, it has been proposed that overactivation of ERK leads to a reduction in proliferation that then drives differentiation through phosphorylation of transcription factors (Kriegsheim et al. 2006; Yeung et al. 2000). In short ERK is involved in cell proliferation and differentiation, at least partly driven by focal adhesions. The predicted increase in activity is indicative of increased proliferation and following that differentiation.

So where it may be straightforward to assume that increased energy expenditure is related to the work required to proliferate and attach on an 'inert' surface, it may be that the ceramic studied here presents surface features than induce more differentiation than the PCL. The results from 'Characterisation of embossed ceramics (2.3.2)' show marked differences in the topography presented to the cells by the two materials provided for culture. The ZTA has a constantly increased landscape noise for cell interaction.

6.4.2 Topographical differences

Topography significantly increased lipid and energy-based metabolisms even further. This has been seen before in polymers and suggests that differentiation is an active metabolic process (Yang et al. 2014; Dalby et al. 2014; Tsimbouri et al. 2012). Further, work on stem cells shows that they tend to be metabolically quiet prior to differentiation (Yanes et al. 2010; Reyes et al. 2006; McMurray et al. 2011).

ERK is implicated. Perhaps sensible as ERK is adhesion stimulated and regulates RUNX2, the master osteogenic transcription factor (Hamamura et al. 2010).

This all ties in well with the standard bio showing enhanced osteogenesis on the topography. Future work might focus on targeting these pathways at gene level to confirm or e.g. inhibiting ERK to block these pathways as that appears to be a central biochemical highlighted by the metabolome analysis.

6.5 Conclusion

The results demonstrate significant differences in metabolic response by cells cultured across these two materials. Whilst this may be (and is likely at least in part to be) due to chemical and physical differences between the materials, the information about the positive effect of topography within each material group provides encouragement about the use of topographical manipulation of differentiation and osteogenesis.

7 Summary

7.1 Why is there a need for this research

Total joint replacement surgery for arthritis has been proven effective. (Shan et al. 2015; Gillespie & Porteous 2007; Sloan et al. 2013; George et al. 2008; Adams et al. 2007; Norris & Iannotti 2002). The basic principle of hip arthroplasty surgery has changed little since the breakthrough success of Charnley with the low frictional torque arthroplasty (CHARNLEY 1972; CHARNLEY 1971).

Modifications to the design of the stem have resulted in huge improvements in survivorship (Hook et al. 2006; Lewthwaite et al. 2008). Some problems with joint arthroplasty remain. The most common reason for failure of arthroplasty is aseptic loosening (Borroff et al. 2014; National Joint Registry for England et al. 2013). This is mediated by the reaction of macrophages to wear debris (Jacobs et al. 2001; Goodman et al. 2013). Other complications are established with joint replacement; periprosthetic infection is perhaps the greatest concern for joint arthroplasty and continues to generate clinical problems (Moore et al. 2015) and extensive costs (Hebert et al. 1996; Kurtz et al. 2012; Waddell et al. 2016). Periprosthetic fracture (Masri et al. 2004; Morrison et al. 2013; Kelley 1994) and dislocation (Dargel et al. 2014; Yuan & Shih 1999) provide separate management challenges. The search to improve longevity has led to interest, research and use of alternative bearing surfaces. Metal on metal articulations have mixed results; small diameter metal on metal hip replacement have some good outcomes (Delaunay 2006; Tardy et al. 2015) and some results showing slightly inferior survivorship (Tardy et al. 2015). Large diameter metal on metal hip surgery, both resurfacing and conventional replacement have fallen dramatically in the face of reactions to metal debris (Langton, Jameson, et al. 2011; Junnila et al. 2015; Langton, Joyce, et al. 2011; Lainiala et al. 2014; Langton et al. 2009). The use of ceramic to prolong the longevity of a joint replacement is still attractive. Currently small amounts of evidence are in favour of this approach particularly with regard to lower rates of wear (Wroblewski 2005; Hamadouche et al. 2002). Real time benefits to the patient are not as clearly seen (Jameson et al. 2015) and data from joint registry follow up has yet to show a benefit to the patients as currently the use of ceramic bearing coupled with polyethylene is associated with a higher revision rate across the

Australian and New Zealand joint registries (AOA 2015) (Rothwell et al. 2014). The results are far from certain though with the Australian registry showing ceramics as a higher revision bearing across the board (AOA 2015) the New Zealand registry shows the best performing bearing couple is ceramic on ceramic (Rothwell et al. 2014)

There has been some progress in tissue engineering with scaffolds for cartilage regeneration (Clatworthy 2011; Pietschmann et al. 2009; Behrens et al. 2006). However these technologies are only applied at this time for cartilage injury, the results if used for arthritis are uncertain at best. Silicated bone graft substitute is a positive step (Hing et al. 2006; Porter et al. 2004; Jenis & Banco 2010) much work is still to be done before this technology will be ready to provide structural reconstruction for arthritic deformity. While a biological reconstruction for arthritis remains a future aim, replacement arthroplasty seems as though it will be the mainstay of treatment for the foreseeable future. Improvement on current biomaterials may allow patient benefit through the development of longer lasting implants with excellent wear characteristics and enhanced stability at the bone implant junction.

7.2 Is it reasonable to make judgements on the bone implant interface based on an in vitro model and cell behaviour?

In a summary of work Davies (Davies 1996) outlines the development of research into the bone implant interface. In addition to provision of a comprehensive review of the development of cell culture methods, examination techniques and pertinent information about proteins and cell behaviour he illustrates several worthy questions.

‘...how do cells make bone on foreign surfaces? What is the differentiation state of the osteogenic cells that colonize an implant? How do these cells adhere to the implant surface in a manner that permits maturation of the osteoblastic phenotype? Is there an identifiable sequence of matrix formation events that characterizes this bone formation at an interface? Is this sequence of events the same that occurs in normal bone tissue, or does it differ as a result of the presence of a non-biological material? In other words, can the sequence of matrix formation events on implant surfaces be affected

in either subtle or overt ways by the surface properties of the material?' (Davies 1996)

The work performed over the past twenty years in cell biology and tissue culture has provided much of the information required to answer these questions and is too great to reference. The conclusion drawn in the abstract justifies the use of the in vitro model as many of the processes evidenced from work in vivo are seen in vitro, additionally in vitro assessment allows for a greater understanding of the process. The experimental work performed for this research has all been gravity dependent, cells placed onto a material. This is not the case for orthopaedic implants in vivo, nevertheless implants impacted into bone will have cell contact and the surface is a possible site for controlled reaction.

7.3 Rationale for research choices

My focus was to investigate the in vitro effects of modifying the surface of ceramic implants as the first step to engineering successful uncemented ceramic implants. Ceramic is an attractive bearing surface for joint replacement. Although it carries some risks not present with polyethylene and metal bearings the fracture rate has been significantly reduced by improvements in the material (Massin et al. 2014) and the possibility of a long lasting bearing system was appealing to me. Uncemented ceramic has not been as successful as other uncemented materials in the hip, neither has it enjoyed great clinical success in other joint arthroplasty (Dawson-Bowling et al. 2012; Kaszap et al. 2012; Hansen & Vainorius 2008; Barwick & Talkhani 2008). Topographic modulation of cell differentiation (McMurray et al. 2011; Tsimbouri et al. 2014; Tsimbouri et al. 2012; Biggs & Dalby 2010; Dalby et al. 2014; Dalby, Gadegaard, G Curtis, et al. 2007; C. Wilkinson et al. 2002) and composite ceramic implants have not been successful in clinical practice (D. S. Hwang et al. 2007; Hasegawa et al. 2003; Viste et al. 2012), I therefore pursued an all ceramic material with topographic features.

7.4 Positive results

Polycaprolactone is readily available and provided a sensible material as a testing ground for a suitable topography to transfer to ceramic. It has a proven history in cell culture (Rohner et al. 2003; Woodruff & Hutmacher 2009; Azevedo

et al. 2003). It is also a suitable material to reproduce small scale patterns (Curtis et al. 2004; Gadegaard & McCloy 2007). Successful reproduction of three micro scale topographies was verified in PCL (4.2.1). Qualitative assessment of focal adhesions, intracellular cytoskeletal tension and OPN protein expression all indicated a positive result for cells cultured on 30 μm circular pitted substrates. Quantitative analysis of alizarin red staining confirmed the impression provided by the focal adhesions and protein expression. The relevance of these results has been discussed in 3.4. To summarise, Focal Adhesions are mechanosensitive contact points to the extracellular matrix (or substrate) (Wozniak et al. 2004). These contact points are able to influence cell behaviour and differentiation (Biggs & Dalby 2010; Teo et al. 2013). Large focal adhesions are a positive indicator of intracellular tension and this in turn infers differentiation to a more osteogenic phenotype.

The presence of larger focal adhesions on the patterned ZTA is encouraging. With specific reference to the presence of large adhesions Figure 5-7 shows the distribution of focal adhesions by size, although all the samples demonstrate a left shift (around 1.8 μm size) the tail into large focal adhesions is much greater for the 40 μm with some reaching over 10 μm , although intracellular cytoskeleton fibres would be an excellent affirmation the presence of these very large focal adhesions is a positive result.

The materials characterisation chapter shows that it is possible to reproduce topography at the micro-scale in alumina zirconia composite ceramic - as shown by AFM and SEM, Figure 4-3 to Figure 4-13. The general pattern is reproduced with some inaccuracies. Shrinkage of ceramic during sintering is a known phenomenon. The results from the SEM images Figure 4-11 show shrinkage between 15% and 30% for these samples. Preparation of masks to account for this expected shrinkage should allow for the production of a more accurate final topography

The overall results from 5.3 are generally positive. OPN production across a range of measured outcomes was more positive on the patterned ceramic surface than on the control. The results for OCN were less strongly positive. OCN is produced only by osteoblasts (Neve et al. 2013; Ducky 2011), it does play a

slightly broader role however with effects on blood insulin levels, glucose tolerance, and energy expenditure (Ducy 2011). There may be significance to the presence of larger OCN particles on the 30 μm and 40 μm substrates it seems more likely the total level of OCN is more reflective of osteoblast activity. For this experiment the total OCN presence was greatest on the control samples.

The results from PCR show a trend to upregulation of favourable genes. RUNX2 has been referred to as the master gene for osteogenic bone formation (Lian et al. 2006) it is expressed early in the differentiation of MSCs, it may play a role in the transition from proliferation to differentiation and it is involved in many of the stages of differentiation from MSC to osteoblast (Lian et al. 2006). Figure 5-24 show up regulation, even if hampered by excessive variation in the samples this indicates activation of one of the established genes in osteogenesis.

The metabolomics data shows clear material and topographic induced differences in cell behaviour. Energy metabolism is certainly greater on patterned surfaces and on ceramic rather than plastic 6.3.1 and 6.3.2. Understanding the metabolomics of MSCs and osteoprogenitor cells as they either maintain a pluripotent capacity or differentiate is beginning (Tsimbouri et al. 2012) but is far from completely understood. There is certainly the possibility that these metabolomics results are all strongly positive for osteogenic differentiation, it is my judgement that there is likely to be a small positive osteogenic effect indicated by the metabolomics, particularly shown by the topographical effect within materials 6.3.2.3, 6.3.2.4 and that ERK is integral to this effect 6.4.2. To say the material effect seen in the metabolomics 6.3.2.1 and 6.3.2.2 is solely positive towards the desired differentiation is unreasonable, however it may be partially correct. I have already explored the differences in the surfaces presented to the cells (4.3) it may be that part of the material difference in this part of the experiment may be due to an increase in the topographic landscape presented by the control ZTA substrates, this may be a positive osteogenic driver. Alternatively the increased surface area may drive the cells to more activity, whether that activity is proliferation, maintenance or differentiation is for further study.

7.5 Other results

Edge detection is an important cue for cells responding to topography (Andersson, Olsson, et al. 2003). The results from 4.2.3 show that the edge feature of the created pit was not sharp. It was gently rounded, and of variable depth. Exactly how important this feature is as part of the topography is uncertain. Previous work indicating the important of edge features has involved step cues (P. Clark et al. 1987) and contact guidance in grooved substrata (P. Clark et al. 1990). The precise clarity of the feature edge is not confirmed for a circular feature; the premise has been carried from the previous work. In this regard the creation of the topography was less in the ZTA than in the PCL

Comparison of the figures from 4.2.1, 4.2.3.3 illustrate well the differences in noise aspect ratio between PCL and ZTA. In Figure 4-1 the embossed features stand out clearly against the background of the material. Even through the cell sheet it is apparent that the material is significantly patterned only by the intended topography. The ZTA ceramic presents an altogether different landscape to the cells. Figure 4-9 shows the grain structure of the material, with a rise to the apex of each grain and the fall to each grain boundary the background noise presented by the material is certainly loud compared to PCL. The high noise to aspect ratio is also seen in the results from the AFM, Figures 4.5 to 4.8, in addition to the presence of the grains, the three dimensional nature of the images from the AFM show that the depth of the features are varied and that some of the 'islands' above the pits are likely to present as a significant feature to the cell. This is inherent to the grain structure of ceramic. Grain size has been significantly reduced over the generations of ceramic and this has contributed to an increase in material toughness and surface hardness (Krell & Blank 1995; Klecka 2007) but will remain an integral feature of the material

The AFM images are clearly not perfectly representing the surface of the ZTA (given the discrepancies between Figure 4-13 and Figure 4-6 (specific reference to the right hand render of a 40 μm pit). However it seems improbable that the material defects seen in Figure 4-7 and Figure 4-8 can be attributed to the method of data capture. This type of material defect will affect the bulk properties of any implant and is therefore unlikely to be of realistic concern in

vivo, however it may still have affected the results of the experiment. Further material defects are seen in the images captured by the SEM (Figure 4-10 and Figure 4-12). The ridges and valleys in Figure 4 -12 are sufficient to act as contact guidance cues for the edges of cells and the defects in Figure 4 - 14 will present as a separate void for the cells. This type of material defect will affect the bulk properties of any implant and is therefore unlikely to be of realistic concern in vivo, however it may still have affected the results of the experiment.

The standard deviations for the PCR array were very high; this made it difficult to draw significant conclusions from the results. However the overall trend was positive to upregulation of genes involved in osteogenesis, this provides some encouragement.

It was difficult to process the results of the OPN and OCN staining of the ZTA substrates. The collection of particle data from the images followed by image processing has allowed some meaningful (and mostly encouraging) conclusions to be interpreted. On considering this I would, in future, assess the production of these proteins by non image based modalities. Perhaps quantification of total amount of protein would be possible via colorimetric analysis of the cells separated from the substrate. This clearly negates any morphological assessment of the cell, but this was not a useful modality in any case.

It was with some interest I noted the difference in Alizarin red deposition between the PCL and ZTA. Where the alizarin red results were strongest for the PCL, there were no demonstrable differences in the ZTA. Nor did qualitative assessment of the cell position or nodule formation relative to the features shed any light on the relationship between cell behaviour and the position of the topography.

7.6 Weaknesses

There are several weaknesses to this research. The initial experiment was performed with a cell line, these cells do not have the same population as the primary extracted human cells used for the rest of the experiments, it is possible that this explains the difference in result seen when comparing the PCL

to the ceramic substrates. For all the experiments the diameters of the features have been intended to be identical - that is the production of embossing dies has been designed to produce the same features. The reproduction of pattern in the different materials has not been identical, some change in size was seen with the PCL but a much greater decrease is seen for the ceramic, along with a greater variation in the change of geometry. These differences make direct comparison of the two materials more difficult.

The variability of ceramic material was not limited to the change in feature size and pitch; it is also seen in the surface roughness. This is due in part to the grain structure but is also due to the different handling characteristics of ceramic during embossing. Several obvious defects are seen in the material surface, Figure 4-7 and Figure 4-8 show flaws in the surface detected by AFM; Figure 4-10 shows a repeated defect across the entire sample for the 30 μm patterned sample, this may be a feature caused by releasing the shim from the green tape. Figure 4-12 shows a crack in the substrate; whilst they may not survive to implant level they provide an indication of the difficulties with patterning this surface.

There are significant differences in the ability to detect and interpret protein production when comparing the PCL to the ceramic. The PCL was straightforward to image, the protein appearance was easy to isolate and interpret. This was not the case for ceramic. This has resulted in different assessment for protein production on the ceramic than for the PCL. Validation of the results from the PCL to the ceramic is very difficult. Additionally quantifying the protein production on the ceramic was very difficult, the background fluorescence has hampered the detection of some protein expression. Provided this level of interference has been consistent across all the experiments the comparison of different samples within the ceramic should not create bias. It is entirely possible that only proteins over a certain size or intensity are detected on the ceramic, this could easily confound the results if one ceramic had a high level of smaller or less intensely stained proteins.

7.7 Future work

ZTA ceramic is a suitable material for creation of controlled topography, it is possible to produce patterns within the scale microns. It may not be possible to induce a controlled topography at the nanoscale secondary to the granular structure of the material. Whilst the results discussed above have shown a positive effect of topography it may be that the optimal geometry of that feature has not yet been uncovered. The work for this thesis was performed with an ordered topography, there is work in the field of nanotopography to show that cells also respond to semi-ordered and random topographical features (Dalby et al. 2005). This is an area that could be investigated at a microtopographical level.

In order to establish a primary stability for the implant some form of macro-scale feature is likely to be required, allowing any microtopography to act as a secondary physical feature. This has previously been a threaded cup (Garcia-Cimbrelo et al. 1996), this method would not meet the modern expectations for survivorship and is unlikely to be reinstated. Some work in this field has already begun with porous graduated ceramic being produced and tested (Theelke et al. 2011). In this work pores in the green ceramic are created using organic pore forming agents in a slurry of ZTA, green machined ceramic bodies are coated with slurry prior to firing. During firing the pore inducing bodies are eradicated. The scale of the pores range from 200 μm to 500 μm (Theelke et al. 2011) making them suitable for a tertiary topography created in negative on the surface of the organic pore forming objects.

The ceramics in this research have not been fully treated in the way that modern implant ceramics are. In order to reduce fracture risk modern implants are subjected to hot isostatic pressing. Research on the material manufacture side would be essential to allow the preservation of a topography in ceramic after hot isostatic pressing had been performed.

7.8 Conclusion.

This work adds to the knowledge on topographic effects in cell behaviour and differentiation specifically as applied to zirconia alumina composite ceramic.

Micro-scale topography is reproducible in modern orthopaedic ceramic; the precise dimensions of the final topography will require adjustment of the created geometry for the embossing stage. The effect of the topography in ceramic shows a small result in several areas. The microtopography in this ceramic has not produced increased mineralisation in vitro. For microtopography in ceramic to be effective and reach manufacturing stages it is likely to be used as a tertiary level feature, that is the primary level morphology being the overall shape, secondary level features as seen in the work by Theelke et al (Theelke et al. 2011) and microtopography within the secondary level morphology as the final ongoing stimulus to produce a bioactive ceramic implant.

List of References

- Adams, J.E. et al., 2007. Outcomes of shoulder arthroplasty in Olmsted County, Minnesota: a population-based study. *Clinical Orthopaedics and Related Research*®, 455, pp.176-182.
- Adler, E., Stuchin, S.A. & Kummer, F.J., 1992. Stability of press-fit acetabular cups. *The Journal of arthroplasty*, 7(3), pp.295-301.
- Agricola, R. et al., 2013. Pincer deformity does not lead to osteoarthritis of the hip whereas acetabular dysplasia does: acetabular coverage and development of osteoarthritis in a nationwide prospective cohort study (CHECK). *Osteoarthritis and Cartilage*, 21(10), pp.1514-1521.
- Al-Hajjar, M. et al., 2013. Wear of novel ceramic-on-ceramic bearings under adverse and clinically relevant hip simulator conditions. *Journal of biomedical materials research. Part B, Applied biomaterials*, 101(8), pp.1456-1462.
- Albrektsson, T. et al., 1981. Osseointegrated titanium implants. Requirements for ensuring a long-lasting, direct bone-to-implant anchorage in man. *Acta Orthopaedica Scandinavica*, 52(2), pp.155-170.
- Aldinger, P.R. et al., 2009. Uncemented grit-blasted straight tapered titanium stems in patients younger than fifty-five years of age. Fifteen to twenty-year results. *The Journal of bone and joint surgery. American volume*, 91(6), pp.1432-1439.
- Amano, M. et al., 1996. Phosphorylation and activation of myosin by Rho-associated kinase (Rho-kinase). *The Journal of biological chemistry*, 271(34), pp.20246-20249.
- Andersson, A., Brink, J., et al., 2003. Influence of systematically varied nanoscale topography on the morphology of epithelial cells. *IEEE Transactions on Nanobioscience*, 2(2), pp.49-57.
- Andersson, A.-S., Bäckhed, F., et al., 2003. Nanoscale features influence epithelial cell morphology and cytokine production. *Biomaterials*, 24(20), pp.3427-3436.
- Andersson, A.-S., Olsson, P., et al., 2003. The effects of continuous and discontinuous groove edges on cell shape and alignment. *Experimental cell research*, 288(1), pp.177-188.
- Annaz, B. et al., 2004. An ultrastructural study of cellular response to variation in porosity in phase-pure hydroxyapatite. *Journal of microscopy*, 216(Pt 2), pp.97-109.
- Anon, 2005. *An account of a new method of treating diseases of the joints of the knee and elbow: in a letter to Mr. Percival Pott*,

- AOA, 2015. Australian Orthopaedic Association National Joint Replacement Registry. pp.1-246.
- Apple, D.J. & Sims, J., 1996. *Harold Ridley and the invention of the intraocular lens*,
- Arocho, A. et al., 2006. Validation of the 2-[DELTA][DELTA]Ct Calculation as an Alternate Method of Data Analysis for Quantitative PCR of BCR-ABL P210 Transcripts. *Diagnostic Molecular Pathology*, 15(1), p.56.
- Arthur, W.T. & Burridge, K., 2001. RhoA inactivation by p190RhoGAP regulates cell spreading and migration by promoting membrane protrusion and polarity. *Molecular biology of the cell*, 12(9), pp.2711-2720.
- Athanasiou, K.A., Niederauer, G.G. & Agrawal, C.M., 1996. Sterilization, toxicity, biocompatibility and clinical applications of polylactic acid/polyglycolic acid copolymers. *Biomaterials*, 17(2), pp.93-102.
- Atkins, G.J., 2011. Role of polyethylene particles in peri-prosthetic osteolysis: A review. *World Journal of Orthopedics*, 2(10), p.93.
- Attwell, S., Roskelley, C. & Dedhar, S., 2000. The integrin-linked kinase (ILK) suppresses anoikis. *Oncogene*, 19(33), pp.3811-3815.
- Aubin, J.E. & Triffitt, J.T., 2002. Principles of Bone Biology, Two-Volume Set - Google Books.
- Azevedo, M.C. et al., 2003. Development and properties of polycaprolactone/hydroxyapatite composite biomaterials - Springer. *Journal of Materials Science: Materials in Medicine*, 14(2), pp.103-107.
- Ballestrem, C. et al., 2001. Marching at the front and dragging behind: differential alphaVbeta3-integrin turnover regulates focal adhesion behavior. *The Journal of cell biology*, 155(7), pp.1319-1332.
- Baltimore, D., 1970. RNA-dependent DNA polymerase in virions of RNA tumour viruses. *Nature*, 226(5252), pp.1209-1211.
- Bartlett, W., 2005. Autologous chondrocyte implantation versus matrix-induced autologous chondrocyte implantation for osteochondral defects of the knee: A PROSPECTIVE, RANDOMISED STUDY. *The Journal of bone and joint surgery. British volume*, 87-B(5), pp.640-645.
- Barwick, T.W. & Talkhani, I.S., 2008. The MOJE total joint arthroplasty for 1st metatarso-phalangeal osteoarthritis: a short-term retrospective outcome study. *Foot (Edinburgh, Scotland)*, 18(3), pp.150-155.
- Batta, V. et al., 2014. Uncemented, custom-made, hydroxyapatite-coated collared distal femoral endoprostheses: up to 18 years' follow-up. *The Bone & Joint Journal*, 96-B(2), pp.263-269.
- BECKER, A.J., McCULLOCH, E.A. & TILL, J.E., 1963. Cytological demonstration of the clonal nature of spleen colonies derived from transplanted mouse marrow cells. *Nature*, 197, pp.452-454.

- Behrens, P. et al., 2006. Matrix-associated autologous chondrocyte transplantation/implantation (MACT/MACI)—5-year follow-up. *The Knee*, 13(3), pp.194-202.
- Bergsma, E.J. et al., 1993. Foreign body reactions to resorbable poly(L-lactide) bone plates and screws used for the fixation of unstable zygomatic fractures. *Journal of Oral and Maxillofacial Surgery*, 51(6), pp.666-670.
- Bershadsky, A.D. et al., 2006. Assembly and mechanosensory function of focal adhesions: experiments and models. *European journal of cell biology*, 85(3-4), pp.165-173.
- Best, S.M. et al., 2008. The Osteogenic Behaviour of Silicon Substituted Hydroxyapatite. *Key Engineering Materials*, 361-363, pp.985-988.
- Betancourt, T. & Brannon-Peppas, L., 2006. Micro- and nanofabrication methods in nanotechnological medical and pharmaceutical devices. *International journal of nanomedicine*, 1(4), pp.483-495.
- Biggs, M. & Dalby, M.J., 2010. Focal adhesions in osteoneogenesis. *Proceedings of the Institution of Mechanical Engineers. Part H, Journal of engineering in medicine*, 224(12), pp.1441-1453.
- Binnig, G., Quate, C.F. & Gerber, C., 1986. Atomic force microscope. *Physical review letters*, 56(9), p.930.
- Bobyn, J.D. et al., 1999. Characteristics of bone ingrowth and interface mechanics of a new porous tantalum biomaterial. *The Journal of bone and joint surgery. British volume*, 81(5), pp.907-914.
- Boccaccini, A.R., Blaker, J.J. & Maquet, V., 2005. Biodegradable and bioactive polymer/Bioglass® composite foams for tissue engineering scaffolds. *Materials Science Forum*, 494, pp.499-506.
- Boehler, M. et al., 1994. Long-term results of uncemented alumina acetabular implants. *The Journal of bone and joint surgery. British volume*, 76(1), pp.53-59.
- Borroff, M. et al., 2014. *National Joint Registry 11th Annual Report 2014*,
- Boskey, A.L. et al., 2012. Post-translational modification of osteopontin: effects on in vitro hydroxyapatite formation and growth. *Biochemical and biophysical research communications*, 419(2), pp.333-338.
- Bottlang, M., 2010. Effects of Construct Stiffness on Healing of Fractures Stabilized with Locking Plates. *The Journal of Bone and Joint Surgery*, 92(Supplement_2), p.12.
- Boutin, P., 1972. [Total arthroplasty of the hip by fritted aluminum prosthesis. Experimental study and 1st clinical applications]. *Revue de chirurgie orthopedique et reparatrice de l'appareil moteur*, 58(3), pp.229-246.
- Boutin, P., 2014. Total arthroplasty of the hip by fritted alumina prosthesis. Experimental study and 1st clinical applications. *Orthopaedics &*

- Traumatology: Surgery & Research*, 100(1), pp.15-21.
- Boutin, P. et al., 1988. The use of dense alumina-alumina ceramic combination in total hip replacement. *Journal of Biomedical Materials Research Part A*, 22(12), pp.1203-1232.
- Böstman, O. et al., 1993. Absorbable polyglycolide pins in internal fixation of fractures in children. *Journal of Pediatric Orthopaedics*, 13(2), pp.242-245.
- Böstman, O. et al., 1990. Foreign-body reactions to fracture fixation implants of biodegradable synthetic polymers. *The Journal of bone and joint surgery. British volume*, 72(4), pp.592-596.
- Böstman, O. et al., 1992. Foreign-body reactions to polyglycolide screws. Observations in 24/216 malleolar fracture cases. *Acta Orthopaedica Scandinavica*, 63(2), pp.173-176.
- Böstman, O.M., 1992. Intense granulomatous inflammatory lesions associated with absorbable internal fixation devices made of polyglycolide in ankle fractures. *Clinical Orthopaedics and Related Research®*, (278), pp.193-199.
- Böstman, O.M., 1991. Osteolytic changes accompanying degradation of absorbable fracture fixation implants. *The Journal of bone and joint surgery. British volume*, 73(4), pp.679-682.
- Brand, R.A., Mont, M.A. & manring, M.M., 2011. Biographical Sketch. *Clinical Orthopaedics and Related Research®*, 469(6), pp.1528-1535.
- Britland, S. et al., 1996. Synergistic and hierarchical adhesive and topographic guidance of BHK cells. *Experimental cell research*, 228(2), pp.313-325.
- Brunski, J.B.J., 1999. In vivo bone response to biomechanical loading at the bone/dental-implant interface. *Advances in Dental Research*, 13, pp.99-119.
- Bunnik, H.M., 1986. Ultrapure water in the electronics industry. *Water Science & Technology*.
- Carvallo, L. et al., 2008. 1alpha,25-dihydroxy vitamin D3-enhanced expression of the osteocalcin gene involves increased promoter occupancy of basal transcription regulators and gradual recruitment of the 1alpha,25-dihydroxy vitamin D3 receptor-SRC-1 coactivator complex. *Journal of cellular physiology*, 214(3), pp.740-749.
- Cassidy, C. et al., 2003. Norian SRS cement compared with conventional fixation in distal radial fractures. A randomized study. *The Journal of Bone and Joint Surgery*, 85-A(11), pp.2127-2137.
- Chambers, T.J., 1985. The pathobiology of the osteoclast. *Journal of clinical pathology*, 38(3), pp.241-252.
- CHARNLEY, J., 1971. Present status of total hip replacement. *Annals of the Rheumatic Diseases*, 30(6), pp.560-564.
- CHARNLEY, J., 1964. THE BONDING OF PROSTHESES TO BONE BY CEMENT. *The*

Journal of bone and joint surgery. British volume, 46, pp.518-529.

- CHARNLEY, J., 1972. The long-term results of low-friction arthroplasty of the hip performed as a primary intervention. *The Journal of bone and joint surgery. British volume*, 54(1), pp.61-76.
- Charnley, J., 2010. The classic: The bonding of prostheses to bone by cement. 1964. *Clinical Orthopaedics and Related Research®*, 468(12), pp.3149-3159.
- Chen, J., Chu, B. & Hsiao, B.S., 2006. Mineralization of hydroxyapatite in electrospun nanofibrous poly (L-lactic acid) scaffolds. *Journal of Biomedical Materials Research Part A*, 79A(2), pp.307-317.
- Chen, Q. et al., 2014. An osteopontin-integrin interaction plays a critical role in directing adipogenesis and osteogenesis by mesenchymal stem cells. *Stem cells (Dayton, Ohio)*, 32(2), pp.327-337.
- Chevillotte, C. et al., 2012. Retrieval analysis of squeaking ceramic implants: are there related specific features? *Orthopaedics & Traumatology: Surgery & Research*, 98(3), pp.281-287.
- Choi, S.T. et al., 2008. Osteopontin might be involved in bone remodelling rather than in inflammation in ankylosing spondylitis. *Rheumatology (Oxford, England)*, 47(12), pp.1775-1779.
- Christie, M.J., 2002. Clinical applications of Trabecular Metal. *American journal of orthopedics (Belle Mead)*.
- Chrzanowska-Wodnicka, M. & Burrige, K., 1996. Rho-stimulated contractility drives the formation of stress fibers and focal adhesions. *The Journal of cell biology*, 133(6), pp.1403-1415.
- Cipriano, A.F. et al., 2014. Bone marrow stromal cell adhesion and morphology on micro- and sub-micropatterned titanium. *Journal of biomedical nanotechnology*, 10(4), pp.660-668.
- Clark, A.E., Pantano, C.G. & Hench, L.L., 1976. Auger Spectroscopic Analysis of Bioglass Corrosion Films. *Journal of the American Ceramic Society*, 59(1-2), pp.37-39.
- Clark, P. et al., 1987. Topographical control of cell behaviour. I. Simple step cues. *Development (Cambridge, England)*, 99(3), pp.439-448.
- Clark, P. et al., 1990. Topographical control of cell behaviour: II. Multiple grooved substrata. *Development (Cambridge, England)*, 108(4), pp.635-644.
- Clatworthy, M., 2011. MACI CARTILAGE TRANSPLANTATION - MEDIUM TERM RESULTS. *Journal of Bone & Joint Surgery, British Volume*, 93-B(SUPP III), pp.374-374.
- Cox, C.L. et al., 2014. Do newer-generation bioabsorbable screws become incorporated into bone at two years after ACL reconstruction with patellar tendon graft?: A cohort study. *The Journal of Bone and Joint Surgery*, 96(3), pp.244-250.

- Creek, D.J. et al., 2012. IDEOM: an Excel interface for analysis of LC-MS-based metabolomics data. *Bioinformatics (Oxford, England)*, 28(7), pp.1048-1049.
- Creek, D.J. et al., 2011. Toward global metabolomics analysis with hydrophilic interaction liquid chromatography-mass spectrometry: improved metabolite identification by retention time prediction. *Analytical Chemistry*, 83(22), pp.8703-8710.
- Crick, F., 1970. Central dogma of molecular biology. *Nature*, 227(5258), pp.561-563.
- Curtis, A.S.G. et al., 2004. Cells react to nanoscale order and symmetry in their surroundings. *IEEE Transactions on Nanobioscience*, 3(1), pp.61-65.
- Dai, Z. et al., 2007. Resveratrol enhances proliferation and osteoblastic differentiation in human mesenchymal stem cells via ER-dependent ERK1/2 activation. *Phytomedicine*, 14(12), pp.806-814.
- Dalby, M., 2002. Increasing Fibroblast Response to Materials Using Nanotopography: Morphological and Genetic Measurements of Cell Response to 13-nm-High Polymer Demixed Islands. *Experimental cell research*, 276(1), pp.1-9.
- Dalby, M., Gadegaard, N., G Curtis, A., et al., 2007. Nanotopographical Control of Human Osteoprogenitor Differentiation. *Current Stem Cell Research & Therapy*, 2(2), pp.129-138.
- Dalby, M.J. et al., 2003. Nucleus alignment and cell signaling in fibroblasts: response to a micro-grooved topography. *Experimental cell research*, 284(2), pp.272-280.
- Dalby, M.J. et al., 2006. Osteoprogenitor response to defined topographies with nanoscale depths. *Biomaterials*, 27(8), pp.1306-1315.
- Dalby, M.J. et al., 2005. Osteoprogenitor response to semi-ordered and random nanotopographies. *Biomaterials*, 27(15), pp.2980-2987.
- Dalby, M.J., Gadegaard, N. & Oreffo, R.O.C., 2014. Harnessing nanotopography and integrin-matrix interactions to influence stem cell fate. *Nature materials*, 13(6), pp.558-569.
- Dalby, M.J., Gadegaard, N., Tare, R., et al., 2007. The control of human mesenchymal cell differentiation using nanoscale symmetry and disorder. *Nature materials*, 6(12), pp.997-1003.
- Dalby, M.J., Riehle, M.O., Johnstone, H., Affrossman, S. & Curtis, A.S.G., 2002a. In vitro reaction of endothelial cells to polymer demixed nanotopography. *Biomaterials*, 23(14), pp.2945-2954.
- Dalby, M.J., Riehle, M.O., Johnstone, H.J.H., Affrossman, S. & Curtis, A.S.G., 2002b. Polymer-Demixed Nanotopography: Control of Fibroblast Spreading and Proliferation. *Tissue engineering*, 8(6), pp.1099-1108.
- Dargel, J. et al., 2014. Dislocation following total hip replacement. *Deutsches*

Ärzteblatt international, 111(51-52), pp.884-890.

- Davies, J.E., 1996. In vitro modeling of the bone/implant interface. *The Anatomical Record*, 245(2), pp.426-445.
- Dawson-Bowling, S. et al., 2012. MOJE ceramic metatarsophalangeal arthroplasty: disappointing clinical results at two to eight years. *Foot & Ankle International*, 33(7), pp.560-564.
- de Groot, K., Wolke, J.G. & Jansen, J.A., 1998. Calcium phosphate coatings for medical implants. *Proceedings of the Institution of Mechanical Engineers. Part H, Journal of engineering in medicine*, 212(2), pp.137-147.
- de Peppo, G.M. et al., 2014. Osteogenic response of human mesenchymal stem cells to well-defined nanoscale topography in vitro. *International journal of nanomedicine*, 9, pp.2499-2515.
- Delaunay, C., 2006. METASUL BEARINGS OF FIRST AND SECOND GENERATION DESIGNS IN PRIMARY THA. *Orthopaedic Proceedings*, 88-B(SUPP I), pp.76-76.
- Dodds, R.A. et al., 1995. Human osteoclasts, not osteoblasts, deposit osteopontin onto resorption surfaces: an in vitro and ex vivo study of remodeling bone. *Journal of Bone and Mineral Research*, 10(11), pp.1666-1680.
- Dorlot, J.M., 1992. Long-term effects of alumina components in total hip prostheses. *Clinical Orthopaedics and Related Research*®, (282), pp.47-52.
- Ducheyne, P. et al., 1977. Influence of a functional dynamic loading on bone ingrowth into surface pores of orthopedic implants. *Journal of Biomedical Materials Research Part A*, 11(6), pp.811-838.
- Ducy, P., 2011. The role of osteocalcin in the endocrine cross-talk between bone remodelling and energy metabolism. *Diabetologia*, 54(6), pp.1291-1297.
- Ducy, P. et al., 1999. A Cbfa1-dependent genetic pathway controls bone formation beyond embryonic development. *Genes & development*, 13(8), pp.1025-1036.
- Ducy, P. et al., 1996. Increased bone formation in osteocalcin-deficient mice. *Nature*, 382(6590), pp.448-452.
- Dunbar, M.J., 2009. Cemented femoral fixation: the North Atlantic divide. *Orthopedics*, 32(9).
- Engh, C.A., Bobyn, J.D. & Glassman, A.H., 1987. Porous-coated hip replacement. The factors governing bone ingrowth, stress shielding, and clinical results. *The Journal of bone and joint surgery. British volume*, 69(1), pp.45-55.
- Engler, A.J. et al., 2006. Matrix Elasticity Directs Stem Cell Lineage Specification. *Cell*, 126(4), pp.677-689.
- Epinette, J.-A. & Manley, M.T., 2008. Uncemented stems in hip replacement--

- hydroxyapatite or plain porous: does it matter? Based on a prospective study of HA Omnifit stems at 15-years minimum follow-up. *Hip international : the journal of clinical and experimental research on hip pathology and therapy*, 18(2), pp.69-74.
- Erdil, M. et al., 2013. Comparison of arthrodesis, resurfacing hemiarthroplasty, and total joint replacement in the treatment of advanced hallux rigidus. *The Journal of foot and ankle surgery : official publication of the American College of Foot and Ankle Surgeons*, 52(5), pp.588-593.
- Erkocak, O.F. et al., 2013. Short-term functional outcomes of first metatarsophalangeal total joint replacement for hallux rigidus. *Foot & ankle international / American Orthopaedic Foot and Ankle Society [and] Swiss Foot and Ankle Society*, 34(11), pp.1569-1579.
- Fink, B. et al., 2002. Monitoring of bone formation during distraction osteogenesis via osteocalcin: a time sequence study in dogs. *Journal of Orthopaedic Science*, 7(5), pp.557-561.
- Freemont, A.J., 1993. Basic bone cell biology. *International journal of experimental pathology*, 74(4), p.411.
- Friedenstein, A.J., 1995. Marrow stromal fibroblasts. *Calcified tissue international*, 56 Suppl 1, pp.S17-S17.
- Friedenstein, A.J., 1976. Precursor Cells of Mechanocytes. In *International review of cytology*. International Review of Cytology. Elsevier, pp. 327-359.
- Friedenstein, A.J., Piatetzky-Shapiro, I.I. & Petrakova, K.V., 1966. Osteogenesis in transplants of bone marrow cells. *Journal of embryology and experimental morphology*, 16(3), pp.381-390.
- Furlong, R.J. & Osborn, J.F., 1991. Fixation of hip prostheses by hydroxyapatite ceramic coatings. *The Journal of bone and joint surgery. British volume*, 73(5), pp.741-745.
- Gadegaard, N. & McCloy, D., 2007. Direct stamp fabrication for NIL and hot embossing using HSQ. *Microelectronic Engineering*, 84(12), pp.2785-2789.
- Gadegaard, N. et al., 2003. Arrays of nano-dots for cellular engineering. *Microelectronic Engineering*, 67-68, pp.162-168.
- Galvin, A.L.A. et al., 2010. Wear and creep of highly crosslinked polyethylene against cobalt chrome and ceramic femoral heads. *Proceedings of the Institution of Mechanical Engineers. Part H, Journal of engineering in medicine*, 224(10), pp.1175-1183.
- Garcia-Cimbrelo, E. et al., 1996. Mittelmeier ceramic-ceramic prosthesis after 10 years. *The Journal of arthroplasty*, 11(7), pp.773-781. Available at: <http://eutils.ncbi.nlm.nih.gov/entrez/eutils/elink.fcgi?dbfrom=pubmed&id=8934316&retmode=ref&cmd=prlinks>.
- Garlotta, D., 2001. A literature review of poly (lactic acid). *Journal of Polymers and the Environment*, 9(2), pp.63-86.

- Ge, C. et al., 2007. Critical role of the extracellular signal-regulated kinase-MAPK pathway in osteoblast differentiation and skeletal development. *The Journal of cell biology*, 176(5), pp.709-718.
- George, L.K., Ruiz, D. & Sloan, F.A., 2008. The effects of total knee arthroplasty on physical functioning in the older population. *Arthritis & Rheumatism*, 58(10), pp.3166-3171.
- Gheorghiu, D., Peter, V. & Lynch, M., 2010. Living history in current orthopaedic hip surgery: intrapelvic teflon granuloma after total hip replacement. *Acta orthopaedica Belgica*, 76(1), pp.129-131.
- Gillespie, G.N. & Porteous, A.J., 2007. Obesity and knee arthroplasty. *The Knee*, 14(2), pp.81-86.
- Girdlestone, G.R., 2008. Acute pyogenic arthritis of the hip: an operation giving free access and effective drainage. *Clinical Orthopaedics and Related Research®*, 466(2), pp.258-263.
- Gluck, T., 2011. *Report on the positive results obtained by the modern surgical experiment regarding the suture and replacement of defects of superior tissue, as well as the utilization of re-absorbable and living tamponade in surgery. 1891,*
- González-García, C. et al., 2010. Effect of nanoscale topography on fibronectin adsorption, focal adhesion size and matrix organisation. *Colloids and Surfaces B: Biointerfaces*, 77(2), pp.181-190.
- Goodman, S.B., Gibon, E. & Yao, Z., 2013. The basic science of periprosthetic osteolysis. *Instructional course lectures*, 62, pp.201-206.
- Gori, F. et al., 2000. The expression of osteoprotegerin and RANK ligand and the support of osteoclast formation by stromal-osteoblast lineage cells is developmentally regulated. *Endocrinology*, 141(12), pp.4768-4776.
- Goto, K. et al., 2005. Bioactive bone cements containing nano-sized titania particles for use as bone substitutes. *Biomaterials*, 26(33), pp.6496-6505.
- Goyenvalle, E. et al., 2003. Bilayered calcium phosphate coating to promote osseointegration of a femoral stem prosthesis. *Journal of Materials Science: Materials in Medicine*, 14(3), pp.219-227.
- Grigoriou, V. et al., 2005. Apoptosis and survival of osteoblast-like cells are regulated by surface attachment. *The Journal of biological chemistry*, 280(3), pp.1733-1739.
- Griss, P. & Heimke, G., 1981. Five years experience with ceramic-metal-composite hip endoprostheses. I. clinical evaluation. *Archives of orthopaedic and trauma surgery*, 98(3), pp.157-164.
- Guglielmi, P.O. et al., 2015. Microstructure and flexural properties of multilayered fiber-reinforced oxide composites fabricated by a novel lamination route. *Ceramics international*, 41(6), pp.7836-7846.

- Guilleminet, M. & Judet, R., 2014. Acrylic prostheses in surgery of the hip (1st report by R. Judet). *Orthopaedics & Traumatology: Surgery & Research*, 100(1), pp.5-14.
- HABOUSH, E.J., 1953. A new operation for arthroplasty of the hip based on biomechanics, photoelasticity, fast-setting dental acrylic, and other considerations. *Bulletin of the Hospital for Joint Diseases*, 14(2), pp.242-277.
- Hamadouche, M. et al., 2002. Alumina-on-alumina total hip arthroplasty: a minimum 18.5-year follow-up study. *The Journal of Bone and Joint Surgery*, 84-A(1), pp.69-77.
- Hamamura, K., Jiang, C. & Yokota, H., 2010. ECM-dependent mRNA expression profiles and phosphorylation patterns of p130Cas, FAK, ERK and p38 MAPK of osteoblast-like cells. *Cell Biology International*, 34(10), pp.1005-1012.
- Hansen, T.B. & Vainorius, D., 2008. High loosening rate of the Moje Acamo prosthesis for treating osteoarthritis of the trapeziometacarpal joint. *The Journal of hand surgery, European volume*, 33(5), pp.571-574.
- Harris, W.H., 1994. Osteolysis and particle disease in hip replacement. A review. *Acta Orthopaedica Scandinavica*, 65(1), pp.113-123.
- Hasegawa, M. et al., 2003. Ceramic acetabular liner fracture in total hip arthroplasty with a ceramic sandwich cup. *The Journal of arthroplasty*, 18(5), pp.658-661.
- Hatton, A. et al., 2002. Alumina-alumina artificial hip joints. Part I: a histological analysis and characterisation of wear debris by laser capture microdissection of tissues retrieved at revision. *Biomaterials*, 23(16), pp.3429-3440.
- Hatton, A. et al., 2003. Effects of clinically relevant alumina ceramic wear particles on TNF- α production by human peripheral blood mononuclear phagocytes. *Biomaterials*, 24(7), pp.1193-1204.
- Hebert, C.K. et al., 1996. Cost of Treating an Infected Total Knee Replacement. *Clinical Orthopaedics and Related Research*®, 331, p.140.
- Heikkilä, J.T. et al., 2011. Bioactive glass granules: a suitable bone substitute material in the operative treatment of depressed lateral tibial plateau fractures: a prospective, randomized 1 year follow-up study. *Journal of Materials Science: Materials in Medicine*, 22(4), pp.1073-1080.
- Hench, L.L., 1991. Bioceramics: from concept to clinic. *Journal of the American Ceramic Society*, 74(7), pp.1487-1510.
- Hench, L.L., 2006. The story of Bioglass. *Journal of Materials Science: Materials in Medicine*, 17(11), pp.967-978.
- Hench, L.L. & Thompson, I., 2010. Twenty-first century challenges for biomaterials. *Journal of The Royal Society Interface*, 7 Suppl 4, pp.S379-91.

- Hench, L.L. & Wilson, J., 1984. Surface-active biomaterials. *Science (New York, N.Y.)*, 226(4675), pp.630-636.
- Hernigou, P., 2014. Smith-Petersen and early development of hip arthroplasty. *International Orthopaedics*, 38(1), pp.193-198.
- Hing, K.A. et al., 2006. Effect of silicon level on rate, quality and progression of bone healing within silicate-substituted porous hydroxyapatite scaffolds. *Biomaterials*, 27(29), pp.5014-5026.
- Hock, J.M. et al., 2001. Osteoblast Apoptosis and Bone Turnover. *Journal of Bone and Mineral Research*, 16(6), pp.975-984.
- Hock, J.M., Fitzpatrick, L.A. & Bilezikian, J.P., 2002. [CITATION][C]. *Principles of bone biology*.
- Hook, S. et al., 2006. The Exeter Universal stem: a minimum ten-year review from an independent centre. *The Journal of bone and joint surgery. British volume*, 88(12), pp.1584-1590.
- Hope, P.G. et al., 1991. Biodegradable pin fixation of elbow fractures in children. A randomised trial. *The Journal of bone and joint surgery. British volume*, 73(6), pp.965-968.
- Howie, D.W., 1990. Tissue response in relation to type of wear particles around failed hip arthroplasties. *The Journal of arthroplasty*.
- Hui, C. et al., 2007. Incidence of intramedullary nail removal after femoral shaft fracture healing. *Canadian journal of surgery. Journal canadien de chirurgie*, 50(1), pp.13-18.
- Hulbert, S.F. et al., 1982. History of bioceramics. *Ceramics international*, 8(4), pp.131-140.
- Hulbert, S.F. et al., 1970. Potential of ceramic materials as permanently implantable skeletal prostheses. *Journal of Biomedical Materials Research Part A*, 4(3), pp.433-456.
- Hulbert, S.F., Morrison, S.J. & Klawitter, J.J., 1972. Tissue reaction to three ceramics of porous and non-porous structures. *Journal of Biomedical Materials Research Part A*, 6(5), pp.347-374.
- Hulmes, D.J., 1992. The collagen superfamily--diverse structures and assemblies. *Essays in biochemistry*, 27, pp.49-67.
- Hulmes, D.J.S., 2002. Building collagen molecules, fibrils, and suprafibrillar structures. *Journal of structural biology*, 137(1-2), pp.2-10.
- Humphreys, F.J. & Hatherly, M., 2002. *Recrystallization and Related Annealing Phenomena* 2nd ed., Elsevier.
- Hunter, G.K., 2013. Role of osteopontin in modulation of hydroxyapatite formation. *Calcified tissue international*, 93(4), pp.348-354.
- Huo, M.H. et al., 1995. Total hip arthroplasty using the Zweymuller stem

- implanted without cement. A prospective study of consecutive patients with minimum 3-year follow-up period. *The Journal of arthroplasty*, 10(6), pp.793-799.
- Hwang, D.S., Kim, Y.M. & Lee, C.H., 2007. Alumina femoral head fracture in uncemented total hip arthroplasty with a ceramic sandwich cup. *The Journal of arthroplasty*.
- Hwang, K.-T. et al., 2012. Total hip arthroplasty using cementless grit-blasted femoral component: a minimum 10-year follow-up study. *The Journal of arthroplasty*, 27(8), pp.1554-1561.
- Illgen, R. & Rubash, H.E., 2002. The optimal fixation of the cementless acetabular component in primary total hip arthroplasty. *Journal of the American Academy of Orthopaedic Surgeons*, 10(1), pp.43-56.
- Jacobs, J.J. et al., 2001. Osteolysis: basic science. *Clinical Orthopaedics and Related Research*®, (393), pp.71-77.
- Jameson, S.S. et al., 2015. No functional benefit of larger femoral heads and alternative bearings at 6 months following primary hip replacement. *Acta orthopaedica*, 86(1), pp.32-40.
- Jazrawi, L.M. et al., 1999. Wear rates of ceramic-on-ceramic bearing surfaces in total hip implants: a 12-year follow-up study. *Journal of Arthroplasty*, 14(7), pp.781-787.
- Jenis, L.G. & Banco, R.J., 2010. Efficacy of Silicate-Substituted Calcium Phosphate Ceramic in Posterolateral Instrumented Lumbar Fusion. *Spine*, 35(20), pp.E1058-E1063.
- Johnson, J.A. & Jones, D.W., 1994. The mechanical properties of PMMA and its copolymers with ethyl methacrylate and butyl methacrylate. *Journal of materials science*, 29(4), pp.870-876.
- Jones, L.C. & Hungerford, D.S., 1987. Cement disease. *Clinical Orthopaedics and Related Research*®, (225), pp.192-206.
- Junaid, A. et al., 2007. Osteopontin localizes to the nucleus of 293 cells and associates with polo-like kinase-1. *American journal of physiology. Cell physiology*, 292(2), pp.C919-26.
- Jungmann, P.M. et al., 2013. Association of trochlear dysplasia with degenerative abnormalities in the knee: data from the Osteoarthritis Initiative. *Skeletal radiology*, 42(10), pp.1383-1392.
- Junnila, M. et al., 2015. Adverse reaction to metal debris after Birmingham hip resurfacing arthroplasty. *Acta orthopaedica*, 86(3), pp.345-350.
- Junqueira, L.C.U. & Carneiro, J., 2003. *Basic Histology* 10 ed., McGraw-Hill Professional.
- Kasemo, B. & Lausmaa, J., 1988. Biomaterial and implant surfaces: a surface science approach. *International Journal of Oral & Maxillofacial Implants*,

3(4), pp.247-259.

- Kasemo, B. & Lausmaa, J., 1994. Material-tissue interfaces: the role of surface properties and processes. *Environmental health perspectives*, 102 Suppl 5, pp.41-45.
- Kaszap, B., Daecke, W. & Jung, M., 2012. High frequency failure of the Moje thumb carpometacarpal joint arthroplasty. *The Journal of hand surgery, European volume*, 37(7), pp.610-616.
- Kelley, S.S., 1994. Periprosthetic femoral fractures. *Journal of the American Academy of Orthopaedic Surgeons*, 2(3), pp.164-172.
- Kessels, M.M. et al., 2001. Mammalian Abp1, a signal-responsive F-actin-binding protein, links the actin cytoskeleton to endocytosis via the GTPase dynamin. *The Journal of cell biology*, 153(2), pp.351-366.
- Kilian, K.A. et al., 2010. Geometric cues for directing the differentiation of mesenchymal stem cells. *Proceedings of the National Academy of Sciences*, 107(11), pp.4872-4877.
- Kim, D.I. et al., 2008. Requirement for Ras/Raf/ERK pathway in naringin-induced G1-cell-cycle arrest via p21WAF1 expression. *Carcinogenesis*, 29(9), pp.1701-1709.
- Kimura, K. et al., 1996. Regulation of Myosin Phosphatase by Rho and Rho-Associated Kinase (Rho-Kinase). *Science (New York, N.Y.)*, 273(5272), pp.245-248.
- Kirsh, G., Roffman, M. & Kligman, M., 2000. Hydroxyapatite-coated total hip replacements in patients 65 years of age and over. *Bulletin (Hospital for Joint Diseases (New York, N.Y.))*, 60(1), pp.5-9.
- Klecka, M.A., 2007. *Grain Size Dependence of Scratch Induced Damage in Alumina Ceramics*,
- Knepper-Nicolai, B. et al., 2002. Influence of osteocalcin and collagen I on the mechanical and biological properties of Biocement D. *Biomolecular engineering*, 19(2-6), pp.227-231.
- Koegler, P. et al., 2012. The influence of nanostructured materials on biointerfacial interactions. *Advanced drug delivery reviews*, 64(15), pp.1820-1839.
- Kolb, A. et al., 2012. Cementless total hip arthroplasty with the rectangular titanium Zweymüller stem: a concise follow-up, at a minimum of twenty years, of previous reports. *The Journal of bone and joint surgery. American volume*, 94(18), pp.1681-1684.
- Komori, T., 2009. Regulation of Osteoblast Differentiation by Runx2. In *Osteoimmunology: interactions of the immune and skeletal systems II*. Advances in Experimental Medicine and Biology. Boston, MA: Springer US, pp. 43-49.

- Korim, M. et al., 2014. Retrieval analysis of alumina ceramic-on-ceramic bearing couples. *Acta orthopaedica*, 85(2), pp.133-140.
- Krell, A. & Blank, P., 1995. Grain Size Dependence of Hardness in Dense Submicrometer Alumina. *Journal of the American Ceramic Society*, 78(4), pp.1118-1120.
- Kriegsheim, von, A. et al., 2006. Regulation of the Raf-MEK-ERK pathway by protein phosphatase 5. *Nature Cell Biology*, 8(9), pp.1011-1016.
- Kureishi, Y. et al., 1997. Rho-associated kinase directly induces smooth muscle contraction through myosin light chain phosphorylation. *The Journal of biological chemistry*, 272(19), pp.12257-12260.
- Kurtz, S.M. et al., 2012. Economic burden of periprosthetic joint infection in the United States. *The Journal of arthroplasty*, 27(8 Suppl), pp.61-5.e1.
- Lai, Y. et al., 2013. Effect of 3D microgroove surface topography on plasma and cellular fibronectin of human gingival fibroblasts. *Journal of Dentistry*, 41(11), pp.1109-1121.
- Lainiala, O. et al., 2014. Adverse reaction to metal debris is more common in patients following MoM total hip replacement with a 36 mm femoral head than previously thought: results from a modern MoM follow-up programme. *The Bone & Joint Journal*, 96-B(12), pp.1610-1617.
- Landy, M.M. & Walker, P.S., 1988. Wear of ultra-high-molecular-weight polyethylene components of 90 retrieved knee prostheses. *The Journal of arthroplasty*, 3, pp.S73-S85.
- Langton, D.J. et al., 2009. Early failure of metal-on-metal bearings in hip resurfacing and large-diameter total hip replacement: A CONSEQUENCE OF EXCESS WEAR. *Journal of Bone & Joint Surgery, British Volume*, 92-B(1), pp.38-46.
- Langton, D.J., Jameson, S.S., et al., 2011. Accelerating failure rate of the ASR total hip replacement. *Journal of Bone & Joint Surgery, British Volume*, 93-B(8), pp.1011-1016.
- Langton, D.J., Joyce, T.J., et al., 2011. Adverse reaction to metal debris following hip resurfacing: THE INFLUENCE OF COMPONENT TYPE, ORIENTATION AND VOLUMETRIC WEAR. *Journal of Bone & Joint Surgery, British Volume*, 93-B(2), pp.164-171.
- Lashkouskaya, L., Hornung, R. & Koltzenburg, C., 2010. Alexander J. Friedenstein (Moscow): On stromal-hematopoietic interrelationships. Maximow's ideas and modern models. In M. A. S. Moore, ed. *Wilsede Meeting 1988*. pp. 1-8. Available at: http://www.science-connections.com/books/other/On_stromal-hematopoietic_interrelationships_AJ_Friedenstein_1988_Wilsede.pdf.
- Lerouge, S. et al., 1997. Ceramic-ceramic and metal-polyethylene total hip replacements: comparison of pseudomembranes after loosening. *The Journal of bone and joint surgery. British volume*, 79(1), pp.135-139.

- Lewthwaite, S.C. et al., 2008. The Exeter Universal hip in patients 50 years or younger at 10-17 years' followup. *Clinical Orthopaedics and Related Research*®, 466(2), pp.324-331.
- Li, S. et al., 2013. Hydroxyapatite-coated femoral stems in primary total hip arthroplasty: a meta-analysis of randomized controlled trials. *International journal of surgery (London, England)*, 11(6), pp.477-482.
- Lian, J.B. et al., 2006. Networks and hubs for the transcriptional control of osteoblastogenesis. *Reviews in Endocrine & Metabolic Disorders*, 7(1-2), pp.1-16.
- Lin, C.-W. & Liao, S.-L., 2016. Long-term complications of different porous orbital implants: a 21-year review. *The British journal of ophthalmology*, epub ahead of print.
- Lin, P.L. et al., 2007. Effects of hydroxyapatite dosage on mechanical and biological behaviors of polylactic acid composite materials. *Materials Letters*, 61(14-15), pp.3009-3013.
- Liu-Snyder, P. & Webster, T.J., 2008. Developing a new generation of bone cements with nanotechnology. *Current Nanoscience*, 4, pp.111-118.
- Livak, K.J. & Schmittgen, T.D., 2001. Analysis of relative gene expression data using real-time quantitative PCR and the 2(-Delta Delta C(T)) Method. *Methods (San Diego, Calif.)*, 25(4), pp.402-408.
- Maccauro, G. et al., 2011. *Alumina and zirconia ceramic for orthopaedic and dental devices* R. Pignatello, ed., Intechopen. Available at: <http://www.intechopen.com/books/biomaterials-applications-for-nanomedicine/alumina-and-zirconia-ceramic-for-orthopaedic-and-dental-devices>.
- Maccauro, G. et al., 2010. In vivo characterization of Zirconia Toughened Alumina material: a comparative animal study. *International journal of immunopathology and pharmacology*, 23(3), pp.841-846.
- Maclaine, S.E. et al., 2012. Optimizing the osteogenicity of nanotopography using block co-polymer phase separation fabrication techniques. *Journal of Orthopaedic Research*, 30(8), pp.1190-1197.
- Maclaine, S.E. et al., 2013. THE PRODUCTION OF LIVING, TISSUE-ENGINEERED, BONE GRAFT FROM PROGENITOR CELLS USING NANOTECHNOLOGY. *Orthopaedic Proceedings*, 95-B(SUPP 33), pp.3-3.
- MacLennan, W.J., 1999. History of arthritis and bone rarefaction: evidence from paleopathology onwards. *Scottish Medical Journal*, (44), pp.18-20.
- Mahalingam, K. & Reidy, D., 1996. Smith-Petersen vitallium mould arthroplasty: a 45-year follow-up. *Journal of Bone & Joint Surgery*.
- Mahoney, O.M. & Dimon, J.H., 1990. Unsatisfactory results with a ceramic total hip prosthesis. *The Journal of Bone and Joint Surgery*, 72(5), pp.663-671.

- Mao, K. et al., 2009. Investigation of the histology and interfacial bonding between carbonated hydroxyapatite cement and bone. *Biomedical materials (Bristol, England)*, 4(4), p.045003.
- Marks, S.C. & Popoff, S.N., 1988. Bone cell biology: The regulation of development, structure, and function in the skeleton. *American Journal of Anatomy*, 183(1), pp.1-44.
- Marrs, B. et al., 2006. Augmentation of acrylic bone cement with multiwall carbon nanotubes. *Journal of Biomedical Materials Research Part A*, 77A(2), pp.269-276.
- Masri, B.A., Meek, R.M.D. & Duncan, C.P., 2004. Periprosthetic Fractures Evaluation and Treatment. *Clinical Orthopaedics and Related Research®*, 420, p.80.
- Massin, P. et al., 2014. Does Biolog Delta ceramic reduce the rate of component fractures in total hip replacement? *Orthopaedics & Traumatology: Surgery & Research*, 100(6 Suppl), pp.S317-S321.
- Mata, A. et al., 2009. Micropatterning of bioactive self-assembling gels. *Soft matter*, 5(6), pp.1228-1236.
- Mathieu, P.S. & Lobo, E.G., 2012. Cytoskeletal and focal adhesion influences on mesenchymal stem cell shape, mechanical properties, and differentiation down osteogenic, adipogenic, and chondrogenic pathways. *Tissue engineering. Part B, Reviews*, 18(6), pp.436-444.
- McBeath, R. et al., 2004. Cell shape, cytoskeletal tension, and RhoA regulate stem cell lineage commitment. *Developmental cell*, 6(4), pp.483-495.
- McKee, G.K., 1970. 10 Development of Total Prosthetic Replacement of the Hip. *Clinical Orthopaedics and Related Research®*, 72, p.85.
- McKee, M.D., Addison, W.N. & Kaartinen, M.T., 2005. Hierarchies of extracellular matrix and mineral organization in bone of the craniofacial complex and skeleton. *Cells, tissues, organs*, 181(3-4), pp.176-188.
- McMurray, R.J. et al., 2011. Nanoscale surfaces for the long-term maintenance of mesenchymal stem cell phenotype and multipotency. *Nature materials*, 10(8), pp.637-644.
- Meloche, S. & Pouyssegur, J., 2007. The ERK1/2 mitogen-activated protein kinase pathway as a master regulator of the G1- to S-phase transition. *Oncogene*, 26(22), pp.3227-3239.
- Meyer, T.S. & Lamberts, B.L., 1965. Use of coomassie brilliant blue R250 for the electrophoresis of microgram quantities of parotid saliva proteins on acrylamide-gel strips. *Biochimica et biophysica acta*, 107(1), pp.144-145.
- Mirmalek-Sani, S.-H. et al., 2006. Characterization and multipotentiality of human fetal femur-derived cells: implications for skeletal tissue regeneration. *Stem cells (Dayton, Ohio)*, 24(4), pp.1042-1053.

- Mittelmeier, H. & Heisel, J., 1992. Sixteen-years' experience with ceramic hip prostheses. *Clinical Orthopaedics and Related Research*®, (282), pp.64-72.
- Mizutani, S., Boettiger, D. & Temin, H.M., 1970. A DNA-dependent DNA polymerase and a DNA endonuclease in virions of Rous sarcoma virus. *Nature*, 226, pp.1211-1213.
- Moore, A.J. et al., 2015. Deep prosthetic joint infection: a qualitative study of the impact on patients and their experiences of revision surgery. *BMJ open*, 5(12), p.e009495.
- Morrison, T.A. et al., 2013. Periprosthetic joint infection in patients with inflammatory joint disease: a review of risk factors and current approaches to diagnosis and management. *HSS Journal*, 9(2), pp.183-194.
- Munevar, S., Wang, Y.L. & Dembo, M., 2001. Distinct roles of frontal and rear cell-substrate adhesions in fibroblast migration. *Molecular biology of the cell*, 12(12), pp.3947-3954.
- Munukka, E. et al., 2008. Bactericidal effects of bioactive glasses on clinically important aerobic bacteria. *Journal of Materials Science: Materials in Medicine*, 19(1), pp.27-32.
- Müller-Rath, R. et al., 2008. Amphiphilic bonder improves adhesion at the acrylic bone cement-bone interface of cemented acetabular components in total hip arthroplasty: in vivo tests in an ovine model. *Archives of orthopaedic and trauma surgery*, 128(7), pp.701-707.
- Nakamura, A. et al., 2009. Osteocalcin secretion as an early marker of in vitro osteogenic differentiation of rat mesenchymal stem cells. *Tissue engineering. Part C, Methods*, 15(2), pp.169-180.
- National Joint Registry for England, Wales & Ireland, N., 2013. National Joint Registry for England, Wales and Northern Ireland. *National Joint Registry for England, Wales and Northern Ireland*, pp.1-240.
- Navarro, E. et al., 2015. Real-time PCR detection chemistry. *Clinica chimica acta; international journal of clinical chemistry*, 439, pp.231-250.
- Neuman, K.C. & Nagy, A., 2008. Single-molecule force spectroscopy: optical tweezers, magnetic tweezers and atomic force microscopy. *Nature methods*, 5(6), pp.491-505.
- Neve, A., Corrado, A. & Cantatore, F.P., 2013. Osteocalcin: skeletal and extra-skeletal effects. *Journal of cellular physiology*, 228(6), pp.1149-1153.
- Ni, G.X. et al., 2006. Strontium-containing hydroxyapatite (Sr-HA) bioactive cement for primary hip replacement: An in vivo study. *Journal of Biomedical Materials Research Part A*, 77B(2), pp.409-415.
- Niinomi, M., Nakai, M. & Hieda, J., 2012. Development of new metallic alloys for biomedical applications. *Acta biomaterialia*, 8(11), pp.3888-3903.
- Nilsson, O. et al., 2007. Gradients in bone morphogenetic protein-related gene

- expression across the growth plate. *The Journal of endocrinology*, 193(1), pp.75-84.
- Norde, W., 1986. Adsorption of proteins from solution at the solid-liquid interface. *Advances in colloid and interface science*, 25(4), pp.267-340.
- Norris, T.R. & Iannotti, J.P., 2002. Functional outcome after shoulder arthroplasty for primary osteoarthritis: A multicenter study. *Journal of shoulder and elbow surgery / American Shoulder and Elbow Surgeons* 11(2), pp.130-135.
- O'Leary, J.F. et al., 1988. Mittelmeier ceramic total hip arthroplasty. A retrospective study. *Journal of Arthroplasty*, 3(1), pp.87-96.
- Oonishi, H. et al., 2000. Hydroxyapatite granules interposed at bone-cement interface in total hip replacements: Histological study of retrieved specimens. *Journal of Biomedical Materials Research Part A*, 53(2), pp.174-180.
- Orishimo, K.F. et al., 2003. Relationship Between Polyethylene Wear and Osteolysis in Hips with a Second-Generation Porous-Coated Cementless Cup After Seven Years of Follow-up. *The Journal of bone and joint surgery. American volume*, 85(6), pp.1095-1099.
- P, B. & D, B., 1981. [A study of the mechanical properties of alumina-on-alumina total hip prosthesis (author's transl)]. *Revue de chirurgie orthopedique et reparatrice de l'appareil moteur*, 67(3), pp.279-287.
- Pate, O. et al., 2009. Implant removal after submuscular plating for pediatric femur fractures. *Journal of pediatric orthopedics*, 29(7), pp.709-712.
- Petsatodis, G.E. et al., 2010. Primary cementless total hip arthroplasty with an alumina ceramic-on-ceramic bearing: results after a minimum of twenty years of follow-up. *The Journal of bone and joint surgery. American volume*, 92(3), pp.639-644.
- Pezzotti, G. et al., 2010. Nano-scale topography of bearing surface in advanced alumina/zirconia hip joint before and after severe exposure in water vapor environment. *Journal of Orthopaedic Research*, 28(6), pp.762-766.
- Pérez-Garnes, M. et al., 2011. Fibronectin distribution on demixed nanoscale topographies. *The International journal of artificial organs*, 34(1), pp.54-63.
- Pietschmann, M.F. et al., 2009. Cell quality affects clinical outcome after MACI procedure for cartilage injury of the knee. *Knee surgery, sports traumatology, arthroscopy : official journal of the ESSKA*, 17(11), pp.1305-1311.
- Pilliar, R.M., Lee, J.M. & Maniopoulos, C., 1986. Observations on the effect of movement on bone ingrowth into porous-surfaced implants. *Clinical Orthopaedics and Related Research®*, (208), pp.108-113.
- Pimenta, L., Pesántez, C. & Oliveira, L., 2008. Silicon matrix calcium phosphate as a bone substitute: early clinical and radiological results in a prospective

- study with 12-month follow-up. *SAS Journal*.
- Plenk, H., 1998. Prosthesis-bone interface. *Journal of Biomedical Materials Research Part A*, 43(4), pp.350-355.
- Porter, A.E. et al., 2004. Effect of sintered silicate-substituted hydroxyapatite on remodelling processes at the bone-implant interface. *Biomaterials*, 25(16), pp.3303-3314.
- Ratliff, A.H., 1983. Ernest William Hey Groves and his contributions to orthopaedic surgery. *Annals of the Royal College of Surgeons of England*, 65(3), pp.203-206.
- Restrepo, C. et al., 2010. Natural history of squeaking after total hip arthroplasty. *Clinical Orthopaedics and Related Research®*, 468(9), pp.2340-2345.
- Revell, P.A., 1983. Histomorphometry of bone. *Journal of clinical pathology*, 36(12), pp.1323-1331.
- Reyes, J.M.G. et al., 2006. Metabolic changes in mesenchymal stem cells in osteogenic medium measured by autofluorescence spectroscopy. *Stem cells (Dayton, Ohio)*, 24(5), pp.1213-1217.
- Rhineland, F.W., Rouweyha, M. & Milner, J.C., 1970. Microvascular and histogenic responses to implantation of a porous ceramic into bone. *Journal of Biomedical Materials Research Part A*, 5(1), pp.81-112.
- RIDLEY, H., 1952. Intra-ocular acrylic lenses after cataract extraction. *Lancet*, 1(6699), pp.118-121.
- Ring, P.A., 1968. Complete replacement arthroplasty of the hip by the ring prosthesis. *The Journal of bone and joint surgery. British volume*, 50(4), pp.720-731.
- Ring, P.A., 1974. Total replacement of the hip joint. A review of a thousand operations. *Journal of Bone & Joint Surgery, British Volume*, 56(1), pp.44-58.
- Rodríguez, J.P. et al., 2004. Cytoskeletal organization of human mesenchymal stem cells (MSC) changes during their osteogenic differentiation. *Journal of cellular biochemistry*, 93(4), pp.721-731.
- Rohner, D. et al., 2003. In vivo efficacy of bone-marrow-coated polycaprolactone scaffolds for the reconstruction of orbital defects in the pig. *Journal of biomedical materials research. Part B, Applied biomaterials*, 66(2), pp.574-580.
- Romanò, C.L. et al., 2014. A comparative study of the use of bioactive glass S53P4 and antibiotic-loaded calcium-based bone substitutes in the treatment of chronic osteomyelitis: a retrospective comparative study. *The Bone & Joint Journal*, 96-B(6), pp.845-850.
- Rothwell, A. et al., 2014. THE NEW ZEALAND JOINT REGISTRY. pp.1-168.

- Saikia, K.C. et al., 2008. Calcium phosphate ceramics as bone graft substitutes in filling bone tumor defects. *Indian journal of orthopaedics*, 42(2), pp.169-172.
- Sakai, T. et al., 2000. Prevention of fibrous layer formation between bone and adhesive bone cement: in vivo evaluation of bone impregnation with 4-META/MMA-TBB cement. *Journal of Biomedical Materials Research Part A*, 52(1), pp.24-29.
- Sanderson, M.J. et al., 2014. Fluorescence microscopy. *Cold Spring Harbor protocols*, 2014(10), p.pdb.top071795.
- Santin, M. et al., 1997. Adsorption of alpha-1-microglobulin from biological fluids onto polymer surfaces. *Biomaterials*, 18(11), pp.823-827.
- Sarmiento, A. & Grimes, H.A., 1963. The use of the Austin T. Moore vitallium prosthesis in the treatment of acute fractures and other diseases of the hip: Review of 123 consecutive cases. *Clinical Orthopaedics and Related Research*®, 28, pp.120-131.
- Scheltema, R.A. et al., 2011. PeakML/mzMatch: A File Format, Java Library, R Library, and Tool-Chain for Mass Spectrometry Data Analysis. *Analytical Chemistry*, 83(7), pp.2786-2793.
- Sela, J. et al., 1987. Ultrastructural tissue morphometry of the distribution of extracellular matrix vesicles in remodeling rat tibial bone six days after injury. *Acta anatomica*, 128(4), pp.295-300.
- Shan, L. et al., 2015. Intermediate and long-term quality of life after total knee replacement: a systematic review and meta-analysis. *The Journal of Bone and Joint Surgery*, 97(2), pp.156-168.
- SIMINOVITCH, L., McCULLOCH, E.A. & TILL, J.E., 1963. The distribution of colony-forming cells among spleen colonies. *Journal of cellular physiology*, 62, pp.327-336.
- Sloan, F.A., George, L.K. & Hu, L., 2013. Longer Term Effects of Total Knee Arthroplasty From a National Longitudinal Study. *Journal of Aging and Health*, 25(6), pp.982-997.
- Smith, C.A. et al., 2006. XCMS: processing mass spectrometry data for metabolite profiling using nonlinear peak alignment, matching, and identification. *Analytical Chemistry*, 78(3), pp.779-787.
- Smith-Petersen, M.N., 1948. Evolution of mould arthroplasty of the hip joint. 1948. *Clinical Orthopaedics and Related Research*®, 30 B(1), pp.59-75.
- Sodek, J. et al., 1995. Regulation of osteopontin expression in osteoblasts. *Annals of the New York Academy of Sciences*, 760, pp.223-241.
- Sodek, J., Ganss, B. & McKee, M.D., 2000. Osteopontin. *Critical Reviews in Oral Biology & Medicine*, 11(3), pp.279-303.
- Sorbie, C. & Saunders, G.A.B., 2008. Hemiarthroplasty in the treatment of hallux

- rigidus. *Foot & Ankle International*, 29(3), pp.273-281.
- Staines, K.A., MacRae, V.E. & Farquharson, C., 2012. The importance of the SIBLING family of proteins on skeletal mineralisation and bone remodelling. *The Journal of endocrinology*, 214(3), pp.241-255.
- Stavropoulos, A. et al., 2012. Histological evaluation of healing after transalveolar maxillary sinus augmentation with bioglass and autogenous bone. *Clinical Oral Implants Research*, 23(1), pp.125-131.
- Stewart, A.F. et al., 2000. Six-Month Daily Administration of Parathyroid Hormone and Parathyroid Hormone-Related Protein Peptides to Adult Ovariectomized Rats Markedly Enhances Bone Mass and Biomechanical Properties: A Comparison of Human Parathyroid Hormone 1-34, Parathyroid Hormo. *Journal of Bone and Mineral Research*, 15(8), pp.1517-1525.
- Stiehl, J.B., MacMillan, E. & Skrade, D.A., 1991. Mechanical stability of porous-coated acetabular components in total hip arthroplasty. *The Journal of arthroplasty*, 6(4), pp.295-300.
- Stupack, D.G. et al., 2001. Apoptosis of adherent cells by recruitment of caspase-8 to unligated integrins. *The Journal of cell biology*, 155(3), pp.459-470.
- Su, B. & Button, T.W., 2009. A comparative study of viscous polymer processed ceramics based on aqueous and non-aqueous binder systems. *Journal of Materials Processing Technology*, 209(1), pp.153-157.
- Su, B. et al., 2002. Embossing of 3D ceramic microstructures. *Microsystem Technologies*, 8(4-5), pp.359-362.
- Sulc, K. et al., 1977. Bone marrow cell separation on Ficoll gradient. *Haematologia*, 11(1-2), pp.41-46.
- Sun, J.-Y. et al., 2009. Treatment of high-energy tibial shaft fractures with internal fixation and early prophylactic NovaBone grafting. *Orthopaedic surgery*, 1(1), pp.17-21.
- Sun, S. et al., 2007. Physical manipulation of calcium oscillations facilitates osteodifferentiation of human mesenchymal stem cells. *FASEB journal : official publication of the Federation of American Societies for Experimental Biology*, 21(7), pp.1472-1480.
- Suzuki, K. et al., 2002. Colocalization of intracellular osteopontin with CD44 is associated with migration, cell fusion, and resorption in osteoclasts. *Journal of Bone and Mineral Research*, 17(8), pp.1486-1497.
- Szmukler-Moncler, S. et al., 1998. Timing of loading and effect of micromotion on bone-dental implant interface: review of experimental literature. *Journal of Biomedical Materials Research Part A*, 43(2), pp.192-203.
- Søballe, K. et al., 1992. Tissue ingrowth into titanium and hydroxyapatite-coated implants during stable and unstable mechanical conditions. *Journal of Orthopaedic Research*, 10(2), pp.285-299.

- Tai, S.M. et al., 2015. Squeaking in large diameter ceramic-on-ceramic bearings in total hip arthroplasty. *The Journal of arthroplasty*, 30(2), pp.282-285.
- Tamama, K., Sen, C.K. & Wells, A., 2008. Differentiation of bone marrow mesenchymal stem cells into the smooth muscle lineage by blocking ERK/MAPK signaling pathway. *Stem cells and development*, 17(5), pp.897-908.
- Tan, J.L. et al., 2003. Cells lying on a bed of microneedles: an approach to isolate mechanical force. *Proceedings of the National Academy of Sciences of the United States of America*, 100(4), pp.1484-1489.
- Tardy, N. et al., 2015. Small diameter metal-on-metal total hip arthroplasty at 13 years - a follow-up study. *Orthopaedics & Traumatology: Surgery & Research*, 101(8), pp.929-936.
- Teo, B.K.K. et al., 2013. Nanotopography modulates mechanotransduction of stem cells and induces differentiation through focal adhesion kinase. *ACS nano*, 7(6), pp.4785-4798.
- Theelke, B., Kuntz, M. & Zipperle, M., 2011. Development of Osseointegrative Ceramic Coatings Based on ZPTA--Mechanical Characterization and Influence on the Substrate. *Bioceramics Development and Applications*, 1, pp.1-4.
- Thomas, M.V. & Puleo, D.A., 2009. Calcium sulfate: Properties and clinical applications. *Journal of biomedical materials research. Part B, Applied biomaterials*, 88(2), pp.597-610.
- THOMPSON, F.R., 1954. Two and a half years' experience with a vitallium intramedullary hip prosthesis. *The Journal of bone and joint surgery. American volume*, 36-A(3), pp.489-502.
- Titushkin, I. & Cho, M., 2011. Altered osteogenic commitment of human mesenchymal stem cells by ERM protein-dependent modulation of cellular biomechanics. *Journal of Biomechanics*, 44(15), pp.2692-2698.
- Titushkin, I.A. & Cho, M.R., 2009. Controlling cellular biomechanics of human mesenchymal stem cells. *Conference proceedings : ... Annual International Conference of the IEEE Engineering in Medicine and Biology Society. IEEE Engineering in Medicine and Biology Society. Annual Conference, 2009*, pp.2090-2093.
- Tonelli, F.M.P. et al., 2012. Stem cells and calcium signaling. *Advances in experimental medicine and biology*, 740, pp.891-916.
- Treiser, M.D. et al., 2010. Cytoskeleton-based forecasting of stem cell lineage fates. *Proceedings of the National Academy of Sciences*, 107(2), pp.610-615.
- Triffitt, J.T. et al., 1998. Osteogenesis: bone development from primitive progenitors. *Biochemical Society transactions*, 26(1), pp.21-27.
- Tsimbouri, P. et al., 2014. Nanotopographical effects on mesenchymal stem cell morphology and phenotype. *Journal of cellular biochemistry*, 115(2), pp.380-390.

- Tsimbouri, P.M. et al., 2012. Using nanotopography and metabolomics to identify biochemical effectors of multipotency. *ACS nano*, 6(11), pp.10239-10249.
- Uribe, J. et al., 2013. Degradation of alumina and zirconia toughened alumina (ZTA) hip prostheses tested under microseparation conditions in a shock device. *The International Conference on BioTribology 2011*, 63 IS -, pp.151-157.
- Valancius, K. et al., 2013. No superior performance of hydroxyapatite-coated acetabular cups over porous-coated cups. *Acta orthopaedica*, 84(6), pp.544-548.
- vidalain, J.-P., 2011. Twenty-year results of the cementless Corail stem. *International Orthopaedics*, 35(2), pp.189-194.
- Vielgut, I. et al., 2013. The modified Harrington procedure for metastatic peri-acetabular bone destruction. *International Orthopaedics*, 37(10), pp.1981-1985.
- Viste, A. et al., 2012. Fractures of a sandwich ceramic liner at ten year follow-up. *International Orthopaedics*, 36(5), pp.955-960.
- Voigt, J.D. & Mosier, M., 2011. Hydroxyapatite (HA) coating appears to be of benefit for implant durability of tibial components in primary total knee arthroplasty. *Acta orthopaedica*, 82(4), pp.448-459.
- Volpato, C., Bondioli, F. & Garbelotto, L., 2011. *Application of zirconia in dentistry: biological, mechanical and optical considerations* C. Siklaidis, ed., InTech.
- W jciak-Stothard, B. et al., 1995. Role of the cytoskeleton in the reaction of fibroblasts to multiple grooved substrata. *Cell Motility and the Cytoskeleton*, 31(2), pp.147-158.
- Waddell, B.S. et al., 2016. Financial Analysis of Treating Periprosthetic Joint Infections at a Tertiary Referral Center. *The Journal of arthroplasty*, 31(5), pp.952-956.
- Wang, A. & Schmidig, G., 2003. Ceramic femoral heads prevent runaway wear for highly crosslinked polyethylene acetabular cups by third-body bone cement particles. *Wear*, 255(7-12), pp.1057-1063.
- Wang, N. & Ingber, D.E., 1995. Probing transmembrane mechanical coupling and cytomechanics using magnetic twisting cytometry. *Biochemistry and cell biology = Biochimie et biologie cellulaire*, 73(7-8), pp.327-335.
- Wang, W. et al., 2014. Fourth-generation ceramic-on-ceramic total hip arthroplasty in patients of 55 years or younger: short-term results and complications analysis. *Chinese Medical Journal-Beijing*, 127(12), pp.2310-2315.
- Ward, D.F. et al., 2007. Mechanical strain enhances extracellular matrix-induced gene focusing and promotes osteogenic differentiation of human

mesenchymal stem cells through an extracellular-related kinase-dependent pathway. *Stem cells and development*, 16(3), pp.467-480.

- Warden, W.H., Chooljian, D. & Jackson, D.W., 2008. Ten-year magnetic resonance imaging follow-up of bioabsorbable poly-L-lactic acid interference screws after anterior cruciate ligament reconstruction. *YJARS*, 24(3), pp.370-373.
- Watts, J.F., 1990. *An Introduction to Surface Analysis by Electron Spectroscopy*, Oxford University Press, USA.
- Wazen, R.M. et al., 2013. Micromotion-induced strain fields influence early stages of repair at bone-implant interfaces. *Acta biomaterialia*, 9(5), pp.6663-6674.
- Weiler, A. et al., 2000. Biodegradable implants in sports medicine: the biological base. *YJARS*, 16(3), pp.305-321. Available at: <http://eutils.ncbi.nlm.nih.gov/entrez/eutils/elink.fcgi?dbfrom=pubmed&id=10750011&retmode=ref&cmd=prlinks>.
- Wilkinson, A. et al., 2011. Biomimetic microtopography to enhance osteogenesis in vitro. *Acta biomaterialia*, 7(7), pp.2919-2925.
- Wilkinson, C. et al., 2002. The use of materials patterned on a nano-and micro-metric scale in cellular engineering. *Materials Science and Engineering, C* 19, pp.263-269.
- Wolf, G., 1996. Function of the bone protein osteocalcin: definitive evidence. *Nutrition reviews*, 54(10), pp.332-333.
- Wood, M.A., 2007. Colloidal lithography and current fabrication techniques producing in-plane nanotopography for biological applications. *Journal of the Royal Society, Interface / the Royal Society*, 4(12), pp.1-17.
- Woodruff, M.A. & Hutmacher, D.W., 2009. The return of a forgotten polymer—Polycaprolactone in the 21st century. *Progress in Polymer Science*, 35(10), pp.1217-1256.
- Worthylake, R.A. & Burridge, K., 2003. RhoA and ROCK promote migration by limiting membrane protrusions. *The Journal of biological chemistry*, 278(15), pp.13578-13584.
- Wozniak, M.A. et al., 2004. Focal adhesion regulation of cell behavior. *Biochimica et biophysica acta*, 1692(2-3), pp.103-119.
- Wójciak-Stothard, B., 1995. Activation of macrophage-like cells by multiple grooved substrata. Topographical control of cell behaviour. *Cell Biology International*, 19(6), pp.485-490.
- Wroblewski, B.M., 2005. Low-Friction Arthroplasty of the Hip Using Alumina Ceramic and Cross-Linked Polyethylene: a 17-Year Follow-Up Report. *Journal of Bone & Joint Surgery, British Volume*, 87-B(9), pp.1220-1221.
- Xia, J. et al., 2009. MetaboAnalyst: a web server for metabolomic data analysis

- and interpretation. *Nucleic Acids Research*, 37(Web Server issue), pp.W652-60.
- Xynos, I.D. et al., 2001. Gene-expression profiling of human osteoblasts following treatment with the ionic products of Bioglass 45S5 dissolution. *Journal of Biomedical Materials Research Part A*, 55(2), pp.151-157.
- Yanes, O. et al., 2010. Metabolic oxidation regulates embryonic stem cell differentiation. *Nature chemical biology*, 6(6), pp.411-417.
- Yang, J. et al., 2014. Nanotopographical induction of osteogenesis through adhesion, bone morphogenetic protein cosignaling, and regulation of microRNAs. *ACS nano*, 8(10), pp.9941-9953.
- Yeo, C. et al., 2009. Ficoll-Paque versus Lymphoprep: a comparative study of two density gradient media for therapeutic bone marrow mononuclear cell preparations. *Regenerative medicine*, 4(5), pp.689-696.
- Yeung, K. et al., 2000. Mechanism of suppression of the Raf/MEK/extracellular signal-regulated kinase pathway by the raf kinase inhibitor protein. *Molecular and Cellular Biology*, 20(9), pp.3079-3085.
- Yuan, L.J. & Shih, C.H., 1999. Dislocation after total hip arthroplasty. *Archives of orthopaedic and trauma surgery*, 119(5-6), pp.263-266.
- Zhu, B. et al., 2004. Osteopontin modulates CD44-dependent chemotaxis of peritoneal macrophages through G-protein-coupled receptors: Evidence of a role for an intracellular form of osteopontin. *Journal of cellular physiology*, 198(1), pp.155-167.
- Zohar, R. et al., 1998. Analysis of intracellular osteopontin as a marker of osteoblastic cell differentiation and mesenchymal cell migration. *European journal of oral sciences*, 106 Suppl 1, pp.401-407.
- Zohar, R. et al., 2000. Intracellular osteopontin is an integral component of the CD44-ERM complex involved in cell migration. *Journal of cellular physiology*, 184(1), pp.118-130.
- Zohar, R. et al., 1997. Single cell analysis of intracellular osteopontin in osteogenic cultures of fetal rat calvarial cells. *Journal of cellular physiology*, 170(1), pp.88-100.
- Zouani, O.F. et al., 2012. Altered nanofeature size dictates stem cell differentiation. *Journal of cell science*, 125(Pt 5), pp.1217-1224.

8 Appendices

8.1 Osteogenic array plate format

	1	2	3	4	5	6
A	18S	GAPDH	HPRT1	GUSB	AHSG	ALPL
B	BMP3	BMP4	BMP5	BMP6	BMP7	BMPR1A
C	COL14A1	COL15A1	COL16A1	COL17A1	COL18A1	COL19A1
D	COL4A5	COL5A1	COL7A1	COL9A2	COPM	CSF2
E	FGF2	FGF3	FGFR1	FGFR2	FGFR3	FLT1
F	MINPP1	MMP13	MMP2	MMP8	MSX1	MSX2
G	SMAD3	SMAD4	SMAD5	SMAD6	SMAD7	SMAD9
H	TGFB1	TGFB2	TGFB3	TGFBR1	TGFBR2	TUFT1
	7	8	9	10	11	12
A	AMBN	AMELY	ARSE	BGLAP	BMP1	BMP2
B	CALCR	CASR	CDH11	COL10A1	COL11A1	COL12A1
C	COL1A1	COL1A2	COL2A1	COL3A1	COL4A3	COL4A4
D	CSF3	DMP1	EGF	EGFR	ENAM	FGF1
E	GDF10	IBSP	IGF1	IGFR1	IGF2	MGP
F	DSPP	PDGFA	PHEX	RUNX2	SMAD1	SMAD2
G	SOST	SOX9	SPARC	SPP1	STATH	TFIP11
H	TWIST	TWIST2	VDR	VEGFA	VEGFB	VEGFC